# A Sensor for Metabolic Profiling of Traumatic Brain Injury

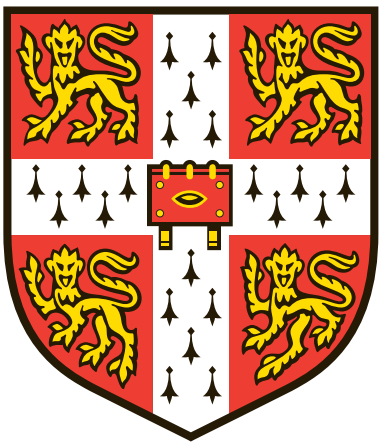

Victoria Helen Highland

Newnham College

University of Cambridge

**This dissertation is submitted for the degree of**
**Doctor of Philosophy**
**January 2018**

# Declaration

This dissertation is the result of my own work and includes nothing which is the outcome of work done in collaboration except as declared in the Preface and specified in the text.

It is not substantially the same as any that I have submitted, or, is being concurrently submitted for a degree or diploma or other qualification at the University of Cambridge or any other University or similar institution except as declared in the Preface and specified in the text. I further state that no substantial part of my dissertation has already been submitted, or, is being concurrently submitted for any such degree, diploma or other qualification at the University of Cambridge or any other University or similar institution except as declared in the Preface and specified in the text.

It does not exceed the prescribed word limit for the relevant Degree Committee.

# Abstract

A Sensor for Metabolic Profiling of Traumatic Brain Injury
Victoria Helen Highland

A Traumatic Brain Injury (TBI) occurs when brain tissue is damaged as a result of an external mechanical force. It is a global health issue which, when serious, can result in death or permanent disability. The damage caused by the initial trauma continues to evolve in the days following the incident and therefore patients with a serious TBI are closely monitored so that, if any change in the condition of the brain is detected, an appropriate medical intervention can be made. Metabolic profiling of extracellular brain fluid can be used to monitor brain health, as it provides data on the efficiency of metabolic processes taking place within the brain. If metabolism is disrupted, causing energy failure in the brain, it can lead to the destruction of brain cells and a poor patient outcome.

D-glucose, L-lactate and pyruvate are the metabolic intermediates most commonly monitored following TBI. Their respective concentrations are currently measured via a two-stage process: the constituents of the extracellular brain fluid are first extracted by microdialysis and are then analysed via a series of colorimetric assays which are carried out using a commercially-available analyser. The use of this analyser presents a number of drawbacks which have prevented the widespread use of metabolic profiling in the management of TBI. For example, the process of manually loading samples into the analyser is both time- and labour-intensive and therefore is carried out only intermittently by clinical staff. As a result, metabolic profiling data cannot be obtained in real time and any necessary medical intervention may consequently be delayed.

This thesis describes the work undertaken to develop a spectroscopic method, and an associated statistical model, for the detection of glucose, lactate and pyruvate that could be directly integrated into the existing microdialysis setup and thus used for continuous metabolic profiling of TBI patients. The techniques of Raman spectroscopy and Fourier Transform Infra-Red (FTIR) spectroscopy were investigated to determine whether they could selectively detect glucose, lactate and pyruvate in solution and whether they possessed the sensitivity required to detect those compounds at clinically-relevant concentrations. Consideration was also given to the practicalities

of adapting each technique to the specific requirements of the clinical setting in which it would be used. These initial studies indicated that FTIR spectroscopy showed the greater promise for development into a sensor and therefore subsequent work focused only on this technique. A detailed study was carried out in order to compare various FTIR spectroscopy methods. The data generated were used to build and test a statistical model for the prediction of clinically-relevant glucose, lactate and pyruvate concentrations from their FTIR spectra. The results of this work provide important insights into the capabilities of currently-available FTIR techniques, when used in combination with predictive statistical modelling, and will be used to guide the next phase of sensor development.

*Dedicated with love to Bill, Helen and John.*

# Acknowledgements

The last four years have been a significant learning curve, often in ways that I had not expected. One of the most important things I have learned over the last four years is that, despite what the declaration at the beginning of every thesis might say, a PhD is very much a team effort. From scientific discussions and demonstrations, to navigating the world of academia, to practical and emotional support, I have been lucky enough to receive help from so many people. As a result, I have many, many people to thank...

Firstly, I must thank my supervisor, Professor Stephen Elliott, for giving me the opportunity to undertake this work and for his financial support during my final year. I am particularly grateful for his help in shaping and proof-reading this thesis. I would also like to thank Dr Tanya Hutter for her enthusiasm and support throughout this project.

I would like to take the opportunity to say a huge 'thank you' to Dr Anna Hüfner for her exceptional mentoring, which included a number of helpful discussions about this project, MATLAB tutoring and wise advice about PhD life in general. Significant thanks are also owed to to Dr Mike Casford, for providing access to the Spectrum 100 and for the many helpful discussions about FTIR spectroscopy, as well as to Dr Yury Alaverdyan for his invaluable guidance with the Raman work. I am sincerely grateful for their help. I am also grateful to the many other people who so generously gave their time to offer advice and/or practical assistance with experiments, many of which did not make it into this thesis. Thank you to Dr Matthew Capener, Dr Thomas Mueller, Dr Jerome Charmet and Duncan Howe. I was also lucky to receive excellent support from the superb technical services teams in the Chemistry Department, particularly Manuel Wentscher and Wayne Bailey, as well as from Clive Tubbs from the Department of Architecture.

Thank you very much to those members of the Department who offered such significant support and guidance during my final year, in particular to Dr Deborah Longbottom and Professor Markus Kalberer. I am also very grateful to have received support from Dr Paul Barker and Rachel MacDonald, as well as financial support from the Graduate Education Committee and Newnham College.

I am extremely grateful to Professor Liz Varga for her invaluable advice which

helped to shape this thesis.

Thank you also to the Elliott Group - Anna, Coco, Farah, Felix, Kostas, João, Marcin, Paul, Sarah, Taehoon, Tas and Yuchen for being such a great group of people to work alongside.

Finally, the biggest thanks of all must go to my family and friends for their support and for so many happy memories, which cover far more than just the last four years:

To my wonderful friends (you know who you are): you are all amazing. Thank you for keeping me sane and for so many good times - I could not have done this without you all. Special thanks to Becky for advising and supporting me through my final year; to Megan, Charlotte and Sophie for their support while writing this thesis; to team 32:52 and to Beth, forever my Head Honcho.

To Diane and Paul, the best in-laws I could ask for: thank you for being the source of so many of the highlights of the last four years. I'm so happy to be a part of the Ackroyd family.

I'm blessed to have a wonderful family who mean the world to me. To Nan, Pops, Chris, Mel, Harry, Ollie, Nick, Corn, Olivia, Vee, Paul and Ted: thank you for your love, support and belief in me.

To Tom and Katie: thank you for your support and friendship - I'm so lucky to have you.

To Mum and Dad: I don't know where to begin. Thank you so much for all you have done and continue to do for me, for inspiring my love of science in the first place and for your constant support.

Finally, to Mike: thank you for being by my side through it all. Here's to the next chapter - I love you.

# List of abbreviations

| | |
|---|---|
| **ANOVA** | Analysis of Variance |
| **ATP** | Adenosine Triphosphate |
| **ATR** | Attenuated Total Reflectance |
| **°C** | Degrees Celsius |
| **CCD** | Charge-Coupled Device |
| **cm** | Centimetres |
| **cm$^{-1}$** | Wavenumbers |
| **DI** | Deionised |
| **DNA** | Deoxyribonucleic Acid |
| **FAD** | Flavin Adenine Dinucleotide |
| **FRET** | Förster Resonance Energy Transfer |
| **FTIR** | Fourier Transform Infra Red |
| **g** | Grams |
| **HATR** | Horizontal Attenuated Total Reflectance |
| **ICP** | Intracranial Pressure |
| **IR** | Infra-Red |
| **k** | Force Constant |
| **k$_B$** | Boltzmann Constant |
| **kDa** | Kilodaltons |
| **LoB** | Limit of Blank |

| | |
|---|---|
| **LoD** | Limit of Detection |
| **LoQ** | Limit of Quantification |
| **LPR** | Lactate:Pyruvate Ratio |
| **$\mu$L** | Microlitre |
| **$\mu$m** | Micrometre |
| **mM** | Millimolar |
| **mW** | Milliwatt |
| **MCT** | Mercury Cadmium Telluride |
| **MIP** | Molecularly Imprinted Polymer |
| **nm** | Nanometre |
| **PCA** | Principal Component Analysis |
| **PCR** | Principal Component Regression |
| **PDMS** | Polydimethylsiloxane |
| **PET** | Polyethylene Terephthalate |
| **PLSR** | Partial Least Squares Regression |
| **QCL** | Quantum Cascade Laser |
| **QCM** | Quartz Crystal Microbalance |
| **RMSECV** | Root Mean Squared Error of Cross-Validation |
| **RMSEP** | Root Mean Squared Error of Prediction |
| **RSS** | Residual Sum of Squares |
| **rsMD** | Rapid Sampling Microdialysis |
| **s** | Second |
| **SERS** | Surface-Enhanced Raman Spectroscopy |
| **SPR** | Surface Plasmon Resonance |
| **TBI** | Traumatic Brain Injury |
| **TCA** | Tricarboxylic Acid |
| **TMB** | 3,3',5,5'-Tetramethylbenzidine |
| **V** | Volt |

# Contents

# List of Figures

# List of Tables

# Chapter 1

# Thesis Overview

## 1.1 Motivation & Aims

A Traumatic Brain Injury (TBI) is a highly heterogeneous condition in which brain tissue is physically damaged as a result of an external mechanical force. Severe TBI can lead to death or permanent disability and therefore patients with a serious injury are closely monitored for signs of injury progression.

The concentrations of metabolic intermediates present in the extracellular brain fluid provide an insight into the metabolic status, and hence the physical health, of brain tissue. This fluid can be sampled using the technique of microdialysis, in which a catheter possessing a permeable outer wall is inserted into the brain. Perfusion fluid (a solution containing a combination of chloride salts) is continuously pumped through the catheter and the resulting concentration gradient causes the constituents of the extracellular brain fluid, including the metabolic intermediates, glucose, lactate and pyruvate, to diffuse into the catheter. The resulting solution, known as microdialysate, is pumped out of the catheter and collected in a vial for analysis.

This thesis describes an investigation to determine whether vibrational spectroscopy could be used as the basis for an on-line sensor to monitor the concentrations of glucose, lactate and pyruvate present in the microdialysate as it is pumped out of the catheter. Two forms of vibrational spectroscopy were studied: Fourier Transform Infra-Red (FTIR) spectroscopy and Raman spectroscopy.

FTIR spectroscopy involves the absorption of specific wavelengths of Infra-Red (IR) radiation by a sample. The absorbed wavelengths correspond to the energy required to increase the vibrational energy of certain bonds within a molecule and hence can be used to determine which bonds are present.

Raman spectroscopy is also used to determine the nature of chemical bonds present in a sample but is based upon the scattering, rather than absorption, of photons. The technique involves the inelastic scattering of photons by a sample, wherein the difference in energy between the incident and scattered photons corresponds to a

difference in the vibrational energy of specific bonds within the molecule.

## 1.2 Experimental Work

During the first phase of this project, synthetic solutions of glucose, lactate and pyruvate in perfusion fluid were analysed via both FTIR and Raman spectroscopy.

The FTIR study was used to investigate two forms of FTIR spectroscopy: transmission-FTIR and Attenuated Total Reflection FTIR (ATR-FTIR). Both techniques were used to acquire FTIR spectra of pure solutions of glucose, lactate and pyruvate, as well as mixtures of all three solutions. Spectra acquired using the same technique were compared in order to identify absorbance peaks unique to each compound. FTIR spectra of additional molecules likely to be present in microdialysate samples were also acquired, in order to estimate the impact that these compounds might have on the detection of glucose, lactate and pyruvate by FTIR spectroscopy. Transmission-FTIR spectroscopy was also used to analyse a small number of clinical samples. Finally, a quantitative study was carried out to determine which ATR-FTIR and transmission-FTIR accessories yielded the lowest detection limits for glucose, lactate and pyruvate and would thus be the most suitable for later, in-depth, studies of each technique.

The Raman study began with attempts to acquire spectra of pure solutions of glucose, lactate and pyruvate. These results prompted a sub-project to determine whether Surface-Enhanced Raman Spectrosopy (SERS) was a more viable technique with which detect these compounds, using cysteine as a model compound.

The second phase of this project entailed systematic studies of the performances of ATR-FTIR and transmission-FTIR spectroscopy. Both techniques were used to acquire spectra of a series of synthetic mixtures containing glucose, lactate and pyruvate at a range of clinically-relevant concentrations. The acquired spectra were used to develop a statistical model which was optimised for the prediction of glucose, lactate and pyruvate concentrations from FTIR spectra of mixtures of all three compounds. This model was used to analyse the transmission-FTIR spectra of a small number of clinical microdialysate samples.

## 1.3 Note on Terminology

Throughout this thesis, the terms ‘Limit of Detection’ (LoD) and ‘Limit of Quantification’ (LoQ) are used to describe aspects of sensor performance. The LoD, as used in this thesis, describes the smallest concentration of an analyte that produces a measurable signal. The LoQ is the smallest concentration of an analyte that can be both detected and differentiated from other concentrations of that analyte, to a predetermined degree of accuracy.

## 1.4 Guide to Chapters

The following paragraphs provide the reader with a brief guide to the contents of each chapter in this thesis. In general, Chapters 2, 3 and 4 cover background information and theory, whilst Chapters 5 – 10 discuss the methods, results and conclusions of the work carried out.

**Chapter 2** provides the clinical context for the work described in this thesis. An introduction to the pathophysiology of TBI is given, as well as a description of the current techniques used for metabolic profiling of patients and a discussion of the roles played by glucose, lactate and pyruvate in TBI. The project aims are also discussed in detail.

**Chapter 3** describes the theory behind the tools and methods used in this work: FTIR spectroscopy, Raman spectroscopy and statistical modelling.

**Chapter 4** provides a review of the scientific literature, discussing recent advances made in the research fields most closely related to this work.

**Chapter 5** provides details of the reagents, instrumentation, experimental methods and statistical methods used routinely in this work.

**Chapter 6** describes the preliminary studies carried out to assess the potential utility of FTIR spectroscopy as a tool for metabolic profiling of TBI patients.

**Chapter 7** describes the preliminary studies carried out to assess the potential utility of Raman spectroscopy and SERS as tools for metabolic profiling of TBI patients.

**Chapter 8** describes a detailed systematic study into the use of ATR-FTIR spectroscopy, combined with predictive statistical modelling, to predict the concentrations of glucose, lactate and pyruvate when combined in mixtures at clinically-relevant concentrations.

**Chapter 9** describes a detailed systematic study into the use of transmission-FTIR spectroscopy, combined with predictive statistical modelling, to predict the concentrations of glucose, lactate and pyruvate when combined in mixtures at clinically-relevant concentrations. The performance of the predictive model when applied to clinical microdialysate samples is also discussed.

**Chapter 10** discusses the conclusions that can be drawn from this work and its application to the development of a sensor for metabolic profiling of TBI patients. Possible next steps and areas of consideration for future sensor development are also discussed.

# Chapter 2

# Project Background

The aim of this chapter is to provide context for the work described in this thesis. It presents a brief introduction to the nature of traumatic brain injury and why it is necessary to study the metabolic profiles of brain-injured patients, an explanation of how this is currently achieved in the clinic and a discussion of the disadvantages of the current system. Finally, it describes the aims of the work undertaken and lists the desired properties of a sensor for metabolic profiling of traumatic brain injury.

## 2.1 Introduction to TBI

A Traumatic Brain Injury (TBI) is an injury to brain tissue caused by an external mechanical force. This force may result from a variety of incidents including: violence, road-traffic accidents, falls or sporting accidents and, as a result, TBI is a global health issue which is prevalent in both low- and high-income countries and across all age groups.

The outcome of TBI varies significantly between patients: some experience only a mild concussion, from which they make a full recovery, whilst severe TBI can result in death or permanent disability. In addition to the personal cost to the patient and their family, severe TBI therefore poses a major socio-economic burden: in Europe, TBI is responsible for the greatest number of years lived with disability resulting from trauma and is among the top three causes of injury-related medical costs.[1] The global incidence of TBI has risen sharply in recent decades: in developing countries, this is predominantly due to an increased use of motor vehicles,[1] whilst in developed countries there is an increasing incidence of TBI in the older population due to falls.[2] Within the UK, a recent report by the National Institute for Health and Care Excellence suggested that head injury is the most common type of trauma seen in hospital emergency departments, accounting for 10% of all emergency department cases each year.[3] Effective management of TBI cases is therefore of critical importance, both within the UK and worldwide.

## 2.2 Mechanism of TBI

The extent and type of damage to the brain following a TBI is dependent on a number of factors: the nature of the external force (for example: direct impact, rapid acceleration or deceleration, penetration by an external object or blast waves from an explosion) as well as its intensity, direction and duration all affect the presentation of the injury. TBI is therefore a highly heterogeneous condition encompassing multiple different types of brain damage, some or all of which may be present to varying degrees in a given individual. This heterogeneity is considered one of the most significant barriers to finding effective therapeutic interventions for treating TBI.[4]

The progression of a TBI can be divided into two phases: the primary injury, which occurs within minutes or hours of the traumatic event, and the secondary injury, which evolves in the following hours and days.

Damage sustained by the brain during the primary injury can include: damage to blood vessels, bruising of brain tissue and the shearing of bundles of axons that connect different regions of the brain. The secondary injury is caused when these early neurotraumatic events trigger additional pathophysiological mechanisms which cause further damage to the brain. In many cases, these secondary mechanisms are induced concurrently and with synergistic effect, thus increasing the damage caused. One example of such a mechanism is the release of excessive amounts of excitatory neurotransmitters, such as glutamate, into the interstitial fluid, which exacerbates brain swelling, raises the intracranial pressure (ICP) and is ultimately a major cause of early necrotic cell death. The extent of the secondary injury is determined by the nature, severity and duration of these secondary mechanisms, combined with the intensity of any systemic insults to the rest of the body.

## 2.3 Monitoring TBI

Secondary brain injury is the leading cause of in-hospital deaths that occur following a TBI.[5] It is therefore essential that patients are closely monitored for secondary brain damage, which may not exhibit any obvious clinical symptoms, so that it can be detected at the earliest possible stage and its progression studied. These observations can then be used to inform treatment decisions, which may lead to an improved outcome for the patient.

In severely brain-injured patients, the condition of the brain is monitored directly via the insertion of up to three different probes into the brain tissue itself. The method by which this is achieved and the region of the brain in which the probes are placed will vary between patients, as these parameters are determined by institutional protocol and the nature of the injury, respectively. The three properties monitored using these probes are: ICP, cerebral tissue oxygenation and the concentrations of metabolites in

the extracellular fluid.

Measurement of ICP, the pressure within the skull, provides information about the blood flow to the brain, whilst measurement of cerebral tissue oxygenation provides information about the oxygen saturation of the brain tissue itself. These parameters are monitored in order to ensure that there is adequate blood flow to the brain and that sufficient oxygen and glucose are delivered to ensure the preservation of any brain tissue that has not been irreparably damaged by the initial physical insult. Monitoring the concentration of brain metabolites provides information on the metabolic processes occurring within the brain. It is known that the cellular damage caused by TBI can induce changes in energy metabolism within the brain, via a number of different pathways, which can ultimately lead to energy failure and the subsequent activation of apoptotic and necrotic pathways.[6] Knowledge of ICP, cerebral tissue oxygenation and metabolic perturbations with the brain has significant implications for how TBI patients are managed.

Patients may be monitored in this way for 3 – 5 days and, whilst the cerebral tissue oxygenation and ICP probes allow for continuous automated measurement of these parameters, the monitoring of extracellular brain chemistry is labour-intensive and requires regular intervention by clinical staff. These factors are thought to limit the number of neurocritical care centres able to study the extracellular brain chemistry of brain-injured patients and therefore there is a clear clinical need to find a more straightforward method of doing so, which this thesis aims to address. In order to put this work in context, the following sections will discuss in more detail the method by which extracellular brain chemistry is currently monitored.

### 2.3.1 Microdialysis in TBI

The probe used to monitor extracellular brain chemistry is a fine catheter consisting of two concentric tubes capped with a gold end, which allows it to be visualised via neuroimaging techniques. The outer tube is connected to a syringe pump that delivers a solution of perfusion fluid at a constant flow rate of 0.3 $\mu$L min$^{-1}$. The lower portion of the wall of the outer tube is composed of a semi-permeable membrane, which typically has a 100 kDa molecular weight cut-off, that allows the bi-directional diffusion of molecules between the catheter and the surrounding extracellular fluid. The continuous flow of perfusion fluid ensures that equilibrium across this membrane is never reached, thus creating a permanent concentration gradient across the membrane which facilitates the movement of molecules from the extracellular brain fluid into the catheter. The tip of the catheter is sealed and therefore, upon reaching the end of the outer tube, the solution is directed upwards through the inner tube where it flows out of the catheter and into an external collection vial. This vial is typically changed hourly and its contents, known as microdialysate, are currently analysed via enzyme-

catalysed colorimetric assays using a commercially-available analyser (Section 2.3.3). This process of extracting the compounds present in extracellular brain fluid, known as microdialysis, is summarised in Figure 2.1.

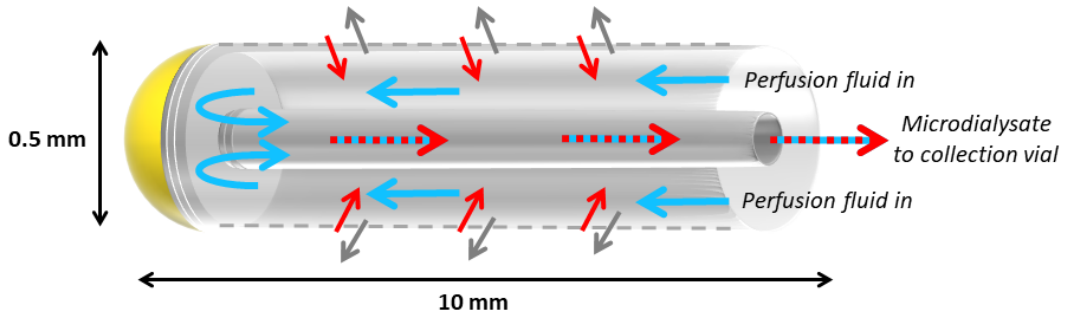


***Figure 2.1:*** *Illustration of the lower portion of a microdialysis catheter, showing the inner and outer tubes and the gold-tipped closed end. The walls of the outer tube are made of a semi-permeable membrane, allowing the exchange of substances between the catheter and surrounding tissue (grey/red arrows). Perfusion fluid is pumped into the outer tube at a rate of 0.3 μL/min (blue arrows), where it mixes with molecules that have entered the catheter from the surrounding tissue. This mixture flows out of the catheter via the inner tube (red and blue striped arrows) and is collected in a vial for analysis.*

Microdialysis does not recover 100% of molecules present in the interstitial brain fluid and therefore the measured concentration of a substance in the microdialysate is not a measure of the true concentration of that substance in the extracellular space. However, the measured concentration can be related to the true concentration by the 'relative mean recovery' value: the microdialysate concentration expressed as a percentage of the true interstitial concentration. The relative mean recovery is affected by two main factors: the location of the catheter itself and the properties of the perfusion fluid used.

The properties of the tissue into which the catheter is placed can affect the relative mean recovery value by altering the amount of a substance available for collection via microdialysis. For example, placement of the catheter into tissue which contains leaking blood vessels, or which is otherwise damaged, reduces the availability of a given substance near the catheter and therefore decreases the relative mean recovery value.

Two properties of the perfusion fluid can affect the relative mean recovery: its flow rate and its components. The flow rate of perfusion fluid through the catheter affects the relative mean recovery as it determines the amount of time available for molecules to diffuse across the catheter membrane: the slower the flow rate, the more time is available for diffusion and the higher the relative mean recovery. The commonly-used

flow rate of 0.3 $\mu$L min$^{-1}$, in combination with a standard 10 mm length membrane, generates an estimated mean recovery of $65-72\%$ for the molecules that are typically monitored in a clinical setting (see Section 2.3.2).

The constituents of the perfusion fluid affect the concentration gradients across the catheter membrane and therefore have an effect on not only the relative mean recovery but also the microenvironment of the extracellular fluid surrounding the catheter. The perfusion fluid routinely used for brain microdialysis in the clinic is an un-buffered solution containing salts of sodium, potassium, calcium and magnesium at concentrations similar to those found in the interstitial fluid: 147 mM NaCl, 2.7 mM KCl, 1.2 mM $CaCl_2$ and 0.85 mM $MgCl_2$. Sodium, potassium and calcium ions play a major role in cell signalling and their inclusion in perfusion fluid at physiological pH is intended to minimise their movement across the microdialysis membrane. Similarly, magnesium ions play an important role in the functioning of certain glutamate receptors, which are involved in the control of memory function and the modification of synapse strength, and therefore they are included in perfusion fluid to ensure that these receptors do not become activated as a result of magnesium depletion. In addition, the solution is un-buffered to prevent any significant shift of hydrogen ions across the microdialysis membrane.[7]

Due to the variability in relative mean recovery values, the concentrations of brain metabolites are typically reported as the values measured within the microdialysate, without being adjusted to predict the true concentration in the interstitial fluid. Although absolute measured concentrations of metabolites are used in the clinic, the reporting of ratios of concentrations is preferred as these are independent of changes in relative mean recovery and depend less on the properties of the tissue being monitored. In addition, details of the catheter location, type and membrane length, as well as the flow rate and constituents of the perfusion fluid, should ideally be reported alongside any measured metabolite concentration.[7]

### 2.3.2 Compounds Recovered using Microdialysis

The membrane of the catheter used for microdialysis is selective only for size, as mentioned in Section 2.3.1, and therefore any compound smaller than 100 kDa can be collected, providing the appropriate concentration gradient is present. A number of compounds meeting these criteria are present in the extracellular brain fluid of TBI patients, in addition to metabolic intermediates. These include: drug molecules such as anti-seizure medication, which is administered as part of the TBI treatment programme for certain sub-types of brain injury;[1] cytokines, which mediate the inflammatory response to injury;[8] nitric oxide products, which are thought to play a role in regulating blood flow;[9] glutamate, a neurotransmitter, and glycerol, a component of cell membranes.

In order for a compound to be selected for routine monitoring as part of a TBI treatment programme, it must meet two main criteria. Firstly, there must exist a detection method for that compound which is sufficiently selective and sensitive to determine its concentration within the dialysate mixture at clinically-relevant levels. In addition, the clinical significance of that compound must be understood, within the context of TBI, in order that the measured concentration can be translated into clinically-useful information regarding the status of the patient and potentially used to initiate a clinical intervention.

Current guidelines, as set out in the Consensus Statement from the 2014 International Microdialysis Forum, suggest that the most important compounds to monitor in TBI patients are the metabolic intermediates D-glucose, L-lactate and pyruvate. Glycerol and glutamate may also be monitored, but their relationship to patient outcome is less well understood.[7]

N.B: The terms 'glucose' and 'lactate' are henceforth used to refer to D-glucose and L-Lactate respectively.

### 2.3.3 ISCUS Flex Microdialysis Analyser

The instrument typically used to analyse microdialysate samples is the ISCUS Flex Microdialysis Analyser. This instrument is designed specifically for the analysis of microdialysate samples and is optimised for use with small sample volumes of 0.2 - 1.0 $\mu$L. It can be used to measure the concentrations of glucose, lactate and pyruvate, in addition to other small organic molecules such as urea, glycerol and glutamate.

The analysis method employed by the ISCUS Flex uses enzyme-mediated reactions in combination with absorbance spectroscopy. Briefly, an enzyme that reacts selectively with the analyte of interest is added to the microdialysate sample, along with any other necessary reagents, and catalyses the conversion of the analyte into another compound. This intermediate compound is typically used in at least one further reaction, the product of which will be highly coloured, allowing it to be detected via absorbance spectroscopy. The rate of formation of the coloured compound is directly proportional to the concentration of the original analyte and therefore calculation of the concentration of the coloured product, via absorbance spectroscopy, allows the concentration of the original analyte to be determined. The enzymes and reactions used by the ISCUS Flex to detect glucose, lactate and pyruvate are summarised in Table 2.1.[10]

The LoD and LoQ of the ISCUS Flex, as determined in a 2011 study aimed at validating its use in the analysis of microdialysate, are listed in Table 2.2. Despite these encouraging results, the use of the ISCUS Flex poses a number of issues which may be limiting the number of neurocritical care centres able to include metabolite profiling as part of their TBI treatment programme. For example, the analyser is a

***Table 2.1:*** *Summary of the multi-step reactions reactions used by the ISCUS Flex Microdialysis Analyser to generate coloured compounds which can be detected via absorbance spectroscopy and used to calculate the concentrations of D-glucose, L-lactate and pyruvate in a sample of microdialysate.[10] $P_i$ = inorganic phosphate, TOOS = 3-(ethyl(m-tolyl)amino)-2-hydroxypropane-1-sulfonic acid.*

| Analyte | | Reaction | Enzyme |
|---|---|---|---|
| D-glucose | Step 1 | D-glucose + $O_2$ → gluconolactone + $H_2O_2$ | Glucose Oxidase |
| | Step 2 | $2H_2O_2$ + phenol + 4-aminoantipyrine → quinoneimine + $4H_2O$ | Peroxidase |
| L-lactate | Step 1 | L-lactate + $O_2$ → pyruvate + $H_2O_2$ | Lactate Oxidase |
| | Step 2 | $H_2O_2$ + 4-chlorophenol + 4-aminoantipyrine → quinoneimine + $2H_2O$ + HCl | Peroxidase |
| Pyruvate | Step 1 | pyruvate + $P_i$ + $O_2$ → acetylphosphate + $CO_2$ + $H_2O_2$ | Pyruvate Oxidase |
| | Step 2 | $2H_2O_2$ +TOOS + 4-aminoantipyrine → quinonediimine + $4H_2O$ | Peroxidase |

separate entity to the microdialysis setup and therefore samples must be manually loaded into the instrument; a process which is both time- and labour-intensive. This fact causes obvious logistical issues and means that samples are typically collected and analysed of the order of once per hour. The resulting delay between the extraction of metabolites from the brain and their analysis by the ISCUS Flex has a number of clinical implications. Firstly, the lack of real-time data on brain-metabolite levels means that any clinical intervention which may be recommended on the basis of this information would also be delayed. An additional consequence of the delay is that the microdialysate, and therefore its constituent metabolites, is collected in a single vial and therefore the measured metabolite concentration is an average of that produced by the brain over the course of the collection period. It is therefore difficult to identify time-dependent trends in metabolite production or consumption, which may cause further delays in the delivery of treatment or prognosis.

## 2.4 Metabolism in TBI

Glucose, lactate and pyruvate are key compounds in the process of cellular respiration: the process by which glucose is metabolised to produce adenosine triphosphate

***Table 2.2:*** *A summary of the LoD and LoQ of the ISCUS Flex in the measurement of glucose, lactate and pyruvate.*[11]

| Compound | Limit of Detection/mM | Limit of Quantification / mM |
|---|---|---|
| Glucose | 0.02 | 0.06 |
| Lactate | 0.06 | 0.18 |
| Pyruvate | 0.0078 | 0.0191 |

(ATP), the source of chemical potential energy used by all cells for intracellular energy transfer. Within the brain, ATP is necessary for a variety of functions, including the maintenance of cells and neurotransmitter production.[12] This section provides a brief overview of the roles of glucose, lactate and pyruvate in cellular respiration and discusses how their concentrations in the brain may change following a TBI.

### 2.4.1 Cellular Respiration

The key reactions of cellular respiration are summarised in Figure 2.2.

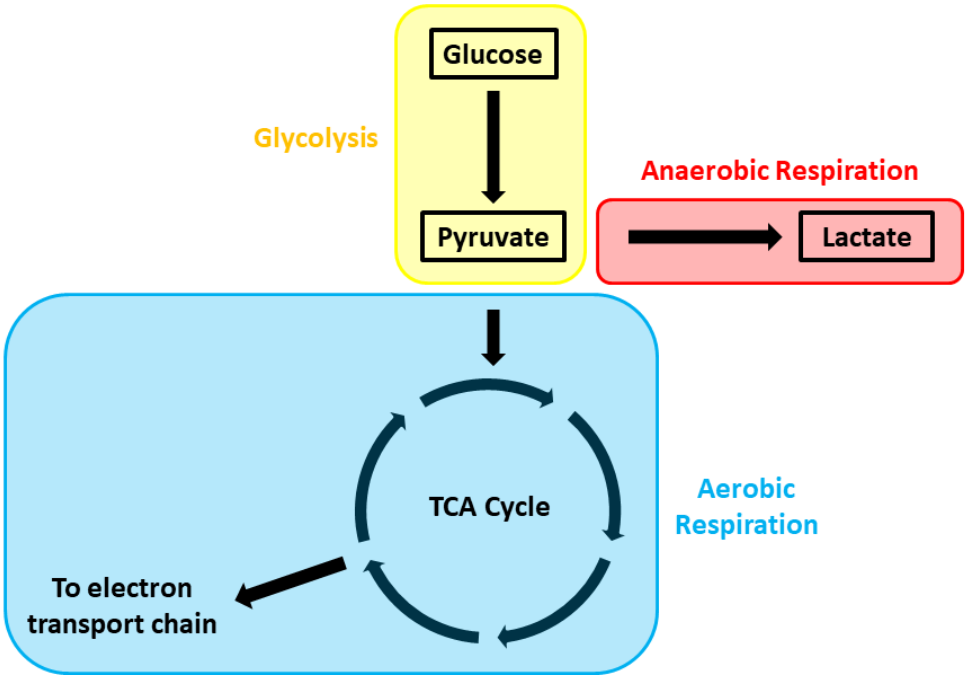


***Figure 2.2:*** *Schematic highlighting the roles of glucose, lactate and pyruvate within the major reactions of cellular respiration.*

The first stage of cellular respiration is glycolysis; a series of enzyme-catalysed reactions through which glucose is converted to pyruvate. This process produces a net yield of two molecules of ATP and two molecules of pyruvate for each molecule of glucose consumed.

The pyruvate produced via glycolyis is subsequently used as a substrate for one of two different reaction pathways, depending upon the availability of oxygen. If oxygen is present, pyruvate is used as the initial substrate for the reactions of aerobic respiration: the Tricarboxylic Acid (TCA) cycle and the electron-transport system. These processes can produce a net yield of up to 36 molecules of ATP for each molecule of glucose originally metabolised to pyruvate.

In the absence of oxygen, pyruvate is converted to lactate via the anaerobic-respiration pathway. This process is significantly less efficient than aerobic respiration, yielding no further molecules of ATP.

The significance of glucose, lactate and pyruvate in cellular respiration allows valuable information regarding the metabolic and redox states of the brain to be inferred from the measured concentrations of these compounds within the extracellular brain fluid. Clinicians are subsequently able to use this information to assess which pathophysiological processes may be occurring within the brain, including: hypoxia, ischemia and mitochondrial dysfunction. The following sections discuss these insights in more detail.

### 2.4.2 Glucose in TBI

Brain-glucose levels are dictated by a balance between glucose supply and demand. The current best estimate of glucose levels in the uninjured human brain, measured during a microdialysis study of patients undergoing neurosurgery for benign lesions, gives a mean glucose concentration of 1.7 $\pm$0.9 mM.[13] This study used a flow rate of 0.3 $\mu$L min$^{-1}$ and a 10 mm microdialysis membrane. Glucose levels in the brains of TBI patients tend to deviate significantly from this healthy range as changes in blood flow or metabolism, both of which are commonly seen in TBI, can have a disproportionate effect on brain glucose.[14]

Low brain-glucose levels (defined as concentrations below 0.8 mM in microdialysate) are commonly observed in TBI and can be caused by a decrease in glucose supply or an increase in glucose demand. A decrease in the amount of glucose being delivered to the brain is due to a deficiency in blood supply which, in turn, may be a result of local capillary damage, elevated intracranial pressue, or failure of blood-flow autoregulation. In healthy individuals, the supply of glucose to the brain is also affected by blood-glucose concentration, but this relationship may be lost in the injured brain.[7] Alternatively, if an increase in glucose demand causes a sufficiently high rate of cellular uptake, the rate of glucose supply is not enough to meet the demand and glucose levels become depleted.[6] Such an increase in glucose demand may result from a number of factors, including: a requirement for anaerobic metabolism;[5] a greater need for ATP in order to restore ionic and neurochemical gradients which have been disturbed; or an increased use of glucose for non-energy pathways, such as those required for repair

and biosynthesis.[15] In addition to the causes discussed here, brain-glucose levels can also be rapidly reduced by certain types of secondary injury, although the mechanisms of these processes are beyond the scope of this work.[7]

Clinical observations have linked levels of brain glucose below 0.8 mM with an unfavourable outcome from TBI. Additional evidence suggests that particularly high brain-glucose levels may also be associated with unfavourable outcome, indicating that there may be an optimal range within which brain-glucose levels should be maintained, but there are currently insufficient data to define these parameters. The consensus statement from the 2014 International Microdialysis Forum therefore proposes pathological thresholds for low glucose levels only: brain tissue is considered to be 'at risk' if the glucose concentration is below 0.8 mM and intervention is recommended for glucose concentrations below 0.2 mM.[7]

### 2.4.3 Lactate and Pyruvate in TBI

As discussed in Section 2.4.1, lactate and pyruvate are derived from glucose during the process of cellular respiration. Their extracellular concentrations therefore partly reflect the glycolytic activity, and relative levels of aerobic vs anaerobic respiration, within a cell.[16]

Analysis of microdialysate derived from patients with no brain injury gave a mean lactate concentration of 2.9 $\pm$0.9 mM.[13] Lactate levels in the microdialysate of TBI patients are often higher than this and concentrations higher than 4 mM are generally linked to unfavourable patient outcomes.[7] It is thought that raised lactate levels indicate increased use of the anaerobic respiration pathway. However, the absolute lactate concentration within the extracellular fluid is also influenced by the amount of glucose that enters the TCA cycle and is therefore not in itself indicative of anaerobic metabolism.[17] As a result, the absolute lactate concentration found in microdialysate samples is not usually used as a clinical marker in TBI.

The mean concentration of pyruvate in microdialysate from uninjured brain was found to be 0.166 $\pm$ 0.047 mM.[13] There is evidence to suggest that a high pyruvate concentration is linked to favourable outcomes from TBI and yet, as with lactate, pyruvate concentration alone is not usually used as a clinical marker.[16]

The relative proportion of lactate and pyruvate, known as the Lactate:Pyruvate Ratio (LPR), is used as a marker of aerobic *vs.* anaerobic metabolism within the brain. It is considered a more reliable indicator of patient outcome than the absolute concentrations of lactate and pyruvate, with a LPR value greater than 25 generally being associated with unfavourable outcome.[16,18] Knowledge of the absolute concentrations of lactate and pyruvate is still of use, however, as they can be used to interpret the causes of a high LPR. An increased LPR, in combination with low pyruvate levels (and low oxygen, if being monitored) indicates a shift to anaerobic respiration due

to insufficient blood flow to the region of the brain being monitored. On the other hand, an increased LPR with high lactate and high pyruvate (and normal oxygen, if being monitored) indicates an increase in anaerobic respiration due to mitochondrial dysfunction.[7]

Interpretation of the LPR is complicated by increasing evidence that the injured brain is able to utilise lactate to produce ATP via the TCA cycle.[19] It has been suggested that the improved patient outcome associated with low extracellular lactate could be due to lactate being taken up by neurons and utilised via the TCA cycle. When neurons are too damaged to utilise this lactate, it accumulates in the extracellular fluid, thus explaining the unfavourable outcome associated with high levels of lactate.[20]

## 2.5 Project Aims

This work was completed as part of a wider collaborative project between two departments at the University of Cambridge: the Department of Chemistry and the Department of Clinical Neurosciences. The aim of the wider project is to develop an alternative to the ISCUS Flex, for the analysis of glucose, lactate and pyruvate levels in the microdialysate of TBI patients, which is capable of delivering a comparable level of accuracy whilst improving upon its shortcomings.

It is envisioned that the developed sensor will take the form of a 'lab-on-a-chip' system, in which sample collection and analyte detection are both integrated and semi-continuous. The proposed 'sensing chip' will be compatible with existing microdialysis equipment used in the clinic, as well as being small enough to sit at the patient's bedside, such that microdialysate samples leaving the brain will flow directly into the chip for analysis before being passed out the other side of the chip to be collected and disposed of as clinical waste or retained for further analysis. The proposed setup is illustrated in Figure 2.3.

Such a system is predicted to bring multiple advantages to the treatment of TBI. By replacing the current hourly analysis with a continuous monitoring system, clinicians would have earlier warning of changes in a patient's neurochemistry which, it is hoped, would allow earlier intervention and lead to a more favourable outcome for the patient. In addition, the setup would be more user-friendly than the existing technology and would require less intervention from clinical staff, due to the direct integration of the sampling and analysis components, making it both cost- and time-effective when compared with the existing technology. It is hoped that these factors would together incentivise and enable more neurocritical care units to adopt microdialysis as a technique.

The aim of the work described in this thesis was to determine whether vibrational spectroscopy would be a suitable technique to form the basis of the developed sen-

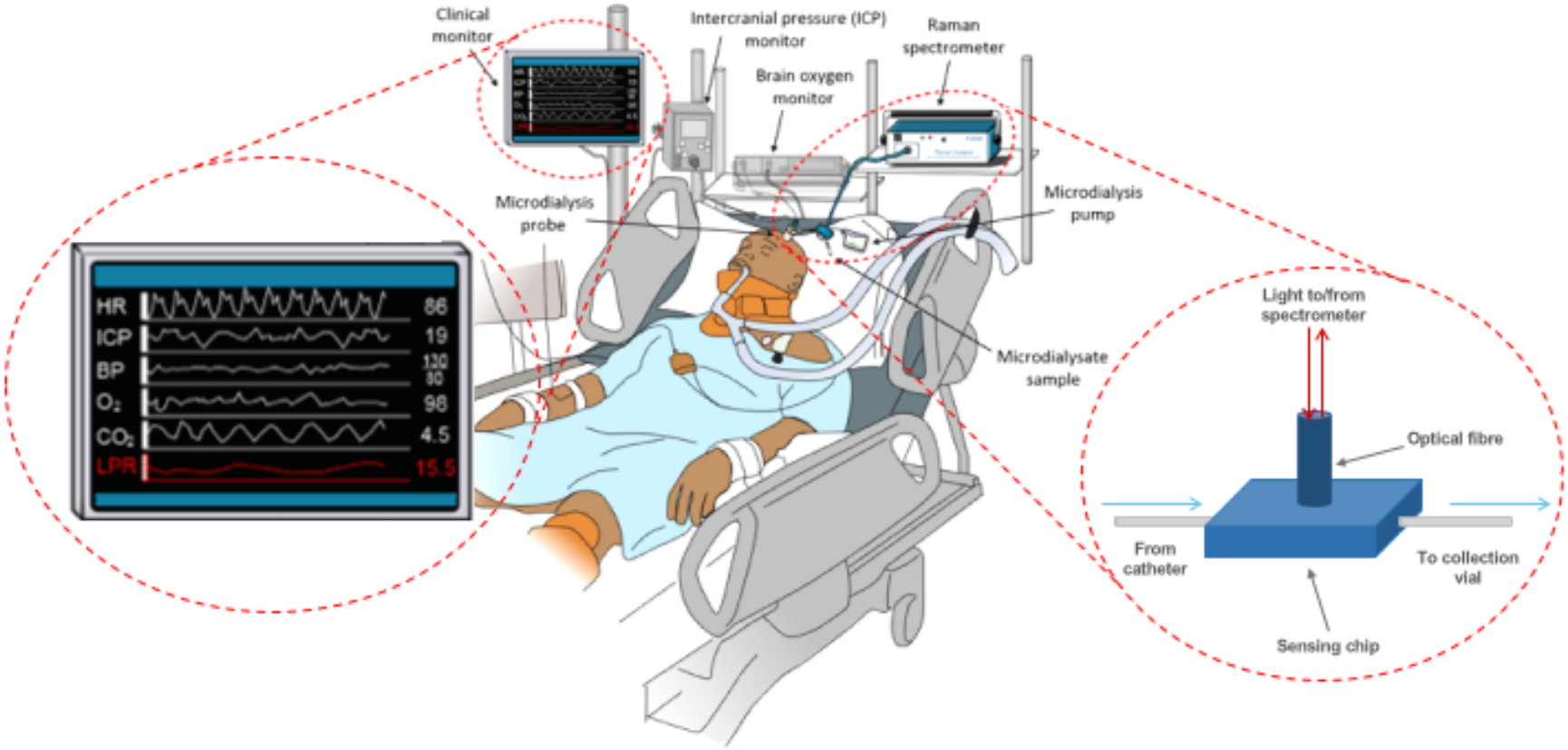


***Figure 2.3:*** *An illustration of the aim of the Department of Chemistry-Department of Clinical Neurosciences collaboration; showing the proposed metabolic profiling setup and its integration into currently-used TBI monitoring systems. Figure adapted from an illustration by Susan Giorgi-Coll. Illustration copyright Susan Giorgi-Coll and reproduced here with her permission.*

sor. Spectroscopy has the potential to operate via a lab-on-a-chip system, with the additional advantage that it eliminates the need for consumables and reagents. This would further decrease the amount of labour required to operate the sensor and has the added benefit of reducing the device cost to a single initial purchase, with minimal ongoing expenditure. The use of spectroscopy would also allow glucose, lactate and pyruvate to be detected directly rather than relying upon chemical reactions and/or the production of intermediates, as in the case of enzyme-based detection, which may increase the reliability of the analysis. Vibrational spectroscopy in particular was identified as a promising candidate due to its sensitivity and potential instrumental simplicity, which provides greater potential for miniaturisation into a bedside device, when compared to other forms of spectroscopy.

Two main factors were to be considered for each form of vibrational spectroscopy studied: sensing performance (sensitivity and accuracy in detecting glucose, lactate and pyruvate) and operation (suitability for the specific clinical environment in which it would be used). Details of the specifications required of the final device are discussed in Section 2.6.

## 2.6 Device Requirements

In order to fulfil the aim of developing a viable alternative to the ISCUS Flex, the developed sensor must meet specific criteria. These were taken into consideration throughout this work and are detailed below:

- Performance requirements:
  - Sensitivity - the ability to detect pyruvate, lactate and glucose within a clinically relevant range:
    - Pyruvate: 0.01 - 1.5 mM
    - Lactate: 0.1 - 24 mM
    - Glucose: 0.1 - 24 mM
  - Selectivity: the ability to measure accurately the individual concentrations of pyruvate, lactate and glucose within the microdialysate mixture
- Operational requirements:
  - The potential for miniaturisation, to allow the instrument to sit at the patient's bedside
  - The ability to measure liquid flowing at 0.3 $\mu$L min$^{-1}$
  - The capacity for continuous measurement, defined here as taking a measurement at least once every five minutes

- The ability to measure multiple analytes simultaneously
- User-friendliness: the device must be straightforward to set up for each new patient and require minimal intervention from clinical staff once it is operational

# Chapter 3

# Theoretical Background

This chapter provides the theoretical background behind the tools and techniques used in this work. It details the theory and operating principles behind both infra-red and Raman spectroscopy, provides an introduction to statistical modelling and describes the methods used to analyse and model spectroscopic data.

## 3.1 Molecular Vibrations

Molecular vibrations are motions of atoms in a molecule which alter the distance between two atoms (a stretch); the angle between two atoms (a bend); or the angle between projections of two bonds onto a plane orthogonal to a common bond (a torsional/twisting motion) within the molecule. The number of vibrational modes of a molecule is dictated by the number of internal degrees of freedom it possesses.

Each atom within a molecule has three degrees of freedom of motion (the $x$, $y$ and $z$ directions) and therefore a molecule of $N$ atoms has $3N$ internal degrees of freedom. Three of these are translational motions in the $x$, $y$ or $z$ directions and rotational motion accounts for a further two (linear molecules) or three (non-linear molecules) degrees of freedom. The remaining degrees of freedom are vibrational motions. A linear molecule therefore possesses $3N-5$ vibrational degrees of freedom, whilst a non-linear molecule possesses $3N-6$ vibrational degrees of freedom. Examples of vibrational motion include symmetric and antisymmetric stretching modes and scissoring, rocking, wagging or twisting bending modes.

### 3.1.1 Classical Harmonic Oscillator

The simplest model for describing a molecular vibration is the simple harmonic oscillator, in which a diatomic molecule is considered as two point masses connected by a massless spring. The stretching/compressive dispacement from the equilibrium position of the two masses varies periodically with time as a sine or cosine function,

whilst the molecular centre of mass remains stationary. Although different masses oscillate along the axis with different amplitudes, they do so with the same frequency and therefore go through their equilibrium positions simultaneously. The potential energy of such a molecule is given by:

$$PE = \frac{1}{2}kX^2 \tag{3.1}$$

where $X$ is the distance between the two point masses and $k$ is the force constant. The latter is a function of the energy of a bond between two nuclei and is related to bond strength: the stronger the bond, the higher the value of $k$. A plot of the potential energy as a function of $X$ gives a parabola that is symmetric about the equilibrium internuclear distance (Figure 3.1(a)).

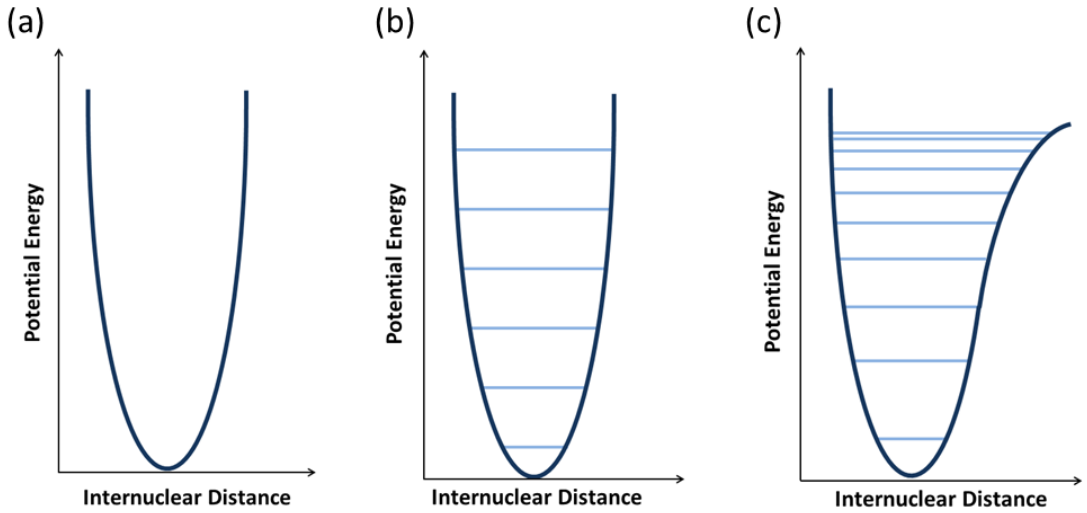


***Figure 3.1:*** *Illustration summarising the potential-energy curves (dark blue) and vibrational energy levels (light blue) of the (an)harmonic oscillator models. (a) The potential energy of a simple harmonic oscillator as a function of distance. (b) The potential energy curve and quantised vibrational energy levels of a diatomic molecule modelled as a quantum-mechanical harmonic oscillator, showing the equal spacing of the vibrational energy levels. (c) The potential energy curve and vibrational energy levels of a diatomic molecule modelled as an anharmonic oscillator, showing the convergence of the quantised vibrational energy levels with increasing vibrational quantum number.*

The vibrational frequency ($\nu$), in wavenumbers, of a diatomic molecule modelled by the harmonic oscillator is given by:

$$\tilde{\nu} = \frac{1}{2\pi c}\sqrt{\frac{k}{\mu}} \tag{3.2}$$

where $c$ is the speed of light and $\mu$ is the reduced mass of the molecule. The reduced mass allows both nuclei to be represented by a single mass which reflects the relative

masses of each nucleus. It is calculated using the equation:

$$\frac{1}{\mu} = \frac{1}{m_1} + \frac{1}{m_2} \tag{3.3}$$

where $m_1$ and $m_2$ are the point masses of the two nuclei.

### 3.1.2 Quantum-Mechanical Harmonic Oscillator

A quantum-mechanical treatment of the simple harmonic oscillator dictates that the vibrational energy of a diatomic molecule is quantised. The allowed values of the vibrational energy are given by:

$$E_v = (v + \frac{1}{2})h\nu \tag{3.4}$$

In this expression, $h$ is Planck's constant, $\nu$ is the classical vibrational frequency of the oscillator (given in Equation 3.2) and $v$ is a quantum number that may only take integer values. When $v = 0$, the molecule retains a vibrational energy of $\frac{1}{2}h\nu$ which corresponds to the fundamental vibrational energy of the system, known as the zero-point energy, and cannot be removed from the molecule. Solving this equation for a series of consecutive values of $v$ gives solutions which are separated by $h\nu$, showing that the vibrational energy levels are equally spaced (Figure 3.1(b)).

Vibrational spectroscopy probes transitions between these vibrational energy levels.

### 3.1.3 Anharmonic Oscillator

The anharmonic oscillator model reflects the fact that, if the internuclear distance between two bonded nuclei becomes too great, the bond will eventually break. The Morse expression for the allowed energy levels in the anharmonic oscillator model is:

$$E_v = (v + \frac{1}{2})h\nu - (v + \frac{1}{2})^2 h\nu\chi \tag{3.5}$$

where $\chi$ is the anharmonicity constant. The solutions to this equation show that consecutive vibrational energy levels in the anharmonic oscillator become closer together, as the value of $v$ increases, and eventually converge at the dissociation limit. The energy difference between the zero-point energy and the convergence limit is the dissociation energy of the bond. Figure 3.1(c) shows the potential energy and vibrational energy levels of a bond described by the anharmonic oscillator model.

It can be seen from Figure 3.1 that the simple harmonic and anharmonic oscillators are similar for low vibrational energy levels. As a result, whilst the anharmonic oscillator is a significantly more accurate model of molecular vibrations at energy levels close to the dissociation limit, the simple harmonic oscillator may be used as a

satisfactory model of low-energy molecular vibrations.

## 3.2 Infra-Red Spectroscopy

IR spectroscopy is a technique which probes the vibrational energy levels of a molecule via the absorption of IR radiation.

The energy required to promote a molecule from one vibrational energy level to a higher energy level of the quantum-mechanical harmonic oscillator corresponds to wavelengths of light in the IR region of the electromagnetic spectrum. It can be seen from Equations 3.4 and 3.2 that the energy of a vibrational level is dictated by the mass of the nuclei within the molecule and the strength of the bond between them. Bonds of different type (such as single vs. double bonds) or those involving different types of atoms will therefore have different vibrational energy levels which will correspond to different wavelengths of IR radiation.

IR spectroscopy takes advantage of these phenomena to enable the identification of the functional groups present in a sample. In a typical IR experiment, a sample is irradiated with a polychromatic IR source. The sample absorbs specific wavelengths from the incident radiation, corresponding to the vibrational transitions of the bonds present in the sample, whilst the remaining wavelengths are transmitted directly through the sample. The resulting IR spectrum shows which wavelengths of light have been absorbed by the sample and these can then be related to the functional groups present.

### 3.2.1 Selection Rules of IR Spectroscopy

According to the quantum-mechanical oscillator model of molecular vibrations and IR absorption, there are are two selection rules which must be obeyed in order for incident IR radiation to cause a vibrational transition in a molecule and thus show a peak in an IR spectrum.

The first selection rule states that a molecular vibration must change the dipole moment of the molecule in order for it to be IR-active. The larger the change in the dipole moment, the stronger the intensity of the band in the resulting IR spectrum. The static dipole moment, $\mu$, is given by:

$$\mu = qx \tag{3.6}$$

where $\pm q$ is the magnitude of the charge and $x$ is the distance between the charges. This selection rule places limits on the types of molecule and vibrational motion that can be detected using IR spectroscopy. For example, homonuclear diatomic molecules cannot be detected via IR spectroscopy as they have a dipole moment of zero and this does not change with vibrational motion. However, a polyatomic molecule

with no overall dipole moment may possess some IR-active vibrational modes. One example of such a molecule is the linear $CO_2$ molecule, which is composed of two symmetrical polar bonds and therefore has an overall equilibrium dipole moment of zero. During the symmetric stretch of $CO_2$, during which the two C=O bonds stretch and compress simultaneously, the dipole moment of each bond changes by the same magnitude and therefore the overall molecular dipole moment does not change. The antisymmetric stretch of the molecule causes one C=O bond to be compressed while the other is stretched and, as a result, the dipole moments of each bond change by different amounts and generate an overall dynamic dipole moment of the molecule. The antisymmetric stretch of CO is therefore IR-active, whilst the symmetric stretch is IR-inactive.

The second selection rule restricts the allowed change in vibrational energy level to $\Delta v = \pm 1$ in the simple harmonic approximation. The distribution of molecules across the differing energy levels can be predicted using the Boltzmann distribution:

$$\frac{N_i}{N_j} = exp(-\frac{\Delta E}{k_B T}) \tag{3.7}$$

where $\frac{N_i}{N_j}$ is the ratio of the number of molecules in two different energy levels, $N_i$ and $N_j$, $\Delta E$ is the difference in energy between the levels, $k_B$ is the Bolzmann constant and $T$ is the temperature. The Boltzmann distribution predicts that, at 298 K, the majority of molecules are in their vibrational ground state because $\Delta E$ is much larger than $k_B T$. Consequently, the vibrational transition most often studied by IR absorption spectroscopy is that from $v = 0$ to $v = 1$.

### 3.2.2 IR Spectroscopy Instrumentation

Routine mid-IR spectroscopy measurements, using light of 2.5 – 10 $\mu$m in wavelength, are typically carried out using a FTIR spectrometer.

The principle behind a generalised FTIR spectrometer is shown in Figure 3.2. An IR light source emits electromagnetic radiation which is split into two beams by a semi-transparent beam-splitter. One beam is directed towards a stationary mirror, where it is reflected back towards the beam-splitter, whilst the other is reflected by a moving mirror. The motion of the moving mirror produces a difference in path length between the two beams and therefore upon recombination there is constructive and destructive interference between them, which generates an interferogram. The recombined beam is directed towards the sample.

The sample absorbs certain wavelengths of the recombined beam, as discussed in Section 3.2, thus removing them from the interferogram. The remaining wavelengths of light are transmitted to a detector which converts the optical signal into a measurable electrical signal, such as voltage. The variation in intensity as a function of time

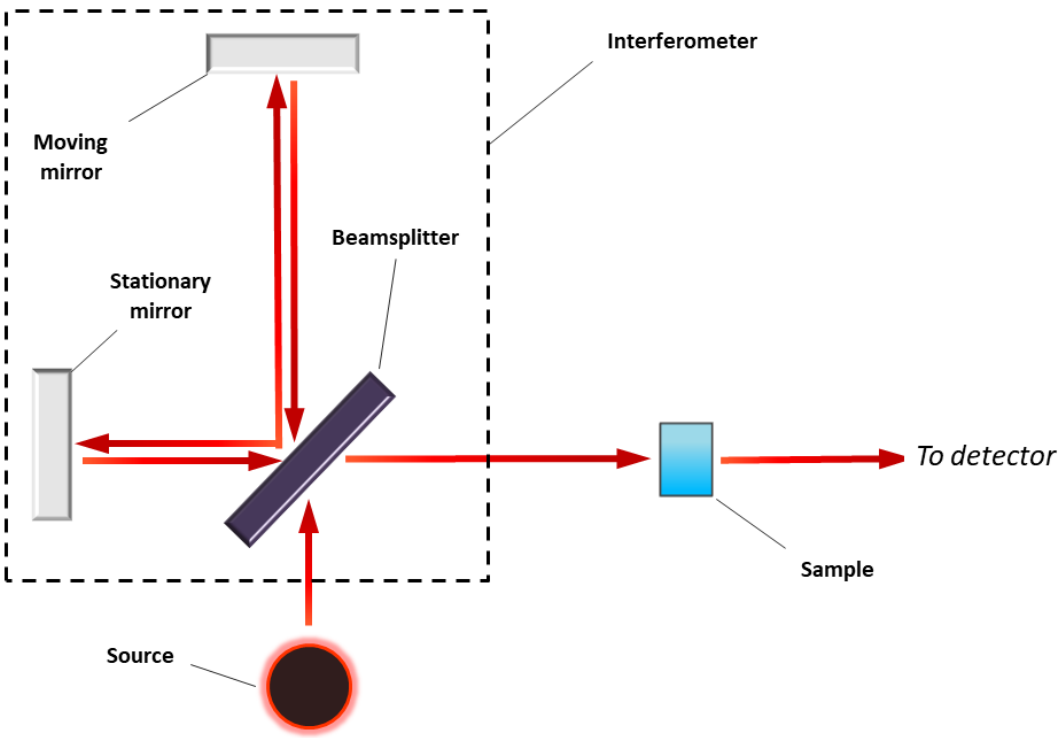


***Figure 3.2:*** *An illustration of the optical path of a typical FTIR spectrometer. Light emitted by an IR source is split by a beam-splitter and the resulting two beams are reflected by different mirrors, one of which is moving. Upon recombination, the beams form an interferogram. The recombined beam is passed through the sample, which absorbs certain wavelengths, and the remaining wavelengths are directed towards a detector.*

is thus recorded for each wavelength of light that reaches the detector.

A computer connected to the instrument performs a Fourier transform for each point of the interferogram to allow the intensity to be expressed as a function of frequency, making it possible to see which frequencies are missing from the interferogram due to their absorption by the sample. These data are typically plotted to show intensity *vs.* inverse wavelength (in $cm^{-1}$) to produce a conventional IR spectrum.

### 3.2.3 Types of IR Spectroscopy

The basic principle of IR spectroscopy has been developed into multiple different techniques. This section provides details of the two techniques utilised in this work.

#### 3.2.3.1 Transmission-FTIR Spectroscopy

Transmission-FTIR is the most simple form of IR spectroscopy. In transmission-FTIR experiments, the sample is held between two windows, which must be composed of an IR-transparent material, and placed directly in the light path of the spectrometer. Incident light enters the cell through one window, passes through the sample and exits

the cell via the second window.

Two main experimental parameters must be considered when planning a transmission-FTIR experiment. The first of these parameters is the choice of material for the sample cell window: the material must be transparent to IR radiation over the wavelength range of interest and must also be inert to the consituents of the sample. The second experimental parameter to consider is the distance between the two windows, which dictates the path length of the sample. Longer path lengths increase the amount of interaction between the IR beam and the sample and therefore lead to increased absorption and stronger peaks in the IR spectrum.

The major advantage of transmission-FTIR is that it is a simple and well-established technique. However, the long path lengths used make it unsuitable for the study of strongly IR-absorbing samples, such as those with a high water concentration, as the signal intensity produced by such molecules can saturate the detector and thus the spectrum. In addition, the study of solid samples by transmission-FTIR can be complicated, as the sample must be ground up and prepared as a suspension in oil in order to allow transmission of the IR beam.

#### 3.2.3.2 Attenuated Total Reflectance FTIR Spectroscopy

ATR-FTIR spectroscopy is based upon the principle of total internal reflection. This phenomenon occurs when a propagating wave travels from a material of a higher refractive index to a material of a lower refractive index. If the wave strikes the boundary between the two materials at an incident angle which is greater than a critical angle, which is measured with respect to the normal to the surface, it will be totally internally reflected within the first material. The critical angle, $\theta_c$, is a function of the refractive indices of the two materials and is given by:

$$\theta_c = sin^{-1}\frac{n_1}{n_2} \tag{3.8}$$

where $n_1$ and $n_2$ are the refractive indices of the first and second materials, respectively.

ATR-FTIR spectroscopy uses a crystal of high refractive index (typically diamond, Ge, Si or ZnSe) which is placed in direct contact with the sample. Total internal reflection of the incident IR beam propagating in the ATR crystal occurs at the crystal-sample interface, generating an evanescent wave outside the crystal which extends into the sample (Figure 3.3). The evanescent wave will be attenuated at the specific wavelengths absorbed by the sample, and thus the IR absorption properties of the sample can be determined as in conventional FTIR spectroscopy. In many ATR crystals, the light is totally internally reflected multiple times, allowing the absorption of IR radiation by the sample at each point of reflection.

The intensity of the evanescent wave decays exponentially with distance from the

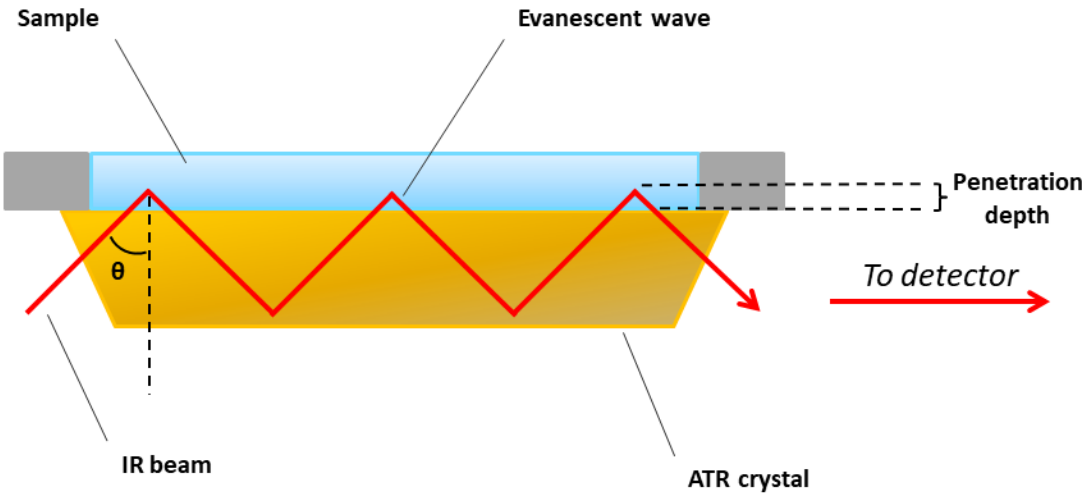


***Figure 3.3:*** *Schematic of the principle behind ATR-FTIR. IR radiation entering the crystal at a particular incident angle ($\theta$) is totally internally reflected inside the ATR crystal, generating an evanescent wave which penetrates into the sample.*

surface of the ATR crystal. The depth of penetration, $d_p$, is defined as the distance from the crystal/sample interface at which the intensity of the evanescent wave decays to $\frac{1}{e}$ of its original value. It is calculated from:

$$d_p = \frac{\lambda}{2\pi(n_1^2 sin^2\theta - n_2^2)^{\frac{1}{2}}} \tag{3.9}$$

where $\lambda$ is the wavelength of the incident radiation and $\theta$ is the angle of incidence of the IR beam. This distance is typically of the order of 2 - 15 $\mu$m and therefore ATR-FTIR spectroscopy is generally considered to be a surface-based technique that is insensitive to sample thickness. As a result, ATR-FTIR is ideal for studying samples which strongly absorb IR radiation, such as dilute aqueous solutions, or are too thick to study by transmission-FTIR. It is also a useful technique for studying material surfaces.

Equation 3.9 highlights the dependency of the penetration depth on wavelength. This relationship has an effect on the resulting ATR-FTIR spectrum, causing a decrease in relative band intensity with increasing wavenumber compared to a transmission-FTIR spectrum of the same sample. As a result, ATR and transmission-FTIR spectra cannot be directly compared. However, the experimental set up of an ATR-FTIR experiment can be approximately compared with that of a transmission-FTIR experiment via a property known as 'effective path length'. This conversion considers two key properties of an ATR crystal, its penetration depth and the number of reflections it allows, and converts them to a distance which can be compared with the path-length

property of transmission-FTIR cells. It is calculated by:

$$\text{Effective Path Length} = d_p \times \text{Number of Reflections} \tag{3.10}$$

These parameters, and therefore the absorbance intensity of the resulting spectrum, can be controlled to some extent by experimental design. The penetration depth is affected by both the choice of ATR crystal material and the angle of incidence. A material with a high refractive index leads to a lower penetration depth and thus reduces the effective path length. Similarly, the higher the angle of incidence, the lower the penetration depth. The angle of incidence also affects the number of reflections, with a high angle of incidence leading to fewer reflections and hence a shorter effective path length and lower absorbance intensity.

Additional experimental parameters which should be considered when designing an ATR-FTIR experiment include the quality of sample contact, which should be as high as possible due to the short penetration depth of the evanescent wave, in addition to the IR-transmission range and chemical reactivity of the ATR crystal material.

## 3.3 Raman Spectroscopy

Raman spectroscopy, like IR spectroscopy, is a technique which can be used to probe the vibrational energy levels of a molecule. However, unlike IR spectroscopy it is based on the scattering, rather than the absorption, of photons. The scattering processes are much weaker than absorption processes and therefore Raman spectra generally contain bands of much weaker intensity than IR spectra.

### 3.3.1 Raman Effect

A photon can interact with a molecule via two main mechanisms: it can be absorbed by the molecule or it can be scattered. The majority of incident photons that undergo a scattering mechanism are scattered elastically: both the photon and the molecule involved possess the same energy after the collision as they did prior to it, a process known as Rayleigh scattering. However, a small number of these collisions (approximately 1 in $10^8$)[21] are inelastic, such that the energy of the scattered photon differs from that of the incident photon. This process is known as the Raman effect and is the principle upon which Raman spectroscopy is based.

The scattering of a photon by a molecule can be described as an excitation of a molecule to a virtual energy state, followed by a relaxation that leads to the release of a photon. When the molecule relaxes, it may return to its original vibrational energy level (Rayleigh scattering) or to a different vibrational energy level (Raman scattering). If the molecule is left in a higher vibrational energy level than before the interaction, releasing a photon of lower energy than the incident photon, the

process is known as Stokes Raman scattering. Conversely, if the molecule is left in a lower vibrational energy level, releasing a photon of higher energy than the incident photon, it is known as Anti-Stokes Raman scattering (Figure 3.4). In both cases, the magnitude of the energy difference between the incident and the scattered photon corresponds to the change in energy of the molecule and therefore reflects the difference in energy between the two vibrational states. Raman spectroscopy uses a monochromatic light source, which may be in the UV, visible or near-IR range, so that the difference in photon energy can easily be measured.

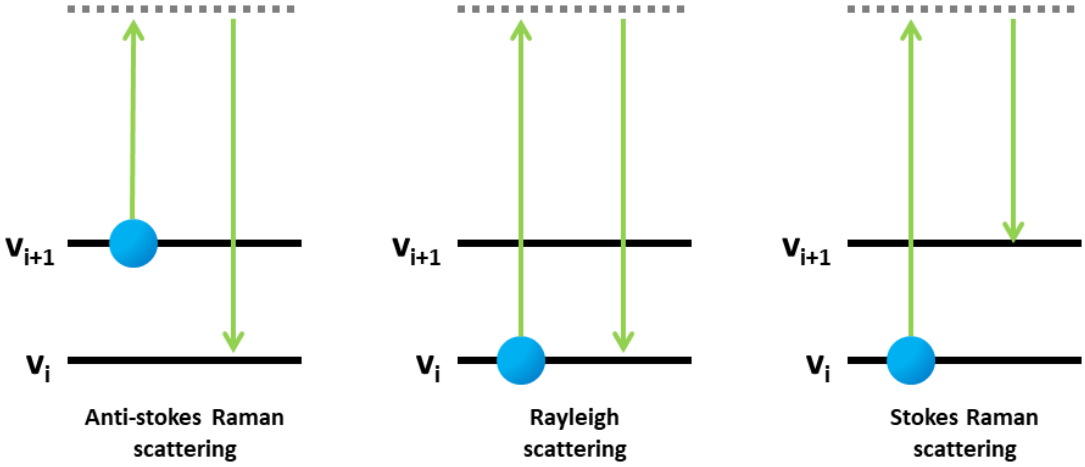


***Figure 3.4:*** *Diagram showing the molecular excitation and corresponding change in vibrational energy level induced by Stokes and anti-Stokes Raman scattering, as well as Rayleigh scattering.*

The intensity of Stokes scattering is much greater than that of anti-Stokes scattering at room temperature due to the relative populations of vibrational energy levels, as discussed in Section 3.2.1. As a result, Raman spectra are generally plotted to show only the signals generated by Stokes scattering.

### 3.3.2 Selection Rules of Raman Spectroscopy

Photon scattering arises when an external electric field, such as that of electromagnetic radiation, induces a dipole moment in a molecule. The size of the induced dipole moment, $P$, is given by:

$$P = \alpha E \tag{3.11}$$

where $\alpha$ is the polarisibility of the molecule, a measure of how easily the electron cloud of a molecule can be distorted, and $E$ is the electric field. The induced dipole causes light to be scattered from the molecule at the optical frequency of the incident light wave (Rayleigh scattering). Raman scattering occurs when the polarisibility of the

molecule is altered, causing a change in the size of the induced dipole and hence in the frequency of the emitted radiation. The polarisibility of a molecule can be altered by molecular vibrations, leading to the first selection rule of Raman spectroscopy: for a vibrational mode to be Raman-active, it must change the polarisibility of the molecule.

The intensity of the scattering is proportional to the change in the polarisibility of a molecule. If a vibration does not significantly change the polarisibility, the scattering intensity and thus the intensity of the Raman band will be low. The vibrations of highly polar species are generally weak and therefore do not greatly alter the polarisibility of the molecule. As a result, an external electric field cannot induce a large change in the dipole moment and therefore these species have a low scattering intensity and show weak bands in their Raman spectra.

One example of a highly polar bond which has a low scattering intensity is the O-H bond. Consequently, water molecules have a low scattering intensity and therefore Raman spectroscopy is a useful technique with which to study aqueous solutions.

The second selection rule dictates that the allowed change in vibrational energy level is restricted to $\Delta v = \pm 1$, as for IR spectroscopy.

### 3.3.3 Surface-Enhanced Raman Spectroscopy

The main limitation of Raman spectroscopy is the low probability with which Raman scattering occurs, which makes it a relatively insensitive technique when compared with IR spectroscopy. SERS is a variation on traditional Raman spectroscopy, in which the intensity of Raman scattering is enhanced through the use of nanostructured noble-metal surfaces.

The increase in Raman scattering intensity observed in SERS is thought to occur via two different mechanisms. The mechanism which provides the greater contribution to the enhancement, generating an average enhancement factor of $10^5$, operates through the phenomenon of Surface Plasmon Resonance (SPR). SPR is made possible due to the high electron density present at the surface of a metal. Whilst the conduction electrons of the bulk metal are held in a lattice by the positive charge at the metal ions, the surface electrons experience a positive charge only on the side closest to the metal bulk and are therefore less tightly bound to the metal. As a result, the electron density extends a considerable distance beyond the surface of the metal and the electrons are able to move freely in a lateral direction along it.

Irradiation of the metal surface with electromagnetic radiation of the correct frequency causes these electrons to oscillate as a collective group across the face of the metal. This process is SPR and is illustrated in Figure 3.5. If SPR is induced on a nanostructured surface, the resulting surface plasmons become localised in the valleys. Excitation of these localised surface plasmons with visible light leads to the

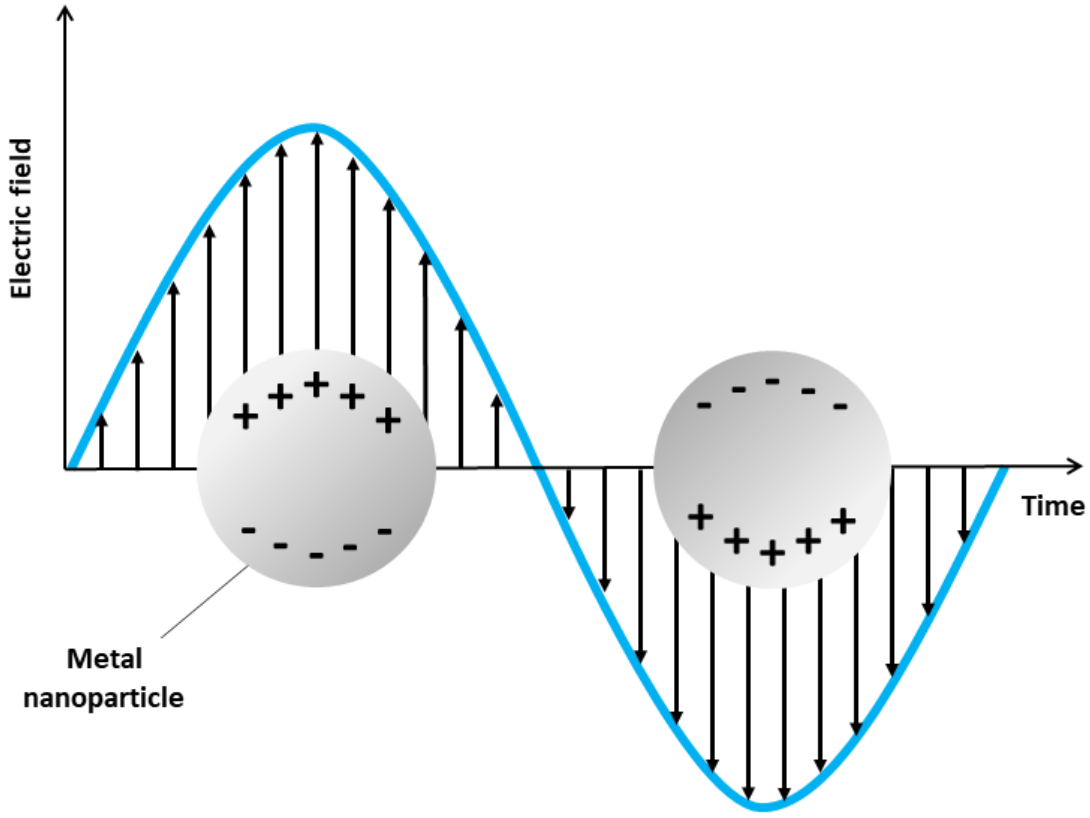


***Figure 3.5:*** *Diagram illustrating the generation of surface plasmon resonance localised about metal nanoparticles. Free conduction electrons at the metal surface oscillate collectively as a result of coupling with incident electromagnetic radiation.*

generation of significant electric fields. Electromagnetic SERS enhancement relies on Raman-active molecules being confined within these electromagnetic fields, which cause a significant increase in the magnitude of their induced dipole and therefore an increase in the scattering intensity.

SERS can also operate via a chemical mechanism. This mechanism has a much smaller impact on the Raman signal than the electromagnetic mechanism and is thought to contribute an average enhancement factor of $10^2$.[22] Chemical enhancement of Raman scattering involves the formation of a bond between the analyte and the surface of the SERS substrate and a subsequent charge-transfer mechanism from the metal to the analyte. The gain in charge increases the polarisibility of the molecule and therefore increases the intensity of Raman scattering. A molecule must be chemically adsorbed to a roughened surface in order to experience the chemical enhancement, and hence the process is both site-specific and and analyte-dependent.

The most critical aspect of a SERS experiment is the choice of noble-metal substrate: the SERS intensity relies largely upon the excitation of localised surface plasmons, it is necessary to control all of the factors influencing the localised SPR in order

to maximise signal strength and ensure reproducibility. The frequency of electromagnetic radiation needed to induce SPR is determined by the type of metal, as well as the size and shape of features on the metal surface. Silver and gold plasmons oscillate at frequencies in the visible region, making them compatible for use with the visible and near-IR lasers used in Raman spectroscopy, and hence these metals are the most commonly used SERS substrates. Common substrates include colloidal nanoparticles or surface-confined nanostructures.

In addition to the obvious advantage of an increase in Raman scattering intensity, SERS has found use in the study of surfaces: the abrupt decay of the enhanced electromagnetic field, which decays as $\frac{1}{r^3}$ from the surface,[23] as well as the requirement for chemisorption of an analyte in order to induce chemical enhancement, ensures that only molecules located on or close to the substrate are probed. Conversely, these factors also mean that SERS has limited applicability when the molecule of interest is not adsorbed directly onto the substrate. The most significant limitation of SERS is its lack of reliability, as minor variations in fabrication processes, or the instability of nanostructures, can lead to surfaces which exhibit spatially inconsistent optical properties and widely varying enhancement factors.

One notable property of SERS is that it can result in the appearance of bands not seen in the conventional Raman spectrum of the same analyte. This occurs when the interaction between the analyte molecule and the SERS substrate, which is necessary for the enhancement to occur, alters the molecule symmetry and affects its polarisibility.

### 3.3.4 Raman Spectroscopy Instrumentation

Raman spectrometers may take a number of different configurations and specifications. This section will discuss the configuration of a generalised dispersive Raman microscope, which is the type of instrument used in this work. A Raman microscope is an instrument in which a microscope forms an integral part of the Raman spectrometer and the sample is placed under the microscope objective. This type of instrument enables the study of extremely small sample sizes or trace amounts of material, despite the weakness of Raman scattering.

Figure 3.6 shows the optical path of a generalised dispersive Raman microscope. Light from a laser source is directed towards a notch filter which removes any unwanted radiation, such as weak emission lines outside the main exciting line of the laser, and thus increases the monochromaticity of the exciting beam. The light is then passed through a lens to produce a parallel beam which is directed into the optics of the microscope. The laser light is focused onto the sample via the microscope objective.

Light scattered or reflected by the sample is also collected by the objective and is returned to the spectrometer via the same optics. In a confocal microscope ar-

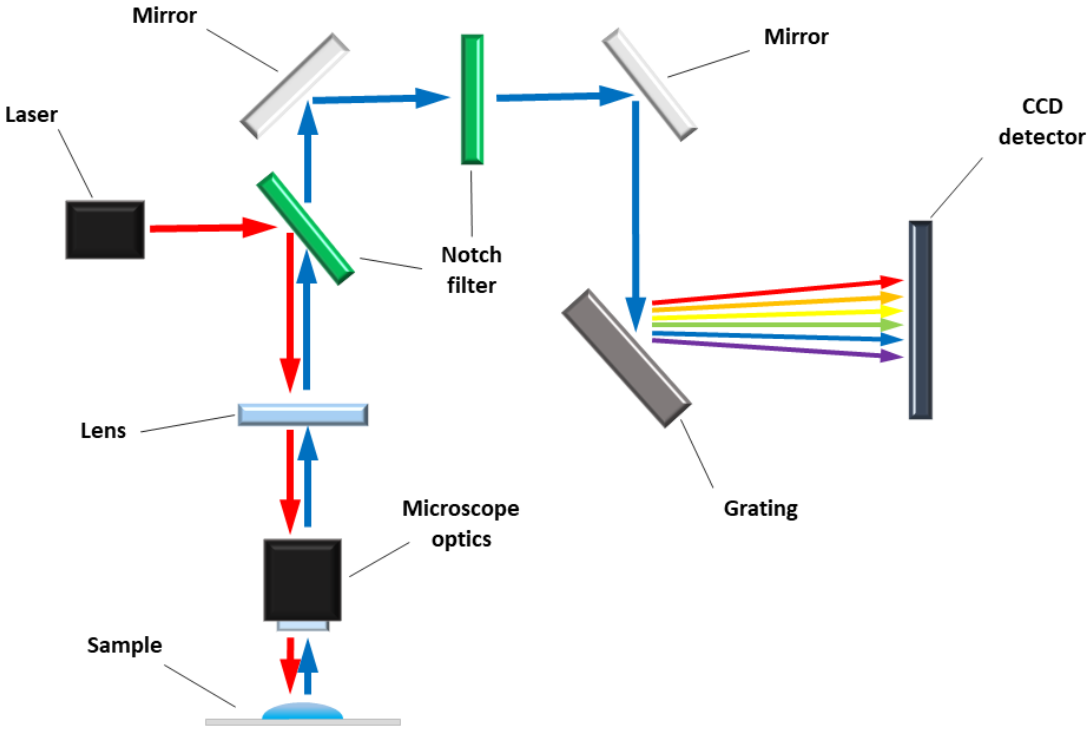


***Figure 3.6:*** *An illustration of the optical path of a generalised dispersive Raman microscope. Laser light is monochromated using a notch filter and passed through a lens to produce a parallel beam. Microscope optics are used to focus the incident light on the sample and collect light scattered by the sample. The scattered light is passed through a notch filter to remove elastically-scattered Rayleigh light and the remaining wavelengths are focused onto a CCD detector by a grating, which separates the beam into its constituent wavelengths.*

rangement, the microscope contains a pinhole in its focal plane which enables only light scattered from the focal plane to be collected efficiently. As a result, confocal microscopes can allow excellent control over depth profiling within the sample.

Once returned to the spectrometer, the scattered light is passed through a notch filter which selectively absorbs all light of the frequency of the incident laser light. This step removes specularly reflected and elastically scattered light, which is a necessary step due to the higher relative intensity of this light compared to inelastically-scatttered light. The remaining scattered light is then directed onto a grating which spatially separates the beam into its constituent wavelengths. These wavelengths are focused onto a Charge-Coupled Device (CCD) detector. Each photon incident on the surface of the CCD generates an electrical charge which allows the signal from the scattered light to be transferred into digital signals.

Raman intensities are measured in units of counts per second. The measured intensity value depends on many apparatus-specific parameters and therefore the ordinate in a Raman spectrum is typically expressed in terms of arbitrary units, or the scale is omitted entirely. The abscissa represents the frequency difference between the

incident photon and the scattered photon and thus should strictly be quoted in units of $\Delta$ cm$^{-1}$ but is often expressed simply as cm$^{-1}$.

## 3.4 Statistical Analysis and Modelling

This section provides an overview of the theory behind the statistical methods used in this work.

### 3.4.1 Analysis of Variance

Analysis Of Variance (ANOVA) is a statistical technique which is used to determine whether there are any statistically significant differences between the means of three or more independent groups. It is used to analyse discrete data sets in which the independent variable is categorical and the dependent variable is continuous. The ANOVA test can be applied to data sets which have any number of independent variables, with each independent variable having multiple different categories.

One-way ANOVA is used for data sets containing only one independent variable. It compares the mean values of each category, or group, of the independent variable and determines whether any of those means are statistically significantly different from each other. Specifically, it tests the null hypothesis:

$$H_0 = \mu_1 = \mu_2 = \mu_3 = ... = \mu_k \tag{3.12}$$

where $\mu$ is the group mean and $k$ is the number of groups. The null hypothesis states that there is no statistically significant difference between the group means. If a one-way ANOVA returns a statistically significant result, the alternative hypothesis is accepted, which states that there are at least two group means that are statistically significantly different from one another.

Three assumptions must be met in order for the ANOVA test to produce a reliable result. Firstly, the residuals (the differences between the mean value and the measured values) of the dependent variable are normally distributed within each group that is being compared. Secondly, the population variances are equal for each group. Finally, it is assumed that observations of the dependent variable are made independently of one another.

One-way ANOVA can only determine whether there are statistically significant differences between the means of any of the groups tested: it cannot identify which specific groups are statistically significantly different from one another. In order to determine which of the groups are statistically significantly different, a multiple comparison *post-hoc* test must be used.

### 3.4.2 Statistical Modelling

Statistical modelling is the generation of a mathematical formula (the 'model') which can be used to describe a set of observed data in which the observations are subject to uncertainty, or randomness, and are therefore regarded as having been drawn from one or more probability distributions. The model is used to estimate the variables, and the relationships between them, that resulted in the observed values of the dataset. It can thus be considered as an approximation of the data-generating process, allowing it to be used to gain deeper insight into the observed dataset or to make predictions about a new set of data.

A statistical model, by definition, provides only an estimation of the data-generating process. As a result, the performance and reliability of a given model is significantly affected by the way in which the model is constructed, with regards to both the formula and the sample data used. The following sections describe some of the most widely-used statistical models.

### 3.4.3 Regression Analysis

Regression analysis is used to construct relationships, of the form $y = f(X)$, between a single dependent variable ($y$) and one or more explanatory variables ($X$). The dependent variable represents the value or process that is being explained or predicted, whilst the explanatory variables are those used to model, or predict, the values of the dependent variables. It should be noted that the statistical relationship between the explanatory and dependent variables does not imply any causation of the dependent variable by the explanatory variable, but represents only an association in the data.

The regression analysis techniques used in this work, Principal Component Regression (PCR) and Partial Least Squares Regression (PLSR), are based upon linear models which specify a linear relationship between the dependent and explanatory variables. This relationship is expressed as a linear function of the form:

$$y = \beta_0 + \beta_1 X_1 + \beta_2 X_2 + ...\beta_n X_n + \varepsilon \tag{3.13}$$

where $\beta_i$ are regresssion coefficients, which take a different value for each explanatory variable, and $\varepsilon$ is the random error term. Regression coefficients are used to quantify the strength and the nature of the relationships between the explanatory variables and the dependent variable. The magnitude of the regression coefficient indicates the strength of the relationship between the explanatory variable and the dependent variable, with a large magnitude indicating a strong relationship, whilst the sign of the regression coefficient indicates whether the association is positive or negative. $\beta_0$ is the regression intercept, which represents the expected value of the dependent variable if all the explanatory variables were zero. As mentioned previously, any statistical model

is only an approximation of the data-generating process and, as a result, the predicted values of the dependent variable will rarely match the observed values exactly. The random error term represents the portion of the dependent variable that cannot be explained by the model.

The development of a regression model begins with a set of known $y$ values, which are often referred to as observed values. These observed values constitute the training dataset and are used to build, or calibrate, the regression model. Prior to developing the model, the data in the training set may be tailored in order to simplify the subsequent calculations. This is often achieved by mean-centering the values of the explanatory variables, a process in which the average value for each explanatory variable is calculated and subtracted from the corresponding variable. During the calibration process, the model can be applied to the training dataset to determine the accuracy with which the identified explanatory variables and regression coefficients can predict the observed values of the dependent variable within the dataset. This process of internal validation is often carried out using the 'leave-one-out' method of cross-validation, in which the model is trained using $n-1$ datasets and is then used to predict the value of the dependent variable in the remaining dataset. The procedure is carried out iteratively until the value of the dependent variable has been predicted for each dataset. Following cross-validation, the performance of the model may be quantified by the Root Mean Square Error of Cross-Validation (RMSECV), which is a measure of the error in the predictive performance of the model during the cross-validation procedure. It provides an estimate of the likely uncertainty that could be expected if the model was used to predict the values of the dependent variable from new datasets. The lower the RMSECV, the more accurate the predictive ability of the model is likely to be.

The calibrated model may then be applied predictively in order to estimate the values of the dependent variable from a new dataset. In order to achieve this, the explanatory variables of one or more samples must be obtained for use as a test dataset. The explanatory variables of the test set, together with the optimised regression coefficients identified during the calibration step, are then used to predict the values of the dependent variable within the test set. This process may be considered as external validation of the model. In this case, the performance of the model may be quantified by the Root Mean Squared Error of Prediction (RMSEP), which is a measure of the uncertainty that can be expected when predicting the values of the dependent variable from new datasets. It is calculated by:

$$RMSEP = \sqrt{\frac{\Sigma(y_i - \hat{y}_i)^2}{n}} \tag{3.14}$$

where $y_i$ and $\hat{y}_i$ are the observed and predicted values of the dependent variable, respectively, and n is the number of values. The lower the RMSEP, the more accurate

the predictive ability of the model.

#### 3.4.3.1 Principal Component Regression

PCR is a form of regression analysis in which the explanatory variables in a dataset are analysed via Principal Component Analysis (PCA) prior to the regression analysis itself.

PCA is a data-reduction technique which is used to reduce the number of explanatory variables to a few linear combinations of the data. Each linear combination is referred to as a 'principal component'. The goal of PCA is to explain the maximum possible amount of variance in the data (the variation of a set of values from their mean) with the fewest principal components.

The first principal component is the linear combination of explanatory variables that has the maximum variance, compared with the other possible linear combinations, and therefore accounts for as much variation in the values of the explanatory variables as possible. The second principal component is the linear combination of explanatory variables that accounts for as much of the remaining variation as possible, under the constraint that the correlation between the first and second principal components is zero. All subsequent principal components follow this pattern: they are linear combinations of the data that account for as much of the remaining variation in the data as possible and are not correlated with the previously-defined principal components.

Following PCA, the values of the dependent variable are regressed on a subset of the identified principal components of the explanatory variables, rather than on the explanatory variables themselves. This process generates a number of estimated regression coefficients equal to the number of principal components. Finally, the regression coefficients are transformed to match the scale of the explanatory variables, in order to obtain values which adequately characterise the original dataset.

#### 3.4.3.2 Partial Least Squares Regression

PLSR is a method of constructing regression equations that involves the generation of new explanatory variables, known as components, which are fewer in number than the original explanatory variables.

The PLSR method is comparable with PCR, as both techniques involve the projection of the explanatory variables into a lower-dimensional space in order to generate new explanatory variables. However, the two methods differ significantly in the manner in which the new explanatory variables are selected. As described previously, the construction of principal components for PCR is based upon accounting for as much of the variation in the values of the explanatory variables as possible. However, this criterion does not guarantee that the principal components, which 'explain' the

explanatory variables optimally, will be relevant for the prediction of the dependent variable. PLSR addresses this issue by incorporating information from the values of the dependent variable when constructing the components to be used in the regression equation.

Each component generated in PLSR is a linear combination of explanatory variables. The first component is selected by finding the linear combination of explanatory variables that explains the maximum variance in the values of the dependent variable. The second component is constructed to explain as much of the remaining variation on the values of the dependent variable as possible, under the constraint that the correlation with the previously-identified component is zero. This process is repeated for the construction of all subsequent components, which are linear combinations of the explanatory variables that account for as much of the remaining variation in the data as possible whilst being uncorrelated to the previously-identified components.

A standard regression analysis is then performed on the components, rather than on the explanatory variables.

#### 3.4.3.3 Model Evaluation

A number of parameters may be used to evaluate the performance of a regression model. This section will discuss the parameters considered in this work.

The $R^2$ value is a statistic, derived from the regression equation, which indicates the degree to which the developed model is able to explain the observed values of the dependent variable. This value can range from 0.0 – 1.0, with higher values indicating that the model is able to explain a greater proportion of the observed data. However, a model with an extremely high $R^2$ value may be heavily biased towards the training data, rendering it less applicable to new datasets, a situation known as model over-fitting. Over-fitting is often caused by the generation of a complex model containing a large number of explanatory variables and poses a problem for models that are intended for predictive use and therefore require generalisation to unknown datasets.

For predictive models, an assessment of the RMSECV or RMSEP often provides a more useful indicator of model performance. The RMSEP is generated following the application of the model to a test dataset and is therefore a more accurate reflection of the predictive performance of the model as applied to unknown datasets than the RMSECV, which is generated via internal cross-validation and is therefore an estimate of the predictive performance of the model. However, the RMSECV may be more convenient to use on relatively small datasets, as it allows all available data to be used in the calibration of the model. Conversely, calculation of the RMSEP requires a dataset to be split into a training set and a test set, which necessarily reduces the amount of data available for model calibration. For small datasets, this reduction in data may result in the generation of a less accurate model which is more strongly

affected by the presence of outlying data points.

# Chapter 4

# Current State of the Art

This chapter describes the current state of the art, as determined by a review of the scientific literature, in four key areas relevant to this thesis: detection of glucose, lactate and pyruvate; IR spectroscopy; Raman spectroscopy; and neurochemical monitoring. Preliminary work into the analysis of microdialysate samples via ATR-FTIR spectroscopy, carried out by a previous member of the Elliott group, is also described.

## 4.1 Detection of Glucose, Lactate & Pyruvate

The ISCUS Flex is the 'gold-standard' commercially-available instrument for analysing glucose, lactate and pyruvate concentrations in microdialysate samples, as discussed in Section 2.3.3. However, the development of alternative methods for detecting these compounds, within a variety of contexts, remains an active area of research. The following sub-sections will provide an overview of the latest developments in this field, as described in the scientific literature, for each compound in turn.

### 4.1.1 Glucose Detection

The development of glucose sensors is a major field of research due to the significant role of glucose detection in the management of *diabetes mellitus*. The research encompasses a range of transducer types, each of which will be addressed separately here.

#### 4.1.1.1 Electrochemical Sensing

The majority of glucose sensors rely upon an electrochemical transducing system due to the rapid respose time it affords.[24] Electrochemical glucose sensors are typically based on amperometric measurements in which the presence of glucose causes a change in current between two electrodes which have an applied potential across them. These sensors are often based upon the glucose oxidase-catalysed oxidation of glucose, a

reaction which requires the flavin adenine dinucleotide (FAD) cofactor and involves the concurrent reduction of molecular oxygen to $H_2O_2$. The process is summarised in Figure 4.1. The use of glucose oxidase in these devices also confers the benefit of selectivity towards glucose.

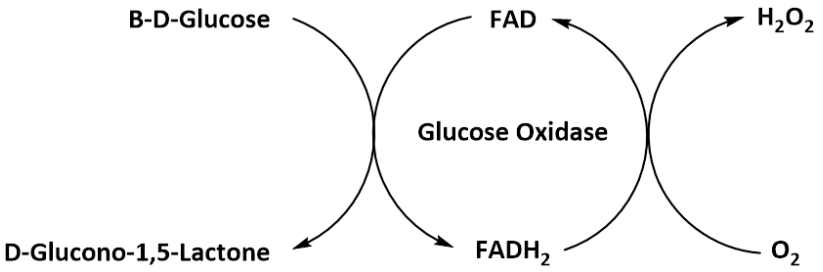


***Figure 4.1:*** *Summary of the reaction between glucose and glucose oxidase, showing the role of FAD and the concurrent reduction of molecular oxygen to $H_2O_2$.*

The glucose oxidase enzyme is immobilised on the anode of an electrochemical cell, allowing the production of $H_2O_2$ to be detected by the generation of a current resulting from the re-oxidation of $H_2O_2$ at the electrode (Figure 4.2). The amplitude of the current is proportional to the concentration of $H_2O_2$ and hence to the concentration of glucose in the sample.

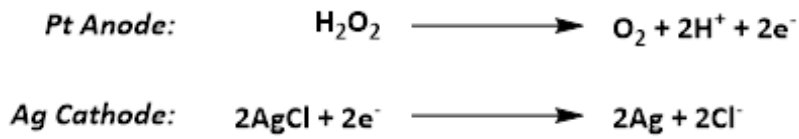


***Figure 4.2:*** *Summary of the reactions which occur at the electrodes of a glucose oxidase-based amperometric glucose sensor.*

A microfabricated amperometric glucose sensor based on this principle has been incorporated into a contact lens for the *in situ* monitoring of tear glucose levels.[25] Glucose oxidase was immobilised in a titania sol-gel layer positioned between the working and counter electrodes, which were fabricated on a polyethylene terephthalate (PET) film. The device exhibited a response time of 20 seconds and demonstrated a linear response to the range of glucose concentrations found in tears (0.1–0.6 mM).

A recent paper describes a graphene-based dermal patch containing an amperometric glucose sensor and an array of polymeric microneedles, which can be thermally activated to deliver drugs transcutaneously, for the simultaneous monitoring and treatment of *diabetes mellitus*.[26] The sensing element of the device, which is used to monitor the glucose concentration in the sweat of the wearer, is based upon the amperometric measurement of $H_2O_2$ as described above. It has been used to measure the sweat glucose levels of two healthy volunteers and the results were compared

with those obtained using a commercially-available glucose sensor. The two set of measurements were correlated with an $R^2$ value of 0.89.

One drawback of devices which operate on this principle is their dependency on the availability of dissolved molecular oxygen at the anode. This dependency can be avoided through the use of chemical mediators, such as ferrocenes, to transfer the electrons directly from the glucose oxidase/FAD complex to the anode as illustrated in Figure 4.3.

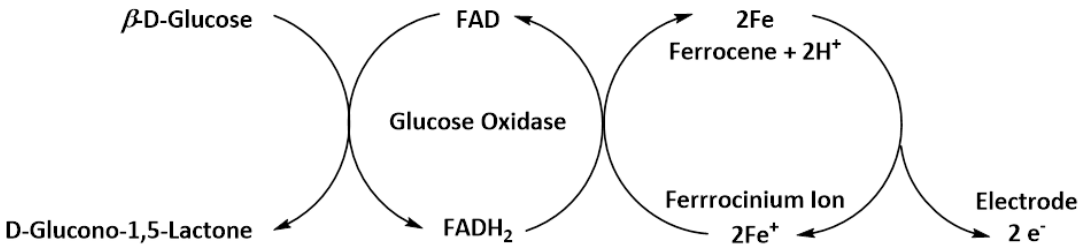


***Figure 4.3:*** *Generation of a current at the anode of an amperometric glucose sensor using glucose oxidase and a ferrocene mediator.*

Some studies report the development of novel electrodes which are able to remove electrons directly from the glucose oxidase enzyme, negating the need for a separate electroactive species. Recently-reported electrodes include a gold electrode coated with chitosan nanoparticles[27] and a palladium/platinum nanocube electrode coated with chitosan.[28]

Other research efforts have focused on the development of electrodes for non-enzymatic amperometric glucose detection. These devices measure the current produced from the direct electro-oxidation of glucose by the electrode. Recently-developed electrodes used for this purpose include: a ZnO nanorod array coated with nickel nanoparticles and covered with graphene oxide nanosheets;[29] multi-walled carbon nanotubes coated with nanoparticles possessing a gold-palladium core and a CuO outer shell;[30] a $Ni(OH)_2/Al(OH)_4^-$ film[31] and $CuWO_4$ microrings.[32]

Non-enzymatic amperometric glucose sensors can suffer from a lack of selectivity due to the absence of a glucose-specific receptor. This problem has been addressed through the integration of molecularly-imprinted polymers (MIPs) with the working electrode of such a sensor.[33] A CuCo electrode, capable of the direct electro-oxidation of glucose, was coated with a polymer imprinted with glucose molecules to enable shape-specific recognition of glucose. The resulting device exhibited a dynamic range of 0.001–25 mM and was successfully used to measure the glucose concentration in whole-blood samples taken from healthy human volunteers.

Electrochemical glucose detection has been achieved using non-amperometric techniques. For example, one group has reported the development of a chemi-resistive sensor based on single-walled carbon nanotubes.[34] The device contained gold electrodes

coated with a polymer-nanotube composite which was functionalised with glucose oxidase. This material exhibited a measurable decrease in electrical resistance upon exposure to glucose, attributed to p-doping of the nanotubes caused by the $H_2O_2$ produced during the reaction between glucose and glucose oxidase. The sensor exhibited a linear response to glucose concentrations between 0.08–2.2 mM.

#### 4.1.1.2 Optical Sensing

A number of studies report the optical detection of glucose via colorimetric assays. Many of these assays are based upon the oxidation of glucose by glucose oxidase: $H_2O_2$ produced during the reaction is used to oxidise 3,3',5,5'-tetramethylbenzidine (TMB), in a reaction catalysed by a peroxidase mimic, to produce a blue colour that can be visually detected. The intensity of the colour, which is typically measured by absoprtion spectroscopy, is proportional to the concentration of glucose in the sample. Multiple peroxidase mimics have been trialled within this system, including chitosan-gold nanoparticles;[35] cobalt oxyhydroxide nanoflakes;[36] metal-organic frameworks;[37] platinum nanoclusters[38] and carbon-coated $Fe_3O_4$ nanoparticles.[39] This method is typically suitable for detection of glucose concentrations within the millimolar range.

A recent study describes a colorimetric glucose assay based on an alternative mechanism, in which $MnO_2$ nanosheets were rapidly decomposed by $H_2O_2$ produced during the glucose oxidase-catalysed oxidation of glucose. The decrease in the $MnO_2$ absorption band at 370 nm was proportional to the concentration of glucose in the sample and exhibited a linear relationship for concentrations of glucose ranging from 0.5–50 $\mu$M.[40]

Other studies have used the generation or quenching of luminescence as a transduction method for the detection of glucose.[41–43] For example, one study describes the synthesis of aluminium-doped ZnO thin films which exhibit stong photoluminescence at 372 nm and 564–775 nm.[44] Immersing the thin film in a solution containing glucose and glucose oxidase resulted in a quenching of luminescence which is believed to be caused by charge transfer from $H_2O_2$, produced during the reaction between glucose and glucose oxidase, to the film. This method was successfully used to detect glucose concentrations ranging from 0.02–20 mM.

Similarly, some studies have reported the detection of glucose via a change in fluorescence intensity.[45–47] For example, the fluorescence intensity of blue-emitting gold nanoclusters capped with haemoglobin was found to increase in the presence of $H_2O_2$.[48] This property was exploited for the detection of glucose in human serum samples: the samples were incubated with glucose oxidase for ten minutes at 37 °C, before being added to a solution of gold nanoclusters. The increase in fluorescence intensity, caused by the $H_2O_2$ produced during the reaction between glucose and glucose oxidase, was compared against a calibration curve which had been created using

synthetic samples of known glucose concentration.This method was able to predict the glucose concentration to within 10% of the actual concentration, although it is noted that the total time required for detection was 40 minutes.

#### 4.1.1.3 Other Sensing Methods

Electrochemical sensing and optical sensing are the most widely-used techniques for the detection of glucose. However, other transducer types have been reported in the literature. For example, a quartz-crystal microbalance (QCM), which detects the adsorption of molecules via a change in the resonance frequency of a quartz-crystal resonator, has been used for the mechanical detection of glucose.[49] The QCM was functionalised with cyclic peptides which were designed to mimic the glucose binding site of glucose binding protein, conferring a degree of selectivity for glucose. However, the nonspecific binding of proteins to the sensor surface interfered with the analysis of glucose in human serum samples. The effect of nonspecific binding could be reduced by a ten-fold dilution of the serum samples in phosphate-buffered saline.

A very different study describes the detection of glucose by a DNAzyme, a sequence of deoxyribonucleic acid (DNA) which possesses catalytic properties, in combination with glucose oxidase.[50] The DNAzyme used in this study is a DNA-cleaving molecule which requires a combination of $H_2O_2$ and $Cu^{2+}$ as cofactors. $H_2O_2$, produced by the glucose oxidase-catalysed oxidation of glucose, therefore induced a self-cleavage reaction of the DNAznyme in the presence of $Cu^{2+}$. The degree of DNA cleavage was observed via gel electrophoresis and could be related to the concentration of glucose present in the sample. This device was successfully used for the analysis of glucose levels in human tears and human saliva.

### 4.1.2 Lactate Detection

Lactate detection has two significant clinical uses. The first of these is the monitoring of patients with a number of medical conditions, including TBI, as lactate concentration is closely linked to both oxygen availability and metabolic status. This relationship between lactate concentration, oxygen availability and metabolic status leads to the second clinical use of lactate: the assessment of athletic performance. Monitoring of tissue-lactate levels during exercise enables the calculation of the anaerobic threshold of an individual, which is considered a key measure of fitness.

Reported detection methods for lactate fall into into two main categories: optical detection and electrochemical detection. Of the studies utilising optical-detection methods, the majority are based on monitoring changes in fluorescence intensity. For example, a recent study used a boron-dipyrromethene derivative, modified with an ester group for optimal binding of hydroxyl compounds, which exhibited an increase in emission upon forming a complex with lactate.[51] The modified compound was

designed to emit light in the near-IR region to allow it to be used for monitoring lactate within biological tissue, athough it is noted that this compound would exhibit the same behaviour upon binding to any hydroxyl-containing compound and thus the detection method is not lactate-specific.

Lactate-specific fluorescent detection has been achieved by introducing the lactate oxidase enzyme, which undergoes a similar set of reactions to glucose oxidase, into the analytical setup. One such study used a tetraphenylethylene-based fluorophore which was readily oxidised by $H_2O_2$, generated from the lactate oxidase-catalysed oxidation of lactate, to produce a compound which released a strong emission at 530 nm.[52] The intensity of the emission was proportional to the concentration of $H_2O_2$ produced and hence to the amount of lactate in the sample. However, this method had an upper limit of 0.02 mM, beyond which the relationship between emission intensity and lactate concentration was non-linear. Another study, which also utilised the reaction between lactate and lactate oxidase, incorporated cupric oxide nanoparticles as an additional reagent.[53] The nanoparticles catalysed the decompositon of $H_2O_2$ and the resulting hydroxyl radicals oxidised terephthalic acid to form a fluorescent product with an emission of 422 nm. This method was used for the quantitative detection of lactate in human serum samples, within the range 2.5–3.5 mM, although it is noted that proteins were filtered out of the sample prior to analysis in order to reduce possible interference.

Colorimetry has been used as an alternative optical-detection method for lactate.[54] This method was based upon a two-step reaction. In the first step, lactate oxidase was used for the analyte-specific oxidation of lactate. The $H_2O_2$ produced by this reaction was then used to oxidise TMB, in a reaction catalysed by horseradish peroxidase, to form a coloured product. The intensity of the colour change was proportional to the concentration of lactate in the sample. This device was produced as a paper-based sensor in which each reagent was immobilised in separate layers atop a paper substrate. Lactate concentrations were determined via reflectance measurements taken using the camera and flash of a smartphone. The group also developed an accessory which was used to ensure consistent positioning of the functionalised paper surface, at the correct distance from the smartphone camera, and to reduce interference from ambient light. The setup was successfully used to monitor lactate levels within saliva samples taken from healthy human volunteers at various stages of a running-based exercise routine, with a limit of detection of 0.1 mM, and required a total of one minute for each measurement.

Multiple studies report the detection of lactate via electrochemical methods. Many of these involve amperometric measurements in which lactate oxidase is immobilised on the working electrode: flexible graphene nanowalls[55] and carbon electrodes coated with gold, copper or platinum nanoflakes[56] have both been trialled as working elec-

trodes in such experiments. One interesting aperometry-based study used printable electrodes placed on a mouthguard for the detection of lactate from saliva.[57] A screen-printing method was used to produce an Ag/AgCl reference electrode and a prussian blue working electrode, which was functionalised with lactate oxidase, on a PET film. A current was produced at the working electrode via the prussian blue-catalysed reduction of hydrogen peroxide, which was produced through the reaction between lactate oxidase and lactate. The PET film was then applied to a mouthguard using double-sided adhesive and connected to an analyser via wires attached to Ag/AgCl contacts on the sensor. This system was used to measure the lactate concentration of human saliva samples spiked with known concentrations of lactate, but has not been tested *in vivo*.

Screen-printed electrodes have also been used to manufacture an electrochemical biosensor that affixes to the skin, in the form of a temporary tattoo, for the measurement of lactate levels in sweat.[58] This system used a carbon working electrode, functionalised with lactate oxidase tethered to multiwalled carbon nanotubes, and an Ag/AgCl reference electrode. Both electrodes were screen-printed using inks which included a dispersion of carbon fibres, in order to improve the tensile strength of the tattoo, and were covered with a chitosan overlayer which served as the tattoo base. Tattoos were applied on the deltoid of a human subject and connected to an electrochemical analyser via stainless steel wires. The temporal sweat lactate profiles of a total of ten subjects were collected via the tattoo, using amperometric measurements, over the course of a cycling exercise session. In each case, the performance of the device was tested against control tattoo sensors, which contained no lactate oxidase, in order to confirm the specificity of the sensor towards lactate. The sensor readout demonstrated a linear response to increasing lactate concentration up to 20 mM.

An alternative electrochemical lactate sensor used MIPs in place of lactate oxidase to achieve specific detection of lactate.[59] The sensor consisted of a planar, screen-printed, carbon electrode modified with poly(3-aminophenylboronic acid) which was molecularly imprinted with lactate to create a shape-specific recognition site. The electrode was used to evaluate the lactate content of human sweat samples via impedence measurements, in which the resistance of the film was found to decrease in response to increasing lactate concentration. Lactate concentrations from 10–40 mM were measured using the device, which exhibited an average response time of 2–3 minutes.

### 4.1.3 Pyruvate Detection

A review of the scientific literature found far fewer studies relating to pyruvate detection than to the detection of glucose or lactate. An early study used a two-stage reaction which began with the pyruvate decarboxylase-catalysed conversion of pyruvate

to acetaldehyde and $CO_2$. The resulting $CO_2$ increased the acidity of a pH-sensitive fluorescent indicator, causing a change in emission at 520 nm. A slice of corn tissue, integrated directly into the sensor, was used as the source of pyruvate decarboxylase. The sensor was assembled in a vertical configuration: the corn tissue was placed at the bottom of the assembly, in direct contact with a gas-permeable membrane placed above it. A reservoir of indicator solution was positioned atop the membrane and was enclosed by a glass slide above it. The tip of an optical fibre, the light source of the sensor, was placed above the glass slide in direct contact with its surface. Finally, the whole assembly was enclosed within a pipette tip, allowing the sensor to be operated by dipping its lower end into a buffer solution containing the analyte. This setup was used to detect pyruvate in buffer solution at concentrations of 0.2 –3 mM. However, the response time of the sensor was slow, requiring between 7 – 35 minutes for detection, depending upon the concentration of pyruvate under investigation.

Another study employed Förster Resonance Energy Transfer (FRET) sensing for the detection of pyruvate.[60] This technique involves a transfer of energy, via dipole-dipole coupling, from an excited-state donor chromophore to an acceptor chromophore. The efficiency of the transfer is correlated to the distance between donor and acceptor, being inversely proportional to the sixth power of the distance between them, and can therefore be used to monitor small changes in the separation between the two. The FRET study utilised PdhR protein, a transcriptional regulator which binds to pyruvate *in vivo*, which was modified to contain a donor and acceptor chromophore at either end of the molecule. Upon binding to pyruvate, the conformation of the protein was altered and hence the distance between the chromophores would change. This allowed pyruvate binding events to be detected as a variation in the ratio of the fluorescence intensities of the two chromophores. The modified protein was introduced to living cells, including neurons, and used in this way to perform real-time quantitative measurements of pyruvate production and consumption in individual cells.

Pyruvate has also been detected electrochemically.[61] In this study, the working electrode consisted of a platinum-coated 0.25 mm gold-wire tip which was coated with a layer of recombinant pyruvate oxidase immobilised in an electron-conducting hydrogel. The recombinant enzyme catalysed the conversion of pyruvate and orthophosphate to acetyl phosphase, with concurrent production of $CO_2$ and $H_2O_2$, at the working electrode. The working electrode was held at 0.4 V compared to an Ag/AgCl reference electrode and this setup was able to detect pyruvate concentrations as low as 0.03 mM against a background of calf serum.

## 4.2 IR Spectroscopy

IR spectroscopy has successfully been used for a wide range of applications, including the detection of HCN in exhaled breath;[62] monitoring $CO_2$ production in human cell cultures;[63] investigating monolayers of membrane proteins,[64] the differentiation of mammalian cell types[65] and the characterisation of wine vinegars to ensure quality control.[66]

A recent study has proposed the use of FTIR spectroscopy as a tool for the forensic analysis of deaths following TBI.[67] The study focuses on traumatic axonal injury, a common secondary brain injury, which involves the shearing and stretching of axons and cannot be detected using conventional neuroimaging techniques: it is usually only diagnosed via histopathological staining during post-mortem examinations. An ability to determine the time interval between the onset of traumatic axonal injury and death may be useful in forensic analysis for estimating the time of the initial traumatic incident. This study used FTIR spectroscopy to analyse differences in the brain tissue of rats euthanased at different time points (12, 24 or 72 hours) following a controlled TBI. The spectra of tissue taken from animals euthanased at different times post-injury were distinguishable from each other, and from tissue taken from a control group of animals with no TBI, due to changes in absorption peaks associated with proteins, lipids and carbohydrates. The spectra were analysed via hierarchical cluster analysis, which produces a diagram that shows the degree of similarity between spectra, and via PLSR in order to produce a calibration model that was successfully used to predict the injury interval of traumatic axonal injury in an unknown sample dataset.

FTIR spectroscopy has been investigated as an alternative to histopathological staining for a number of other tissues,[68–71] including the oesophagus. A recent study describes the use of FTIR spectroscopy mapping to develop an automated histology tool for the discrimination of normal, pre-malignant and malignant cells of the oesophagus.[72] It is hoped that this automated method could provide a more objective method of assessing histopathology, as the interpretation of conventional histopathological staining can vary between indiviuals carrying out the examination. A total of 22 tissue samples were biopsied from human patients, frozen and cut into sections 8 $\mu$m thick. Frozen sections were mounted on $CaF_2$ slides and thawed prior to the acquisition of FTIR spectra. Sections immediately adjacent to those examined by FTIR spectroscopy were analysed using conventional histological staining techniques to provide reference data. A total of 737,280 FTIR spectra were acquired, across all tissue samples, using a FTIR spectrometer connected to a microscope. A series of data-analysis steps were carried out on the spectral region 1800–950 $cm^{-1}$ in order to create a diagnostic classification model based on the differences between tissue spectra. After normalisation and mean-centring of the dataset, PCA was performed

to analyse the variance in the data. An ANOVA test was carried out on the first 50 principal components identified by PCA in order to find the components which provided the greatest discrimination between pathology groups. Linear discriminant analysis was then carried out on the principal components selected by the ANOVA analysis and used to assign samples into groups to build a diagnostic classification model. Linear discriminant analysis is a technique used to find a linear combination of features which separates two or more classes of object and is used for datasets in which the independent variable is continuous and the dependent variable is catagorical. The categorical predictions for each spectrum were then combined to generate a prediction for the whole tissue sample. In samples where multiple pathologies were found, it was determined that each sample would be categorised as having the worst pathology if at least 30% of the spectra exhibited that pathology. The resulting model was tested using leave-one-out cross-validation. Classification of normal vs. abnormal tissue samples using this method was found to have 100% sensitivity and specificity.

### 4.2.1 Detection of Metabolites by IR Spectroscopy

IR spectroscopy has also been used for quantitative analysis of two of the compounds relevant to this work: glucose and lactate. One early study attempted to measure exercise-induced changes to blood glucose and lacate levels in human subjects.[73] Three replicates of 50 $\mu$L blood samples were taken from human subjects at rest, following medium-intensity exercise and following high-intensity exercise, producing a total of 198 samples. Two samples from each set of replicates were analysed using well-establised techniques to determine their glucose and lactate concentrations, while the third was studied via FTIR spectroscopy. Prior to the acquisition of FTIR spectra, samples were diluted with water, homogenised and then dried. Spectra were acquired via transmission-FTIR spectroscopy using 32 accumulations to generate each spectrum. Glucose and lactate concentrations were determined by analysing a single absorbance peak for each compound: the 1033 $cm^{-1}$ glucose peak and the 1127 $cm^{-1}$ lactate peak. A calibration curve was created for each peak, using solutions of known concentrations of glucose and lactate, and used to estimate glucose and lactate concentrations from the FTIR spectra of the test samples. This approach was complicated by the fact that the lactate peak of interest partially overlapped with a glucose absorbance peak and, as a result, required the subtraction of the glucose absoption spectrum from the overall spectrum to allow an analysis of the lactate concentration. Despite this adjustment, large prediction errors were found in lactate concentrations below 0.5 mM or above 15 mM.

A later study also investigated exercise-induced changes in metabolite levels in the blood, but focused only on the detection of lactate. This work used near-infrared spectroscopy, covering the 11500–4000 $cm^{-1}$ spectral range, to measure changes in human

blood-lactate levels before, immediately following and ten minutes after exercise.[74] The analysis was carried out on whole-blood samples, which were collected into tubes and immediately treated to arrest glycolysis. Spectra were acquired via transmission-FTIR using a 1 mm optical path length. In this study, the spectra were analysed using statistical methods rather than using a calibration curve. Prior to analysis, the spectra were mean-centred, to emphasise subtle variations in spectra, and the second derivative of each spectrum was calculated in order to enhance the spectral variation of lactate over the background spectrum and minimise baseline variation. PLSR using the 'leave-N-out' method of cross-validation was used to analyse the spectral range from 4962–4167 $cm^{-1}$, which was selected to minimise interference from water, whilst reference concentrations were determined by enzymatic measurements using a commercially-available analyser. The final PLSR model contained seven components and was able to predict blood-lactate concentrations ranging from 0.3–25 mM with a standard error of cross validation of 0.65 mM.

An alternative analytical approach was taken in a 2008 study which aimed to measure glucose levels in whole-blood samples taken from healthy human volunteers.[75] Samples were initally analysed by ATR-FTIR spectroscopy, using a ZnSe crystal, but it was found that the spectra changed with time as they were affected by the sedimentation of red blood cells onto the crystal surface. An alternative method was devised which utilised transmission-FTIR spectroscopy in combination with a dual-wavelength $CO_2$ laser tuned to the isosbestic point at 950 $cm^{-1}$, for background correction, and to the glucose absorption band at 1080 $cm^{-1}$. Whole blood was placed directy into an optical cell possessing a path length of 50 $\mu$m and the ratio of the two wavelengths of light detected after passing through the optical cell was used to determine the glucose concentration. These measurements could be carried out in milliseconds and were therefore unaffected by red blood cell sedimentation. Reference measurements were carried out separately on each sample and a comparison of predicted vs. refererence values, for glucose concentrations ranging from 0.2 - 2 mM, gave an $R^2$ value of 0.997.

Mid-IR spectroscopy has been used for noninvasive measurements of blood-glucose levels in human subjects by focusing IR light directly at the skin.[76] A mid-IR, broadly tunable, quantum cascade laser (QCL) was coupled with a hollow-core fibre to deliver IR radiation to a region of skin between thumb and forefinger. Light was able to penetrate to the dermis layer of the skin, where the interstitial glucose concentration has the closest correlation to blood-glucose levels.[77] Backscattered light was collected via a bundle of 6 fibres, identical in composition and size to the delivery fibre, which was coupled directly to a commercially-available detector. Measurements were taken on three healthy volunteers before, during and after the consumption of food. The process was repeated multiple times over a period of weeks in order to

build a sufficiently large data set for PLSR analysis. Calculated values of the glucose concentration were compared with measurements of blood-glucose acquired using a commercially-available electrochemical blood-glucose meter immediately before and after each optical reading. The PLSR model was able to predict blood-glucose concentrations between 0.5 and 0.9 mM to clinical accuracy, defined as being within 20% of the actual value, for 84% of measurements.

### 4.2.2 IR Spectroscopy & Microfluidics

An on-line spectroscopy-based sensor for metabolic profiling of TBI patients may be required to detect glucose, lactate and pyruvate within flowing microdialysate samples, which will be of low volume as a result of the low flow rate (0.3 $\mu$L min$^{-1}$) used in microdialysis, depending upon the design of the sensor chip. It is therefore encouraging to note a number of examples in the literature describing the successful integration of IR spectroscopy with microfluidics.[78]

A recent example of such a study combined ATR-FTIR spectroscopy with microfluidics to analyse pharmaceutical formulations.[79] The study used microfluidic chips that were created by casting Polydimethylsiloxane (PDMS) over a 3D printed acrylic mould, producing a device with microfluidic channels imprinted on its lower face. This imprinted surface was placed directly against a commercially-available ATR-FTIR crystal and secured using a perspex top-plate, creating sealed channels in which the upper and side walls formed by the PDMS chip and the lower wall of the channel was the ATR crystal itself. This setup was used to study the dissolution of micro-formulations of ibuprofen and polyethylene glycol under flowing conditions via ATR-FTIR spectroscopy. The technique was also used to monitor the recrystallisation of ibuprofen upon contact with acidic solutions, using a flow rate of 10 $\mu$L min$^{-1}$.

## 4.3 Raman Spectroscopy

Raman spectroscopy has been used in multiple applications, including the histological imaging of a human polyp sample,[80] differentiation of prostatic adenocarcinoma cell lines[81] and determining the level of carbonation in cement paste with a view to monitoring the status of concrete structures.[82]

A number of studies have described the development of accessories for the acquisition of Raman spectra which extend the range of potential applications for which it can be used. For example, a hand-held contact Raman spectroscopy probe, capable of identifying cancer cells that have invaded healthy brain tissue at cellular resolution, has been developed and used intraoperatively during the resection of grade 2–4 gliomas.[83] The probe contains fibre-optic cables, fitted with micrometre scale in-line filters for the attenuation of elestically-scattered light, which are connected to a CCD

and PC to enable the visualisation of spectra in real time. A 785 nm laser was focused to a spot size of 0.2 $mm^2$ and used to measure the Raman signal at several points in the surgical cavity. The total acquisition time used for the examination of a site was 0.2 seconds, which corresponded to the acquisition of three Raman spectra and a background measurement in which there was no laser excitation. A corresponding tissue biopsy was taken from each interrogation site and examined via histological staining to allow verification of the results of the Raman study. A total of 161 Raman measurements were taken across 17 patients and the spectra were analysed by the 'boosted trees' machine-learning algorithm, which was used to classify each region of tissue as 'normal', 'dense cancer' or 'normal tissue invaded by cancer cells', based upon its Raman spectra. Comparison of the algorithm results with histological staining indicated that the method could be used to classify brain tissue with a sensitivity of 93% and a specificity of 91%. It is hoped that this method could facilitate the intraoperative identification of tumour boundaries, leading to improved patient outcome and reducing the need for repeated operations.

Another study reports the development of a multifibre Raman probe that fits inside the bore of a hypodermic needle, enabling its use for subcutaneous Raman spectroscopy of tissues.[84] The probe consists of a central excitation fibre surrounded by six collection fibres, composed of low-OH silica, and has a total diameter of 720 $\mu$m which allows it to be easily inserted into a 19-gauge disposable hypodermic needle. Crucially, the expensive optical components of the system are positioned outside the needle probe, meaning that the portion of fibre within the needle is relatively inexpensive and can therefore be disposable. The properties of the probe were tested using a two-layer tissue phantom and an excised human lymph node, using an excitation wavelength of 830 nm and excitation powers ranging from 20–100 mW. A comparison with data generated in a previous study by the same group suggests that the signal-to-noise ratio demonstrated by the probe is 3–4 times higher than that required for discrimination between benign lymph nodes, primary lymph node malignancies and secondary lymph node malignancies.[85] These results suggest that the developed probe has potential for the *in vivo* diagnosis of Hodgkin's and non-Hodgkin's lymphomas.

### 4.3.1 SERS

Much of the current research into SERS is focused on the development of novel SERS substrates offering improved enhancement factors. This often involves the creation of new nanostructures for the generation of localised surface plasmons. Previously-reported nanostructures include: vertical silver nanorod zig-zag arrays containing nanogaps at the joins between rods;[86] vertically-oriented ZnO nanorod arrays coated with a 30 nm gold layer;[87] a three-dimensional carbon foam coated with silver nanosheets;[88] flower-like silver mesoparticles;[89] silver nanowires coated with silver nanoparticles;[90]

porous ZnO microspheres coated with silver nanoparticles[91] and gold nanostar arrays coated with a layer of graphene followed by a layer of gold nanoparticles.[92] One group has reported the development of a 'smart' SERS substrate consisting of silver nanoparticles encapsulated in polyacryloyl hydrazide.[93] Polyacryloyl hydrazide is a pH-responsive polymer which swells at high pH and shrinks as the pH decreases. This property allowed the spacing of the silver nanoparticles, and hence the characteristics of the local surface plasmons, to be tuned by controlling the pH of the substrate.

Many groups report the functionalisation of SERS substrates with analyte-specific receptors to enable SERS-based detection of a compound of interest. Analyte-specific aptamers (nucleotide or peptide sequences which enable shape-specific recognition through their three-dimensional structure) have been used in the detection of a number of substances, including $Hg^{2+}$ ions;[94–96] circulating tumour cells[97] and ATP.[98] Sequence-specific DNA probes have also been coupled with SERS for the detection of nucleic acids, such as micro-ribonucleic acid[99] and hepatitis B viral DNA,[100] at femtomolar concentrations.

### 4.3.2 Detection of Metabolites by Raman Spectroscopy & SERS

A number of studies describe the detection of metabolic intermediates by Raman spectroscopy or SERS, with the majority of studies focusing on glucose detection. The van Duyne group, in particular, has carried out a significant amount of work on the development of a SERS substrate for the detection of glucose and lactate. The substrate, known as a 'film-over-nanosphere' surface, is chemically modified in order to concentrate the analyte molecules within 2 nm of the substrate surface to ensure that they are exposed to the high electric fields necessary for SERS.[101] It consists of silica nanospheres arranged in a hexagonal close-packed array on a silicon or titanium substrate and coated with a 200 nm layer of silver or gold. The metallic layer is then functionalised with a mixed self-assembled monolayer of 1-decanethiol and mercaptohexanol to which glucose and lactate are able to adsorb. This system was initially used to detect aqueous glucose concentrations from 0–25 mM using a 633 nm excitation source, with a power at the sample of 3.25 mW, and an acquisition time of 30 seconds. Attempts to detect aqueous glucose using an unfunctionalised substrate were unsuccessful, indicating that the 1-decanethiol/mercaptohexanol monolayer plays a significant role in glucose detection.

This method has also been applied to the quantitative *in vitro* detection of lactate, at concentrations ranging from 0.5–22 mM, using a 532 nm excitation source with a power of 10 mW at the sample.[102] The substrate was incubated in lactate solution for two minutes prior to performing measurements, to ensure adsorption onto the monolayer, and a 2 minute acquisition time was used for each spectrum. Significant spectral pre-processing was carried out prior to data analysis, including: smoothing,

cosmic-ray removal and the removal of background changes that occurred over time. PLSR analysis of the resulting data set, in combination with leave-one-out cross-validation, yielded a RMSEP of 3.4 mM.

A silver film-over-nanosphere substrate has been used to demonstrate *in vivo*, transcutaneous, monitoring of glucose in live rats.[103] The substrate was implanted subcutaneously in a rat and regular measurements were taken using surface-enhanced spatially offset Raman spectroscopy, a variation of SERS in which the excitation of molecules and collection of scattered light are spatially separated. This technique is useful for measuring layered samples in which the analyte of interest lies below an opaque external layer, such as the skin. It requires the acquisition of multiple spectra, one in which light is collected at the source and others where light is collected at an offset position typically millimetres away from the excitation point, and subsequent calculation of the differences between spectra allows the spectra of sub-surface components to be revealed. Using this technique, combined with PLSR analysis and leave-one-out calibration, the group were able to monitor the glucose concentration of the animal for 17 days with a RMSEP of 0.8 mM. Beyond this time, the quality of the spectrum was found to deteriorate significantly. A 785 nm excitation source was used for all measurements, generating a surface power of 50 mW, and each spectrum was acquired over two minutes.

Recently, the group have developed an alternative chemical modification for film-over-nanosphere substrates based on an analogue of the 4-amino-3-fluorophenylboronic acid molecule.[104] Boronic acid derivatives are able to covalently bond, through their diol functional groups, to saccharide molecules to form cyclic boronate esters. The particular analogue used by the van Duyne group has been shown to exhibit a degree of chemical selectivity by preferentially binding to glucose over fructose in an equimolar mixture of the two. Gold film-over-nanosphere substrates functionalised with this molecule were used, in combination with a 785 nm excitation source, to detect glucose in phosphate buffer at physiologically-relevant concentrations ranging from 1 mM–10 mM. PCA was performed on the resulting data set and a hierarchical cluster analysis was carried out on the first six principal components of the data. With no prior knowledge of the glucose concentrations involved, this procedure was able to accurately group the spectra into distinct categories corresponding to the level of glucose: no glucose, hypoglycaemia, normal blood glucose and hyperglycaemia. No prediction of absolute glucose concentrations from the spectra was attempted. It should also be noted that substrates were incubated in the appropriate glucose solutions for an undisclosed period of time prior to measurement, indicating that the system is not currently capable of real-time measurement.

Another group has used conventional Raman spectroscopy for the non-invasive, transcutaneous, determination of blood-glucose levels in human volunteers.[105] An 830

nm excitation source was focused directly on the skin, producing a spot size of 1 $mm^2$ and a power of 300 mW, and backscattered light was collected by a mirror and transferred to a spectrometer via a notch filter and an optical-fibre bundle. Each spectrum was acquired via 90 two-second acquisitions and were taken every five minutes for a period of 2-3 hours following food consumption. A total of 461 Raman spectra in the range 355–1545 $cm^{-1}$ were collected from 17 human volunteers and the data set from each volunteer was analysed individually via PLSR combined with the leave-one-out cross-validation method. The measured blood-glucose levels ranged from 3.8–2.4 mM and the mean error in prediction, as compared to reference values obtained by standard capillary blood analysis, across all 17 subjects was 7.8%.

### 4.3.3 Raman Spectroscopy & Microfluidics

Raman spectroscopy and SERS have been used in combination with microfluidics to study analytes under continuous flow.[106] One such study is notable for not only carrying out SERS analysis, but also the synthesis of the SERS substrate used, using a microfluidic system.[107] The system used a square glass capillary with an internal diameter of 200 $\mu$m. A silver-nanoparticle based SERS substrate was synthesised through the continuous injection of a solution containing silver nitrate and sodium citrate into the capillary, at a flow rate of 3.3 $\mu L\ s^{-1}$, whilst a laser beam with a wavelength of 515 nm was focused on the lower inner face of the capillary. Exposing the solution to the laser beam for 40s resulted in the *in situ* photoinduced synthesis of silver nanoparticles in a compact 7 $\mu$m spot on the capillary surface. The synthesised SERS substrate was then used to study a 0.01 mM solution of malachite green, an antimicrobial agent controversially used in aquaculture in certain countries, which was continuously injected into the capillary at a rate of 5 $\mu L\ s^{-1}$. Saturation of the strongest malachite green SERS peak at 1617 $cm^{-1}$ occurred 40 seconds after beginning the injection of the solution. Desorption of malachite green and regeneration of the SERS substrate was monitored by reintroducing the silver nitrate/sodium citrate solution through the capillary at a rate of 3.3 $\mu L\ s^{-1}$ and observing a decrease in the band at 1617 $cm^{-1}$.

## 4.4 Neurochemical Monitoring

Multiple studies report attempts to improve the time resolution of neurochemical monitoring. The most notable of these is the development of rapid sampling microdialysis (rsMD), a technique that combines clinical microdialysis with an online enzyme-based electrochemical assay system for the simultaneous detection of glucose and lactate.[108]

The rsMD system connects directly to the microdialysis tubing. Microdialysate from the patient is fed into a valve where it is mixed with a solution containing

ferrocene monocarboxylate. Every 30 seconds, the valve injects the sample into two parallel flow streams which each feed into a differenct enzyme reactor: one for glucose detection and one for lactate detection. Each assay utilises an enzyme bed consisting of two immobilised enzymes, horseradish peroxidase and either glucose oxidase or lactate oxidase. The assay consists of four main steps: firstly, any glucose and lactate present in the sample reacts with their respective oxidase enzyme to produce $H_2O_2$ as a by-product. $H_2O_2$ is then converted to water by horseradish peroxidase. This reaction involves the simultaneous oxidation of ferrocene monocarboxylate which regenerates the horseradish peroxidase enzyme. The resulting charged ferrocene species is then reduced by a glassy carbon electrode, located downstream of the enzyme bed, and the resulting change in current with respect to an Ag—AgCl reference electrode is detected. This process is summarised in Figure 4.4. The working electrode is held at -100 mV relative to the reference electrode. The amplitude of the current peak is related to the concentration of analyte by a calibration process in which solutions of known concentration are manually injected into the device. Using a flow rate of 2 $\mu$L $min^{-1}$, the device is able to sample the microdialysate at 30 second intervals.

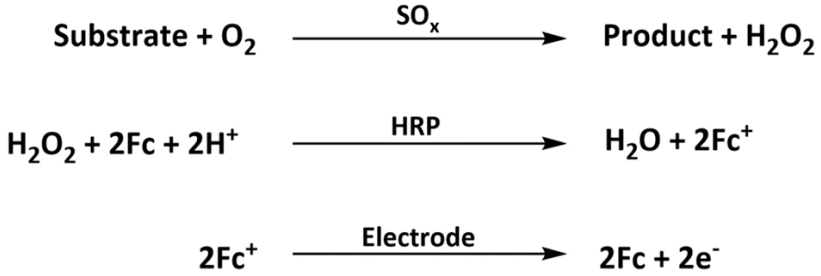


***Figure 4.4:*** *Summary of the reactions of rsMD. The substrate is typically glucose or lactate and $SP_x$ is the substrate oxidase enzyme. HRP is the horseradish peroxidase enzyme and Fc is a ferrocene species.*[109]

The device has been used in a number of clinical applications, including the monitoring of TBI patients in a critical care unit and during surgery to repair a brain aneurysm.[108] The high time resolution of this system, when compared with conventional analysis of microdialysate samples, has enabled its use in the study of spreading depolarizations in injured brain tissue. Spreading depolarisations are an acute event, which can occur spontaneously in the injured brain, involving a large dynamic change in the distribution of ions between intracellular and extracellular compartments within the brain. These events typically last 2–5 minutes and therefore a monitoring system with high time resolution is required to study metabolic changes that occur during this process. Time-stamped rsMD data were correlated with data generated through electrocorticography, an electrophysiological monitoring system which used electrodes placed direcctly on the surface of the brain to record electrical activity, to measure the metabolic profile of spreading depolarisations.[110]

Another study used the rsMD to monitor the health of tissue used in free-flap reconstruction survey, a technique used to transfer healthy tissue from one region of the body to another.[111] The associated disconnection and reconnection of blood supply to the transferred tissue is critical to the success of the procedure. rsMD was used to assess the metabolic status of the tissue, which could be used to infer the quality of its blood supply, both during surgery and in the post-operative phase. In this set-up, the working electrodes were held at 0 V compared to the reference electrodes.

The rsMD setup has recently been miniaturised in order to further improve the time resolution of the system.[112] The new device is based upon a microfluidic PDMS chip contaning a 50 $\mu$m platinum disc microelectrode coated in a polyethylene glycerol hydrogen matrix containing entrapped glucose oxidase or lactate oxidase, for glucose or lactate detection respectively, in addition to an Ag—AgCl reference microelectrode. This setup utilises molecular oxygen, which is readily accessible due to the permeability of PDMS to $O_2$, as a mediator for the oxidation of $H_2O_2$ produced by the substrate-substrate oxidase reactions. A potassium sensor, based on a miniaturised ion-sensing electrode which selectively binds to the ion of interest, is also incorporated into the system to detect the onset of spreading depolarisation, which is associated with an increase in potassium levels in the microdialysate. Whilst in use, calibration of the instrument is carried out every three hours via the introduction of solutions of known concentration. This device has been used in conjunction with electrocorticography for *in vivo* monitoring of spreading depolarisation in a rat model[112] and in a study of human TBI patients.[113] The time resultion of this system, including the time taken for the sample to reach the sensor chip, is estimated to be 68 seconds from *in vitro* experiments.

Although this method has undoubtedly improved the time resolution of microdialysate monitoring, it does not address all of the disadvantages of the ISCUS Flex. For example, the setup still requires the use of reagents and consumables, including enzymes, which must be purchased on an on-going basis and have a limited lifespan: the enzyme beds are estimated to be stable for 1-2 months.[108] In addition, glucose and lactate are indirectly detected, as in the ISCUS Flex, whereas a spectroscopy-based masurement would allow the direct detection of analytes. It is also noted that the current rsMD setup enables the monitoring of only two analytes simultaneously, meaning that pyruvate detection is omitted. Moreover, the reported detection limit of 0.025 mM for glucose and lactate would not be low enough to encompass the complete clinical range of pyruvate.[111] On a more speculative note, it is also possible that biofouling of the electrodes could present a problem after prolonged use.

An alternative approach to electrochemical on-line monitoring of microdialysate samples utilised carbon-film electrodes coated onto a glass plate.[114] The device con-

tained four electrodes: two working electrodes, which were coated with horseradish peroxidase followed by a layer of either glucose oxidase or lactate oxidase, and two silver-coated reference electrodes. A 1 mm × 23 $\mu$m flow channel contained the two working electrodes, which were arranged in parallel to reduce chemical cross-talk between them, with a micro-separator between them. The assembly was sealed by placing a second glass plate on top of the first and the completed device could then be connected to a standard microdialysis probe. During device operation, the working electrode potentials were held at -50 mV, compared to their respective reference electrodes, and flow rates of 0.5–4 $\mu$L min$^{-1}$ could be used. The device was successfully used for continuous electrochemical monitoring of glucose and lactate levels within the brain of a live rat.

Microdialysis sampling has also been combined with fluorescence-based detection methods for *in vivo* on-line monitoring of rat-brain extracellular glucose and lactate.[115] The study used a 3D-printed flow reactor containing separate reaction chambers for glucose and lactate detection, each of which was internally coated with the appropriate oxidase enzyme. The introduction of microdialysate samples to a reaction chamber resulted in the oxidation of glucose or lactate, leading to the production of $H_2O_2$ as a byproduct. This reacted with Amplex UltraRed, a $H_2O_2$ molecular probe, to produce a fluorescence-emitting product which was detected by a downstream fluorescence spectrophotometer. The assay was designed to ensure that microdialysate passed through only one of the reaction chambers at a given point, so that $H_2O_2$ production could be correctly correlated with either glucose or lactate detection. Microdialysate loading into each chamber occurred at 4 minute intervals and was pumped through the system at a rate of 1 $\mu$L min$^{-1}$. The working concentration range of the device was 0.1–5.0 mM.

## 4.5 Metabolic Profiling of TBI: Preliminary Work

A previous student in the Elliott group carried out a study into the feasibility of detecting glucose, lactate and pyruvate, at concentrations relevant to TBI, using ATR-FTIR spectroscopy in combination with PLSR.[116] All measurements were carried out using a Perkin Elmer Spectrum 100, coupled with a Specac Heated Golden Gate ATR Accessory containing a single-reflection diamond ATR crystal, at room temperature.

The first stage of the study involved the analysis of synthetic solutions of glucose, lactate and pyruvate in perfusion fluid. The data from each experiment was analysed in the same way: spectral data were randomly organised into two groups. The first group was used to build a predictive PLSR model using cross-validation and the predictive properties of the model were then tested on the second data set. A plot of the actual *vs.* predicted concentration of analyte was then extrapolated to predict the limit of detection of that compound.

This method was initially used to study pure solutions of glucose, lactate and pyruvate. Each compound was analysed using a different selection of PLSR models, each of which examined a different spectral range. Three models were used for the analysis of glucose spectra, three models were used for the analysis of lactate spectra and a single model covering a wider spectral range was used for the analysis of pyruvate spectra. Each model used to analyse the glucose and lactate spectra was found to possess a different predicted limit of detection. The lowest predicted limits of detection for each compound are listed in Table 4.1.

Mixtures of glucose and lactate in perfusion fluid were analysed in the same way. The lowest predicted limits of detection of each compound in the mixture are also reported in Table 4.1.

***Table 4.1:*** *The limits of detection of glucose, lactate and pyruvate in synthetic solutions, using single-reflection ATR-FTIR spectroscopy, as predicted from the extrapolation of results from a predictive PLSR model.*[116]

| **Analyte** | **Sample** | **Limit of Detection / mM** |
|---|---|---|
| Glucose | Glucose in perfusion fluid | 0.3 |
| Lactate | Lactate in perfusion fluid | 0.5 |
| Pyruvate | Pyruvate in perfusion fluid | 0.09 |
| Glucose | Glucose & lactate in perfusion fluid | 0.7 |
| Lactate | Glucose & lactate in perfusion fluid | 0.4 |

Subsequent work focused on the analysis of clinical microdialysis samples via ATR-FTIR spectroscopy. ATR-FTIR spectra of ten microdialysate samples, all of which were obtained from the same patient, were acquired as described previously. The PLSR models developed in the first phase of the study were used to predict individually the concentrations of glucose, lactate and pyruvate in the samples. The predictions generated by each model were compared with the actual concentrations of glucose, lactate and pyruvate in each sample, as measured using the ISCUS Flex Microdialysis Analyser. Table 4.2 lists the RMSEP of the best-performing PLSR model for each compound.

***Table 4.2:*** *The RMSEP of the best-performing PLSR models used to predict the concentrations of Glucose, Lactate and Pyruvate in clinical microdialysate samples.*[116]

| **Analyte** | **Spectral Range of Model / $cm^{-1}$** | **RMSEP / mM** |
|---|---|---|
| Glucose | 1600–750 | 0.28 |
| Lactate | 1600–750 | 1.07 |
| Pyruvate | 1800–1000 | 0.023 |

This study provided encouraging results to suggest that ATR-FTIR spectroscopy may be a suitable technique upon which to base a sensor for metabolic profiling of

TBI patients. However, many outstanding questions remained following this work. Firstly, spectra were acquired using only a single-reflection diamond ATR crystal. It is possible that a crystal which provides a longer effective path length would yield a lower limit of detection, due to a greater interaction of the IR beam with the sample, and therefore it would be interesting to compare the performances of different crystals. Similarly, transmission-FTIR was not used in this study and it is not clear how its performance would compare to that of ATR-FTIR.

This study did not attempt to detect glucose, lactate and pyruvate using Raman spectroscopy or SERS. It would be interesting to compare the performance of these techniques with FTIR spectroscopy, in order to analyse the relative merits of the two forms of vibrational spectroscopy when applied to the specific circumstances of TBI monitoring.

It is also noted that only a single type of statistical model was applied in this work. In addition, the performance of the model across different regions of the FTIR spectrum was not studied systematically. Ideally, the performance of multiple statistical models should be compared and the chosen model should be optimised in a systematic manner.

Finally, the analysed microdialysate samples were obtained from a single patient and therefore did not cover the full concentration range of glucose, lactate and pyruvate expected in clinical samples. It is therefore unclear how the technique would perform at the extreme ends of the clinical range.

# Chapter 5

# Materials & Methods

This chapter provides details of the materials and methods used for experiments and procedures that were carried out routinely during this work. Any materials or techniques used only for select experiments are described in the relevant results chapters.

## 5.1 Sample Preparation

### 5.1.1 Perfusion Fluid

Stock solutions of perfusion fluid were prepared to the same recipe as that used for microdialysis of TBI patients used in the clinic.[19] The compounds listed in Table 5.1 were dissolved in the appropriate volume of deionised (DI) water at room temperature and mixed thoroughly. The resulting solution was stored at 4 °C.

***Table 5.1:*** *Components of lab-made perfusion fluid*

| **Compound** | **Supplier** | **Concentration / mM** |
|---|---|---|
| NaCl | Breckland Scientific | 147 |
| KCl | Sigma Aldrich | 2.7 |
| $CaCl_2$ | Sigma Aldrich | 1.2 |
| $MgCl_2$ | Sigma Aldrich | 0.85 |

### 5.1.2 Synthetic Samples

D-(+)-glucose, sodium L-lactate and sodium pyruvate used in the preparation of synthetic samples were purchased from Sigma Aldrich.

A pure solution of each compound at a concentration of either 1 M or 100 mM was freshly prepared at the outset of each experiment. The required mass of compound was weighed to an accuracy of ±0.0001 g and dissolved in lab-made perfusion fluid at room temperature. Solutions of lower concentration were prepared by serial dilution

of the master solution with perfusion fluid. All solutions were stored at 4 °C.

### 5.1.3 Clinical Samples

Microdialysate samples from brain-injured patients were collected by clinical staff at the Neurosciences Critical Care Unit at Addenbrooke's Hospital over a period of months. Samples were stored at -80 °C and kept on the Unit until required for use in this project. All patient data remained anonymous.

## 5.2 FTIR Spectroscopy

FTIR spectra were acquired using a Perkin Elmer Spectrum 100 FTIR spectrometer, which was operated via the Perkin Elmer 'Spectrum' software. The spectrometer was equipped with a SiC hot spot-stabilised IR light source, a KBr beamsplitter, a Michelson interferometer and a liquid $N_2$-cooled mercury cadmium telluride (MCT) detector. An accessory appropriate to the FTIR technique being used was fitted into the connection port located in the rear of the sample compartment (Figure 5.1).

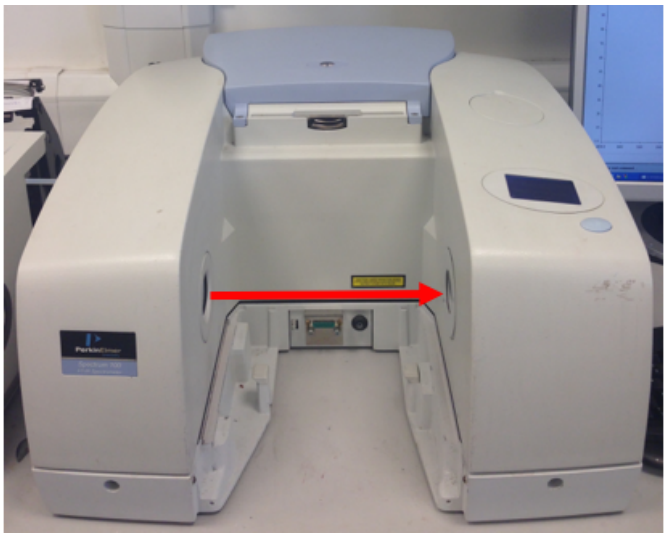

***Figure 5.1:*** *The Perkin Elmer Spectrum 100 IR Spectrometer. Accessories for performing variations of IR spectroscopy were fitted into the sample compartment, via the connection port on its rear wall, and aligned with the IR beam, as indicated by the red arrow.*

The $N_2$ reservoir of the MCT detector was filled approximately 15 minutes prior to commencing spectrum acquisition to allow the temperature of the detector to stabilise. It was later re-filled at 4-hourly intervals to ensure that a contant temperature was maintained at the detector. The required accessory was cleaned and fitted to the system and a sample was loaded (see Sections 5.2.1.1, 5.2.1.2 and 5.2.2 for details). Wherever possible, samples were measured in order of increasing concentration to

minimise the contamination of consecutive measurements. The relevant sample-holder was cleaned between each sample using deionised (DI) water which was deemed to be a suitable solvent due to the high water solubility of the compounds being measured.

Mid-IR spectra were collected over the range 4000 - 450 $cm^{-1}$. Each spectrum was generated via the accumulation of 150 scans with a resolution of 4 $cm^{-1}$. Two types of spectra were routinely generated: single-beam spectra and ratio spectra. Single-beam spectra displayed the Fourier transform of the raw spectrum. Ratio spectra were generated by dividing the spectrum of a test sample by the spectrum of a suitable chemical background, enabling the absorption peaks of the sample to be visualised, as illustrated in Figure 5.2. The work described in this thesis used perfusion fluid as the chemical background for the acquisition of FTIR ratio spectra.

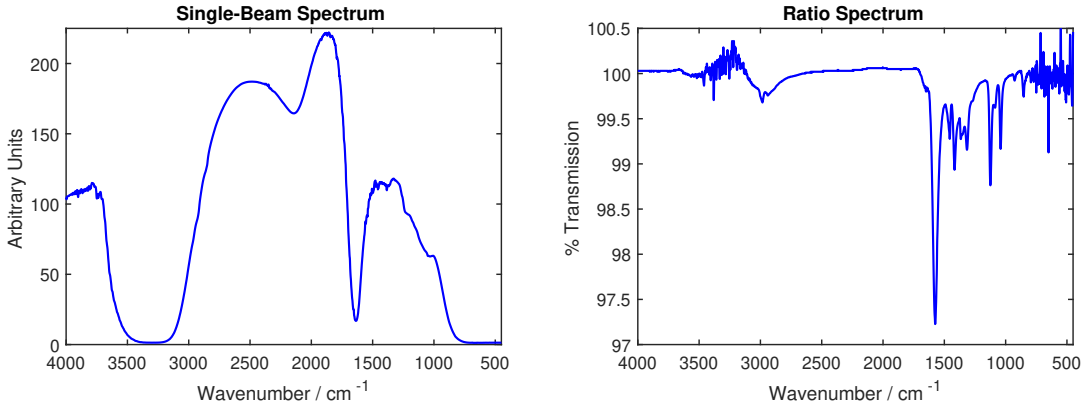


***Figure 5.2:*** *The single-beam and ratio FTIR spectrum of a 24 mM solution of lactate in perfusion fluid. The ratio spectrum was acquired using perfusion fluid as a background sample. Both spectra were acquired via ATR-FTIR spectroscopy using a seven-reflection ZnSe crystal.*

### 5.2.1 ATR-FTIR Protocol

Three different ATR-FTIR crystals were used in this work: a single-reflection diamond crystal and two seven-reflection crystals, one composed of Ge and the other composed of ZnSe. The accessories used to integrate these crystals into the Perkin Elmer Spectrum 100 are shown in Figure 5.3.

#### 5.2.1.1 Single-Reflection ATR-FTIR Protocol

Single-reflection ATR-FTIR measurements were conducted using the Spectrum 100 coupled with a Specac Heated Golden Gate ATR Accessory containing a single-reflection diamond ATR crystal (Figure 5.3(a)).

The diamond was cleaned thoroughly at the outset of an experiment and between samples. Firstly, any liquid sample already present was soaked up using a clean lint-free wipe. 20 $\mu$L DI water was then deposited on the surface of the diamond, left for

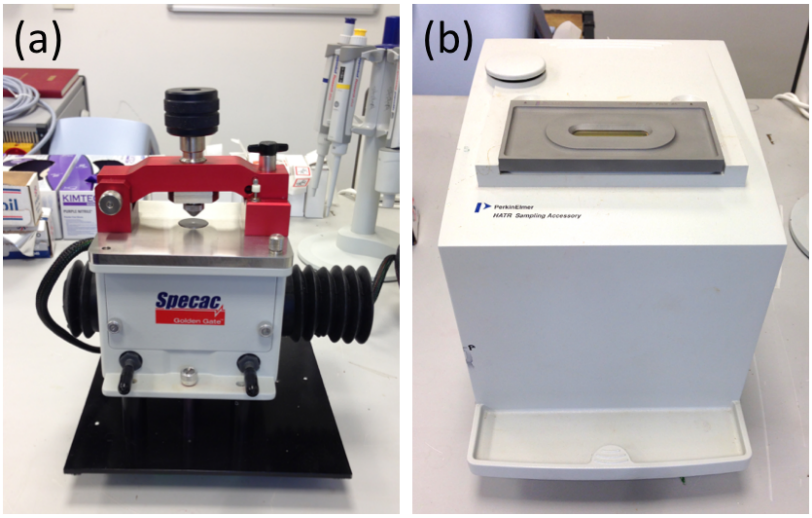


***Figure 5.3:*** *Accessories used for ATR-FTIR measurements. (a) Heated Golden Gate ATR Accessory containing a single-reflection diamond ATR crystal. (b) Horizontal ATR Sampling Accessory (shown containing a trough plate fitted with a seven-reflection ZnSe ATR crystal).*

30-60 seconds and wiped away. This process was repeated twice. Liquid samples were loaded by dropping 20 $\mu$L of sample directly onto the surface of the diamond using a micropipette and the anvil was left in the upright position during measurements.

#### 5.2.1.2 Seven-Reflection ATR-FTIR Protocol

Seven-reflection ATR-FTIR measurements were carried out using the Spectrum 100 coupled with a Horizontal ATR (HATR) Sampling Accessory from Perkin Elmer (Figure 5.3(b)). A trough plate containing either a ZnSe or germanium crystal, both of which had an angle of incidence of 45°, was mounted into a slot on the upper face of the accessory.

Identical protocols were used for the measurement and cleaning of both top plates. The crystal was cleaned thoroughly before beginning an experiment and between samples. Any residual liquid in the sample trough was removed using a pipette and the trough was then filled with approximately 1 ml deionised water which was left for 30-60 seconds before being removed. This process was repeated twice. A sample volume of 1 ml was used for all measurements and samples were loaded into the trough using a micropipette.

### 5.2.2 Transmission-FTIR Protocol

Transmission-FTIR spectra were acquired using a Specac Pearl Liquid Transmission Accessory coupled with a Specac Oyster Lift and Tilt Cell Assembly (Figure 5.4). The Oyster cell is the sample holder for this accessory and is manufactured with a fixed

path length. Each Oyster cell used in this work was fitted with ZnSe windows. The bottom window of each cell was fixed at an angle of 0.1° relative to the top window to minimise the generation of interference fringes in the IR spectra. The Oyster cell was held in a horizonal configuration within the Pearl unit, which contained the optics necessary to direct the IR beam through the cell and into the detector.

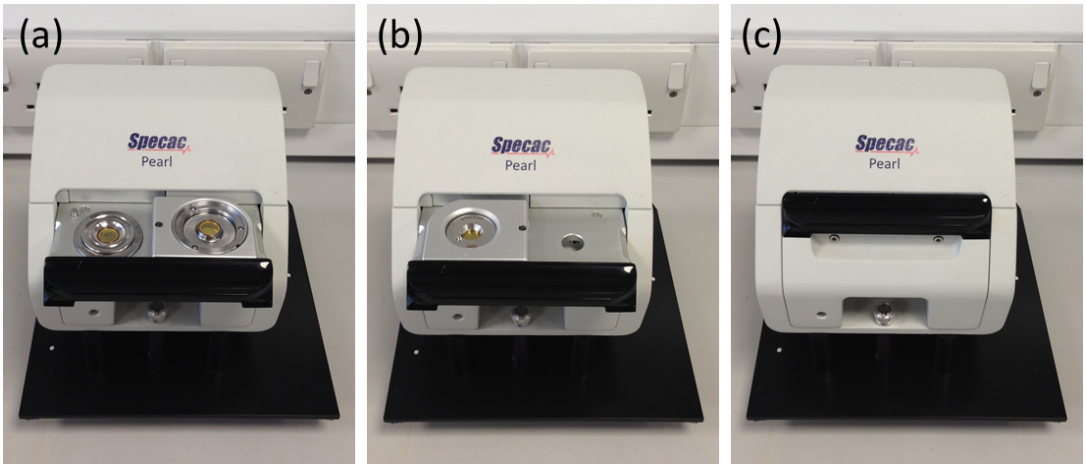


***Figure 5.4:*** *The Pearl Liquid Transmission Accessory used for transmission-FTIR measurements. Images show the accessory with an open sample tray containing an open Oyster Lift and Tilt Cell, ready for sample loading (a); an open sample tray with a closed Oyster Lift and Tilt Cell containing a liquid sample (b); a closed sample tray (c).*

In order to load a sample into the accessory, an open Oyster cell was placed on the Pearl sample tray (Figure 5.4(a)) and a micropipette was used to load a 10 $\mu$L sample onto the bottom window of the cell. The cell was then closed, causing the sample to spread evenly between the two windows (Figure 5.4(b)) and the sample tray pushed into the Pearl unit (Figure 5.4(c)).

The Oyster cell was cleaned before use and between samples. Initially, any residual sample was soaked up using lint-free wipes. A pipette was then used to cover both windows of the cell with DI water, which was left for approximately 30-60 s before being soaked up using a lint-free wipe. This was repeated twice.

## 5.3 Raman Spectroscopy

### 5.3.1 Instrument Specifications

Raman spectra were acquired using a dispersive HORIBA LabRAM HR Evolution Raman microscope which was operated via LabSpec 6 software (HORIBA Jobin Yvon). The system was equipped with laser light sources of four different wavelengths (785 nm, 633 nm, 532 nm, 473 nm) and an air-cooled CCD detector. An upright confocal microscope was integrated into the instrument and its objectives were surrounded by

a Class 1 enclosure to control ambient light interference.

The system contained two options for mounting samples within the microscope enclosure (Figure 5.5). Solid or liquid samples could be placed on a glass slide and mounted on the motorised $XY$ stage beneath the microscope objectives. Liquid samples could alternatively be contained within a cuvette and mounted in the 'macro sampler', an accessory that connected directly to the microscope nose piece and contained the optics necessary to direct laser light from the instrument through the cuvette and reflect scattered light back into the instrument.

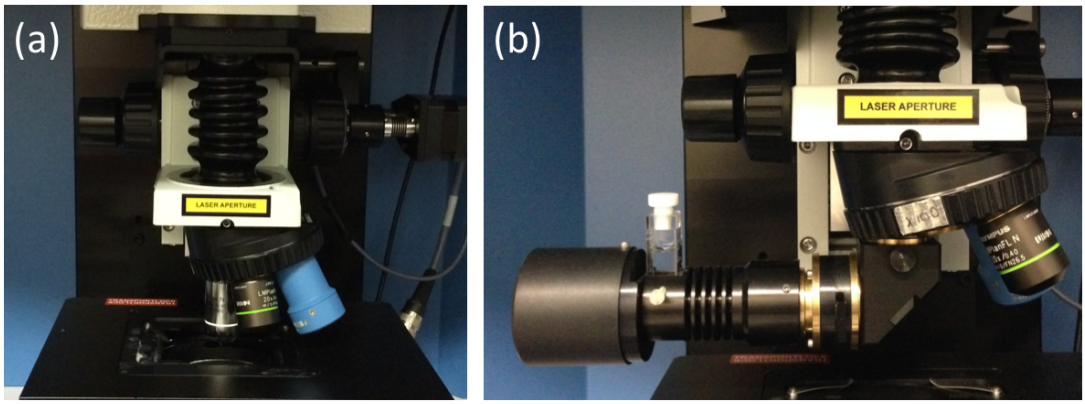


***Figure 5.5:*** *Raman spectroscopy sample-mounting options. Samples could be placed under a microscope objective (a) or within the macro sampling accessory (b). The blue auto-calibration objective is also visible in Figure (a).*

### 5.3.2 Instrument Operation

The instrument was calibrated prior to the start of a series of measurements and was re-calibrated each time there was a change to the laser or grating being used. Auto-calibration was carried out using a proprietary calibration objective from HORIBA, the Standard PRO (seen in Figure 5.5(a)). The objective contained a disc of polystyrene which was used as a reference sample. This was fixed at a constant distance from the objective lens and therefore increased the consistency of calibration measurements by eliminating the need to manually focus on the sample. The system was calibrated to a Raman peak of polystyrene at 1001 $cm^{-1}$, corresponding to the breathing mode of its aromatic ring.

Samples mounted on the $XY$ stage were illuminated using a white-light source and imaged using a camera via the LabSpec 6 software. A positioning joystick was used to alter both the $XY$ stage position and the distance of the microscope objective from the sample, until the desired region of the sample was in focus. Liquid samples mounted in the macro sampler did not require any further adjustment. The parameters used for spectrum acquisition, including acquisition time, number of accumulations, laser

power and grating, were then set using the LabSpec 6 software and acquisition was initiated.

Acquisition parameters were varied with each experiment and are detailed with the corresponding experimental results in Chapter 7. Data files were saved in .txt format for importing to MATLAB and also in LabSpec 6 format in order to preserve the experimental details.

## 5.4 Data Analysis

All data analysis was carried out using MATLAB version R2016b.

### 5.4.1 ANOVA and Multiple Comparison Tests

One-way ANOVA tests were performed using the 'anova1' function of the Statistics and Machine Learning Toolbox™. The multiple comparison tests were carried out using the 'multcompare' function, also included in the Statistics and Machine Learning Toolbox™.

### 5.4.2 Statistical Modelling: Pre-Processing

Two pre-processing steps were carried out on spectral data used for statistical modelling. Firstly, the transmission data were converted into values of absorbance using the equation:

$$A = log_{10}\frac{100}{\%T} \tag{5.1}$$

where $A$ is absorbance and $\%T$ is percentage transmission. Absorbance data were used in the modelling process because they have a linear relationship to concentration (the independent variable in the model) as defined by the Beer-Lambert law:

$$log\frac{I_0}{I} = \varepsilon cl \tag{5.2}$$

where $I_0$ is the intensity of the incident radiation, $I$ is the intensity of the transmitted radiation, $c$ is the sample concentration, $l$ is the path length of the sample and $\varepsilon$ is the extinction coefficient, which is a constant for a given transition within a particular molecule.

Secondly, the absorbance data were mean-centred. The mean value of the absorbance at each wavenumber was subtracted from the value of the absorbance at the corresponding wavenumber, resulting in a dataset which had a mean absorbance value of zero at each wavenumber.

### 5.4.3 Statistical Modelling: PCR

A PCA was performed on the absorbance data using the 'pca' function of the Statistics and Machine Learning Toolbox™. A linear regression of the absorbance data was then performed on the principal components using the 'regress' function. The PCR results were subsequently transformed to regression coefficients for the original variables of absorbance and concentration for interpretation.

The mean-squared error in prediction of the model was calculated using the leave-one-out method of cross-validation, in which the model was constructed using the data from all but one of the spectra within the dataset and the resulting model was used to predict the concentrations of glucose, lactate and pyruvate represented by the remaining 'test' spectrum. This process was repeated until each spectrum in the dataset had been used as a test spectrum.

### 5.4.4 Statistical Modelling: PLSR

A PCA was performed on the absorbance data prior to carrying out the PLSR in order to compress the dataset and therefore speed up the procedure. The regression analysis was carried out using the 'plsregress' function of the Statistics and Machine Learning Toolbox™and was calibrated using the leave-one-out method of cross-validation.

# Chapter 6

# IR Spectroscopy of Glucose, Lactate & Pyruvate

This chapter describes the preliminary work undertaken to determine whether mid-FTIR spectroscopy could be used to detect glucose, lactate and pyruvate in clinical microdialysate samples, within the context of the device requirements set out in Section 2.6. Two methods of FTIR spectroscopy were evaluated: ATR-FTIR and transmission-FTIR. ATR-FTIR was selected for investigation as it is relatively insensitive to the effect of strongly IR-absorbing samples, such as water, and the final device will be required to detect glucose, lactate and pryuvate in highly dilute aqueous solutions. Transmission-FTIR was chosen, despite its sensitivity to strongly IR-absorbing samples, due to its instrumental simplicity which renders it likely to be the most straightforward of the FTIR techniques to develop into a miniaturised bedside device.

Both techniques were used to acquire the FTIR spectra of glucose, lactate and pyruvate, as individual solutions and as a mixture, which were qualitatively analysed to identify spectral peaks unique to each compound. Differences between the ATR-FTIR and transmission-FTIR spectra of each compound were also noted. Consideration was given to compounds other than the analytes of interest which are likely to be present in perfusion fluid and, where possible, their IR spectra were analysed to determine regions of overlap with the spectra of glucose, lactate and pyruvate. Transmission-FTIR spectroscopy was subsequently used to analyse six clinical microdialysate samples in order to establish whether any compound-specific peaks identified from this preliminary work could be observed. Finally, quantitative studies were carried out in order to determine which ATR-FTIR crystal and transmission-FTIR path length should be used in the next phase of work.

## 6.1 FTIR Spectra of Glucose, Lactate & Pyruvate

The aim of this section of work was to characterise the mid-FTIR spectra of glucose, lactate and pyruvate, both individually and in a mixture, in order to find peaks specific to each compound which are not compromised by the presence of the other two analytes. Each compound was prepared both as a pure 100 mM solution and as part of a mixture of glucose, lactate and pyruvate in which all compounds were present at a concentration of 100 mM: this concentration was chosen to ensure that absorbance peaks would be clearly visible whilst not saturating the measured spectrum. All solutions were prepared with perfusion fluid, to better reflect the conditions under which these compounds would be detected in the clinic, and a spectrum of pure perfusion fluid was used as a background reference. The following sections discuss, in turn, the FTIR spectra of glucose, lactate, pyruvate and a mixture of all three compounds. All spectra shown are ratio spectra, which have been corrected for the presence of perfusion fluid, in order to facilitate the identification of IR absorption peaks corresponding to the target molecules.

### 6.1.1 FTIR Spectrum of Glucose

The ATR-FTIR and transmission-FTIR spectra of a 100 mM solution of glucose in perfusion fluid, in addition to their associated peak assignments, are shown in Figure 6.1 and Figure 6.2, respectively. The most distinctive feature of both spectra is a cluster of strong peaks in the region 1152 – 994 $cm^{-1}$, which correspond to vibrations of the C–O and C–C bonds within the glucose molecule. Literature values indicate that these are the most significant peaks for the identification of glucose via mid-FTIR spectroscopy.[73]

A clear difference between the ATR-FTIR and transmission-FTIR spectra is the presence in the latter of a high level of noise in the regions 3700 – 3000 $cm^{-1}$, 1700 – 1600 $cm^{-1}$ and 900 – 450 $cm^{-1}$. This is caused by the strong absorption of IR radiation by water which, due to the significant interaction between the IR beam and the sample, has saturated the detector of the instrument. The ATR-FTIR spectrum does not exhibit the same level of noise in these water-absorption regions, as the effective path length used to acquire the spectrum is significantly shorter than that used in transmission-FTIR spectroscopy (Section 3.2.3.2). It should be noted that a proportion of the noise seen in the 800 – 450 $cm^{-1}$ region of both spectra is due to the limited IR transmission range of ZnSe, the material from which the transmission cell windows and ATR crystal material are composed, which extends from 20,000 – 650 $cm^{-1}$.

The water-induced noise in the transmission-FTIR spectrum of glucose leads to the loss of approximately 40% of the peaks seen in the ATR-FTIR spectrum of the

molecule. However, the majority of these are weak bands seen at the extreme ends of the spectrum and the strongest peaks in the region 1152 – 994 $cm^{-1}$ are still visible.

An additional consequence of the short effective path length of ATR-FTIR, in comparison with transmission-FTIR, is a decrease in the intensity of all IR absorption bands in the ATR-FTIR spectrum when compared with transmission-FTIR. It can be seen from Figures 6.1 and 6.2 that the strongest IR absorption peak at 1035 $cm^{-1}$ is approximately 30% stronger in the transmission-FTIR spectrum of glucose than in the ATR-FTIR spectrum.

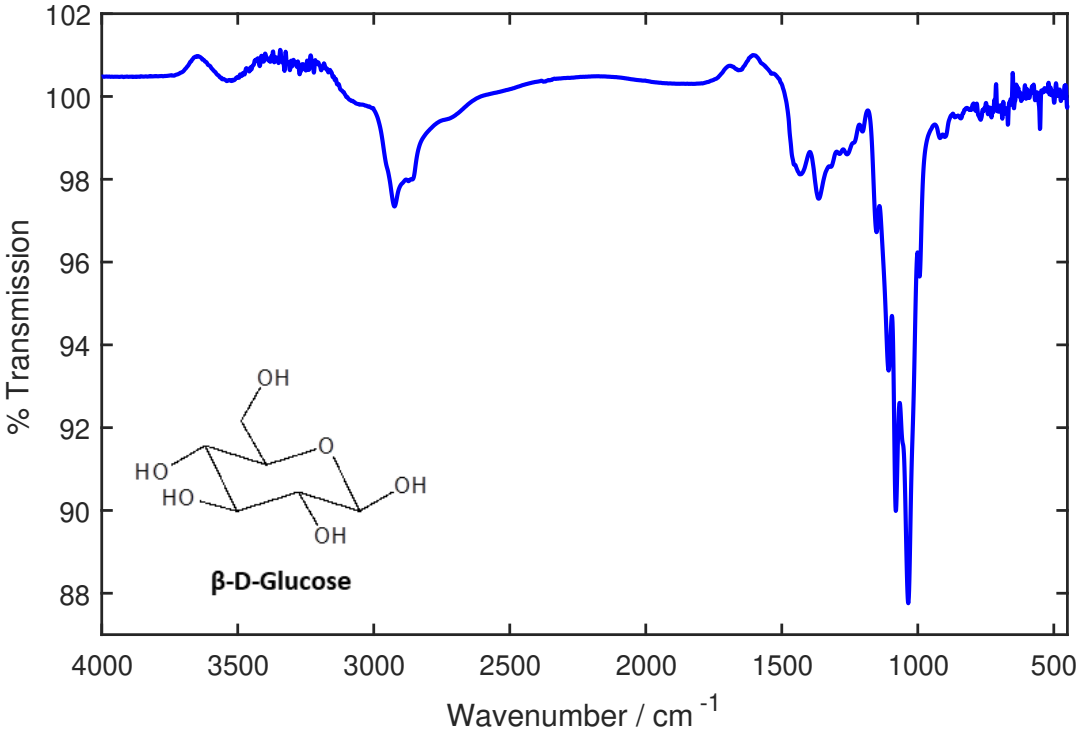


| Peak Position / $cm^{-1}$ | Peak Description | Assignment |
|---|---|---|
| 3531 | Weak, Broad | O–H Stretch |
| 2924 | Medium | C–H Stretch |
| 2873 | Weak | O–H Stretch |
| 2858 | Weak | O–H Stretch |
| 1433 | Medium | $CH_2$ Bend |
| 1364 | Medium | O-H bend |
| 1319 | Weak | C-C (Alicyclic) Vibration |
| 1287 | Weak | C-C (Alicyclic) Vibration |
| 1260 | Weak | C-C (Alicyclic) Vibration |
| 1204 | Weak | C-C (Alicyclic) Vibration |
| 1152 | Medium | C-C (Alicyclic) Vibration |
| 1107 | Medium | C-C (Alicyclic) Vibration |
| 1081 | Strong | C–O Stretch |
| 1035 | Strong | C–O Stretch |
| 994 | Medium | C-C (Alicyclic) Vibration |
| 919 | Weak | C–O–C Stretch |
| 901 | Weak | C–O–C Stretch |
| 864 | Weak | C–O–C Stretch |
| 842 | Weak | C–O–C Stretch |

***Figure 6.1:*** *The ATR-FTIR ratio spectrum and associated peak assignments*[117] *of a 100 mM solution of glucose in perfusion fluid, acquired using a seven-reflection ZnSe crystal.*

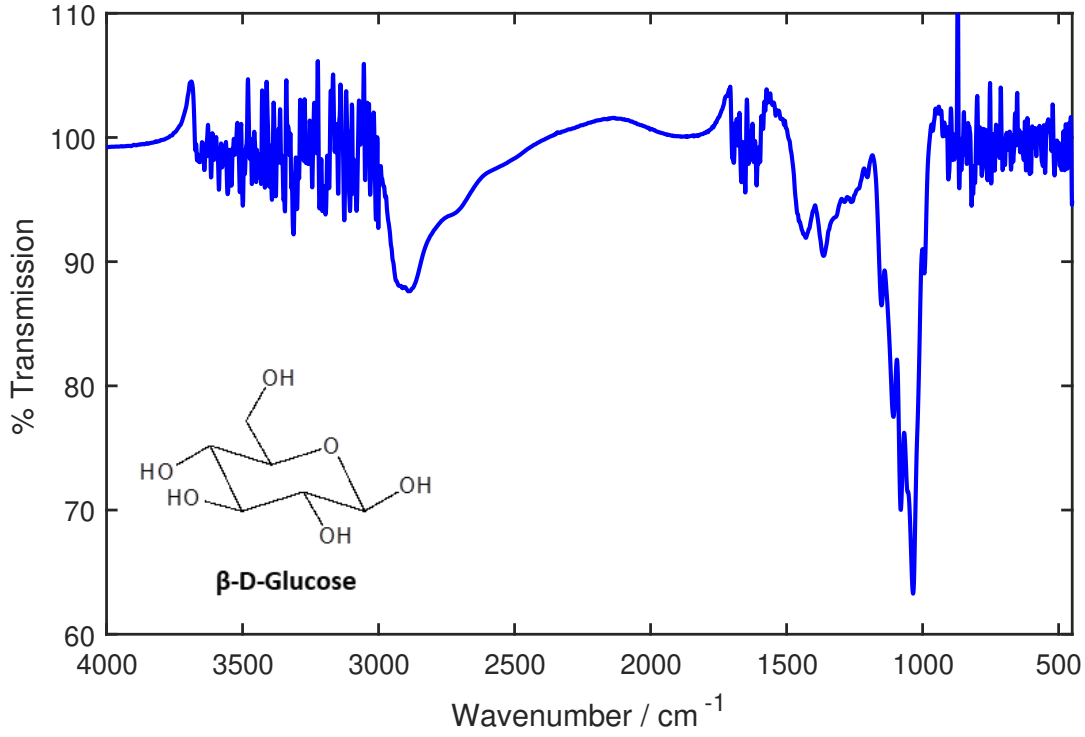


| Peak Position / $cm^{-1}$ | Peak Description | Assignment |
|---|---|---|
| 2892 | Medium, Broad | O–H Stretch |
| 1429 | Medium | $CH_2$ Bend |
| 1364 | Medium | C–O–H bend |
| 1287 | Weak | C–C (Alicyclic) Vibration |
| 1262 | Weak | C–C (Alicyclic) Vibration |
| 1203 | Weak | C–C (Alicyclic) Vibration |
| 1151 | Medium | C-C (Alicyclic) Vibration |
| 1107 | Medium | C–C (Alicyclic) Vibration |
| 1080 | Strong | C–O Stretch |
| 1035 | Strong | C–O Stretch |
| 994 | Medium | C-C (Alicyclic) Vibration |

***Figure 6.2:*** *The transmission-FTIR ratio spectrum and associated peak assignments*[117] *of a 100 mM solution of glucose in perfusion fluid, acquired using a 50 µm path length.*

### 6.1.2 FTIR Spectrum of Lactate

The ATR-FTIR and transmission-FTIR spectra, and associated peak assignments, of a 100 mM solution of lactate in perfusion fluid are shown in Figures 6.3 and 6.4. Both spectra are characterised by three distinct regions: a variable number of strong peaks at approximately 1576 $cm^{-1}$, corresponding to the stretching of the $CO_2^-$ functional group, and two groups of medium-intensity peaks at approximately 1456–1315 $cm^{-1}$ and 1125–1041 $cm^{-1}$. The IR absorption peak centred around 1576 $cm^{-1}$ is not a specific indicator of the presence of lactate when used in isolation, despite producing the strongest peaks, as all molecules with a carbonyl group are known to strongly absorb IR radiation in that region of the spectrum. Literature values suggest that the peak at 1125 $cm^{-1}$, which corresponds to a C–O stretching vibration, is therefore the most useful in the identification of lactate.[73]

A comparison of the ATR-FTIR and transmission-FTIR spectra of lactate yields broadly similar conclusions to those drawn from the comparison of glucose FTIR spectra. Significant water-induced noise is seen in the transmission-FTIR spectrum, but not in the ATR-FTIR spectrum, resulting in the loss of peaks at the extreme ends of the transmission-FTIR spectrum. In addition, the transmission-FTIR spectrum yields more intense peaks than the ATR-FTIR spectrum, with the strongest peaks appearing approximately 30% more intense in the transmission-FTIR spectrum.

One further difference between the ATR-FTIR and transmission-FTIR spectra of lactate is the appearance of additional peaks in the transmission-FTIR spectrum. These peaks are seen at 1580 $cm^{-1}$, 1567 $cm^{-1}$ and 1556 $cm^{-1}$ and overlap very strongly with the central peak, which is attributed to an asymmetric stretch of the $CO_2^-$ functional group, at 1572 $cm^{-1}$.

The additional peaks are also thought to correspond to asymmetric stretching modes of the $CO_2^-$ group. It is throught that their absence from the ATR-FTIR spectrum is due to an orientation effect caused by the preferential adsorption of the lactate ion in a particular orientation on the ZnSe crystal surface. Orientation effects in ATR-FTIR spectroscopy arise due to the fact that the electric field of incident IR radiation has components both parallel to and perpendicular to the plane of incidence. The effective path length of a ZnSe crystal is known to be higher for the component of the electric field which is parallel to the plane of incidence, increasing the relative intensity of absorption peaks that correspond to vibrational modes with a dipole change in the plane of incidence.[118,119] If the lactate ion exhibits prefential adsorption in a particular orientation on the crystal surface, it would result in certain vibrational modes always having a dipole change perpendicular to the plane of incidence and therefore their associated absorption peaks would be of significantly lower relative intensity. Alternatively, the preferential adsorption of the lactate ion in a particular orientation on the ZnSe ATR crystal surface may cause the restriction of specific

vibrational modes of the $CO_2^-$ group or render them IR-inactive. These phenomena would not affect transmission-FTIR spectra as the bulk of the solution is sampled, causing any orientation effects to be averaged out, and thus the absorption peaks of all IR-active vibrational modes can be seen.

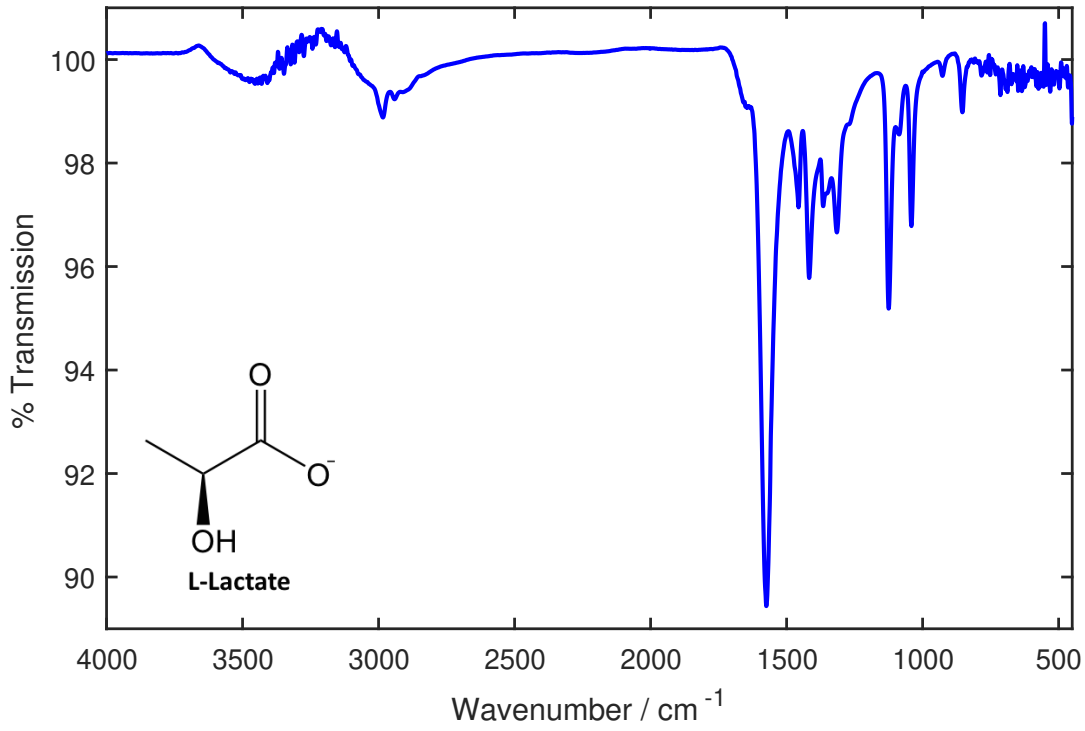


| Peak Position / $cm^{-1}$ | Peak Description | Assignment |
|---|---|---|
| 2984 | Weak | O–H Stretch |
| 2941 | Weak | O–H Stretch |
| 1575 | Strong | $CO_2^-$ Stretch (Asym.) |
| 1456 | Medium | $CH_3$ Bend |
| 1417 | Medium | $CO_2^-$ Stretch (Sym.) |
| 1367 | Medium | $CH_3$ Bend |
| 1315 | Medium | C–O–H Bend |
| 1125 | Medium | C–O Stretch |
| 1086 | Weak | C–O Stretch |
| 1041 | Medium | C–O Stretch |
| 927 | Weak | C–C (Aliphatic) Vibration |
| 854 | Weak | C–C (Aliphatic) Vibration |

***Figure 6.3:*** *The ATR-FTIR ratio spectrum and associated peak assignments*[117] *of a 100 mM solution of lactate in perfusion fluid, acquired using a seven-reflection ZnSe crystal. Asym. = asymmetric vibration, Sym. = symmetric vibration.*

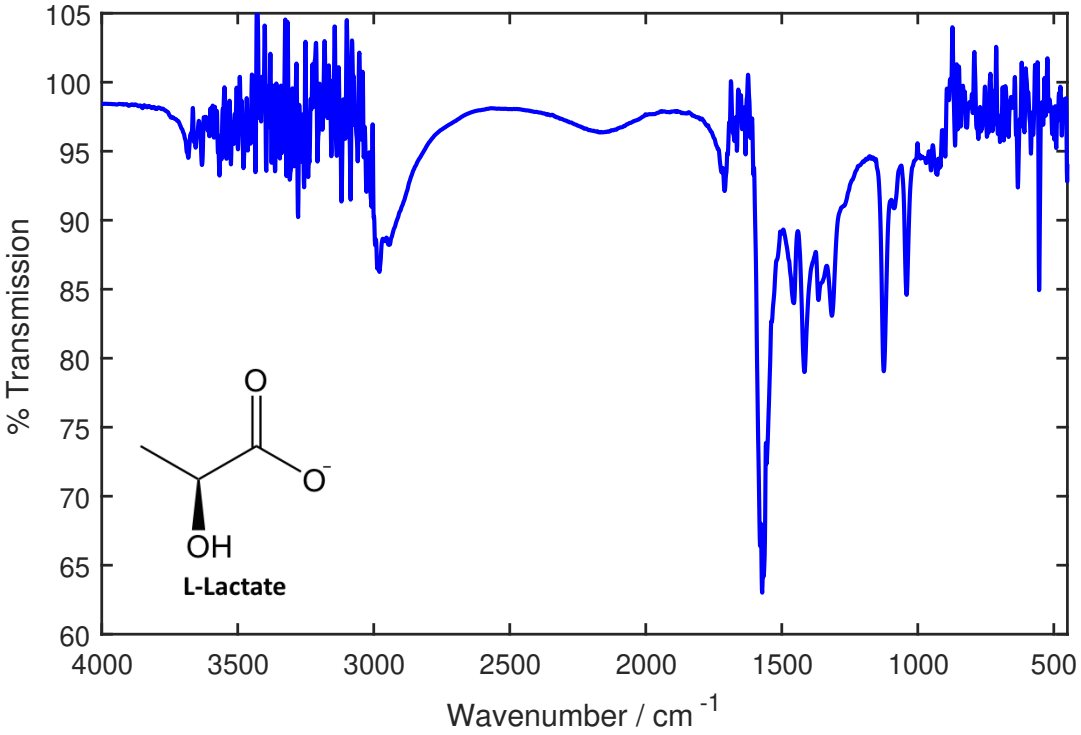


| Peak Position / $cm^{-1}$ | Peak Description | Assignment |
|---|---|---|
| 2945 | Medium, broad | O–H Stretch |
| 1580 | Strong | $CO_2^-$ Stretch (Asym.) |
| 1572 | Strong | $CO_2^-$ Stretch (Asym.) |
| 1567 | Strong | $CO_2^-$ Stretch (Asym.) |
| 1556 | Medium | $CO_2^-$ Stretch (Asym.) |
| 1456 | Medium | $CH_3$ Bend |
| 1417 | Medium | $CO_2^-$ Stretch (Sym.) |
| 1365 | Medium | $CH_3$ Bend |
| 1316 | Medium | C–O–H Bend |
| 1125 | Medium | C–O Stretch |
| 1087 | Weak | C–O Stretch |
| 1041 | Medium | C–O Stretch |

***Figure 6.4:*** *The transmission-FTIR ratio spectrum and associated peak assignments[117] of a 100 mM solution of lactate in perfusion fluid, acquired using a 50 µm path length. Asym. = asymmetric vibration, Sym. = symmetric vibration.*

### 6.1.3 FTIR Spectrum of Pyruvate

The ATR-FTIR and transmission-FTIR spectra of a 100 mM solution of pyruvate in perfusion fluid can be seen in Figures 6.5 and 6.6, respectively. Peak assignments for both spectra are also given.

The ATR-FTIR and transmission-FTIR spectra of pyruvate are both distinguished by four groups of medium/strong intensity peaks, which are approximately equidistant from each other, in the regions 1710 $cm^{-1}$, 1600 $cm^{-1}$, 1425 – 1356 $cm^{-1}$ and 1176 $cm^{-1}$. However, a clear difference is observed in the appearance of these peaks between the two spectra: in the ATR-FTIR spectrum, the peaks are of varying intensity, with that at 1708 $cm^{-1}$ being the strongest, whilst in the transmission-FTIR spectrum, the peaks at 1711 $cm^{-1}$, 1583 $cm^{-1}$, and 1356 $cm^{-1}$ are of similar intensity and the peak at 1176 $cm^{-1}$ is notably stronger.

There also exists a difference in the number and position of peaks between the ATR-FTIR and transmission-FTIR spectra of pyruvate. The ATR-FTIR spectrum peak at 1600 $cm^{-1}$ is absent in the transmission-FTIR spectrum and is replaced by two peaks at 1583 $cm^{-1}$ and 1572 $cm^{-1}$. All peaks are attributed to the asymmetric stretching of the $CO_2^-$ functional group. It is theorised that these variations in peak intensity, number and position are a result of the orientation effect observed in the FTIR spectra of lactate. Preferential adsorption of the pyruvate ion in a specific orientation on a ZnSe surface may cause a relative loss of intensity of peaks arising from vibrational modes which have a dipole change perpendicular to the plane of incident IR radiation. Alternatively, orientation-specific adsorption may restrict certain vibrational modes of the molecule or render them IR-inactive. The effect of this would be noticeable in an ATR-FTIR spectrum, which is acquired through analysing the sample surface, but in transmission-FTIR the effect would be negligible as the bulk of the sample is analysed.

Differences between the ATR-FTIR and transmission-FTIR spectra due to water absorption, as observed for glucose and lactate, are also seen in the spectra of pyruvate. Water-induced noise is present in the 3700 – 3000 $cm^{-1}$, 1700 – 1600 $cm^{-1}$ and 900 – 450 $cm^{-1}$ regions of the transmission-FTIR spectrum, resulting in the loss of peaks at either end of the spectrum.

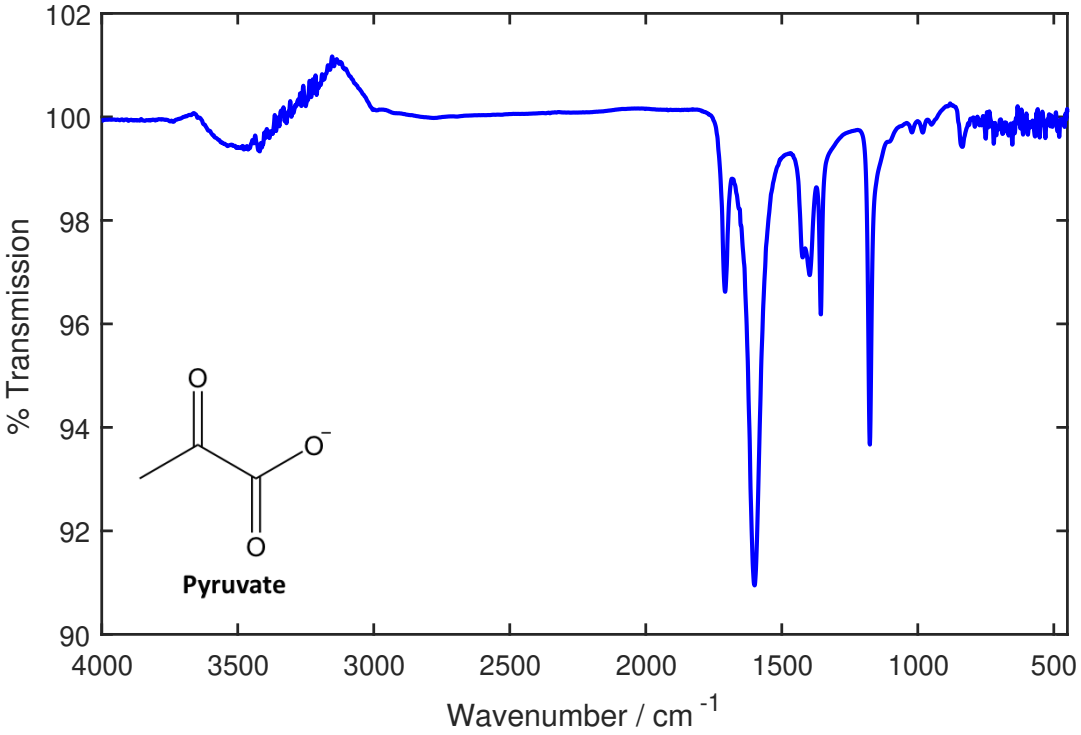


| Peak Position / $cm^{-1}$ | Peak Description | Assignment |
|---|---|---|
| 3511 | Weak, broad | O-H Stretch |
| 1708 | Medium | C=O stretch |
| 1600 | Strong | $CO_2^-$ Stretch (Asym.) |
| 1423 | Medium | $CO_2^-$ Stretch (Sym.) |
| 1397 | Medium | $CO_2^-$ Stretch (Sym.) |
| 1356 | Medium | $CH_3$ Bend |
| 1176 | Strong | C–C (Aliphatic) Vibration |
| 1021 | Weak | C–C (Aliphatic) Vibration |
| 982 | Weak | $CH_3$ Bend |
| 950 | Weak | C–C (Aliphatic) Vibration |
| 836 | Weak | C–C (Aliphatic) Vibration |

***Figure 6.5:*** *The ATR-FTIR ratio spectrum and associated peak assignments*[117] *of a 100 mM solution of pyruvate in perfusion fluid, acquired using a seven-reflection ZnSe crystal. Asym. = asymmetric vibration, Sym. = symmetric vibration.*

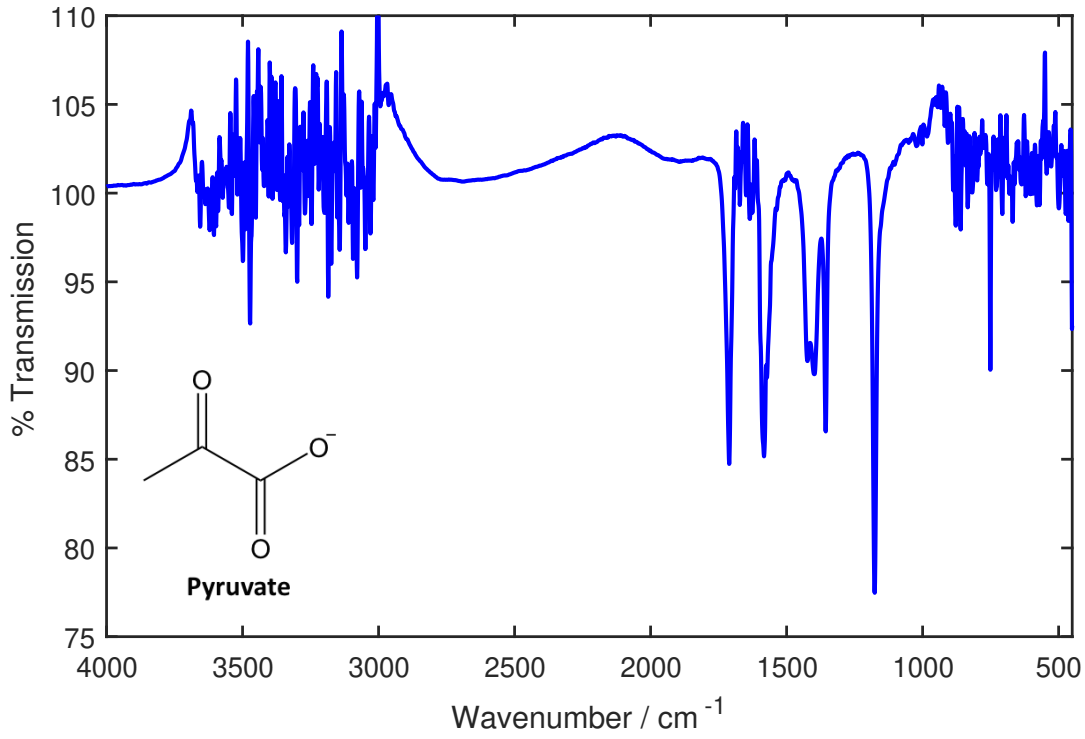


| Peak Position / $cm^{-1}$ | Peak Description | Assignment |
|---|---|---|
| 1711 | Strong | C=O stretch |
| 1583 | Strong | $CO_2^-$ Stretch (Asym.) |
| 1572 | Medium | $CO_2^-$ Stretch (Aym.) |
| 1424 | Medium | $CO_2^-$ Stretch (Sym.) |
| 1398 | Medium | $CO_2^-$ Stretch (Sym.) |
| 1356 | Strong | $CH_3$ Bend |
| 1176 | Strong | C–C (Aliphatic) Vibration |
| 1021 | weak | C–C (Aliphatic) Vibration |

***Figure 6.6:*** *The transmission-FTIR ratio spectrum and associated peak assignments*[117] *of a 100 mM solution of pyruvate in perfusion fluid, acquired using a 50 µm path length. Asym. = asymmetric vibration, Sym. = symmetric vibration.*

### 6.1.4 Mixtures of Glucose, Lactate and Pyruvate

A mixture containing 100 mM glucose, 100 mM lactate and 100 mM pyruvate in perfusion fluid was analysed via both ATR-FTIR and transmission-FTIR spectroscopy. The aim of these measurements was to allow a comparison of the mixture spectra with those of the pure compounds, in order to identify any compound-specific peaks which remain visible in the mixture spectra, as well as those which are lost due to overlap with the peaks of another compound. In this way, it was possible to determine key peaks which could be used to identify each individual compound from a mixture of the three.

The contribution of each compound to the overall mixture spectrum is most easily visualised by overlaying the spectra of individual compounds with that of the mixture. This is exemplified in Figure 6.7 which, for clarity, shows only the fingerprint region of each spectrum.

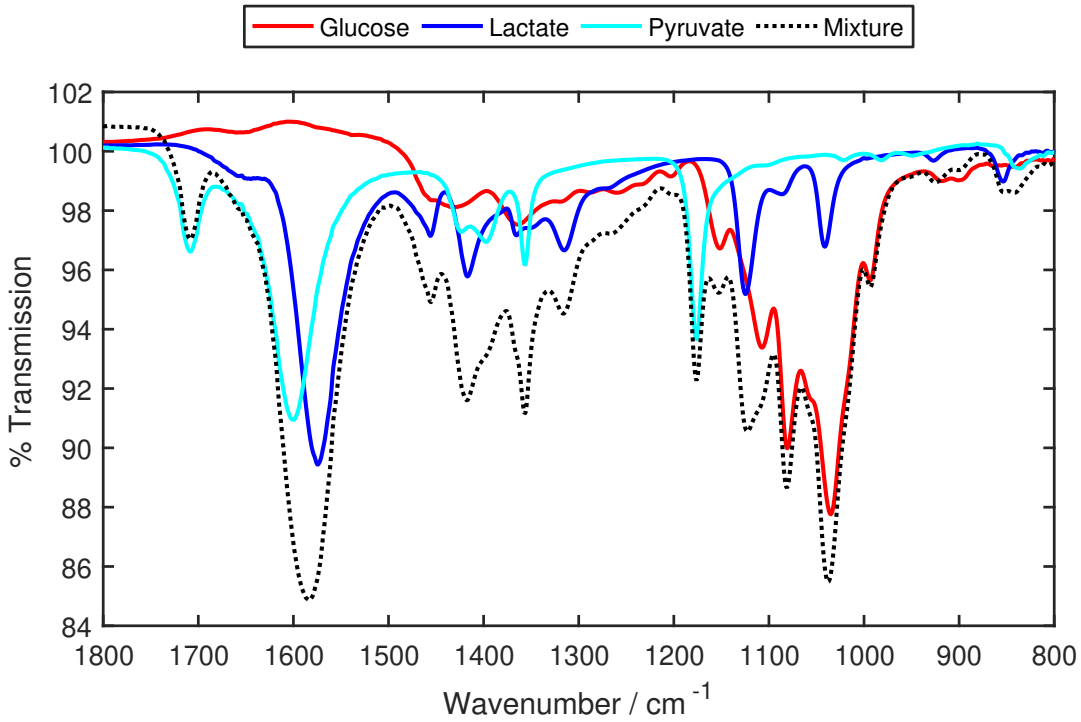


***Figure 6.7:*** *The ATR-FTIR ratio spectrum of a mixture containing 100 mM glucose, 100 mM lactate and 100 mM pyruvate in perfusion fluid, overlaid with the ATR-FTIR spectra of pure 100 mM solutions of each compound to show the contribution of each individual compound to the mixture spectrum. All spectra were acquired using a seven-reflection ZnSe crystal.*

The ATR-FTIR and transmission-FTIR spectra of the mixture are shown in Figures 6.8 and 6.9, respectively, in addition to an estimate of the molecular origin of each peak.

The resulting spectra indicate that a number of molecule-specific peaks remain

visible when glucose, lactate and pyruvate are combined in solution. Within the ATR-FTIR spectrum, peaks unique to glucose can be found at 3524 $cm^{-1}$, 2926 $cm^{-1}$, 1266 $cm^{-1}$, 1153 $cm^{-1}$, 1081 $cm^{-1}$, 993 $cm^{-1}$ and 900 $cm^{-1}$. All but two of these peaks are retained in the transmission-FTIR spectrum, with only the peaks at 3524 $cm^{-1}$ and 900 $cm^{-1}$ being lost. The strongest of the glucose-specific peaks are those at 1081 $cm^{-1}$ and 993 $cm^{-1}$, corresponding respectively to a C–O stretching vibration, and a C–C vibration. The peak at 1035 $cm^{-1}$, which is one of those identified in the literature as being important for glucose identification, overlaps strongly with the 1041 $cm^{-1}$ peak corresponding to a C–O stretching mode of lactate. This overlap results in a single strong peak, positioned at 1038 $cm^{-1}$, in both the ATR-FTIR and the transmission-FTIR spectra of the mixture. The data in Figure 6.7 suggests that, when both compounds are present at equal concentrations, glucose makes a more significant contribution to this peak, yet nevertheless it cannot be considered glucose-specific.

Lactate-specific peaks can be seen in the ATR-FTIR spectrum at 2982 $cm^{-1}$, 1456 $cm^{-1}$, 1316 $cm^{-1}$, 925 $cm^{-1}$ and 853 $cm^{-1}$. The strongest of these peaks are those at 1456 $cm^{-1}$ (corresponding to a $CH_3$ bend) and at 1316 (corresponding to a C–O–H bend). An analysis of the transmission-FTIR spectrum shows that the peaks at 2982 $cm^{-1}$, 925 $cm^{-1}$ and 853 $cm^{-1}$ are lost due to water-induced spectral noise, but additional strong peaks are seen at 1567 $cm^{-1}$ and 1556 $cm^{-1}$. These peaks correspond to asymmetric stretching vibrations of the $CO_2^-$ group and represent two of the additional peaks seen in the transmission-FTIR spectrum of pure lactate. Additional peaks corresponding to vibrations of the $CO_2^-$ functional group are present in both the ATR-FTIR and the tranmsission-FTIR spectra of the mixture, but these overlap entirely with peaks corresponding to the vibration of the same moiety within the pyruvate molecule and hence are not lactate-specific.

There are 3 pyruvate-specific peaks present in both the ATR-FTIR and the transmission-FTIR spectra: one corresponding to a C=O stretch (approximately 1710 $cm^{-1}$), one corresponding to a bending mode of the $CH_3$ group (1357 $cm^{-1}$) and one corresponding to a C–C vibration (1176 $cm^{-1}$). All of these are of medium/strong intensity. The ATR-FTIR spectrum contains an additional weak pyruvate-specific peak at 842 $^{-1}$ which is lost in the transmission-FTIR spectrum due to water-induced spectral noise.

### 6.1.5 Mid-FTIR Spectra of Glucose, Lactate & Pyruvate: Conclusions

The key conclusion of this section of work is that both the ATR-FTIR and transmission-FTIR spectra of glucose, lactate and pyruvate exhibit peaks which allow each compound to be individually identified from the FTIR spectra of an equimolar mixture of all three compounds. These peaks occur primarily in the fingerprint region of the

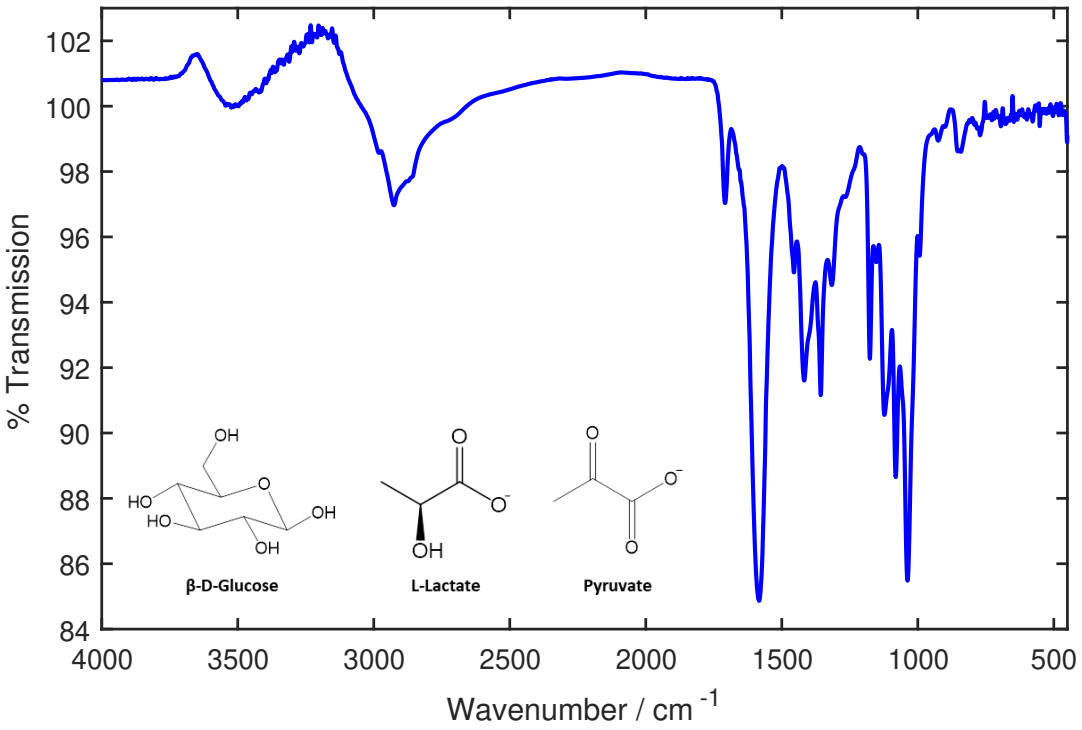


| Peak Position / $cm^{-1}$ | Peak Description | Assignment |
|---|---|---|
| 3524 | Weak, Broad | O–H Stretch: Glu |
| 2982 | Weak, Broad | O–H Stretch: Lac |
| 2926 | Medium, Broad | C–H Stretch: Glu |
| 1709 | Medium | C=O Stretch: Pyr |
| 1583 | Strong | $CO_2^-$ Stretch (Asym.): Lac & Pyr |
| 1456 | Medium | $CH_3$ Bend: Lac |
| 1418 | Medium, broad | $CO_2^-$ Stretch (Sym.): Lac & Pyr |
| 1357 | Medium | $CH_3$ Bend: Pyr |
| 1316 | Medium | C–O–H Bend: Lac |
| 1266 | Weak | C–C (Alicyclic) Vibration: Glu |
| 1176 | Medium | C–C (Aliphatic) Vibration: Pyr |
| 1153 | Weak | C–C (Alicyclic) Vibration: Glu |
| 1123 | Medium, Broad | C–O Stretch: Lac & Glu |
| 1081 | Strong | C–O Stretch: Glu |
| 1038 | Strong | C–O Stretch: Glu & Lac |
| 993 | Medium | C–C (Alicyclic) Vibration: Glu |
| 925 | weak | C–C (Aliphatic) Vibration: Lac |
| 900 | Weak | C–O–C Stretch: Glu |
| 853 | Weak | C–C (Aliphatic) Vibration: Lac |
| 842 | Weak | C–C (Aliphatic) Vibration: Pyr |

***Figure 6.8:*** *The ATR-FTIR ratio spectrum and associated peak assignments[117] of a mixture containing 100 mM glucose, 100 mM lactate and 100 mM pyruvate in perfusion fluid, acquired using a seven-reflection ZnSe crystal. Glu = glucose, Lac = lactate, Pyr = pyruvate, Asym. = asymmetric vibration, Sym. = symmetric vibration.*

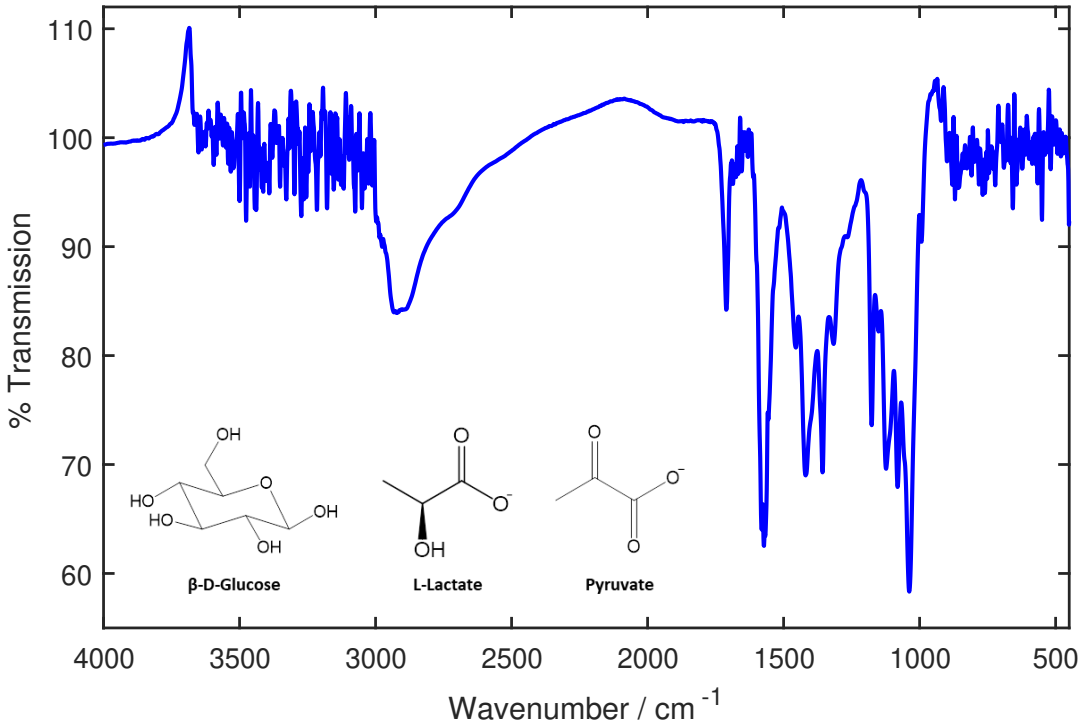


| Peak Position / $cm^{-1}$ | Peak Description | Assignment |
|---|---|---|
| 2923 | Medium, Broad | C–H Stretch: Glu |
| 1711 | Medium | C=O Stretch: Pyr |
| 1580 | Strong | $CO_2^-$ Stretch (Asym.): Lac & Pyr |
| 1572 | Strong | $CO_2^-$ Stretch (Asym.): Lac & Pyr |
| 1567 | Strong | $CO_2^-$ Stretch (Asym.): Lac |
| 1556 | Medium | $CO_2^-$ Stretch (Asym.): Lac |
| 1455 | Medium | $CH_3$ Bend: Lac |
| 1419 | Strong, Broad | $CO_2^-$ Stretch (Sym.): Lac & Pyr |
| 1357 | Strong | $CH_3$ Bend: Pyr |
| 1316 | Medium | C–O–H Bend: Lac |
| 1266 | Weak | C–C (Alicyclic) Vibration: Glu |
| 1176 | Strong | C–C (Aliphatic) Vibration: Pyr |
| 1151 | Medium | C–C (Alicyclic) Vibration: Glu |
| 1123 | Strong, Broad | C–O Stretch: Lac & Glu |
| 1081 | Strong | C–O Stretch: Glu |
| 1038 | Strong | C–O Stretch: Glu & Lac |
| 994 | Medium | C–C (Alicyclic) Vibration: Glu |

***Figure 6.9:*** *The transmission-FTIR ratio spectrum and associated peak assignments*[117] *of a mixture containing 100 mM glucose, 100 mM lactate and 100 mM pyruvate in perfusion fluid, acquired using a 50 µm path length. Glu = glucose, Lac = lactate, Pyr = pyruvate, Asym. = asymmetric vibration, Sym. = symmetric vibration.*

spectrum and are listed in Table 6.1.

***Table 6.1:*** *FTIR peaks of glucose, lactate and pyruvate that allow the distinction of each compound when combined in an equimolar mixture.*

| Compound | Spectrum Type | Unique Peaks / $cm^{-1}$ |
|---|---|---|
| Glucose | ATR-FTIR | 3524, 2926, 1266, 1153, 1081, 993, 900 |
| | Transmission-FTIR | 2923, 1266, 1151, 1081, 994 |
| Lactate | ATR-FTIR | 2982, 1456, 1316, 925, 853 |
| | Transmission-FTIR | 1567, 1556, 1455, 1316 |
| Pyruvate | ATR-FTIR | 1709, 1357, 1176, 842 |
| | Transmission-FTIR | 1711, 1357, 1176 |

This work has also highlighted differences between the ATR-FTIR and transmission-FTIR spectra of a given compound. The ATR-FTIR spectrum is less affected by the presence of water, meaning that a greater number of analyte peaks can be seen, but the overall peak intensity is lower than that of transmission-FTIR. Conversely, the transmission-FTIR spectrum exhibits a higher peak intensity at the expense of a higher level of water-induced noise, causing the loss of peaks at the extreme ends of the spectrum. In addition, the transmission-FTIR spectra of lactate and pyruvate exhibited differences in the number and relative intensity of peaks in the fingerprint region of the spectrum, which have been attributed to orientation-specific adsorption of the $CO_2^-$ group on the surface of the ATR-FTIR crystal.

## 6.2 Interference from Competing Molecules

The clinical microdialysate samples to be analysed by the developed sensor are likely to contain compounds other than glucose, lactate and pyruvate, as discussed in Section 2.3.2. The aim of the work in this section was to consider the 'competing molecules' which are likely to be present in clinical microdialysate samples and assess the degree to which they may affect the performance of a mid-FTIR spectroscopy sensor for glucose, lactate and pyruvate.

Of the compounds discussed in Section 2.3.2, the effect of drug molecules on the performance of the sensor is the most difficult to estimate. Patients with TBI often have multiple medical needs and may be treated with a variety of different drugs, in addition to the prophylactic anti-seizure medication mentioned in Section 2.3.2. Furthermore, the concentration of a given medication in the microdialysate will vary between patients, depending upon the dose administered and the rate at which it is metabolised. As a result, it was concluded that the only way to account for the effect of drug molecules on the performance of the sensor would be to carry out extensive

measurements on multiple clinical samples. This was not possible in this work due to the scarcity of clinical samples and is recommended as a priority during the clinical testing phase of the final device.

Cytokines are a group of proteins which mediate the inflammatory response to injury or infection and are small enough to be recovered by microdialysis. However, these molecules are reported to be present in microdialysate at picomolar concentrations,[8] which are approximately $10^6$ times lower than the lowest expected concentration of any of the analytes of interest, and are therefore not considered likely to have a significant impact on sensor performance.

Nitric oxide is used within the body to regulate blood flow. It is highly reactive and is therefore unlikely to be present in significant concentrations in microdialysate, yet its products (nitrates and nitrites, collectively termed $NO_x$) have been successfully collected by microdialysis. A pilot study which measured the total concentration of all $NO_x$ products recovered using microdialysis, across 13 catheters placed in 12 patients, established a mean concentration of 32.7 $\pm$ 16.8 $\mu$M.[9] This concentration is 3-fold lower than the minimum expected concentrations of glucose and lactate in perfusion fluid but is within the range of expected pyruvate concentrations, although at the lower end. However, it is difficult to investigate the impact that $NO_x$ may have on the performance of an IR-based sensor, as the measured mean concentration encompasses a large number of different compounds. It is not clear which specific compounds are present, nor the level of contribution they make to the overall concentration of $NO_x$. It was therefore concluded that, as with drug molecules, the effect of $NO_x$ on the final sensor would be best established during the clinical testing phase.

Glycerol is a component of cell membranes and therefore its presence in the extracellular fluid has been implicated as an indicator of cellular breakdown. The reported range of observed glycerol concentrations in the microdialysate of TBI patients extends from approximately 10 – 400 $\mu$M.[16,120,121] This range overlaps with the expected clinical pyruvate concentration range, and with the lower end of the expected glucose and lactate concentration ranges, and it was thus considered appropriate to investigate the FTIR spectrum of glycerol to identify regions of possible overlap with the spectra of pyruvate, lactate and glucose. The ATR-FTIR and transmission-FTIR spectra of a 100 mM solution of glycerol in perfusion fluid are shown in Figures 6.10 and 6.11, respectively.

Glutamate, a neurotransmitter, is also found in the microdialysate of TBI patients. A 2011 analysis of microdialysate samples from 223 patients reported glutamate concentrations of 1 – 13 $\mu$M.[16] The presence of glutamate in microdialysate samples may therefore affect pyruvate detection, as the upper end of this range overlaps with the lower end of the pyruvate concentration range expected in microdialysate samples. The detection of glucose and lactate is unlikely to be affected, as the reported glu-

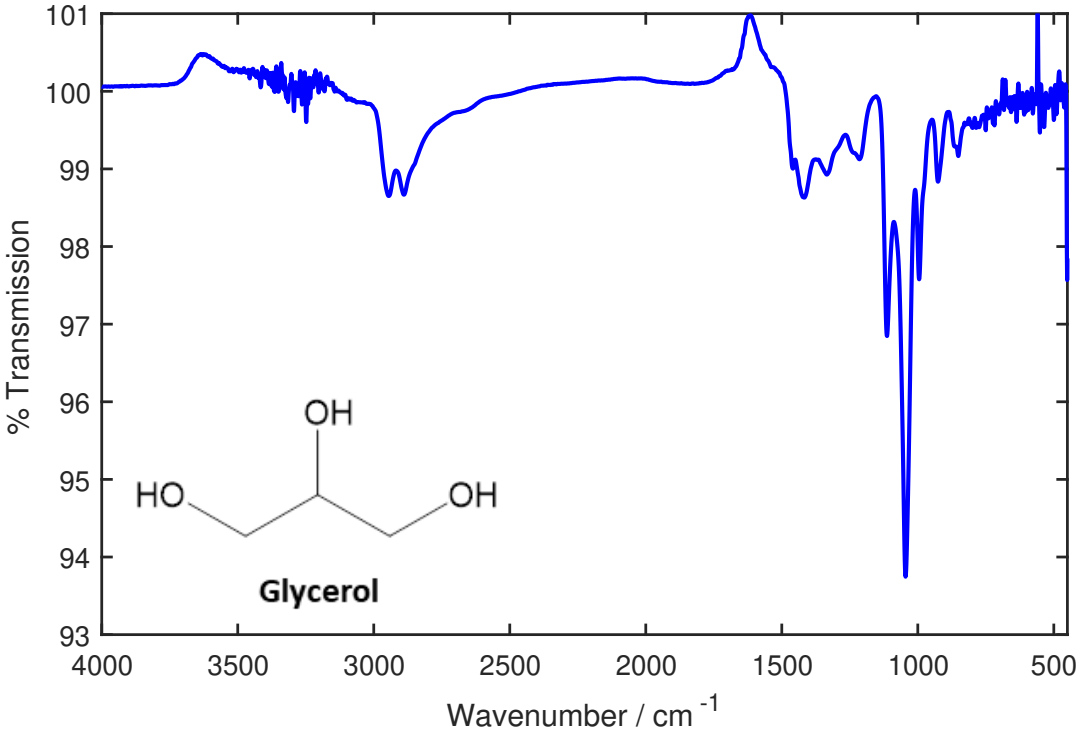


| Peak Position / $cm^{-1}$ | Peak Description | Assignment |
|---|---|---|
| 2945 | Weak | $CH_2$ Stretch |
| 2889 | Weak | $CH_2$ Stretch |
| 1461 | Weak | $CH_2$ Bend |
| 1419 | Weak | C–H Bend |
| 1334 | Weak | C–H Bend |
| 1215 | Weak | C–C (Aliphatic) Vibration |
| 1113 | Medium | C–O Stretch |
| 1045 | Strong | C–O Stretch |
| 996 | Medium | C–C (Aliphatic) Vibration |
| 925 | Weak | C–C (Aliphatic) Vibration |
| 852 | Weak | C–C (Aliphatic) Vibration |

***Figure 6.10:*** *The ATR-FTIR ratio spectrum and associated peak assignments[117] of a 100 mM solution of glycerol in perfusion fluid, acquired using a seven-reflection ZnSe crystal.*

tamate concentration range is 10 – 100-fold lower than the lowest expected levels of glucose and lactate in microdialysate. The ATR-FTIR and transmission-FTIR spectra of a solution of L-glutamic acid in perfusion fluid are shown in Figures 6.12 and 6.13, respectively.

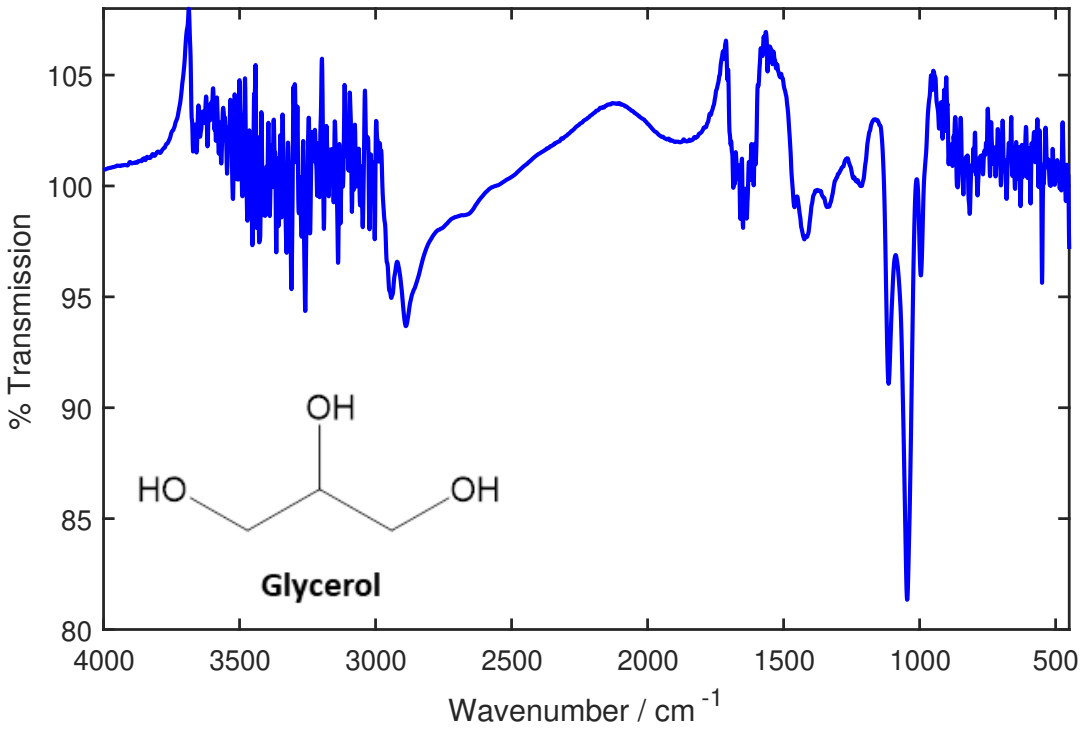


| Peak Position / $cm^{-1}$ | Peak Description | Assignment |
|---|---|---|
| 2943 | Medium | $CH_2$ Stretch |
| 2888 | Medium | $CH_2$ Stretch |
| 1461 | Weak | $CH_2$ Bend |
| 1424 | Weak | C–H Bend |
| 1415 | Weak | C–H Bend |
| 1337 | Weak | C–H Bend |
| 1217 | Weak | C–C (Aliphatic) Vibration |
| 1114 | Medium | C–O Stretch |
| 1045 | Strong | C–O Stretch |
| 996 | Medium | C–C (Aliphatic) Vibration |

***Figure 6.11:*** *The transmission-FTIR ratio spectrum and associated peak assignments*[117] *of a 100 mM solution of glycerol in perfusion fluid, acquired using a 50 µm path length.*

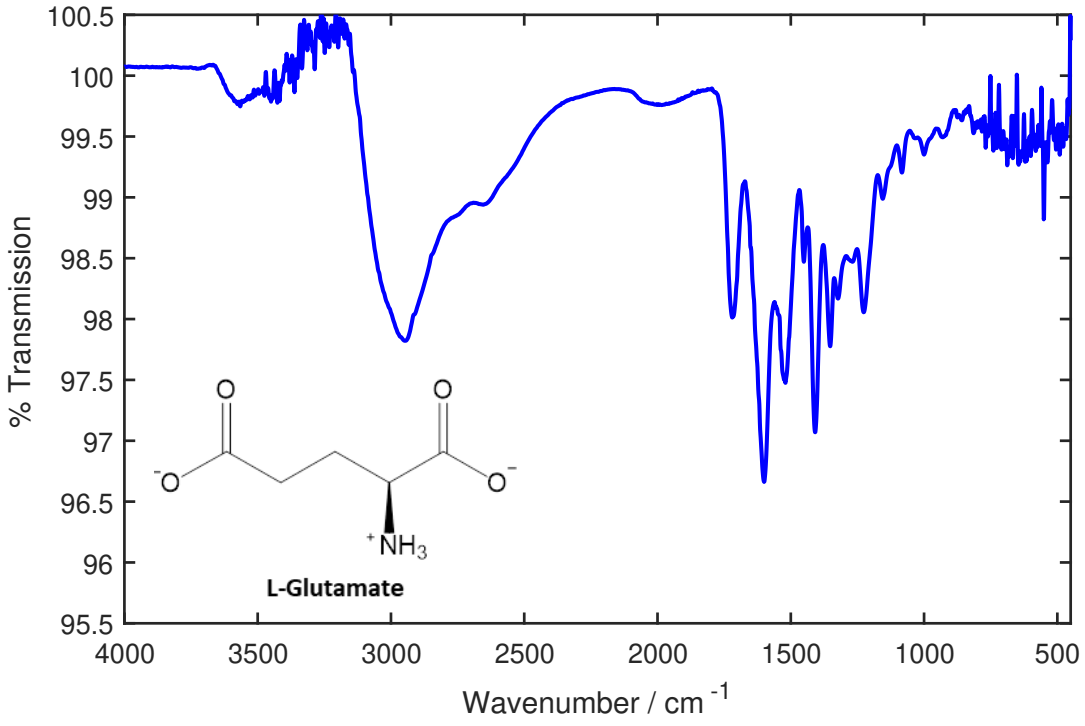


| Peak Position / $cm^{-1}$ | Peak Description | Assignment |
|---|---|---|
| 2947 | Strong, Broad | $CH_2$ Stretch |
| 2648 | Weak, Broad | C–H Stretch |
| 1996 | Weak, Broad | $NH_3^+$ Bend (Overtone) |
| 1720 | Medium | C=O Stretch |
| 1715 | Medium | C=O Stretch |
| 1600 | Strong | $CO_2^-$ Stretch (Asym.) |
| 1520 | Medium | $NH_3^+$ Bend (Sym.) |
| 1451 | Weak | $CH_2$ Bend |
| 1408 | Strong | $CH_2$ Bend |
| 1353 | Medium | $CO_2^-$ Stretch (Sym.) |
| 1323 | Weak | N–C–H Bend |
| 1269 | Weak | C–O Stretch |
| 1226 | Medium | C–O Stretch |
| 1155 | Weak | C–O Stretch |
| 1083 | Weak | C–O Stretch |
| 1000 | Weak | C–C (Aliphatic) Vibration |
| 930 | Weak | C–C (Aliphatic) Vibration |

***Figure 6.12:*** *The ATR-FTIR ratio spectrum and associated peak assignments*[117] *of a 50 mM solution of L-glutamic acid in perfusion fluid, acquired using a seven-reflection ZnSe crystal. Asym. = asymmetric vibration, Sym. = symmetric vibration.*

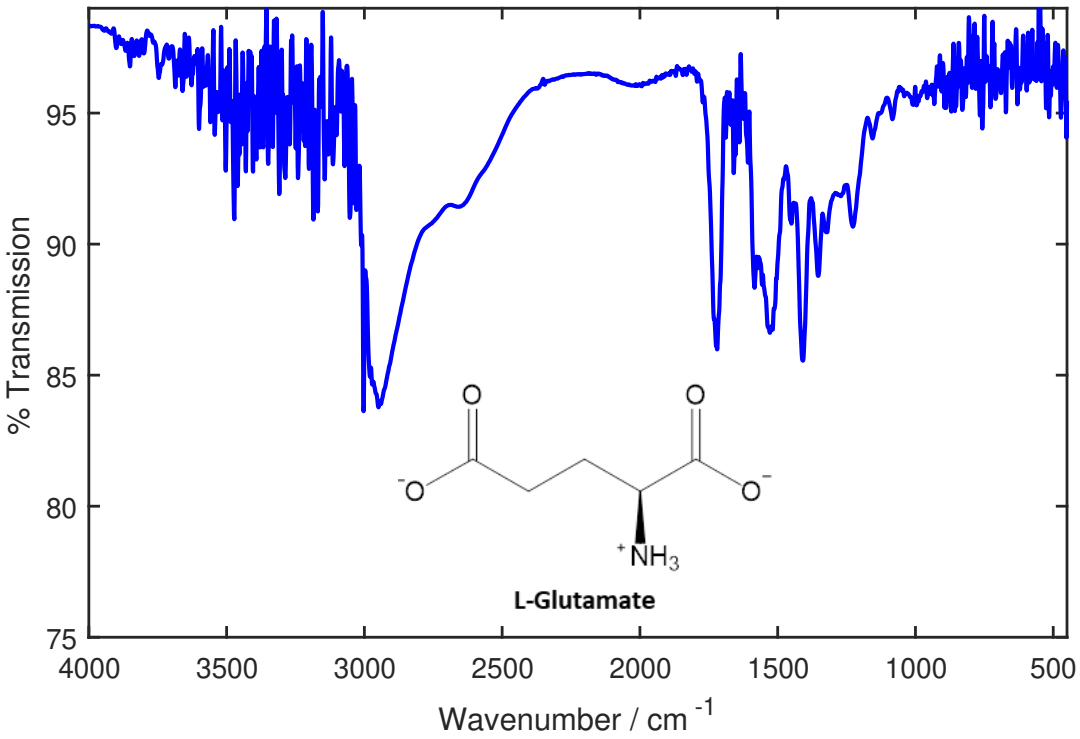


| Peak Position / $cm^{-1}$ | Peak Description | Assignment |
|---|---|---|
| 2949 | Strong, Broad | $CH_2$ Stretch |
| 2940 | Strong, Broad | $CH_2$ Stretch |
| 2658 | Weak, Broad | C–H Stretch |
| 1998 | Weak, Broad | $NH_3^+$ Bend (Overtone) |
| 1723 | Strong | C=O Stretch |
| 1720 | Strong | C=O Stretch |
| 1584 | Medium | $CO_2^-$ Stretch (Asym.)/$NH_3^+$ Bend (Asym.) |
| 1573 | Medium | $CO_2^-$ Stretch (Asym.)/$NH_3^+$ Bend (Asym.) |
| 1557 | Medium | $CO_2^-$ Stretch (Asym.)/$NH_3^+$ Bend (Asym.) |
| 1536 | Medium | $NH_3^+$ Bend (Sym.) |
| 1528 | Strong | $NH_3^+$ Bend (Sym.) |
| 1524 | Medium | $NH_3^+$ Bend (Sym.) |
| 1518 | Strong | $NH_3^+$ Bend (Sym.) |
| 1512 | Medium | $NH_3^+$ Bend (Sym.) |
| 1450 | Weak | $CH_2$ Bend |
| 1437 | Weak | $CO_2^-$ Stretch (Sym.) |
| 1409 | Strong | $CH_2$ Bend |
| 1353 | Medium | $CO_2^-$ Stretch (Sym.) |
| 1323 | Weak | N–C–H Bend |
| 1227 | Medium | C–O Stretch |
| 1156 | Weak | C–O Stretch |
| 1084 | Weak | C-O Stretch |

***Figure 6.13:*** *The transmission-FTIR ratio spectrum and associated peak assignments[117] of a 50 mM solution of L-glutamic acid in perfusion fluid, acquired using a 50 µm path length. Asym. = asymmetric vibration, Sym. = symmetric vibration.*

ATR-FTIR and transmission-FTIR spectra of a mixture containing equimolar amounts of glucose, lactate, pyruvate, glycerol and L-glutamic acid were also acquired (Figures 6.14 and 6.15, respectively). L-glutamic acid is less soluble in aqueous media than the other compounds under investigation and therefore all compounds were present in the mixture at 50 mM to account for the lower aqueous solubility of L-glutamate. Peak assignments for the mixture spectra were based on those already described for glucose, lactate, pyruvate, glycerol and glutamate. This proved to be difficult due to the overlap of peaks and the potential for multiple compounds to contribute to a single peak. Where it was not possible to ascertain the origin of a peak, the possible contributing compounds are indicated.

Both the ATR-FTIR and the transmission-FTIR spectra of the glucose, lactate, pyruvate, glycerol and glutamate mixure show peaks specific to glucose, lactate and pyruvate.

Two weak glucose-specific peaks are observed in the ATR-FTIR spectrum of the mixture, at 3524 $cm^{-1}$ and 1265 $cm^{-1}$. The former is lost in the transmission-FTIR spectrum, due to noise, but the 1265 $cm^{-1}$ peak still remains. However, it is possible that the peak at 1081 $cm^{-1}$, which is present in both spectra, would be the most useful peak for glucose detection despite the fact that it is attributed to the C–O stretches of both glucose and glutamate in Figures 6.14 and 6.15. This is due to the fact that glutamate levels in clinical microdialysate samples are likely to be 10 – 100-fold lower than the lowest expected concentration of glucose and are thus expected to have a negligible impact upon the FTIR spectrum of glucose. This assumption is particularly applicable when considering the 1081 $cm^{-1}$ peak, as it is one of the strongest in the glucose spectrum.

The ATR-FTIR spectrum of the mixture does not show any peaks specific to lactate. However, two peaks have been attributed to both lactate and glutamate: one at 1454 $cm^{-1}$, corresponding to the $CH_3$ bend of lactate and the $CH_2$ bend of glutamate, and the other at 1319 $cm^{-1}$ (corresponding to the C–O–H bend of lactate and the N–C–H bend of glutamate). Using the same argument as that presented for the 1081 $cm^{-1}$ peak of glucose, it could be concluded that these peaks may be considered lactate-specific for the analysis of microdialysate samples. The transmission-FTIR spectrum contains a single peak which is clearly lactate-specific: a strong peak at 1567 $cm^{-1}$, corresponding to one of the $CO_2^-$ stretching modes that is present in the transmission-FTIR spectrum of a pure solution of lactate but absent from its ATR-FTIR spectrum. In addition to this, the transmission-FTIR spectrum contains three peaks which are attributed to both lactate and glutamate and so may be considered to be lactate-specific for the analysis of clinical microdialysate samples: 1555 $cm^{-1}$, 1453 $cm^{-1}$, 1321 $cm^{-1}$.

Both the ATR-FTIR and the transmission-FTIR spectra of the mixture contain

three peaks which have been attributed solely to pyruvate, at 1710 $cm^{-1}$, 1356 $cm^{-1}$ and 1176 $cm^{-1}$. All of the peaks are of medium intensity and are therefore clearly visible in the spectra.

The presence of these peaks indicates that it may be possible to detect glucose, lactate and pyruvate against a background of additional compounds recovered via microdialysis. Although this is not a comprehensive experimental study of all possible competing molecules, it is encouraging to note that these analyte peaks have been detected from an equimolar mixture of all compounds, yet in clinical microdialysate samples many of the additional competing compounds are likely to be present at concentrations significantly lower than those of glucose, lactate and pyruvate.

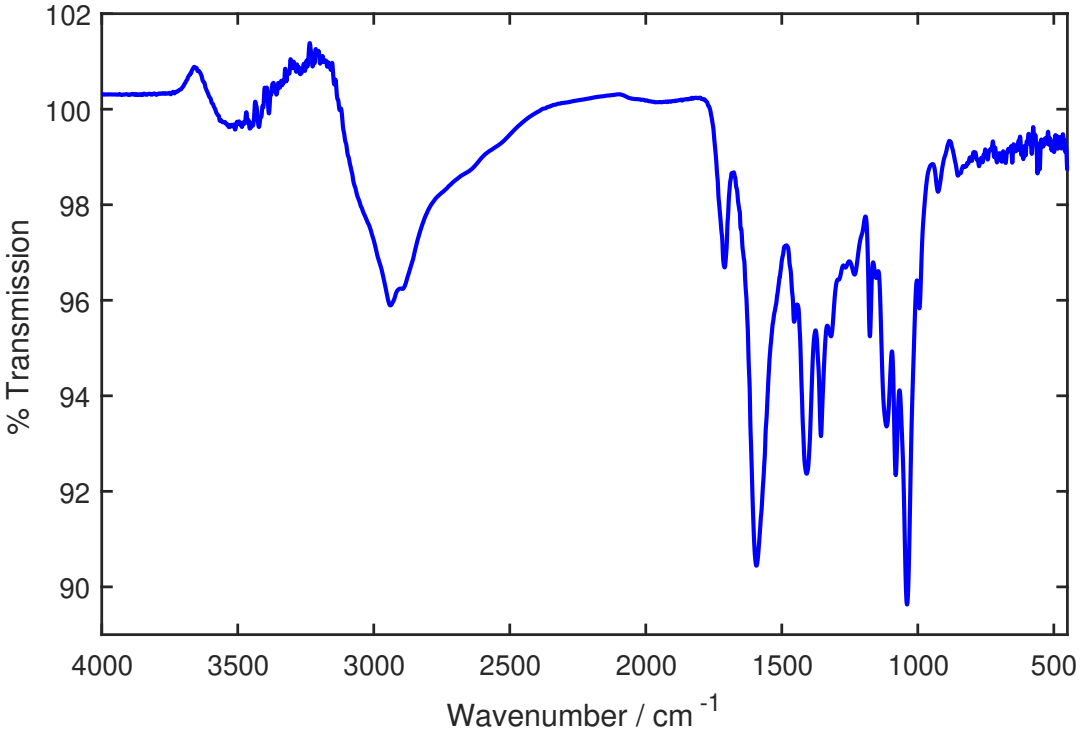


| Peak Position / $cm^{-1}$ | Peak Description | Assignment |
|---|---|---|
| 3524 | Weak, Broad | O–H Stretch: Glu |
| 2941 | Medium, Broad | $CH_2$ Stretch: Glut / $CH_2$ Stretch: Gly |
| 2892 | Medium, Broad | O–H Stretch: Lac / $CH_2$ Stretch: Gly |
| 1710 | Medium | C=O Stretch: Pyr |
| 1593 | Strong | $CO_2^-$ Stretch: Glut |
| 1454 | Weak | $CH_2$ Bend: Glut / $CH_3$ Bend: Lac |
| 1409 | Strong | $CH_2$ Bend: Glut |
| 1356 | Medium | $CH_3$ Bend: Pyr |
| 1319 | Weak | C–O–H Bend: Lac / N–C–H Bend: Glut |
| 1265 | Weak | C–C (Alicyclic) Vibration: Glu |
| 1233 | Weak | C–O Stretch: Glut |
| 1176 | Medium | C–C (Aliphatic) Vibration: Pyr |
| 1153 | Weak | C–C (Alicyclic) Vibration: Glu / C–O Stretch: Glut |
| 1115 | Medium | C–O Stretch: Gly |
| 1081 | Strong | C–O Stretch: Glu & Glut |
| 1039 | Strong | C–O Stretch: Glu & Lac |
| 994 | Weak | C–C (Alicyclic) Vibration: Glu & Gly |
| 925 | Weak | C–C (Aliphatic) Vibration: Lac & Gly |

***Figure 6.14:*** *The ATR-FTIR ratio spectrum and associated peak assignments[117] of a mixture of glucose, lactate, pyruvate, glycerol and glutamate in perfusion fluid. All compounds were present at a concentration of 50 mM. The spectrum was acquired using a seven-reflection ZnSe crystal. Glu = glucose, Lac = lactate, Pyr = pyruvate, Asym. = asymmetric vibration, Sym. = symmetric vibration.*

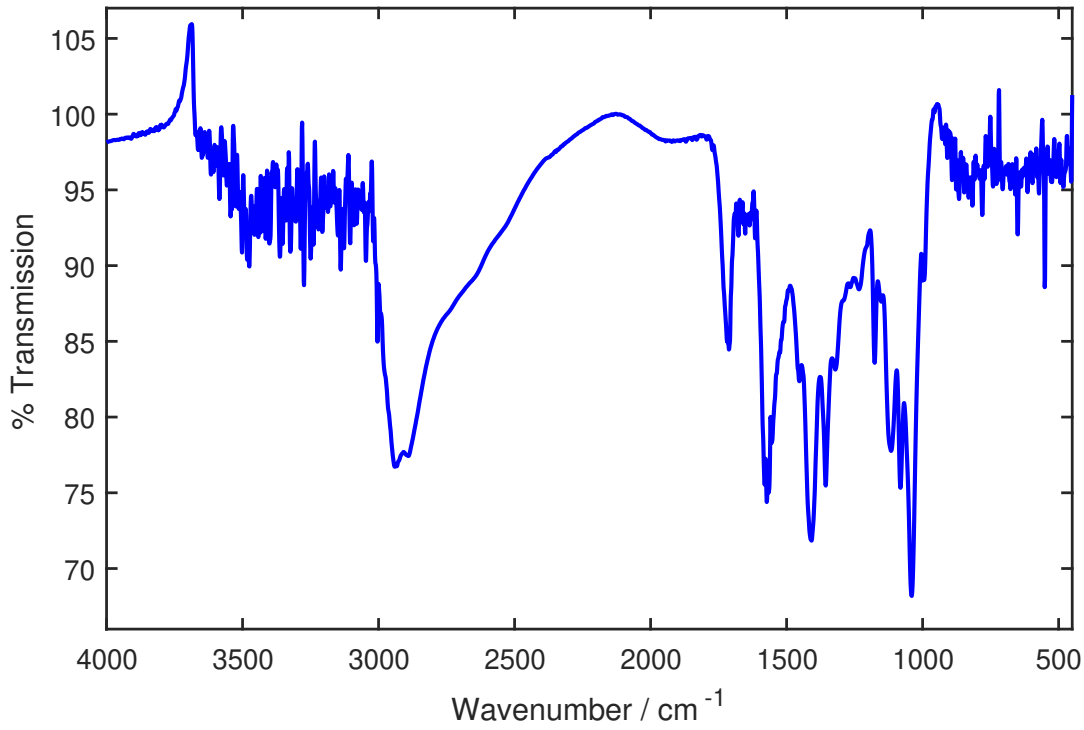


| Peak Position / $cm^{-1}$ | Peak Description | Assignment |
|---|---|---|
| 2940 | Strong, Broad | $CH_2$ Stretch: Glut / Gly |
| 2891 | Strong, Broad | $CH_2$ Stretch: Gly |
| 1712 | Medium | C=O: Pyr |
| 1581 | Strong | $CO_2^-$ Stretch: Glut, Lac, Pyr / $NH_3^+$: Glut |
| 1573 | Strong | $CO_2^-$ Stretch: Glut, Lac, Pyr / $NH_3^+$: Glut |
| 1567 | Strong | $CO_2^-$ Stretch: Lac |
| 1555 | Medium | $CO_2^-$ Stretch: Glut, Lac / $NH_3^+$: Glut |
| 1453 | Medium | $CH_2$ Bend: Glut / $CH_3$ Bend: Lac |
| 1409 | Strong | $CH_2$ Bend: Glut |
| 1356 | Strong | $CH_3$ Bend: Pyr |
| 1321 | Weak | C–O–H Bend: Lac / N–C–H Bend: Glut |
| 1266 | Weak | C–C (Alicyclic) Vibration: Glu |
| 1233 | Weak | C–O Stretch: Glut |
| 1176 | Medium | C–C (Aliphatic) Vibration: Pyr |
| 1152 | Weak | C–C (Alicyclic) Vibration: Glu / C–O Stretch: Glut |
| 1116 | Medium | C-O Stretch: Gly |
| 1081 | Strong | C–O Stretch: Glut / Glu |
| 1040 | Strong | C–O Stretch: Glu / Lac |
| 994 | Weak | C-C: Glu / Gly |

***Figure 6.15:*** *The transmission-FTIR ratio spectrum and associated peak assignments[117] of a mixture of glucose, lactate, pyruvate, glycerol and glutamate in perfusion fluid. All compounds were present at a concentration of 50 mM. The spectrum was acquired using a seven-reflection ZnSe crystal. Glu = glucose, Lac = lactate, Pyr = pyruvate, Asym. = asymmetric vibration, Sym. = symmetric vibration.*

### 6.2.1 Interference from Competing Molecules: Conclusions

This section has identified a number of molecules which are likely to be present in clinical microdialysate samples in addition to glucose, lactate and pyruvate. It was concluded that several of these molecules cannot be accounted for in the current work and their investigation must be a priority when carrying out clinical testing on the final device. It has also been demonstrated that absorbance peaks unique to glucose, lactate and pyruvate can be identified from transmission-FTIR spectra of the three compounds in an equimolar mixture with two key competing molecules: glycerol and glutamate. ATR-FTIR spectra of the same mixture yield unique peaks for glucose and pyruvate but not for lactate. However, the concentrations of glycerol and glutamate in clinical microdialysate samples are expected to be significantly lower than those of lactate and thus certain lactate absorbance peaks may be considered unique to lactate under these circumstances. All unique peaks identified are listed in Table 6.2.

***Table 6.2:*** *FTIR peaks of glucose, lactate and pyruvate that allow the distinction of each compound when combined in an equimolar mixture containing glycerol and glutamate. Peaks marked with an asterisk are not unique to that compound when in an equimolar mixture of glycerol and glutamate, but are considered likely to be unique in clinical samples due to the expected low concentrations of glycerol and glutamate.*

| Compound | Spectrum Type | Unique Peaks / $cm^{-1}$ |
|---|---|---|
| Glucose | ATR-FTIR | 3524, 1081*, 1265 |
| | Transmission-FTIR | 1081*, 1266 |
| Lactate | ATR-FTIR | 1454*, 1319* |
| | Transmission-FTIR | 1567, 1454*, 1319* |
| Pyruvate | ATR-FTIR | 1710, 1356, 1176 |
| | Transmission-FTIR | 1712, 1356, 1176 |

## 6.3 FTIR Spectroscopy of Clinical Samples

Single microdialysate samples taken from six different patients were analysed via transmission-FTIR spectroscopy only: the samples could not be measured using ATR-FTIR spectroscopy due to the small sample volumes available. The aim of this study was to determine whether any of the compound-specific peaks identified in Sections 6.1 and 6.2 were visible in the spectra and hence whether any of the compounds of interest could be detected directly from a clinical sample using transmission-FTIR spectroscopy. Prior to the acquisition of FTIR spectra, each sample was analysed using the ISCUS Flex to determine the concentrations of glucose, lactate and pyruvate present. Concentration data for glycerol, glutamate and other competing molecules

present in the sample were unavailable. The ISCUS Flex measurements were carried out by Dr Susan Giorgi-Coll.

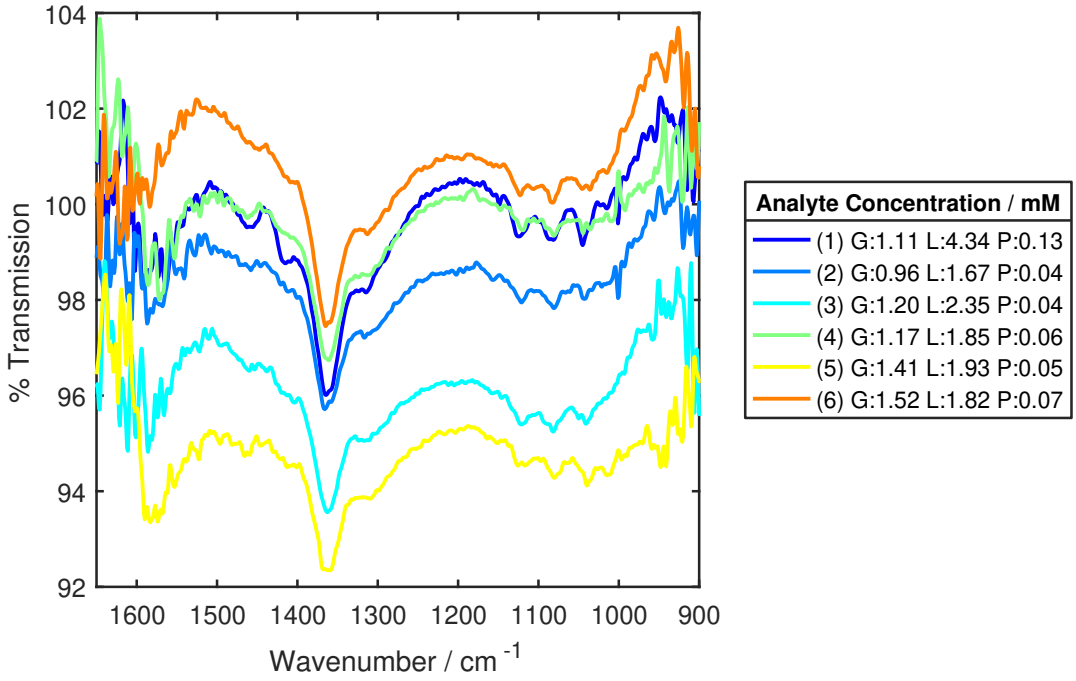


***Figure 6.16:*** *The transmission-FTIR ratio spectra of six clinical microdialysate samples, acquired using a 50 $\mu$m path length. G = glucose, L = lactate, P = pyruvate.*

Transmission-FTIR spectra were acquired using the same protocol as that used for synthetic samples, described in Section 5.2.2, using a 50 $\mu$m path length. The spectra have been shown in the region 1650–900 cm$^{-1}$, which is where the majority of the peaks of interest are located.

All spectra show weak peak intensities as a result of the very low concentrations of glucose, lactate and pyruvate present and consequently only a few could be distinguished from the spectral noise. Table 6.3 highlights only those peaks which could be unequivocally identified and assigned to a particular compound without further data processing.

In each spectrum, there are four peaks which are clearly visible: 1365 cm$^{-1}$, 1124 cm$^{-1}$, 1081 cm$^{-1}$ and 1042 cm$^{-1}$. The peak at 1365 cm$^{-1}$ has possible contributions from both the $CH_3$ bend of lactate and the C–O–H bend of glucose, which may help to explain why it is the strongest band in the spectrum. The remaining strong bands are due to C–O stretches of lactate (1124 cm$^{-1}$ and 1043 cm$^{-1}$) and glucose (1081 cm$^{-1}$). In Section 6.2 it was noted that, while the C–O stretch of glutamate may contribute to the peak at 1081 cm$^{-1}$ in the FTIR spectrum of equimolar amounts of glucose and glutamate, the contribution of glutamate to this peak in the FTIR spectrum of clinical samples is likely to be negligible due to its expected low clinical concentration range. As a result, the peak has been attributed solely to glucose in this analysis. There

***Table 6.3:*** *Peak assignments for the transmission-FTIR spectra of clinical microdialysate samples.*

| **Peak Position / $cm^{-1}$** | **Sample Number** | **Assignment** |
|---|---|---|
| 1365 | 1, 2 , 3, 4, 5, 6 | $CH_3$ Bend: Lac / C–O–H Bend: Glu |
| 1315 | 1, 2, 3, 6 | C–O–H Bend: Lac |
| 1124 | 1, 2, 3, 4, 5, 6 | C–O Stretch: Lac |
| 1086 | 1 | C–O Stretch: Lac |
| 1081 | 1, 2, 3, 4, 5, 6 | C–O Stretch: Glu |
| 1043 | 1, 2, 3, 4, 5, 6 | C–O Stretch: Lac |
| 1034 | 2, 4, 6 | C–O Stretch: Glu |
| 992 | 1, 2, 3, 4, 5, 6 | C–C (Alicyclic) Vibrations: Glu |

are no visible peaks corresponding to vibrations of the pyruvate molecule, which is reflective of the very low concentration of this compound in comparison to glucose and lactate.

It is noted that the locations of certain peaks in the clinical microdialysate samples are different to those in the equimolar mixtures studied in Sections 6.1 and 6.2. For example, the FTIR spectra of an equimolar mixture of glucose, lactate and pyruvate show a peak at 1038 $cm^{-1}$, which is attributed to an overlap of the 1035 $cm^{-1}$ peak due to the C–O stretch of glucose and the 1041 $cm^{-1}$ peak corresponding to the C–O stretch of lactate. In Figure 6.16, these vibrations have been resolved as two separate peaks, possibly due to the difference in concentration between glucose and lactate in the clinical microdialysate samples.

### 6.3.1 FTIR Spectroscopy of Clinical Samples: Conclusions

This section has indicated that transmission-FTIR spectroscopy can be used to detect glucose and lactate directly from clinical microdialysate samples via the identification of compound-specific peaks. However, this method was not able to detect pyruvate directly from the samples without further processing of the data, indicating that a device based on FTIR spectroscopy would most likely require a statstics-based method for analysing spectral data.

## 6.4 FTIR Spectroscopy Accessory Selection

This section describes two quantitative studies that were carried out to determine which FTIR accessories would be used for an in-depth analysis of the capability of FTIR to detect glucose, lactate and pyruvate at concentrations relevant to TBI monitoring. The studies were used to select an ATR-FTIR crystal for future ATR-FTIR

studies and a path length for future transmission-FTIR studies.

### 6.4.1 Crystal Selection for ATR-FTIR

The performances of three ATR-FTIR crystals were compared by carrying out an identical series of ATR-FTIR measurements with each crystal and analysing the resulting spectra to estimate the limits of detection of glucose, lactate and pyruvate afforded by each one. The crystals available for comparison were a single-reflection diamond, a seven-reflection Ge crystal and a seven-reflection ZnSe crystal.

Pure solutions of glucose, lactate and pyruvate, at ten different concentrations per compound, were prepared in perfusion fluid. Three separate samples of each solution were measured using ATR-FTIR spectroscopy. Two spectra of each sample were acquired: one ratio spectrum, in which perfusion fluid was used as a reference sample, and one raw spectrum. The concentrations used in this study were selected to cover the full clinical ranges of glucose, lactate and pyruvate that the developed sensor will be required to detect (0.1 –24 mM for glucose and lactate, 0.01 – 1.5 mM for pyruvate) and are listed in Table 6.4.

***Table 6.4:*** *Concentrations of glucose, lactate and pyruvate used in the performance comparison of ATR-FTIR crystals.*

| **Glucose Solutions / mM** | **Lactate Solutions / mM** | **Pyruvate Solutions / mM** |
|---|---|---|
| 0 | 0 | 0 |
| 0.05 | 0.05 | 0.005 |
| 0.1 | 0.1 | 0.01 |
| 0.19 | 0.19 | 0.05 |
| 0.4 | 0.4 | 0.10 |
| 0.75 | 0.75 | 0.15 |
| 1.5 | 1.5 | 0.75 |
| 3.0 | 3.0 | 1.0 |
| 6.0 | 6.0 | 1.5 |
| 12.0 | 12.0 | 7.5 |
| 24.0 | 24.0 | 15.0 |

The limits of detection of glucose, lactate and pyruvate afforded by each crystal were determined by identifying the lowest concentration of each compound that could be detected from the spectrum via an analysis of peak intensities: this method was chosen in preference to a statistical modelling approach due to the large number of spectra required for a robust statistical model. A comparison of peak intensities was assumed to be a valid method of determining the limit of detection due to the known relationship between peak intensity, the absorption of IR radiation and the concentration of an analyte. The peak intensity is proportional to the amount of IR radiation absorbed by a species which, in turn, is related to the concentration of that

species via the Beer-Lambert law (Section 5.4.2).

The spectra acquired in this study all exhibited relatively flat baselines. However, many spectra were found to have a significant vertical offset with respect to other spectra acquired using the same crystal, meaning that a comparison of the absolute peak intensities generated by each concentration would not yield meaningful results. These features can be observed in Figure 6.17 which provides an example of the range of spectra generated by a single compound, at multiple concentrations, using a single type of ATR-FTIR crystal.

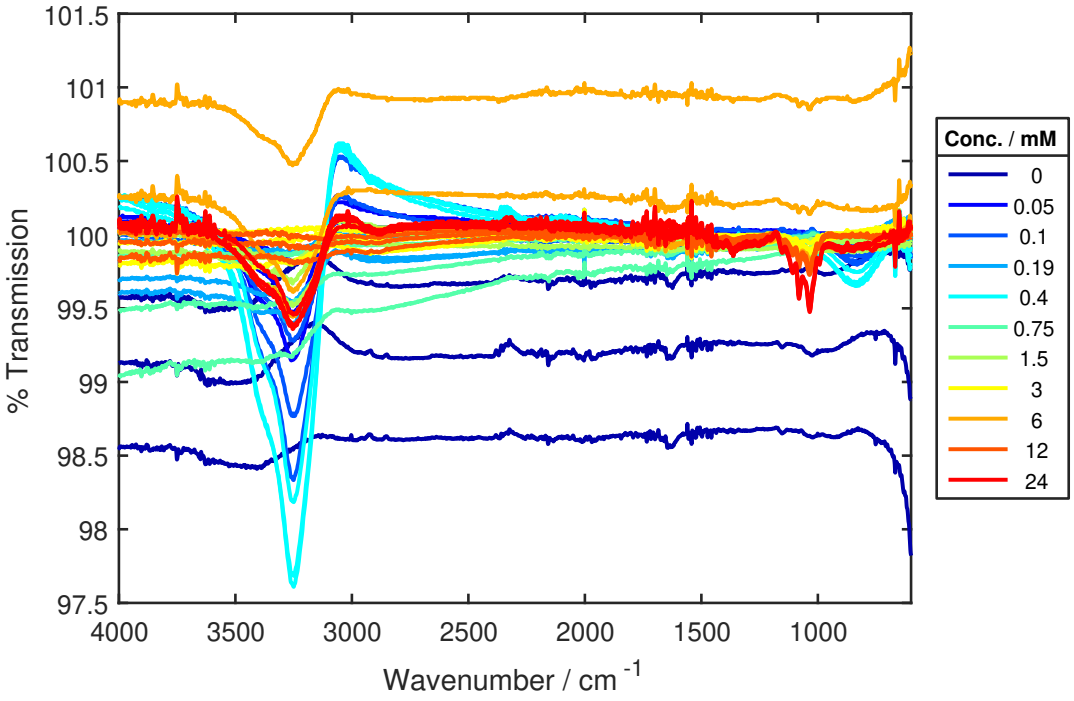


***Figure 6.17:*** *The ATR-FTIR ratio spectra of glucose in perfusion fluid, at a range of concentrations, acquired using a single-reflection diamond crystal. Spectra have flat baselines but are vertically offset with respect to one another.*

As a result of this offset, relative peak intensities were calculated and compared for each spectrum. The relative peak intensity is the measured difference in transmission between a peak maximum and an isosbestic point on the spectrum. This concept can be illustrated graphically by normalising the spectra to an isosbestic point, as shown in Figure 6.18.

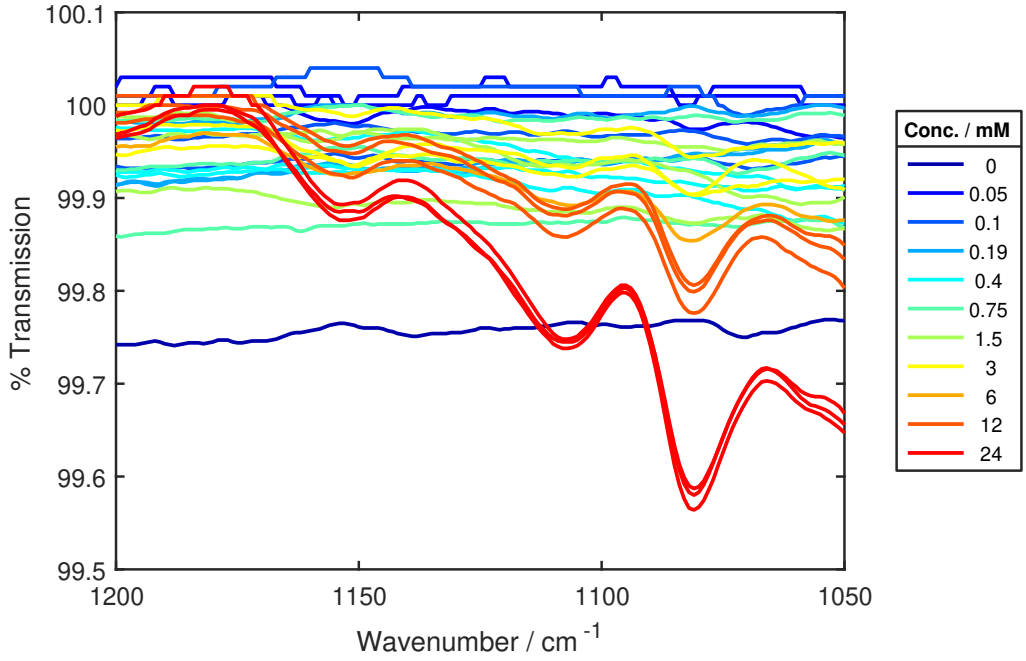


***(a)*** *The unmodified ATR-FTIR ratio spectrum of glucose in perfusion fluid. For clarity, only the 1200 – 1050 $cm^{-1}$ region of the spectrum is shown.*

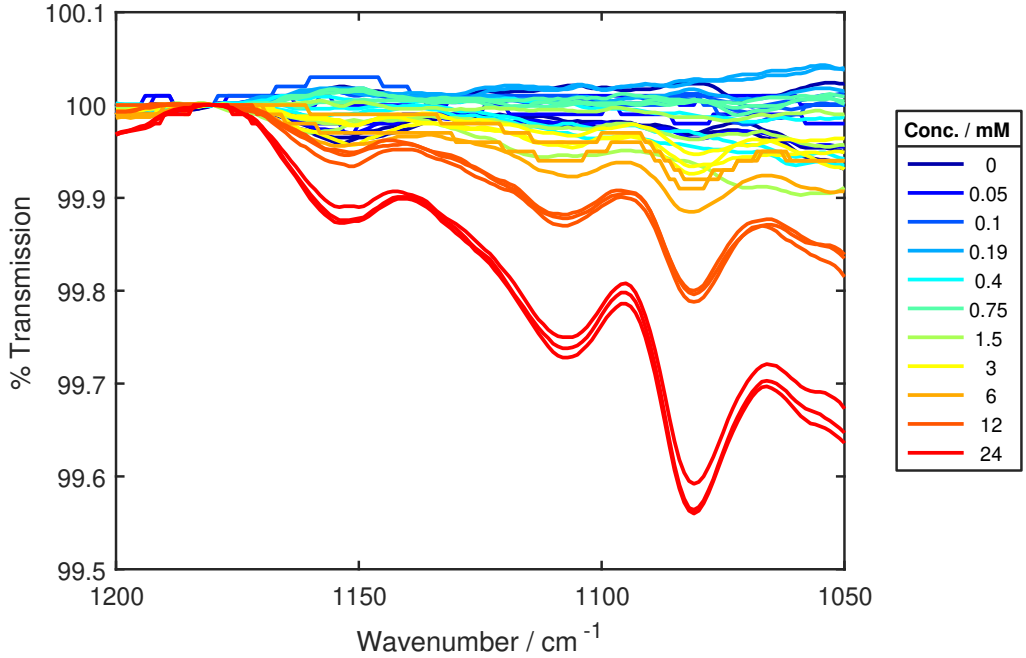


***(b)*** *The ATR-FTIR ratio spectrum of glucose in perfusion fluid, normalised to 1180 $cm^{-1}$. For clarity, only the 1200 – 1050 $cm^{-1}$ region of the spectrum is shown.*

***Figure 6.18:*** *An illustration of spectrum normalisation on the ATR-FTIR ratio spectra of glucose at various concentrations, acquired using a single-reflection diamond ATR crystal. In the unmodified spectrum (Figure 6.18(a)) the absolute peak intensity at 1081 $cm^{-1}$ does not correlate well with the glucose concentration. After normalisation to the isosbestic point at 1180 $cm^{-1}$ (Figure 6.18(b)), the absolute peak intensity at 1081 $cm^{-1}$ increases with increasing glucose concentration.*

The peaks used in this study were selected from those identified in Section 6.1 as being unique to each compound when combined in a mixture of glucose, lactate and pruvate. The two strongest unique peaks of each compound were chosen, whilst isosbestic points were determined from an examination of the spectra of each compound. The same isosbestic point was used in the calculation of the relative intensity of both glucose absorption peaks, as was the case for lactate. However, a single isosbestic point which yielded satisfactory measurements of the relative intensity of both pyruvate absorption peaks could not be found and so different isosbestic points were used for each peak. The spectral positions used to calculate the relative intensities of each peak are summarised in Table 6.5.

***Table 6.5:*** *The spectral peak positions of glucose, lactate and pyruvate selected for calculation of relative peak intensity.*

| **Analyte** | **Position of Peak Maximum / cm$^{-1}$** | **Position of Isosbestic Point / cm$^{-1}$** |
|---|---|---|
| Glucose | 1081 | 1180 |
| | 993 | 1180 |
| Lactate | 1456 | 1280 |
| | 1316 | 1280 |
| Pyruvate | 1357 | 1340 |
| | 1176 | 1200 |

An analysis of relative peak intensity with changing concentration is shown in Figure 6.19. This analysis was performed on ATR-FTIR spectra of glucose, acquired using the single-reflection diamond ATR crystal, and is focused on the absorption peak at 1081 cm$^{-1}$. The relationship between relative peak intensity and concentration was assumed to be linear and therefore a line of best fit is superimposed on the data. For this reason, data from the spectra containing only perfusion fluid (a glucose concentration of zero) was omitted from the analysis as it would not have fitted a linear regime. The data for each peak, acquired using each ATR-FTIR crystal, were treated separately and all datasets were analysed in the same way.

Two parameters derived from this analysis were used to assess crystal performance: the gradient of the line of best fit, which indicates the degree of response of the mean relative peak intensity to an increase in concentration, and the coefficient of determination ($R^2$) which quantifies the linearity of the relationship. The values of these parameters, calculated for all datasets, are summarised at the end of this section in Table 6.6.

A one-way ANOVA test was performed on each dataset to determine whether any of the mean values of the relative peak intensity were statistically significantly different from one another. The results of the test confirmed that all datasets contained at least two mean values of the relative peak intensity which were statistically significantly

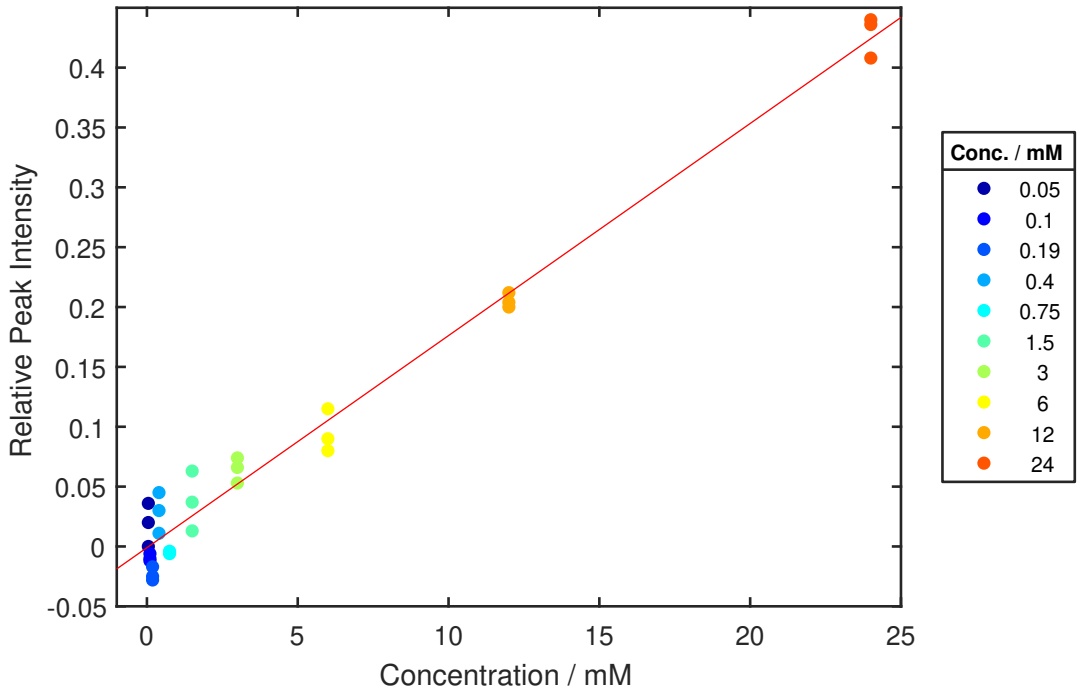


***Figure 6.19:*** *A plot showing the relationship between glucose concentration and the relative intensity of the glucose absorption peak at 1081 $cm^{-1}$ in ATR-FTIR spectra acquired using a single-reflection diamond crystal. The results of each repeat are shown here. Gradient = 0.018, $R^2$ = 0.978.*

different. A *post-hoc* multiple comparison test was subsequently performed in order to identify which of the mean values of the relative peak intensity within a dataset were statistically significantly different from one another. The test compared the mean relative peak intensity at a given concentration with those at all other concentrations. This process was repeated for each concentration and hence the mean relative peak intensities at all concentrations were systematically compared with one another. The resulting interactive graphical output was used to determine which concentrations could be detected and differentiated from other concentrations and hence provided a measure of the LoQ, for the range of concentrations investigated, for each peak and each crystal. An example of this is shown in Figure 6.20, which compares the mean relative peak intensities of the 1081 $cm^{-1}$ peak of glucose, acquired using the single-reflection diamond crystal, at 12 mM and 6 mM. In this example, the mean relative peak intensity at 12 mM is statistically significantly different to those at all other concentrations, but the mean relative peak intensity at 6 mM is not. The LoQ of glucose, as detected using a single-reflection diamond ATR crystal combined with an analysis of peak intensities, is therefore between 6 mM and 12 mM. The results of the *post-hoc* multiple comparison test performed on each dataset are given at the end of this section in Table 6.6.

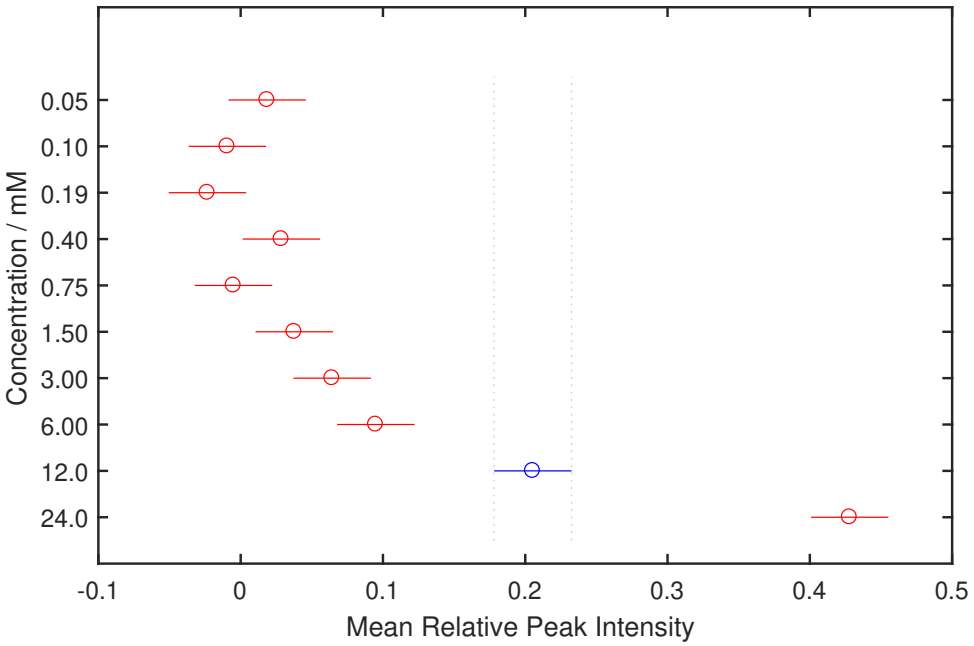


***(a)*** *The mean relative peak intensity at 12 mM (highlighted in blue) is statistically significantly different to those at all other concentrations (highlighted in red).*

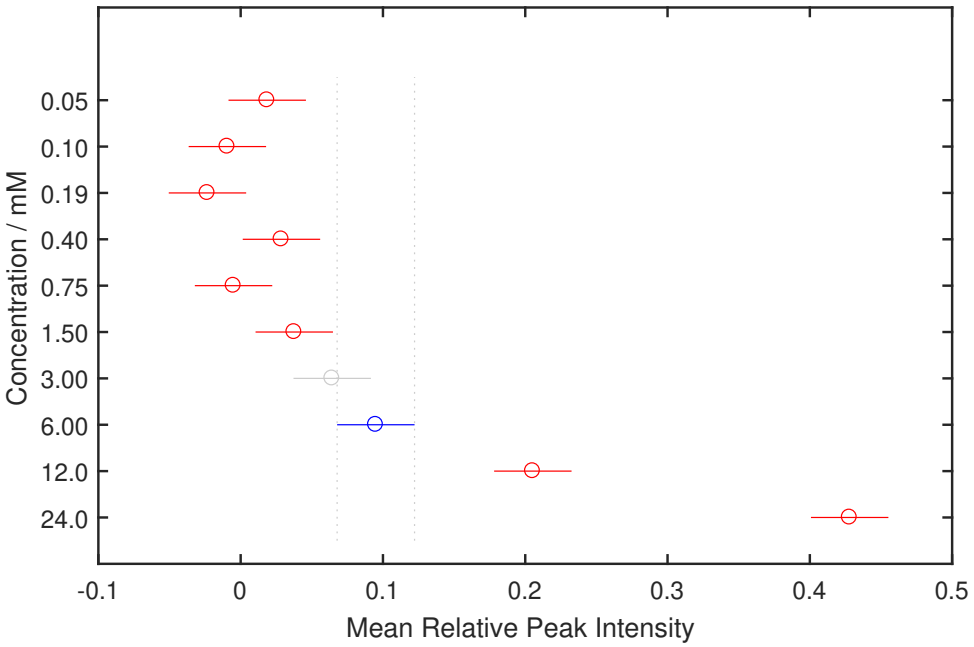


***(b)*** *The mean relative peak intensity at 6 mM (highlighted in blue) is statistically significantly different to those concentrations highlighted in red. However, it is not statistically significantly different to that at 3 mM, as indicated by the grey marker.*

***Figure 6.20:*** *The output of the multiple comparison test performed on the relative peak intensity vs. concentration data of the 1081 $cm^{-1}$ peak of glucose, acquired using the single-reflection diamond crystal. The selected concentration is highlighted in blue. Concentrations with mean relative peak intensities which are statistically significantly different from those of the selected concentration are highlighted in red. Those which are not statistically significantly different are shown in grey.*

The magnitude of the gradient of the line of best fit between the concentration of a compound and the relative intensity of a given peak indicates the strength of the relationship between the two variables: the greater the magnitude of the gradient, the greater the increase in peak intensity with increasing concentration. A high gradient is thus desirable for a sensor based on FTIR spectroscopy. This value was highest for spectra acquired using the seven-reflection ZnSe, for every peak and compound analysed. The highest gradient (0.093) was observed for the line of best fit between the concentration of glucose and the relative intensity of the glucose absorption peak at 1081 $cm^{-1}$. This data is shown in Figure 6.21.

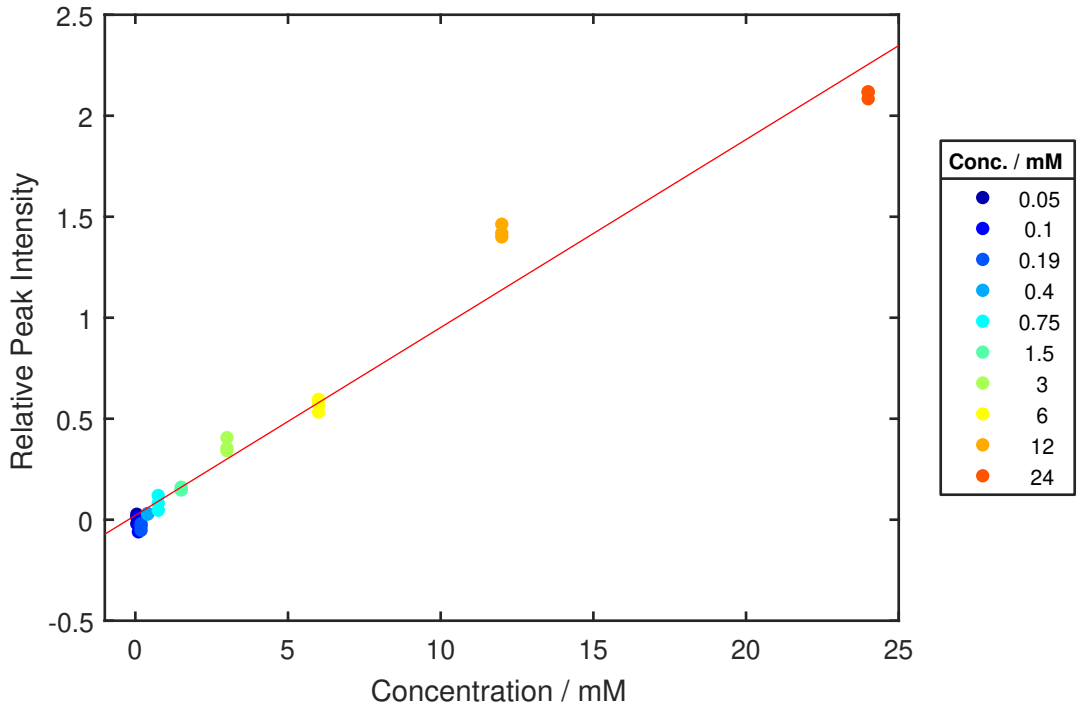


***Figure 6.21:*** *A plot showing the relationship between glucose concentration and the relative intensity of the glucose absorption peak at 1081 $cm^{-1}$ in ATR-FTIR spectra acquired using a seven-reflection ZnSe crystal. The results of each repeat are shown here. The gradient of the line of best fit is 0.093, the highest seen for any of the peaks or crystals studied.*

The $R^2$ value is a measure of the linearity of the relationship between peak height and relative peak intensity. It can range from $0 - 1$, with values close to one indicating a highly linear relationship. A linear relationship is highly desirable for a FTIR-based sensor as it renders the prediction of glucose, lactate and pyruvate concentrations more straightforward. This value was consistently lower for spectra acquired using the seven-reflection Ge crystal than for spectra acquired using the single-reflection diamond crystal or the ZnSe crystal. The diamond and ZnSe crystals exhibited comparable $R^2$ values for all peaks and compounds studied. The highest $R^2$ value (0.995) was observed for the relationship between the intensity of the 1357 $cm^{-1}$ absorption

peak of pyruvate, as calculated from spectra obtained using the seven-reflection ZnSe crystal, and the concentration of pyruvate. This relationship is shown in Figure 6.22.

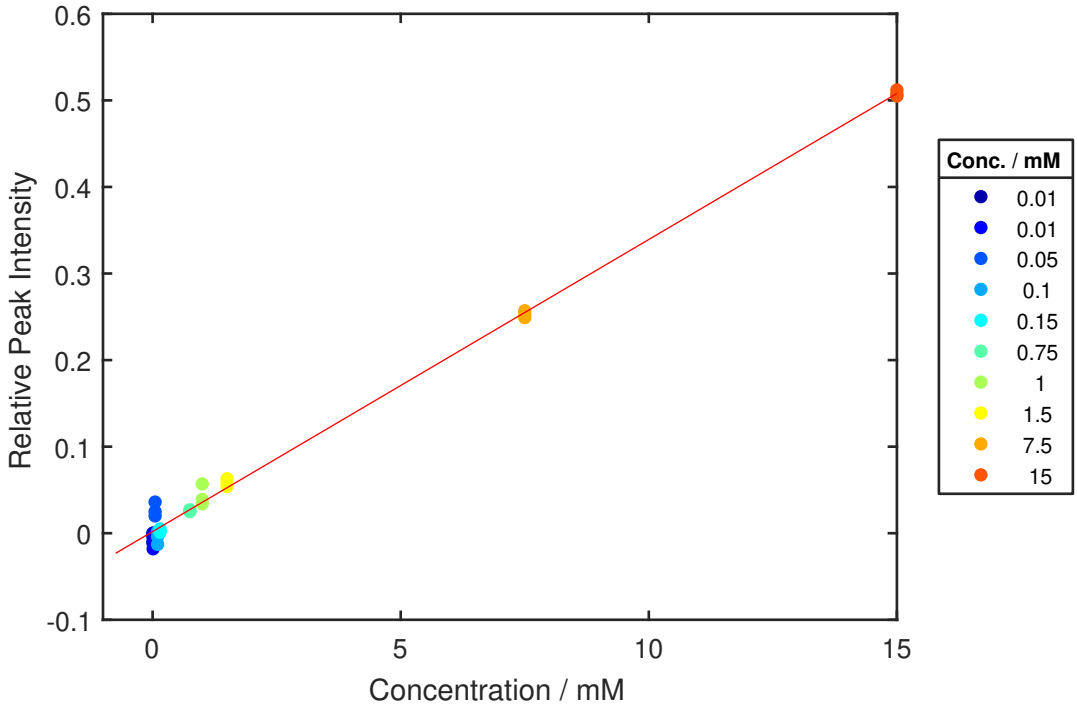


***Figure 6.22:*** *A plot showing the relationship between pyruvate concentration and the relative intensity of the pyruvate absorption peak at 1357 $cm^{-1}$ in ATR-FTIR spectra acquired using a seven-reflection ZnSe crystal. The results of each repeat are shown here. The gradient of the line of best fit is 0.034 and the $R^2$ value is 0.995, the highest seen for any of the peaks or crystals studied.*

The seven-reflection ZnSe crystal gave the lowest LoQ of glucose and lactate, at all analysed peak positions, and equalled the LoQ of pyruvate achieved by the other two crystals. A low limit of quantitation, within the expected clinical concentration range of glucose, lactate and pyruvate, is a necessary reqirement of the developed sensor. The lowest calculated LoQ (0.75–1.5 mM) was obtained for lactate, using an analysis of the 1316 $cm^{-1}$ absorption peak of spectra acquired using the seven-reflection ZnSe crystal. The results of the multiple comparison test carried out on these spectra are shown in Figure 6.23.

Overall, it was concluded that the seven-reflection ZnSe crystal was the best-performing ATR-FTIR crystal of those tested and would be used for a future analysis of the performance of ATR-FTIR spectroscopy. This superior performance was explained by the fact that it was the crystal with the longest effective path length: it allowed a greater number of reflections of the IR beam than the diamond crystal (seven reflections *vs.* one reflection, respectively) and, for a given IR wavelength, exhibited a greater penetration depth than the seven-reflection germanium crystal.[122] A longer

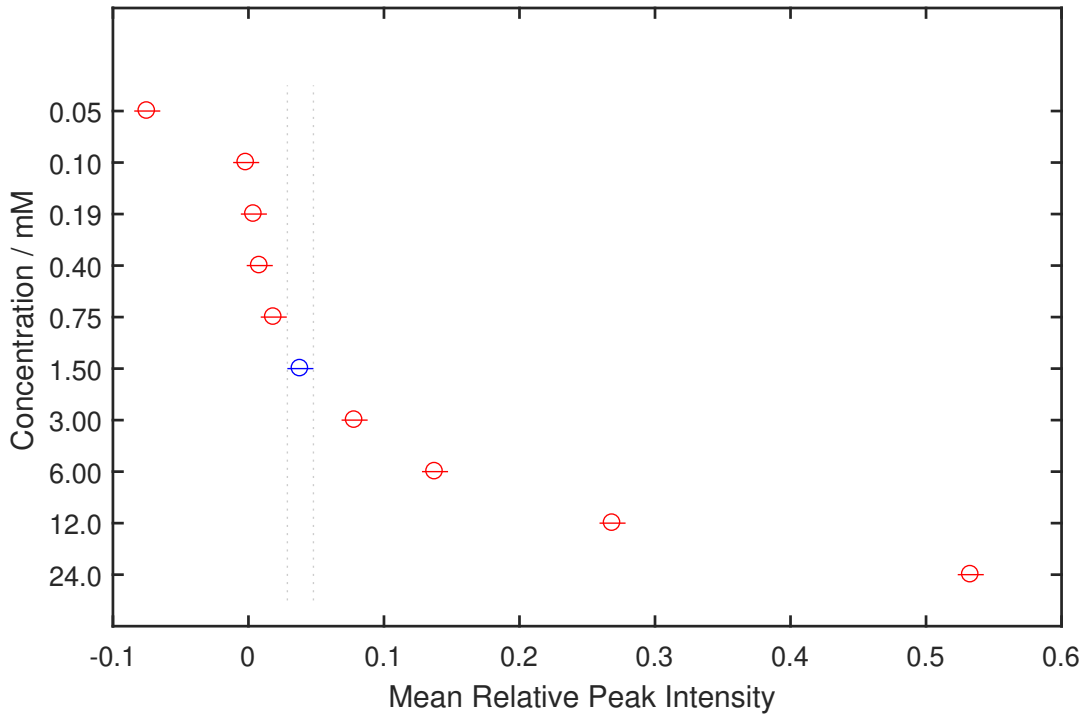


***Figure 6.23:*** *The output of the multiple comparison test performed on the relative peak intensity vs. concentration data of the 1316 $cm^{-1}$ peak of lactate, acquired using a seven-reflection ZnSe crystal. The mean relative peak intensity at 1.5 mM (highlighted in blue) is statistically significantly different from those of all other concentrations analysed, as indicated by the data points highlighted in red, showing that the LoQ of lactate using this system is below 1.5 mM. This was the lowest LoQ observed for any of the peaks or crystals studied.*

effective path length allows for increased interaction of the IR beam with the sample and hence a higher absorption of IR radiation, leading to more intense peaks in the ATR-FTIR spectrum. With this in mind, the poor performance of the seven-reflection Ge crystal in comparison with the single-reflection diamond crystal is surprising. It is possible that the performance of the Ge crystal was negatively affected by its physical condition, as its surface was observed to be significantly more scratched than that of the other crystals.

***Table 6.6:*** *The summarised results of the ATR-FTIR crystal study. The following properties of each data set are given: the gradient of the line of best fit from a plot of concentration vs. relative peak intensity; the $R^2$ value of the linear relationship between concentration and relative peak intensity; and the LoQ within the range of analysed concentrations.*

| Parameter | Crystal | Glucose | | Lactate | | Pyruvate | |
|---|---|---|---|---|---|---|---|
| | | **1081** | **993** | **1456** | **1316** | **1357** | **1176** |
| Gradient | Diamond 1R | 0.018 | 0.007 | 0.004 | 0.003 | 0.007 | 0.011 |
| | Germanium 7R | 0.027 | 0.004 | 0.004 | 0.005 | 0.008 | 0.016 |
| | ZnSe 7R | 0.093 | 0.036 | 0.020 | 0.023 | 0.034 | 0.072 |
| $R^2$ | Diamond 1R | 0.978 | 0.833 | 0.769 | 0.985 | 0.972 | 0.993 |
| | Germanium 7R | 0.860 | 0.017 | 0.503 | 0.943 | 0.959 | 0.976 |
| | ZnSe 7R | 0.973 | 0.939 | 0.771 | 0.980 | 0.995 | 0.971 |
| LoQ / mM | Diamond 1R | 6–12 | 12–24 | 12–24 | 6–12 | 1.5–7.5 | 1.5–7.5 |
| | Germanium 7R | 12–24 | >24 | >24 | 12–24 | 1.5–7.5 | 1.5–7.5 |
| | ZnSe 7R | 1.5–3 | 6–12 | 6–12 | 0.75–1.5 | 1.5–7.5 | 1.5–7.5 |

### 6.4.2 Path Length Selection for Transmission-FTIR

All of the transmission cells used in this work were fitted with ZnSe windows. This material was chosen based upon four properties: broad IR transmission range (20,000 – 454 $cm^{-1}$), lack of IR absorption bands within the mid-IR spectral region, chemical inertness and insolubility in water.[123]

An optimum path length for use in a future transmission-FTIR study was selected by carrying out an identical series of transmission-FTIR measurements using each path length and analysing the peak intensities of the resulting spectra to estimate the limit of detection of glucose afforded by each one. The path lengths available for comparison were 25 $\mu$m, 50 $\mu$m and 100 $\mu$m. These accessories were acquired on a short-term loan from the manufacturer, Specac, and thus time limitations restricted the number of compounds and sample concentrations that could be tested.

Glucose was selected as a test analyte as its IR absorbance peaks are more thoroughly characterised in the literature than those of lactate and pyruvate. Pure solutions of glucose in perfusion fluid were prepared at five concentrations, which were selected to cover the full clinical range that the final device will be required to detect: 0.1 mM, 0.4 mM, 1.5 mM, 6 mM and 24 mM.

The transmission-FTIR spectra of glucose at all analysed concentrations, acquired using a path length of 100 $\mu$m, are shown in Figure 6.24. These spectra exhibit relatively flat baselines but are vertically offset with respect to one another, as was the case with the spectra gathered using ATR-FTIR, and therefore relative peak intensites were once again calculated and compared for each spectrum.

The glucose absorption peaks at 1081 $cm^{-1}$ and 993 $cm^{-1}$, which were analysed

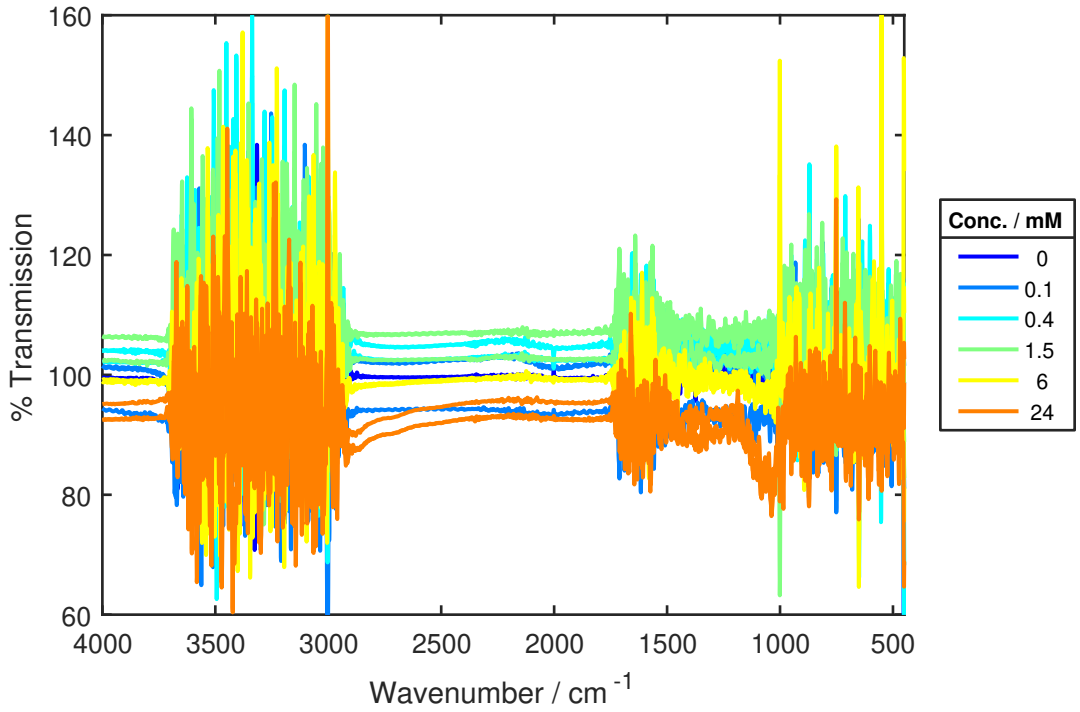


***Figure 6.24:*** *The transmission-FTIR spectra of glucose in perfusion fluid, at a range of concentrations, acquired using a path length of 100 µm. Spectra have flat baselines but are vertically offset with respect to one another.*

for the ATR-FTIR crystal study, were once again selected for analysis in this study. The isosbestic point at 1180 $cm^{-1}$, which was used in the ATR-FTIR crystal study to calculate the relative intensities of each peak, was also found to be effective when calculating the relative intensities of the peaks in the transmission-FTIR spectrum and was therefore used in this study.

The methodology used to compare the performace of each transmission-FTIR path length was the same as that used to compare the performance of ATR-FTIR crystals and thus the details of the analysis will not be repeated here. The results of the analysis are presented in Table 6.7.

***Table 6.7:*** *A summary of the results of the study conducted to analyse the performance of different path lengths of a transmission-FTIR cell with ZnSe windows.*

| **Path Length / µm** | **Peak / $cm^{-1}$** | **Gradient** | **$R^2$** | **LoQ / mM** |
|---|---|---|---|---|
| 25 | 1081 | 0.201 | 0.993 | 1.5–6 |
| | 993 | 0.072 | 0.967 | 6–24 |
| 50 | 1081 | 0.402 | 0.999 | 0.4–1.5 |
| | 993 | 0.101 | 0.854 | 6–24 |
| 100 | 1081 | 0.471 | 0.893 | 6–24 |
| | 993 | 0.148 | 0.434 | >24 |

The effect of increasing concentration on the increase in mean relative peak intensity, as measured by the gradient of the line of best fit through a plot of concentration *vs.* mean relative peak intensity, is proportional to the path length used. This result is expected, as an increased path length allows greater interaction of the IR beam with the sample and thus the absorption of radiation will be more strongly affected by the amount of analyte molecules present. However, the linearity of this relationship, as measured by the $R^2$ value, and the LoQ do not follow this pattern. The $R^2$ values do not have a clear relationship with the path length. This is due to the fact that the water-induced noise increases with longer path lengths. As the level of noise increases the degree of saturation of the detector of the instrument also increases, causing a reduction in the size of the region of the spectrum unaffected by noise. This was observed when comparing the spectra of a 24 mM solution of glucose in perfusion fluid, acquired using all three tested path lengths, as seen in Figure 6.25. In regions of the spectrum which are close to saturation, the relationship between peak intensity and concentration becomes non-linear, as observed in these results.

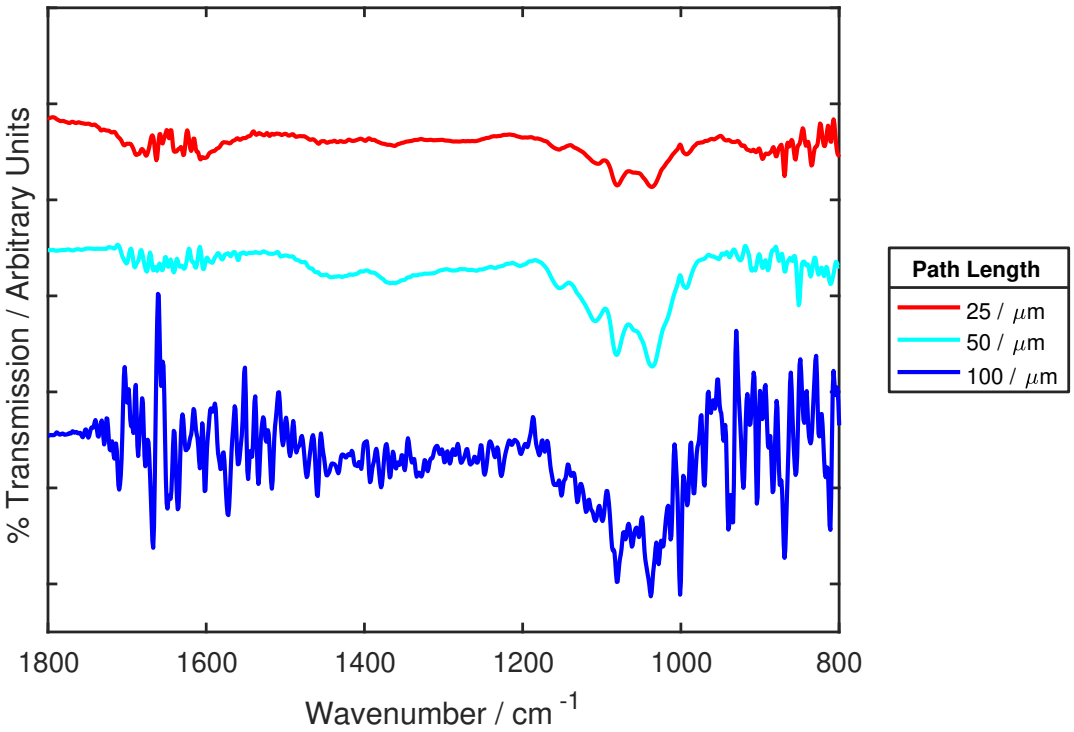


***Figure 6.25:*** *The transmission-FTIR spectra of a 24 mM solution of glucose in perfusion fluid, acquired using different path lengths. For clarity, each spectrum has been plotted with a vertical offset with respect to the other spectra. When the shorter path length (25 μm) is used, the 1600 – 900 $cm^{-1}$ region of the spectrum, where the majority of glucose absorption peaks are located, is free from water-induced noise. However, when the longest path length (100 μm) is used, water-induced noise is visible in the 1600 – 900 $cm^{-1}$ region of the spectrum.*

According to the data presented in Table 6.7, the balance between these com-

peting factors is optimised at a path length of 50 $\mu$m, which yields the lowest limits of detection. This path length was therefore selected for use in a later study of transmission-FTIR spectroscopy. A plot showing the relationship between relative peak intensity and glucose concentration for transmission-FTIR spectra acquired using this path length, as measured for the 1081 $cm^{-1}$ absorption peak of glucose, is shown in Figure 6.26. The output of the multiple comparison plot carried out on the same dataset is shown in Figure 6.27. This plot highlights the fact that the LoQ of glucose using this system is below 1.5 mM, the lowest achieved by any of the tested path lengths.

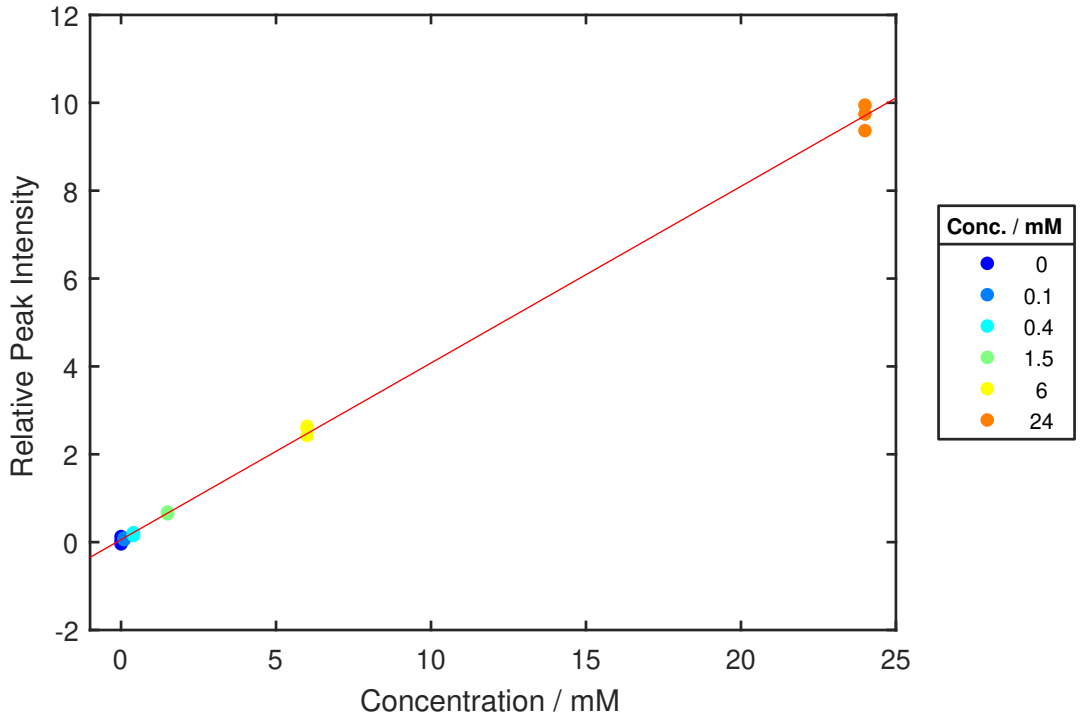


***Figure 6.26:*** *A plot showing the relationship between glucose concentration and the relative intensity of the glucose absorption peak at 1081 $cm^{-1}$ in transmission-FTIR spectra acquired using a 50 $\mu$m path length. The results of each repeat are shown here. Gradient = 0.402, $R^2$ = 0.999.*

### 6.4.3 FTIR Spectroscopy Accessory Selection: Conclusions

The aim of the work described in this section was to select an ATR-FTIR crystal, to use in a future study of ATR-FTIR spectroscopy, and a path length to use in a future study of transmission-FTIR spectroscopy. A methodology allowing quantitative analysis of the performance of a selection of ATR-FTIR crystals and a selection of transmission-FTIR path lengths, based on an analysis of relative peak intensities, has been presented. The results of this analysis indicated that a seven-reflection ZnSe

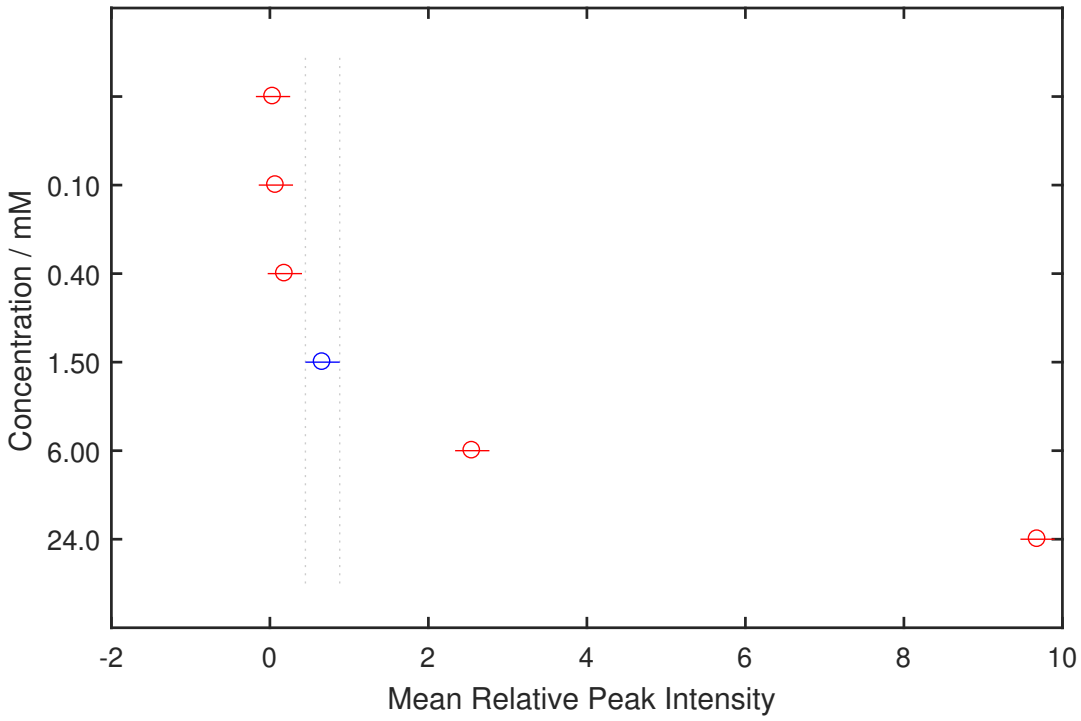


***Figure 6.27:*** *The output of the multiple comparison test performed on the relative peak intensity vs. concentration data of the 1081 $cm^{-1}$ peak of glucose, acquired using a 50 $\mu m$ path length. The mean relative peak intensity at 1.5 mM (highlighted in blue) is statistically significantly different from those of all other concentrations analysed, as indicated by the data points highlighted in red, showing that the LoQ of glucose using this system is below 1.5 mM.*

ATR-FTIR crystal should be used for the study of ATR-FTIR spectroscopy and a 50 $\mu$m path length should be used for the study of transmission-FTIR spectroscopy.

The results achieved using ATR-FTIR spectroscopy cannot be directly compared to those obtained using transmission-FTIR spectroscopy. This is due to the fact that the two studies were carried out using a different series of glucose concentrations, which has a significant impact on the *post-hoc* multiple comparison test used to calculate the LoQ. However, it is noted that none of the ATR-FTIR or transmission-FTIR accessories tested were able to achieve a LoQ close to that required for the developed sensor.

## 6.5 Conclusions

This chapter describes an analysis of the performance of two forms of FTIR spectroscopy, ATR-FTIR and transmission-FTIR, for the detection of glucose, lactate and pyruvate in solution. All data were considered within the context of the requirements of a sensor for the metabolic profiling of TBI patients, in order to assess the suitability of FTIR for use in such a sensor.

The results presented here suggested that both ATR-FTIR and transmission-FTIR spectroscopy showed promise for use in the metabolic profiling of TBI patients. Both techniques yielded spectra which allowed absorption peaks unique to glucose, lactate or pyruvate to be identified from an equimolar mixture of all three compounds. Some of these peaks remained visible when the two techniques were used to analyse an equimolar mixture containing all three compounds in combination with glycerol and glutamate, two competing molecules which are likely to be present in clinical microdialysate samples.

Encouragingly, specific absorption peaks of glucose and lactate were shown to be identifiable from transmission-FTIR spectra of clinical microdialysate samples.

Several outstanding questions remained following this work. The limits of performance of ATR-FTIR spectroscopy and transmission-FTIR spectroscopy were unknown: in particular, the accuracy with which each technique could be used to determine the concentrations of pyruvate, lactate and glucose when combined in a mixture was not known. In a typical clinical microdialysate sample, the concentration of pyruvate is ten-fold lower than those of glucose and lactate: the effect of this difference on the accuracy with which the levels of each compound could be determined from an FTIR spectrum of the sample was also unknown.

The optimum method for determining the concentrations of glucose, lactate and pyruvate from their FTIR spectra was an additional unknown. Some of the results presented in this chapter had suggested that an analysis based on the calculation of peak intensities would not yield a sufficiently low limit of detection, but no alternative methods had been investigated.

Finally, it was not clear which of the two techniques would be most suitable for development into a sensor for metabolic profiling of TBI patients. Although differences between the two techniques had been observed, the degree to which they would affect the detection of glucose, lactate and pyruvate was unknown.

It was therefore concluded that a more detailed study of each technique was required in order to address the questions presented here. Two quantitative studies were therefore carried out: one to determine the most suitable ATR-FTIR crystal to be used in a study of ATR-FTIR spectroscopy and another to determine the most suitable path length to use for a study of transmission-FTIR spectroscopy. These studies concluded that a seven-reflection ZnSe crystal should be used for a study of ATR-FTIR spectroscopy and a 50 $\mu$m path length should be used for a study of transmission-FTIR spectroscopy.

# Chapter 7

# Assessment of a Raman Spectroscopy-Based Sensor

This chapter describes the work undertaken to assess whether Raman spectroscopy could be used to detect glucose, lactate and pyruvate in microdialysate samples from TBI patients, within the constraints of the device requirements set out in Section 2.6. Raman spectroscopy was selected for investigation due to its insensitivity to water, which would be of significant benefit in the analysis of microdialysate samples as they are highly dilute. Furthermore, Raman spectroscopy has previously been used in clinical applications, as discussed in Section 4.3, and has potential for miniaturisation into a bedside device.

Attempts were initally made to acquire the Raman spectra of pure solutions of glucose in perfusion fluid. Following this attempt, a SERS-based system for the on-line detection of glucose, lactate and pyruvate in perfusion fluid was proposed. The viability of the proposed system was subsequently assessed using cysteine as a model analyte.

## 7.1 Raman Spectroscopy of Glucose

It was assumed that the acquisition of Raman spectra of glucose, lactate or pyruvate would be non-trivial as they are small molecules with low polarisibility and thus exhibit a low Raman-scattering intensity. Glucose was considered to be the most polarisible of these compounds, due to the increased electron density caused by its ring structure, and was thus expected to exhibit the strongest Raman-scattering intensity. Initial work therefore focused on the acquisition of a Raman spectrum of glucose.

A concentrated 1M solution of glucose in perfusion fluid was initially analysed, to account for the low Raman-scattering intensity of glucose. Spectral acquisition was focused on the 750 – 1450 $cm^{-1}$ range, which contains three peaks that are considered to be the 'Raman fingerprints' of glucose.[124] These peaks are found at approximately

910 $cm^{-1}$, 1060 $cm^{-1}$ and 1125 $cm^{-1}$ and are attributed to C–C and C–O vibrations within the molecule. A 785 nm laser was used to acquire the spectrum in order to minimise the effect of photoluminescence. The resulting Raman spectrum and associated peak assignments are shown in Figure 7.1.

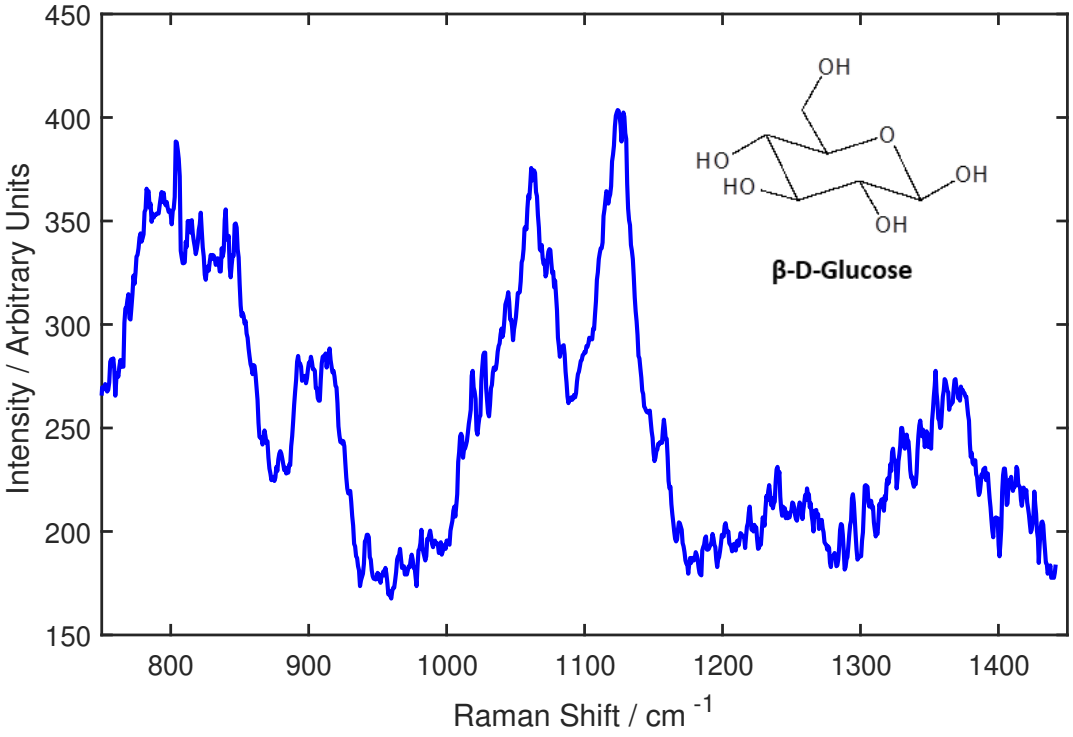


| Raman Shift / $cm^{-1}$ | Peak Intensity | Assignment |
|---|---|---|
| 796 | Medium | C–C (Alicyclic) Vibration |
| 844 | Medium | C–C (Alicyclic) Vibration/C–O–C Stretch |
| 897 | Medium | C–C (Alicyclic) Vibration/C–O–C Stretch |
| 913 | Medium | C–C (Alicyclic) Vibration/C–O–C Stretch |
| 1061 | Strong | C–O Stretch |
| 1126 | Strong | C–C (Alicyclic) Vibration |
| 1240 | Weak | C–C (Alicyclic) Vibration |
| 1366 | Weak | C-O-H Bend/$CH_2$ Bend |

***Figure 7.1:*** *The Raman spectrum and associated peak assignments of a 1M solution of glucose in perfusion fluid mounted in the macro sampler. Characteristic Raman peaks of glucose can be seen at 913 $cm^{-1}$, 1061 $cm^{-1}$ and 1125 $cm^{-1}$. Laser wavelength = 785 nm, power at sample = 100 mW, acquisition time = 1 × 600 s.*

The spectrum shown in Figure 7.1 shows the expected peaks at 913 $cm^{-1}$, 1061 $cm^{-1}$ and 1125 $cm^{-1}$, indicating that a Raman spectrum of glucose was successfully acquired. However, an acquisition time of 600 s was required in order to obtain the spectrum. This is significantly longer than the desired temporal resolution of a sensor for metabolic profiling of TBI patients, which will require a measurement to be taken

at least every five minutes (Section 2.6). A test was therefore carried out to determine whether the characteristic Raman peaks of glucose could be seen when an acquisition time appropriate to the device was used. Solutions of glucose in perfusion fluid at various concentrations were mounted in the macro sampler and Raman spectra were acquired using a 785 nm laser with a power at the sample of approximately 100 mW and an acquisition time of 120 seconds. This acquisition time was selected as it is comparable with the time taken to acquire the FTIR spectra discussed in Chapter 6. The resulting spectra are shown in Figure 7.2.

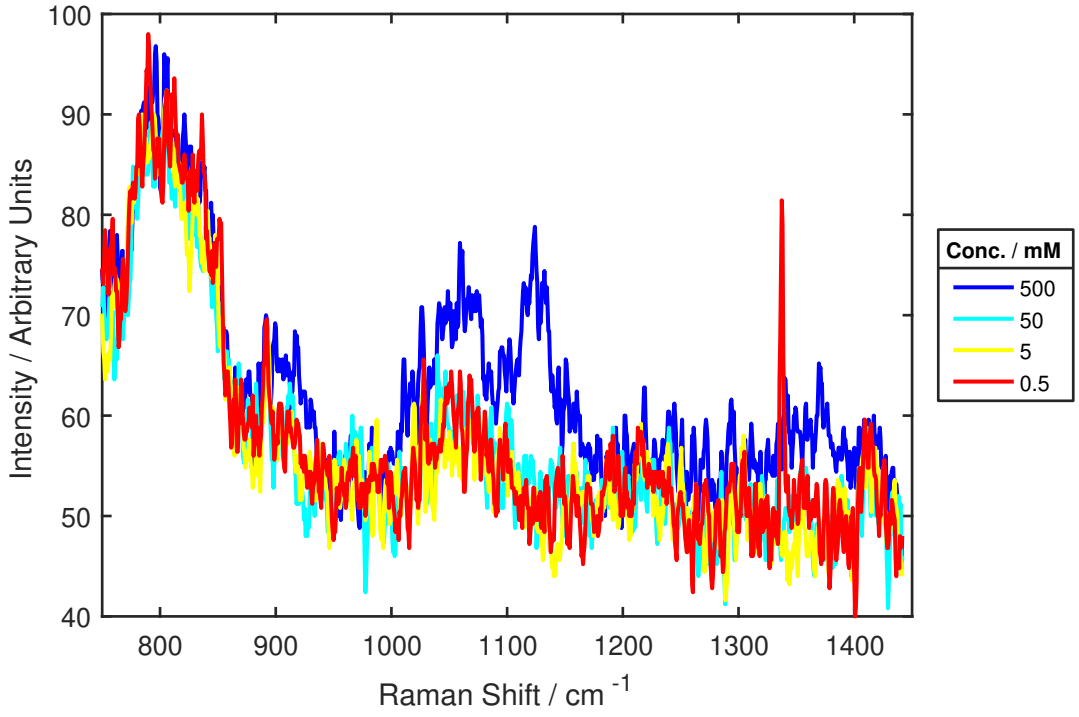


***Figure 7.2:*** *The Raman spectra of glucose in perfusion fluid at various concentrations, obtained using a single acquisition of 120 s. Characteristic glucose peaks at 913 $cm^{-1}$, 1061 $cm^{-1}$ and 1125 $cm^{-1}$ were observed when a glucose concentration of 500 mM was used, but could not be seen at lower concentrations. Samples were mounted in the macro sampler for measurement. Laser wavelength = 785 nm, power at sample = 100 mW.*

An acquisition time of 120 s yielded characteristic glucose peaks at 913 $cm^{-1}$, 1061 $cm^{-1}$ and 1125 $cm^{-1}$ in the Raman spectrum of 500 mM glucose. However, a qualitative analysis of the spectra shown in Figure 7.2 suggested that these peaks could not be detected in the Raman spectra of glucose at concentrations of 50 mM or lower. A peak at approximately 1060 $cm^{-1}$ is visible in the spectra of glucose at concentrations of 50 mM, 5 mM and 0.5 mM. However, this peak does not appear to vary in intensity as the glucose concentration is varied and therefore it was assumed not to be a 'true' Raman peak. These results suggested that, if an acquisition time of 120 s was used with the available Raman setup, the detection limit of glucose via

Raman spectroscopy was between 50 and 500 mM.

### 7.1.1 Raman Spectroscopy of Glucose: Conclusions

This section describes the successful acquisition of Raman spectra of glucose, as evidenced by the presence of characteristic Raman peaks of glucose at 913 $cm^{-1}$, 1061 $cm^{-1}$ and 1125 $cm^{-1}$. However, when using an acquisition time compatible with the requirements of a sensor for metabolic profiling of TBI patients, the detection limit of glucose using the available Raman spectroscopy setup was predicted to be between 50 and 500 mM. This is significantly higher than the maximum expected concentration of glucose in clinical microdialysate (24 mM). Furthermore, detection of lactate and pyruvate via Raman spectroscopy was expected to yield higher detection limits due to their lower polarisibility.

Raman scattering intensity is proportional to $\frac{1}{\lambda^4}$ and thus it may have been possible to obtain a stronger Raman signal using a light source of shorter wavelength. However, the use of such a light source may also have increased the intensity of the fluorescence visible in the Raman spectrum and therefore would not have provided sufficient improvement in the signal to allow the detection of clinically-relevant concentrations of glucose, lactate or pyruvate. It was therefore concluded that clinically-relevant concentrations of the compounds of interest would only be detected via Raman spectroscopy if surface-enhancement techniques were used. A decision was thus made to investigate the possibility of developing a SERS-based sensor for glucose, lactate and pyruvate.

## 7.2 Proposed SERS Sensor

When considering the possible designs of a SERS-based sensor for on-line monitoring of glucose, lactate and pyruvate in microdialysate samples from TBI patients, it was concluded that a fixed nanostructured surface would not be suitable as a SERS substrate. This was due to the fact that SERS substrates are typically not re-usable due to instability of the nanostructures. There were additional concerns that the nanostructures may prevent the complete removal of analyte molecules adsorbed on the substrate surface, resulting in a build up of analyte molecules over time and therefore a false reading of the analyte concentration. If a fixed SERS substrate was incorporated into a sensor, these factors would result in a need to regularly replace the SERS substrate. This process would be labour-intensive and would not be compatible with the requirement that the developed sensor be capable of continuous on-line operation, without the need for regular interference from clinical staff.

These concerns led to the proposal of an alternative SERS-based sensor design in which colloidal nanoparticles were used to provide surface enhancement. Colloids

composed of aggragated nanoparticles have highly nanostructured surfaces and their use as SERS substrates has previously been reported.[125,126] The proposed sensor design involved a setup in which microdialysate from the patient was combined with a solution of silver colloids prior to entering the sensing chip, to allow time for the analyte molecules to adsorb on the colloid surface. Upon entering the sensing chip, analyte molecules adsorbed on silver colloids would be detected via SERS. The colloid-analyte complexes would then be flushed from the chip and disposed of, allowing new silver colloids to enter the system and effectively regenerate the SERS substrate. This concept is summarised in Figure 7.3.

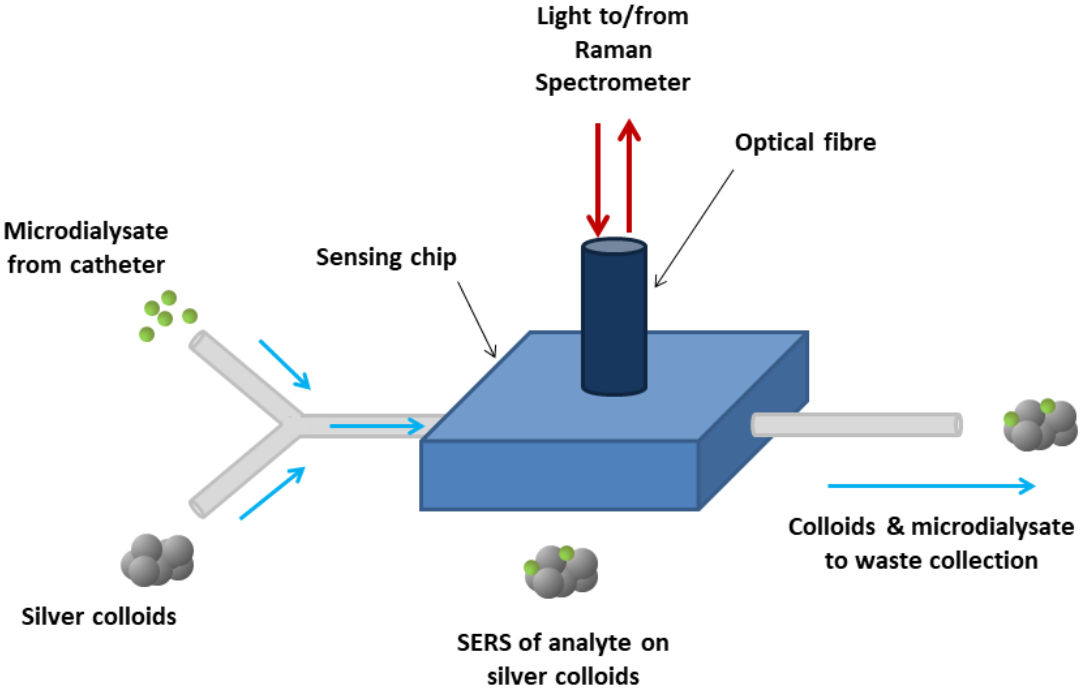


***Figure 7.3:*** *A diagram showing the set up of the proposed SERS sensor. Microdialysate from the catheter is mixed with fresh silver colloids prior to entering the sensing chip. Analyte molecules adsorb on the surface of the colloids and are detected via SERS. Colloid particles with adsorbed analyte are then flushed from the sensing chip and disposed of.*

It was decided that silver colloids would be used for an initial investigation of the viability of this sensing approach, due to the high enhancement factor provided by silver nanoparticles and the ease with which they can be synthesised.[127]

### 7.2.1 Synthesis of Silver Nanoparticles

Silver nanoparticles for aggregation were synthesised using a method based on the reduction of $AgNO_3$ by sodium citrate.[128] Briefly, 50 mL of an aqueous solution of 1 mM $AgNO_3$ was heated to 90 °C, with constant stirring, and a 0.1 mL aliquot of aqueous 1% sodium citrate was added. The temperature of the resulting mixture was

maintained at 90 °C whilst a further three aliquots of 0.3 mL of aqueous 1% sodium citrate solution were added at 15 minute intervals. When all of the sodium citrate had been added, the temperature of the resulting solution was maintained at 90 °C for a further 30 minutes, after which it was cooled to room temperature. The silver nanoparticles were protected from light and stored at 4°C.

## 7.3 Testing SERS Sensor Viability: Cysteine Study

The detection of glucose, lactate and pyruvate via SERS was predicted to be non-trivial due to the low Raman-scattering intensities exhibited by these compounds. As the proposed SERS sensor was an unfamiliar system, it was decided that it would be advantageous to assess the viability of the system first using a model analyte so that any problems with the setup could be unambigously identified. It was felt that if glucose, lactate or pyruvate were used to characterise the system, it would be unclear whether any difficulties in spectrum acquisition were due to problems with the setup or due to the inherent low Raman-scattering intensity of the analyte.

It was concluded that the model analyte should exhibit comparable properties to glucose, lactate and pyruvate to ensure that the results of the viability study were relevant. L-cysteine, a naturally-occurring amino acid, was selected as a suitable candidate because it has a similar molecular structure to glucose, lactate and pyruvate. Its molecular weight is 121.15 g $mol^{-1}$, compared to molecular weights of 180.06 g $mol^{-1}$, 89.07 g $mol^{-1}$ and 87.06 g $mol^{-1}$ for glucose, lactate and pyruvate, respectively, and it possesses a simple non-aromatic structure, suggesting that it would exhibit similar Raman-scattering properties. However, cysteine contains a thiol functional group and was therefore expected to form a bond with a silver substrate, which would allow chemical enhancement of its Raman signal and thus make it easier to detect via SERS than glucose, lactate or pyruvate.

This study was conducted in two phases. Initially, the Raman spectra of the solid and aqueous phases of cysteine were characterised. The SERS behaviour of aqueous cysteine on silver was then analysed using a fixed SERS substrate comprised of a glass surface coated with a dense layer of silver nanoparticles. Finally, SERS of aqueous cysteine was attempted using silver colloids as a SERS substrate. All spectra were acquired using a 785 nm laser due to the lower background fluorescence observed at longer laser wavelengths.

### 7.3.1 Raman Spectroscopy of Solid Cysteine

The Raman spectrum of solid cysteine crystals, mounted on a standard 76 mm × 25 mm × 1.2 mm glass slide, was acquired using a 785 nm laser, a power at the sample of approximately 0.45 mW and an acquisition time of 300 s. The resulting spectrum is

shown in Figure 7.4. A low laser power was used in the acquisition of this spectrum in order to minimise laser-induced damage to the sample. The 200 – 1600 $cm^{-1}$ region of the spectrum is displayed, as this is where the majority of the Raman peaks of solid cysteine are located.

The Raman spectrum of cysteine is well-characterised in the literature, allowing the peaks in the acquired spectrum to be compared with literature values.[129–131] The acquired spectrum was found to correlate with these literature values and the observed peaks were assigned to specific vibrational modes of each functional group, based on the results of a comprehensive study of the Raman spectrum of solid cysteine, as seen in Figure 7.4.[131]

A broad bump in the spectrum baseline, centred at a Raman shift of approximately 1400 $cm^{-1}$, is observed in the acquired spectrum. This feature was observed in all Raman spectra of solid cysteine and is thought to indicate thermally-induced molecular damage that has resulted in the breaking of C–C bonds.

### 7.3.2 Raman Spectroscopy of Aqueous Cysteine

Raman spectroscopy of aqueous cysteine was predicted to be challenging due to the low polarisability and consequent low Raman-scattering intensity of the molecule. A concentrated 1M solution of L-cysteine in DI water was therefore analysed. The sample was mounted in the macro sampler and a weak spectrum of aqueous cysteine was successfully acquired using a total acquisition time of 1500 s, comprised of three acquisitions of 500 s each, and a power at the sample of 100 mW. The spectrum and associated peak assignments are shown in Figure 7.5.

The Raman spectrum of aqueous cysteine was studied in the same spectral region as that investigated for solid cysteine to allow the spectra of the two phases to be compared. However, the acquired spectrum of aqueous cysteine displayed a low signal:noise ratio and Raman peaks were observed only in the region 550–1500 $cm^{-1}$. The spectrum displayed in Figure 7.5 has been limited to this region to allow the peaks to be visualised. Observed peaks in this region are consistent with previous studies reporting Raman spectroscopy of aqueous cysteine.[130,132]

The Raman spectrum of aqueous cysteine retains approximately 30% of the peaks observed in the Raman spectrum of the solid. The resolution of the aqueous-phase spectrum also appears to be lower than that of the solid-phase spectrum. This is evidenced by a broad peak with a Raman shift of 782 $cm^{-1}$ that is thought to be a combination of two peaks observed in the Raman spectrum of solid cysteine at 772 $cm^{-1}$ and 806 $cm^{-1}$, which respectively correspond to a $CH_2$ rocking vibration and $CO_2$ scissoring vibration.

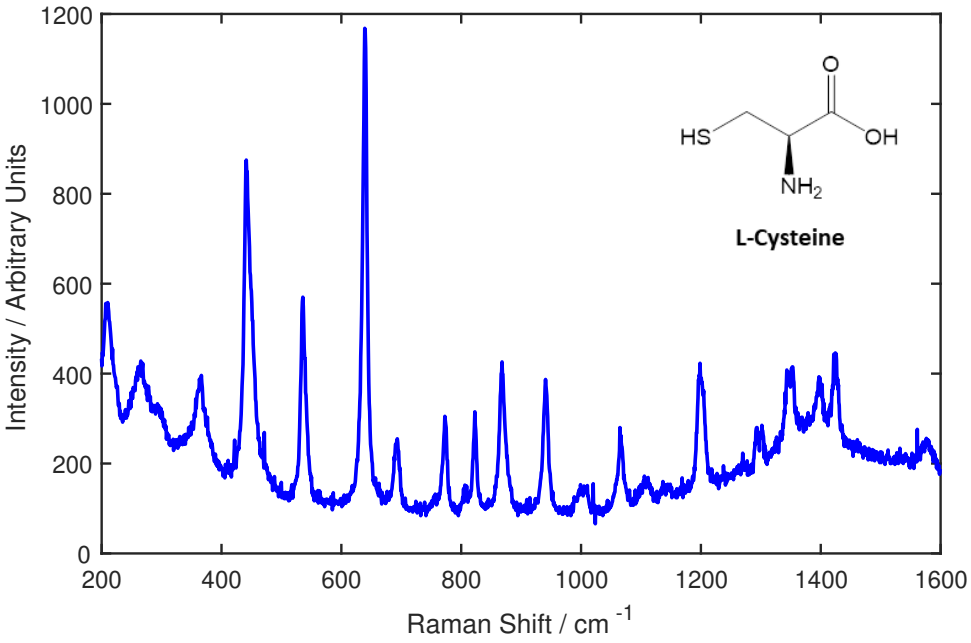


| Raman Shift / $cm^{-1}$ | Peak Intensity | Assignment |
|---|---|---|
| 210 | Medium | $CH_2$–CH torsion |
| 265 | Medium | C–C (Aliphatic) Vibration |
| 366 | Medium | S–H bend |
| 411 | Strong | C–C (Aliphatic) Vibration |
| 536 | Strong | $CH_2$–CH–N Bend |
| 639 | Strong | CH–$CO_2$ Stretch |
| 692 | Weak | C–S Stretch |
| 772 | Medium | $CH_2$ Rock |
| 806 | Weak | $CO_2$ Scissors |
| 823 | Medium | C–C (Aliphatic) Vibration |
| 868 | Medium | $CO_2$ Wag |
| 940 | Medium | N–CH Stretch |
| 1001 | Weak | $CH_2$–CH Stretch |
| 1065 | Medium | S–H Bend |
| 1106 | Weak | $NH_3$ Rock |
| 1142 | Weak | $NH_3$ Rock |
| 1199 | Medium | $CH_2$ Twist |
| 1293 | Weak | C–H Bend |
| 1302 | Weak | C–H Bend |
| 1343 | Weak | $CO_2$ Symmetric Stretch |
| 1353 | Weak | $CO_2$ Symmetric Stretch |
| 1399 | Weak | $CH_2$ Scissors |
| 1424 | Weak | $CH_2$ Scissors |
| 1579 | Weak | $NH_3$ Asymmetric Bend |

***Figure 7.4:*** *The Raman spectrum and associated peak assignments[131] of solid cysteine. Cysteine crystals were mounted on a glass slide and the spectrum was acquired using a 785 nm laser, a power at the sample of approximately 0.45 mW and an acquisition time of 1 × 300 s.*

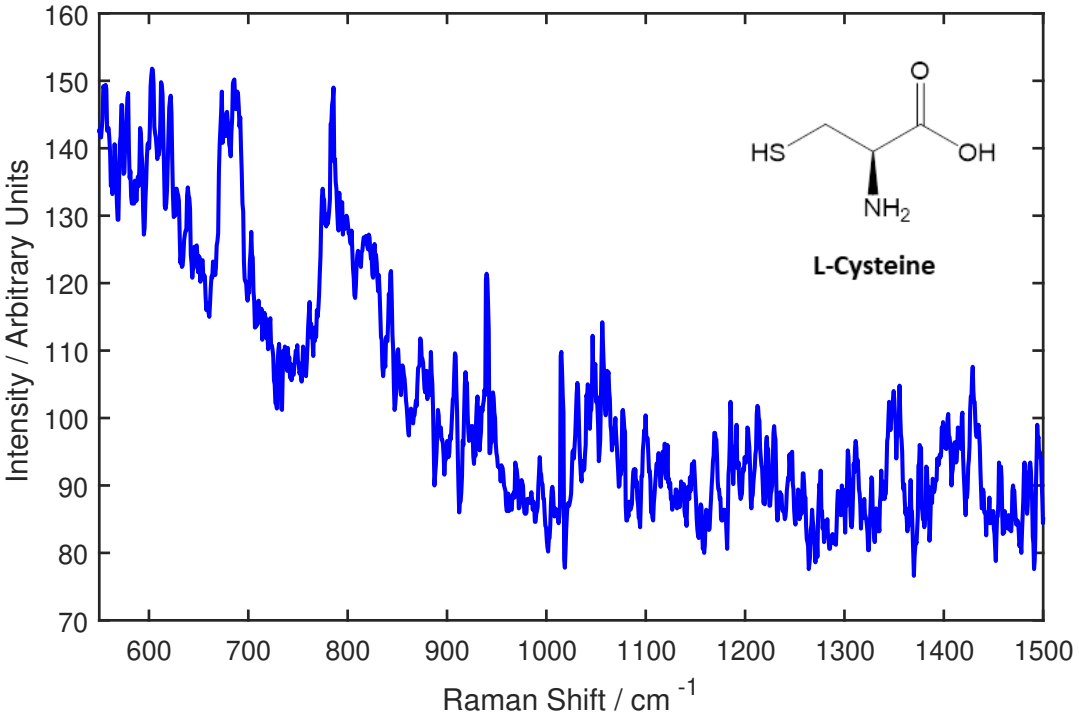


| Raman Shift / $cm^{-1}$ | Peak Intensity | Assignment |
|---|---|---|
| 687 | Weak | C–S Stretch |
| 782 | Weak | $CH_2$ Rock/$CO_2$ Scissors |
| 822 | Weak | C–C (Aliphatic) Vibration |
| 939 | Medium | N–CH Stretch |
| 1063 | Weak | S–H Bend |
| 1202 | Medium | $CH_2$ Twist |
| 1303 | Weak | C–H Bend |
| 1351 | Weak | $CO_2$ Symmetric Stretch |
| 1419 | Weak | $CH_2$ Scissors |

***Figure 7.5:*** *The Raman spectrum and associated peak assignments of a 1M solution of aqueous cysteine mounted in the macro sampler. Laser wavelength = 785 nm, power at sample = 100 mW, acquisition time = 3 × 500 s. A software-based multi-spectrum spike filter, which eliminated any sharp peaks that were only seen in one of the three spectra, was used to remove the presumed influence of cosmic rays from the spectrum.*

### 7.3.3 SERS of Aqueous Cysteine: Fixed Substrates

The SERS behaviour of cysteine was initially investigated using a fixed substrate comprised of a glass surface coated with a dense layer of silver nanoparticles. This intermediate step in the viability study was taken because it was assumed that the acquisition of a SERS spectrum of cysteine bound to a fixed substrate would be more straightforward than that of cysteine bound to a colloid in suspension.

A silver nanoparticle-coated SERS substrate was produced using 25 mm × 25 mm × 1 mm glass coverslips. Coverslips were cleaned prior to functionalisation by sonication in acetone, followed by sonication in isopropanol, for five minutes each. Clean coverslips were placed in individual 10 ml glass beakers containing a solution of 10 % (3-aminopropyl)trimethoxysilane (APTMS) in methanol and incubated for 24 hours at room temperature. The size of the beaker allowed the slides to stand diagonally, ensuring that both faces of the slide were exposed to the APTMS/methanol solution. Following incubation, the slides were rinsed thoroughly with methanol and were visually tested for hydrophobicity. 100 $\mu$L of silver nanoparticle solution was drop-cast on the slide and incubated at room temperature for one hour. The functionalised surface was then gently rinsed with methanol and 100 $\mu$L of aqueous cysteine was drop cast on the area of the slide coated with nanoparticles, which was identifiable as a dark grey spot on the glass surface. After incubation at room temperature for 30 minutes, the slide was rinsed with methanol and used immediately.

Substrates were mounted on a standard 76 mm × 25 mm × 1.2 mm glass slide and covered with 100 $\mu$L DI water during SERS measurements and a 50X water-immersion objective was used to focus the laser beam on the sample. A SERS spectrum of 10 $\mu$M aqueous cysteine obtained in this way is presented in Figure 7.6. Spectra were acquired in the region 400 – 1600 cm$^{-1}$, as this was the region in which peaks were observed in the Raman spectra of solid and aqueous cysteine.

A comparison of the Raman peaks observed in the spectrum shown in Figure 7.6 with previously-acquired Raman spectra or literature values was not straightforward, as SERS spectra of a given compound are known to vary, depending upon the particular vibrational modes that are enhanced. However, a sufficient number of peaks correlated with reported literature values of the SERS spectrum of cysteine on silver substrates to be confident that a SERS spectrum of cysteine had been successfully acquired.[130,133] In addition, the observed peak intensity in the spectrum is approximately 100× higher than that observed in the Raman spectrum of aqueous cysteine, despite the concentration of cysteine being $10^5$ lower than that used to acquire the Raman spectrum, indicating that surface enhancement has taken place.

Many of the peaks in the acquired SERS spectrum are within 20 cm$^{-1}$ of those acquired in the Raman spectra of solid and aqueous cysteine. Where this is the case, the peak assignment given to the Raman spectrum was applied, as denoted by a '**' symbol. Peaks which correspond exactly to quoted literature values of the SERS peaks of cysteine are denoted by a '*' symbol and an assignment based on that reported in the literature was given. The peaks correspponding to Raman shifts of 603 and 1267 cm$^{-1}$ do not closely correspond to reported literature values or previously-observed Raman shifts and were assigned using standard correlation tables.[134]

Generation of a SERS spectrum of cysteine was not straightforward due to the sig-

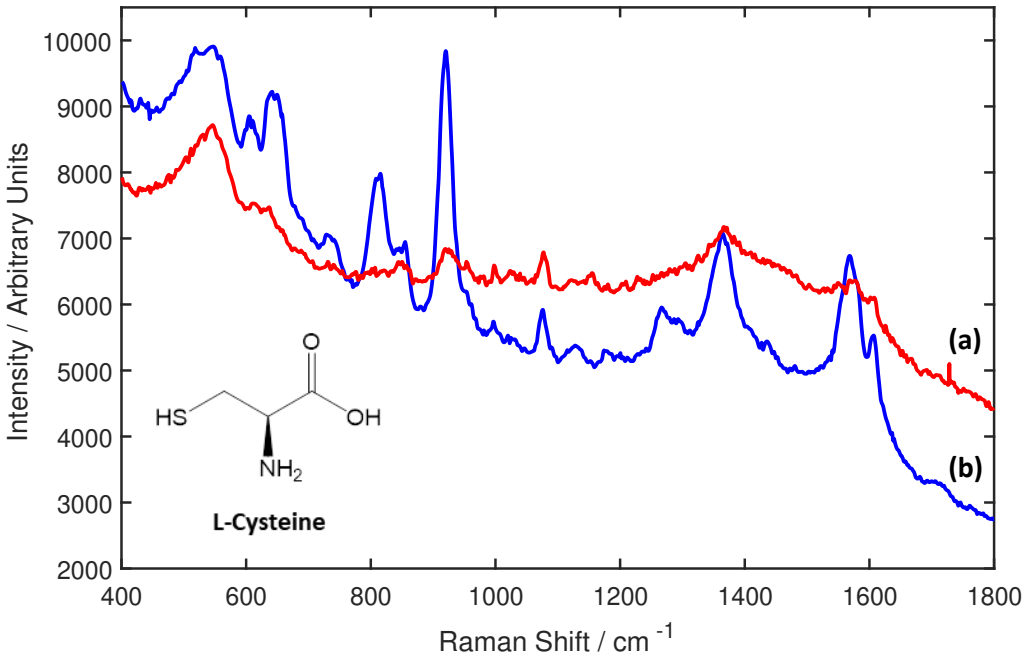


| Raman Shift / $cm^{-1}$ | Peak Intensity | Assignment |
|---|---|---|
| 547 | Medium | $CH_2$–CH–N Bend** |
| 603 | Weak | C–C (Aliphatic) Vibration |
| 642 | Weak | CH–$CO_2$ Stretch** |
| 731 | Weak | C–S Stretch* |
| 814 | Medium | $CH_2$ Wag / H–C–S Bend* |
| 855 | Weak | CO−2 Wag** |
| 920 | Strong | N–CH Stretch** |
| 997 | Weak | $CH_2$–CH Stretch* ** |
| 1076 | Weak | S–H Bend** |
| 1128 | Weak | $NH_3$ Rock** |
| 1181 | Weak | $CH_3$ Twist** |
| 1267 | Weak | C–C (Aliphatic) Vibration |
| 1293 | Weak | $CH_2$ Wag / C–C–H Bend* ** |
| 1364 | Medium | $CO_2$ Symmetric Stretch** |
| 1436 | Weak | $CH_2$ Scissors** |
| 1569 | Medium | NH3 Asymmetric Bend** |
| 1607 | Weak | $NH_3$ Bend* |

***Figure 7.6:*** *SERS spectra of 10 µM cysteine on a layer of silver nanoparticles. The same sample and acquisition settings were used to acquire spectra (a) and (b): laser = 785 nm, power at sample = 10 mW, acquisition time = 1 × 15 s. Differences in the spectra are attributed to inadvertent collection of scattered light from different focal planes in the sample. Peak assignments correspond to Spectrum (a). * = peaks corresponding to literature spectra,*[130,133] *** = peaks corresponding to observed Raman spectra of cysteine.*

nificant fluorescent background exhibited by the silver nanoparticles. Spectra acquired using silver nanoparticle-covered fixed SERS substrates were anecdotally observed to

be highly variable. Significant differences between SERS spectra were observed, depending upon how accurately the laser beam was focused on the surface of the sample. An example of these differences is shown in Figure 7.6, in which Spectrum B is shown to exhibit high fluorescence and a poorer signal-to-noise ratio than Spectrum A, despite both spectra being acquired using the same sample and with identical acquisition parameters. It is thought that the difference between spectra was caused by the inadvertent selection of different focal planes within the sample. This effect was predictable, as the SERS effect is known to exponentially decay with distance from the substrate surface.

The successful detection of cysteine at 10 $\mu$M is significant, as this is the lowest analyte concentration that a sensor for metabolic profiling of TBI patients would be required to detect. However, although the spectrum was acquired whilst the substrate surface was submerged in water, it is noted that a 30 minute incubation of analyte molecules on the substrate surface prior to SERS analysis would not be practical to adopt in a clinical application.

### 7.3.4 SERS of Aqueous Cysteine: Colloidal Substrates

Silver nanoparticles were aggregated into colloids by mixing in a 1:1 ratio with perfusion fluid. Aqueous cysteine was then added to the aggregated nanoparticles and incubated for 30 minutes. Following the incubation, a 50$\mu$L sample was removed from the solution and placed on a standard 76 mm $\times$ 25 mm $\times$ 1.2 mm glass slide for analysis via SERS.

The acquisition of a SERS spectrum of cysteine on the surface of silver colloids proved to be very difficult. As discussed in Section 7.3.3, the successful acquisition of a SERS spectrum requires accurate focus of the laser beam on the surface of the sample. This was challenging to achieve due to the motion of the colloids within the perfusion fluid. It is also possible that the high levels of fluorescence observed in the spectra masked underlying peaks. Examples of the spectra acquired from a sample of 10 $\mu$M cysteine, and their associated acquisition parameters, are shown in Figure 7.7. Once again, these spectra were acquired in the region 400 – 1600 cm$^{-1}$ to allow comparison with previously-acquired spectra.

None of the acquired spectra could be confirmed as being a SERS spectrum of cysteine. All spectra were characterised by relatively high fluorescent backgrounds and contained few, or no, Raman peaks as exemplified in Figure 7.7. Some spectra displayed two peaks in the 650 – 750 cm$^{-1}$ region of the spectrum, as seen in two of the spectra shown in Figure 7.7. One of these peaks is centred around 658 cm$^{-1}$, which does not correlate with the peaks observed in any of the previously-acquired Raman or SERS spectra of cysteine. The second peak is centred at approximately 738 cm$^{-1}$. This loosely correlates with a peak observed in the SERS spectrum of cysteine

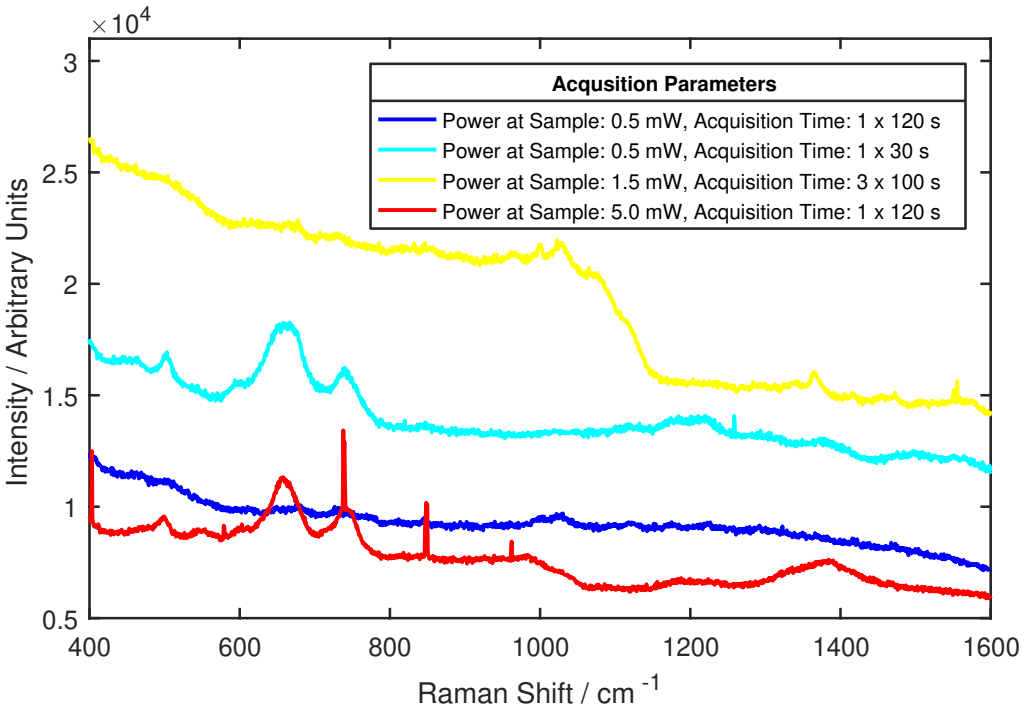


***Figure 7.7:*** *SERS spectra of 10 $\mu M$ cysteine in a mixture with silver colloids suspended in perfusion fluid, acquired using a variety of acquisition parameters. The spectra show relatively few features, aside from two peaks with Raman shifts betwen 650 – 750 $cm^{-1}$ which appear in two of the spectra. Laser wavelength = 785 nm for all spectra.*

on a fixed SERS substrate, at 731 $cm^{-1}$, and may be attributed to a C–S stretching vibration.

### 7.3.5 Testing SERS Sensor Viability: Conclusions

This section has described the characterisation of the Raman spectra of cysteine in solid and aqueous phases and the assessment of two different substrates for SERS of cysteine. A fixed substrate of densely-packed silver nanoparticles on a glass surface was successfully used to acquire a SERS spectrum of cysteine at a concentration of 10 $\mu$M, the lowest analyte concentration that a sensor for metabolic profiling of TBI patients would be required to detect. However, significant variability was observed in the quality of the acquired spectra. It was also noted that the 30 minute incubation time allowed for the binding of cysteine to the substrate surface would not be practical to adopt in a clinical application.

Finally, attempts were made to acquire the SERS spectrum of cysteine adsorbed on the surface of silver colloids in suspension, as suggested in the proposed SERS sensor design. This proved to be challenging, due to the difficulty of focusing the laser beam on the surface of a moving colloid, and the results of these attempts were

inconclusive.

Although it would have been possible to further refine the process of obtaining SERS spectra from molecules adsorbed on the surface of the colloidal silver substrates, experimental work was concluded at this point. The reasons for this are explained in the following section.

## 7.4 Conclusions

This chapter presents an exploration of the use of Raman spectroscopy in an on-line sensor for continuous monitoring of glucose, lactate and pyruvate concentrations in the microdialysate of TBI patients. Initial attempts to acquire the Raman spectrum of aqueous glucose suggested that detection of clinical concentrations of glucose, lactate and pyruvate by Raman scattering-based techniques would only be possible using surface enhancement. A sensor design, based on the use of silver colloids as SERS substrates, was proposed and investigated using cysteine as a model analyte. These studies showed some promising results, including the detection of 10 $\mu$M cysteine adsorbed on a fixed substrate of densely-packed silver nanoparticles.

The use of SERS appeared to successfully overcome the problem of the inherent insensitivity of Raman spectroscopy and the low scattering intensity exhibited by glucose, lactate and pyruvate. Following this work, it seemed possible that SERS could be used to generate Raman peaks corresponding glucose, lactate and pyruvate, even at the lower limit of the clinical concentration range. In addition to this, the proposed SERS sensor design addressed the re-usability issues associated with fixed SERS substrates. However, this study also highlighted serious problems with the proposed SERS sensor. The significant differences in spectra, depending upon the focus of the laser beam, and the associated difficulty in obtaining a spectrum of cysteine on the surface of a silver colloid in suspension, were of particular concern, as it was assumed that these factors would significantly increase the complexity of device operation. In addition to this, it was noted that the development of a method for measurement of glucose, lactate and pyruvate concentrations from SERS spectra would be very difficult, as the spectra can vary significantly, depending upon the location and orientation of an analyte molecule with respect to the surface plasmon.

It was noted that, for all Raman and SERS spectra acquired, an increase in signal intensity may have been achieved via the use of a light source of shorter wavelength. However, the use of shorter wavelengths can also increase the amount of fluorescence present in the spectrum and therefore the overall increase in signal:noise ratio was unlikely to have been significant enough to allow the detection of clinically-relevant concentrations of glucose, lactate or pyruvate via Raman spectroscopy alone. This factor was deemed less relevant to the consideration of SERS as a potential sensor technology, as the difficulties associated with the technique were unrelated to sensor

sensitivity.

This work was conducted in parallel with the FTIR spectroscopy studies described in Chapter 6. When compared with the technical issues described here, it was clear that FTIR spectroscopy showed significantly more promise as an on-line sensor for metabolic profiling of TBI patients. The decision was thus taken to cease work on the proposed SERS-based sensor and focus on the development of an FTIR sensor.

# Chapter 8

# Analysis of Glucose, Lactate and Pyruvate Mixtures via ATR-FTIR Spectroscopy

This chapter describes the selection and optimisation of a statistical model for the prediction of glucose, lactate and pyruvate concentrations from ATR-FTIR spectra of solutions containing one, two or all three compounds. The primary aim of this study was to determine the accuracy with which clinically-relevant concentrations of glucose, lactate and pyruvate could be predicted from ATR-FTIR spectra, in order to assess the feasibility of using ATR-FTIR for metabolic profiling of TBI patients.

A decision was made not to use clinical microdialysate samples for this study or for the transmission-FTIR study described in Chapter 9. This was due to the fact that clinical samples were relatively scarce and of low volume. In order to carry out a comprehensive study, a large number of samples would have been needed and it was considered more important to conserve clinical samples for use in testing the final sensor-chip design. This problem was exacerbated by the fact that the seven-reflection ATR-FTIR crystal used in this work required sample volumes of 1 ml, meaning that 5 – 10 clinical samples would need to be combined to obtain a single spectrum.

Instead, pure solutions of glucose, lactate and pyruvate in perfusion fluid were prepared at a number of different, clinically-relevant, concentrations and then combined systematically to produce a series of solutions containing one, two or three compounds. ATR-FTIR spectra of these solutions were acquired using a seven-reflection ZnSe ATR crystal and analysed in a number of ways. Initially, an analysis based on the measurement of relative peak intensity, as used in Chapter 6, was considered. It was concluded that predictive statistical modelling was likely to be a more robust method for the prediction of analyte concentrations from spectra and therefore two commonly-used predictive statistical models, PLSR and PCR, were employed. The

PLSR model produced more promising results and thus the remainder of the work focused on optimising this model to minimise its error in prediction.

## 8.1 Mixture Selection

The aim of this study was to analyse mixtures containing glucose, lactate and pyruvate. This section describes the analysis and decision-making process used to determine which mixtures should be investigated.

### 8.1.1 Three-Component Mixtures

Two factors were considered to ensure that the mixtures used in this study were as relevant as possible to the clinical context in which a developed ATR-FTIR sensor would be used. The first factor to be addressed was the ratio of glucose:lactate:pyruvate that should be used in order to most closely mimic those found in the microdialysate of TBI patients. The relationship between the relative amounts of glucose, lactate and pyruvate present in the extracellular brain fluid of TBI patients is non-trivial to determine and is a subject of active research. It was therefore decided that the most logical approach would be to analyse every possible combination of the glucose, lactate and pyruvate concentrations selected for use in the study, to ensure that a range of ratios was systematically examined.

The second factor was the selection of glucose, lactate and pyruvate concentrations that were considered most relevant to the monitoring of TBI. It was considered impractical to conduct a thorough study covering the whole range of glucose, lactate and pyruvate concentrations observed in the clinic and therefore a subset of concentrations with particular clinical significance was selected for investigation. This subset was partially identified via an analysis of anonymised patient data, collected by the Department of Clinical Neurosciences at the University of Cambridge over a period of six years (2009 – 2015), which listed the measured glucose, lactate and pyruvate concentrations in the microdialysate of 50 TBI patients at approximately hourly intervals for periods of 1 – 5 days. The resulting dataset contained approximately 24,000 data points. These data were analysed by Dr Anna Hüfner (Department of Chemistry) to determine the number of times that each concentration of glucose, lactate and pyruvate had been observed. A summary of this analysis is shown in Figure 8.1.

The histograms shown in Figure 8.1 were used to identify a concentration range for each compound which encompassed the majority of observed concentrations. The identified concentration ranges were:

- **Glucose** 0.1–3 mM
- **Lactate** 0.1–6 mM

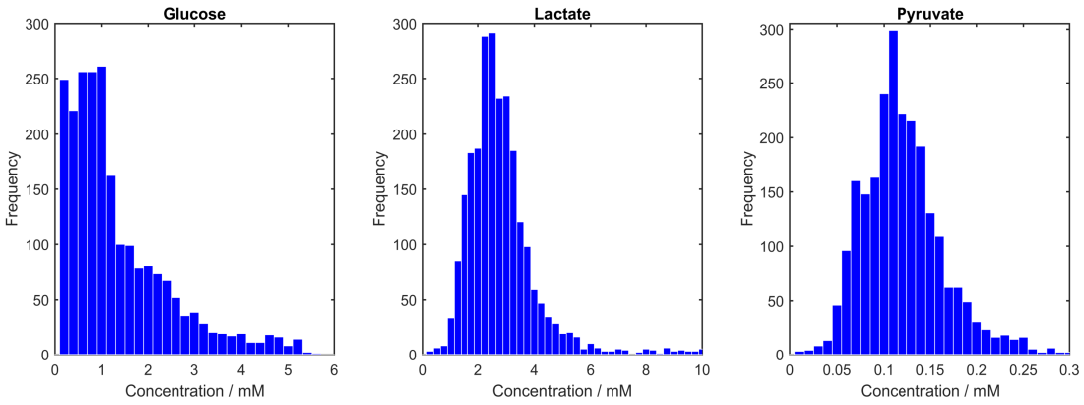


***Figure 8.1:*** *Histograms summarising the frequency with which various concentrations of glucose, lactate and pyruvate were observed in an analysis of patient data. Figures are adapted from plots generated by Dr Anna Hüfner.*

- **Pyruvate** 0.01–0.2 mM

The highest concentration of each range was selected as the maximum concentration that would be used to form a mixture. It was assumed that accurate prediction of analyte concentrations from ATR-FTIR spectra would be easier to achieve at higher concentrations and therefore it was not considered necessary to place additional focus on concentrations higher than this. It was noted that the maximum concentrations of glucose, lactate and pyruvate that a developed sensor would be required to detect (24 mM, 24 mM and 1.5 mM, respectively) were not recorded in any of the patient samples.

The lowest clinical concentrations of glucose, lactate and pyruvate that a developed sensor would be required to detect (0.1 mM, 0.1 mM and 0.01 mM, respectively) were also used to form three-component mixtures. The ability to accurately measure these concentrations was considered to be the greatest challenge in sensor development and therefore it was considered necessary to place additional focus on detecting these compounds by including them in the mixtures. For pyruvate only, a concentration below this lower limit (0.005 mM) was included in the study. This additional concentration was chosen to acknowledge the fact that the clinical concentration range of pyruvate is approximately ten-fold lower than those of glucose and lactate and was therefore likely to be the most difficult compound to detect accurately. It was decided that additional focus should be placed on the lower limit of clinical pyruvate concentrations to determine the accuracy with which it could be predicted. In order to do this, it was necessary to include a concentration below the concentration limit, to assess whether concentrations at that limit could be accurately differentiated from concentrations that are lower still.

The conclusions of the Consensus Statement from the 2014 International Micro-

dialysis Forum were also taken into account when selecting clinically significant concentrations for inclusion in mixtures. These conclusions identified pathological thresholds for the concentrations of glucose, lactate and pyruvate, as discussed in Sections 2.4.2 and 2.4.3. It was decided that the ability to accurately differentiate concentrations lying close to these boundaries would be a key indicator of sensor performance and therefore concentrations close to these thresholds were included in this study. A glucose concentration below 0.8 mM is considered an indicator of poor patient outcome in TBI and therefore glucose concentrations of 0.7 mM and 1.0 mM were included in this study. The pathological threshold of lactate is 4 mM and thus lactate concentrations of 2 mM and 4 mM were selected for use in this study.

No pathological threshold for the absolute concentration of pyruvate is given in the Consensus Statement. Instead, the remaining concentrations of pyruvate to be included in the three-component mixtures were selected by evenly dividing the key concentration range of pyruvate, identified from the patient histograms (Figure 8.1), in order to cover the entire range. It was hoped that the small differences between these concentrations would lead to more accurate predictions of the pyruvate concentration and hence a higher resolution of the sensor.

The concentrations of glucose, lactate and pyruvate used to form the three-component mixtures analysed in this study are summarised in Table 8.1.

The concentrations of glucose, lactate and pyruvate listed in Table 8.1 were systematically mixed, in every possible combination which included all three compounds, to produce a total of 96 three-component mixtures. An additional three three-component mixtures, considered 'special cases', were also studied:

- **Glu: 0.05 mM, Lac: 0.05 mM, Pyr: 0.005 mM** - All three compounds below the expected clinical range.
- **Glu: 0.05 mM, Lac: 2.00 mM, Pyr: 0.005 mM** - Glucose and pyruvate below the clincal concentration range, lactate within it.
- **Glu: 1.00 mM, Lac: 0.05 mM, Pyr: 0.005 mM** - Lactate and pyruvate below the clinical concentration range, glucose within it.

A full list of all three-component mixtures analysed in this study can be found in Appendix A.1.

### 8.1.2 Two-Component Mixtures

It was theorised that it may also be useful to analyse spectra containing just two of the three compounds. It was also decided that a slightly different set of concentrations to those used in the three-component mixtures should be used for the two-component mixtures, in order to allow a greater range of concentrations to be studied overall. An

***Table 8.1:*** *Concentrations of glucose, lactate and pyruvate used to form the three-component mixtures analysed via ATR-FTIR spectroscopy.*

| Glucose / mM | Lactate / mM | Pyruvate / mM |
|---|---|---|
| 0.1 | 0.1 | 0.005 |
| 0.7 | 2.0 | 0.01 |
| 1.0 | 4.0 | 0.05 |
| 3.0 | 6.0 | 0.10 |
| | | 0.15 |
| | | 0.20 |

additional concentration of 0.05 mM was included for both glucose and lactate, in order to allow an assessment of the accuracy with which the lowest clinical concentrations of those compounds (0.1 mM for both) could be detected. This decision meant that, for practical reasons, the upper concentration limits used in the three-component mixture study were not used. One pyruvate concentration (0.1 mM) was also removed for practical reasons. The concentrations of glucose, lactate and pyruvate used to form two-component mixtures are listed in Table 8.2.

***Table 8.2:*** *Concentrations of glucose, lactate and pyruvate used to form the two-component mixtures analysed via ATR-FTIR spectroscopy.*

| Glucose / mM | Lactate / mM | Pyruvate / mM |
|---|---|---|
| 0.05 | 0.05 | 0.005 |
| 0.1 | 0.1 | 0.01 |
| 0.7 | 0.5 | 0.05 |
| 1.0 | 4.0 | 0.15 |
| | | 0.2 |

A list of two-component mixtures included in this study is shown in Appendix A.2.

### 8.1.3 Pure Solutions

Spectra of pure solutions of glucose, lactate and pyruvate were also included in this study. The concentrations used in the two- and three-component mixtures were all analysed as pure solutions. Additional concentrations, close in value to those used in the mixtures, were added in an attempt to improve the resolution in the prediction of concentrations. At a later date, the data generated using the ZnSe ATR-FTIR crystal during the ATR-FTIR crystal study, described in Section 6.4.1, were also included in the analysis to increase the size of the dataset. Table 8.3 lists the concentrations of glucose, lactate and pyruvate studied as pure solutions, including those used in the ATR-FTIR crystal study.

***Table 8.3:*** *Concentrations of glucose, lactate and pyruvate studied as pure solutions via ATR-FTIR spectroscopy, including those from the ATR-FTIR crystal study.*

| Glucose / mM | Lactate / mM | Pyruvate / mM |
|---|---|---|
| 0.05 | 0.05 | 0.005 |
| 0.10 | 0.10 | 0.01 |
| 0.19 | 0.19 | 0.02 |
| 0.20 | 0.20 | 0.05 |
| 0.40 | 0.40 | 0.10 |
| 0.70 | 0.50 | 0.15 |
| 0.75 | 0.75 | 0.20 |
| 1.00 | 1.50 | 0.75 |
| 1.50 | 2.00 | 1.00 |
| 3.00 | 3.00 | 1.50 |
| 5.00 | 4.00 | 7.50 |
| 6.00 | 6.00 | |
| 10.0 | 10.0 | |
| 12.0 | 12.0 | |
| 24.0 | 24.0 | |

## 8.2 Mixture Selection: Conclusions

This section has described the reasoning used to select solutions of glucose, lactate and pyruvate for use in a study to determine the feasibility of using ATR-FTIR spectroscopy as the basis of an on-line sensor for metabolic profiling of TBI patients.

## 8.3 Data Acquisition

The chosen solutions were prepared in perfusion fluid and their spectra acquired using a Perkin Elmer Spectrum 100 FTIR Spectrometer, coupled with a seven-reflection ZnSe HATR Sampling Accessory, as described in Section 5.2. The seven-reflection ZnSe ATR-FTIR crystal was that identified in Section 6.4.1 as exhibiting the best performance for the detection of pure solutions of glucose, lactate and pyruvate (6.4.1).

Three aliquots of each solution were analysed via ATR-FTIR spectroscopy. Two spectra were acquired of each aliquot: one ratio spectrum, in which perfusion fluid was used as the background, and one single-beam spectrum. Spectra of pure perfusion fluid were also acquired. A total of 16 aliquots of perfusion fluid were analysed and two spectra were acquired of each aliquot: one ratio spectrum in which perfusion fluid was also used as the background and one single-beam spectrum.

The spectra of three-component mixtures, two-component mixtures and pure solutions of glucose, lactate and pyruvate were combined into two large datasets, one consisting of all of the acquired ratio spectra and one consisting of all the acquired single-beam spectra. A total of 643 ratio and 643 single-beam spectra were acquired.

Each dataset was used in its entirety for the analysis described in this chapter, without differentiating between the spectra of one-, two- and three-component solutions.

A sample of the spectra from each dataset can be seen in Figures 8.2 and 8.3. The spectra plotted in this figure were selected by choosing every 37th spectrum from a list of all spectra ordered by increasing glucose concentration.

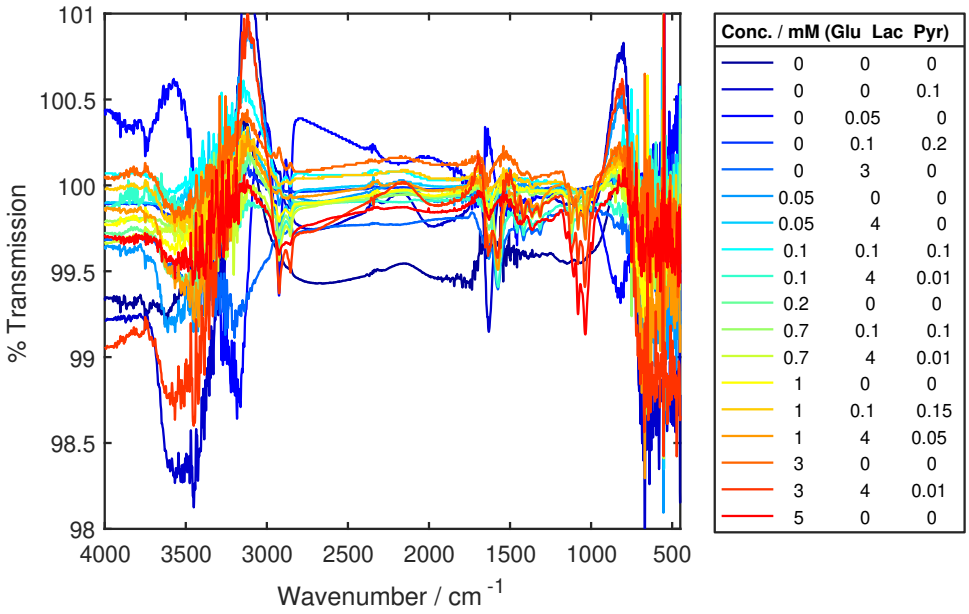


***Figure 8.2:*** *A randomly-selected sample of the ratio ATR-FTIR spectra acquired for the ATR-FTIR mixture study. Concentrations are listed in the horizontal order: glucose - lactate - pyruvate.*

### 8.3.1 Data Acquisition: Conclusions

This section has described the process used to generate two large datasets of ATR-FTIR spectra, one consisting of ratio spectra and one consisting of single-beam spectra, for use in this study of ATR-FTIR spectroscopy.

## 8.4 Spectrum Analysis Methods

The solutions of glucose, lactate and pyruvate selected in Section 8.1 were chosen with the intention of analysing their spectra via statistical modelling rather than an analysis of peak intensities. This decision was made following the results of the ATR-FTIR crystal study described in Section 6.4.1, in which the LoQ of each compound, as determined from the relationship between peak intensity and concentration, were found to be significantly higher than those required of the developed sensor. These results indicated that an analysis of peak intensities would not be a sufficiently sensitive method of analysing the acquired spectra.

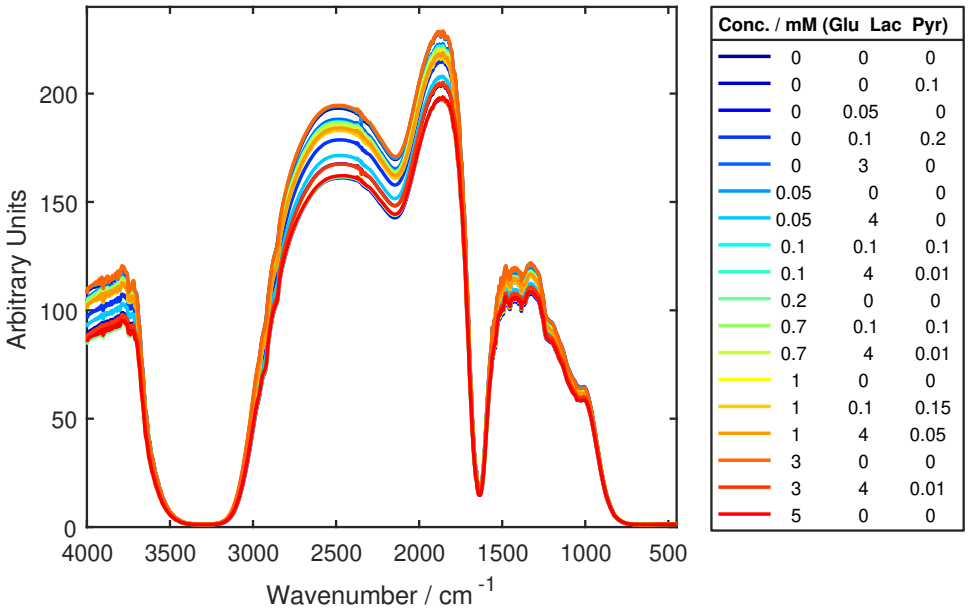


***Figure 8.3:*** *A randomly-selected sample of the single-beam ATR-FTIR spectra acquired for the ATR-FTIR mixture study. Concentrations are listed in the horizontal order: glucose - lactate - pyruvate.*

The use of peak intensity measurements to analyse the spectra of mixtures of glucose, lactate and pyruvate raised additional concerns. Although peaks unique to glucose, lactate and pyruvate had been identified from a mixture of all three compounds (Section 6.1) there was concern that, if any of these peaks were positioned close to an absorption peak of another compound in the sample, the intensity of the unique peak may be affected by the shoulder of the adjacent peak. This effect was addressed quantitatively through a statistical analysis of the ratio ATR-FTIR spectra acquired in this study.

The statistical analysis was conducted on spectral positions corresponding to two unique glucose peaks, 993 $cm^{-1}$ and 1081 $cm^{-1}$. The mean and standard deviation of the percentage transmission were calculated at each position. Initially, the mean and standard deviation of the ATR-FTIR ratio spectra of perfusion fluid ('blank spectra') at both 993 $cm^{-1}$ and 1081 $cm^{-1}$ were calculated. This process was then repeated for three additional subsets of the ATR-FTIR ratio spectra dataset: spectra of pure solutions of lactate, spectra of pure solutions of pyruvate and spectra of two-component mixtures containing lactate and pyruvate. None of the analysed spectra represented solutions containing glucose. It was hypothesised that, if the glucose peaks at 993 $cm^{-1}$ and 1081 $cm^{-1}$ were unaffected by the presence of pyruvate or lactate in the solution, the mean and standard deviation of the percentage transmission at each peak position of the blank spectra would be similar to those of the spectra with additional compounds added. The results of this analysis are shown in Table 8.4.

***Table 8.4:*** *The mean and standard deviation (SD) of spectra at the positions of two unique glucose peaks.*

| Compound | 1081 $cm^{-1}$ Peak | | 993 $cm^{-1}$ Peak | |
|---|---|---|---|---|
| | Mean | SD | Mean | SD |
| (Blank) | 100.003 | 0.0186 | 100.001 | 0.0264 |
| Lactate | 99.946 | 0.0599 | 100.014 | 0.0445 |
| Pyruvate | 100.001 | 0.0241 | 100.000 | 0.0214 |
| Lactate & Pyruvate | 99.983 | 0.0250 | 100.002 | 0.0201 |

It can be seen from Table 8.4 that the mean and standard deviation at both peak positions increased from their blank spectra values when lactate was present in the sample. The effect was greater in spectra of solutions containing lactate only than in spectra of solutions containing both lactate and pyruvate. It is thought that this is due to the fact that higher concentrations of lactate were used in single-component solutions than in two-component solutions. This provided an indication that glucose peak intensity may be affected by the presence of lactate.

### 8.4.1 Spectrum Analysis Methods: Conclusions

The evidence presented in this chapter, in combination with results described in Chapter 6.4.1, was considered sufficient to conclude that an ATR-FTIR-based sensor for glucose, lactate and pyruvate which incorporated an analysis of peak intensities to determine the levels of each compound would not be suitable for use in the clinic. It was therefore decided that the use of predictive statistical modelling in the analysis of the ATR-FTIR spectral dataset would be assessed.

## 8.5 ATR-FTIR Spectrum Analysis: Comparison of Statistical Models

The first stage in the analysis of the acquired ATR-FTIR spectral dataset was the selection of a predictive statistical model. It was initially assumed that the data were linear and could therefore be analysed using a linear regression model, which would be more straightforward to implement than a non-linear model. Two of the most widely-used linear regression models are PCR and PLSR, and it was therefore decided that the performance of these two models should be compared.

Both statistical models were individually applied, in turn, to the ATR-FTIR ratio spectra and ATR-FTIR single-beam spectra datasets. Little was known about the potential of the data to be modelled and therefore it was deemed logical to apply the model to as much of the spectral range as possible. Although all spectra were acquired over the range 4000 – 450 $cm^{-1}$, noise was seen below 650 $cm^{-1}$ due to the IR transmission cut-off of the ZnSe crystal, as seen in Figure 8.2. Attemping to model

this noise would worsen the performance of both models, as it is by definition random, and therefore both models were applied over the spectral range 4000 – 650 $cm^{-1}$.

Three criteria were used to evaluate the performance of the two models. The first criterion was the number of model components required to reach a maximum $R^2$ value, with the use of fewer components considered desirable as it reduced the likelihood of model over-fitting. A maximum limit of 30 components was imposed for this analysis.

The predictive capacity of each model was the feature of most interest to the development of a sensor based on ATR-FTIR spectroscopy. This was assessed by calculating the RMSECV in the prediction of glucose, lactate and pyruvate concentrations, as determined from the results of a leave-one-out cross-validation. The RMSECV was selected as a measure of predictive accuracy, rather than the RMSEP, in order to retain the size of the dataset and reduce the effect of any outlying values. The number of model components required to minimise the RMSECV was one way in which the model was assessed, with fewer components once again considered preferable. In addition, the RMSECV in the prediction of the concentration of each compound, using a model with 20 components, was measured.

### 8.5.1 PCR *vs.* PLSR: Ratio ATR-FTIR Spectra

A summary of the performance of a PCR model applied to the dataset of ATR-FTIR ratio spectra is shown in Figure 8.4.

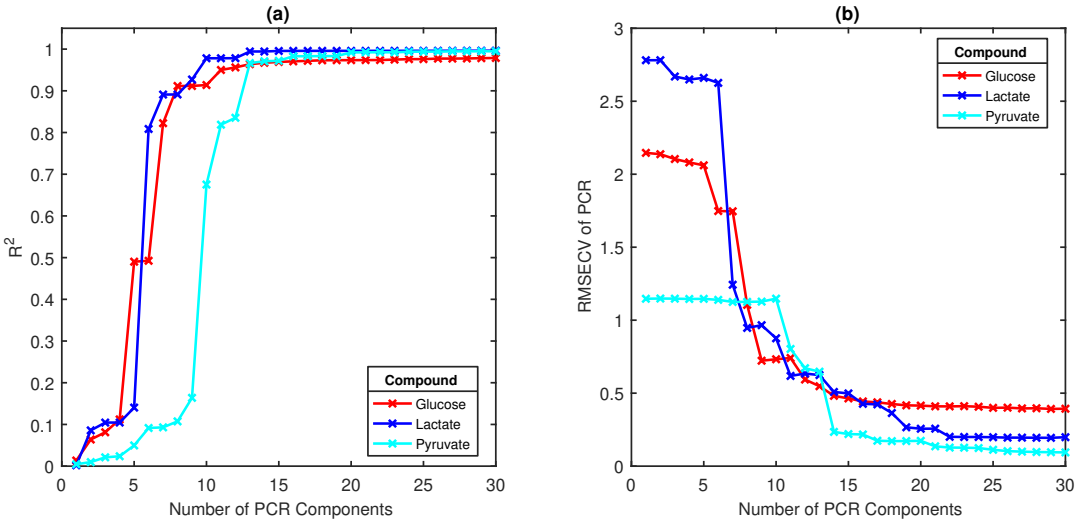


***Figure 8.4:*** *A summary of the performance of a PCR model applied to the dataset of ATR-FTIR ratio spectra of glucose, lactate and pyruvate. The change in $R^2$ with an increasing number of model components and the change in the RMSECV in concentration predictions, calculated using leave-one-out cross-validation, are shown for each compound.*

It can be seen from Figure 8.4 that the model required more components to accurately model pyruvate than to model glucose or lactate. This was expected, as

pyruvate is present at concentrations approximately ten-fold lower than those of glucose and lactate. The $R^2$ values of the models of all three compounds appear to converge at a value very close to 1.0 when more than 25 components are used, which is a possible sign of over-fitting. Conversely, the RMSECV for each compound does not appear to converge, even when 30 model components are used. The prediction of glucose concentrations generates the highest absolute error, although the error in pyruvate prediction is proportionally higher.

A summary of the performance of a PLSR model on the same dataset of ATR-FTIR ratio spectra is shown in Figure 8.5. The results generated by this model appear to follow broadly similar trends to those generated by the PCR model: more components were required to accurately model pyruvate than to model glucose or lactate, though $R^2$ values converged when a large number of components were used, and the prediction of glucose concentrations generated the highest absolute error. However, a quantitative comparison of the data, as shown in Table 8.5, showed that there were distinct differences between the performances of the two models.

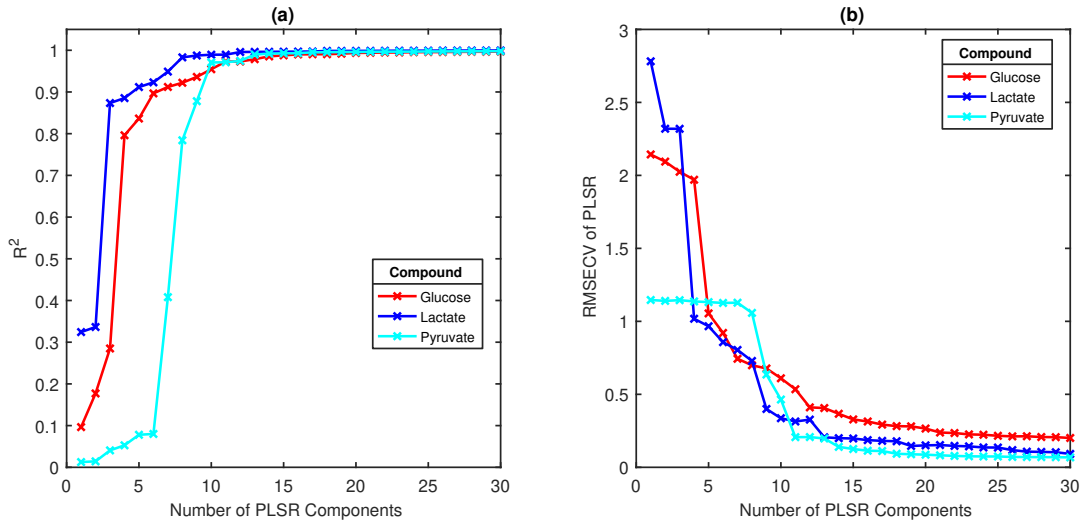


***Figure 8.5:*** *A summary of the performance of a PLSR model applied to the dataset of ATR-FTIR ratio spectra of glucose, lactate and pyruvate. The change in $R^2$ with an increasing number of model components and the change in the RMSECV in concentration predictions, calculated using leave-one-out cross-validation, are shown for each compound.*

The data summarised in Table 8.5 show that, by all of the assessed criteria, the PLSR model performed better than the PCR model. The PLSR model required fewer components to accurately model the lactate and pyruvate data, as measured by the $R^2$ value, and used an equal number of components to model the glucose data. In addition, the PLSR model required fewer components to minimise the RMSECV in predicted glucose, lactate and pyruvate concentrations and showed a lower RMSECV for all compounds when a model with 20 components was used to analyse the data.

***Table 8.5:*** *A comparison of the performances of PCR and PLSR statistical models when applied to the same set of ATR-FTIR ratio spectra.*

| Compound | Parameter | PCR | PLSR |
|---|---|---|---|
| Glucose | Number of components for max. $R^2$ Value | 11 | 11 |
| | Number of components for min. RMSECV | 18 | 21 |
| | RMSECV with 20 Components | 0.41 | 0.27 |
| Lactate | Number of components for max. $R^2$ Value | 13 | 8 |
| | Number of components for min. RMSECV | 22 | 19 |
| | RMSECV with 20 Components | 0.26 | 0.15 |
| Pyruvate | Number of components for max. $R^2$ Value | 20 | 13 |
| | Number of components for min. RMSE | 21 | 18 |
| | RMSECV with 20 Components | 0.173 | 0.087 |

### 8.5.2 PCR *vs.* PLSR: Single-Beam ATR-FTIR Spectra

The performances of a PCR model and a PLSR model applied to the dataset of ATR-FTIR single-beam spectra are shown in Figures 8.6 and 8.7, respectively. PLSR was once again the better-performing model, based on the assessed criteria, although the differences between the performances of the two models were observed to be more significant when applied to single-beam spectra. The PLSR model was able to accurately model the data with significantly fewer components than the number required by the PCR model, which required more than 30 components to achieve an $R^2$ value greater than 0.8. Similarly, the RMSECV decreased more rapidly with an increasing number of model components when PLSR was used to model the data.

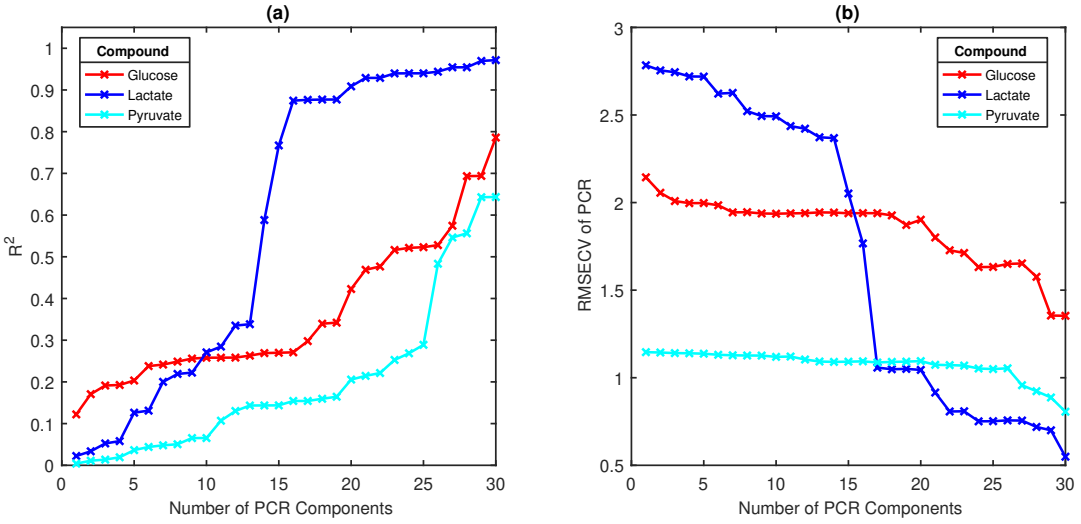


***Figure 8.6:*** *A summary of the performance of a PCR model applied to ATR-FTIR single-beam spectra of glucose, lactate and pyruvate. The change in $R^2$ with an increasing number of model components and the change in the RMSECV in concentration predictions, calculated using leave-one-out cross-validation, are shown for each compound.*

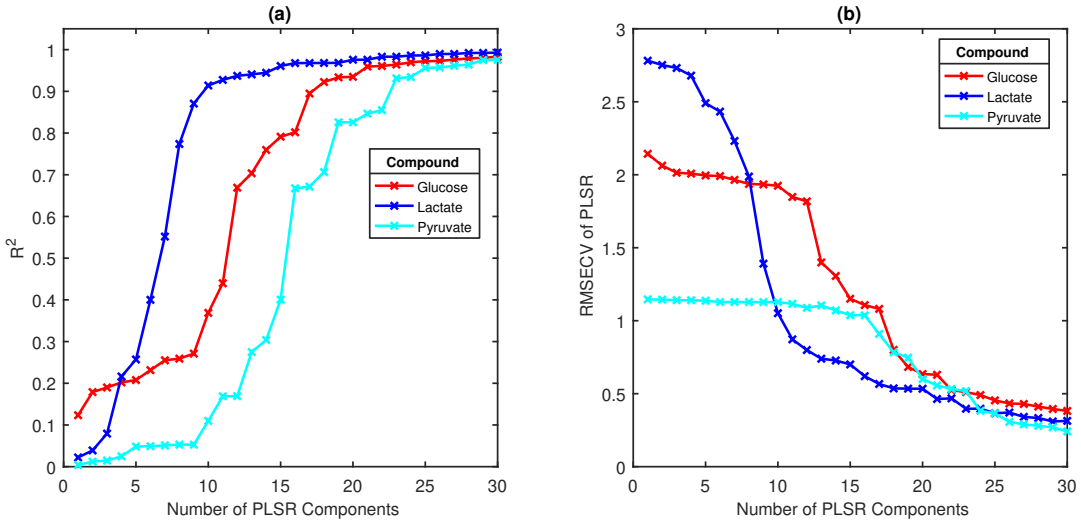


***Figure 8.7:*** *A summary of the performance of a PLSR model applied to ATR-FTIR single-beam spectra of glucose, lactate and pyruvate. The change in $R^2$ with an increasing number of model components and the change in the RMSECV in concentration predictions, calculated using leave-one-out cross-validation, are shown for each compound..*

The differences between the performance of the two models are quantified in Table 8.6. It is also noted that the performances of both models were poorer when applied to single-beam spectra than when they were applied to ratio spectra. This is thought to be due to the fact that single-beam spectra contain influences from multiple factors, such as the instrument optics and environment. These influences are removed from ratio spectra, as they are created by the division of two single-beam spectra. It is therefore likely that more information is contained within the single-beam spectra and hence a greater number of components would be needed to account for the variation in the data.

***Table 8.6:*** *A comparison of the performances of PCR and PLSR statistical models when applied to the same set of ATR-FTIR single-beam spectra.*

| Compound | Parameter | PCR | PLSR |
|---|---|---|---|
| Glucose | Number of components for max. $R^2$ Value | >30 | 21 |
| | Number of components for min. RMSECV | 29 | 26 |
| | RMSECV with 20 Components | 1.9 | 0.63 |
| Lactate | Number of components for max. $R^2$ Value | 29 | 20 |
| | Number of components for min. RMSECV | 30 | 26 |
| | RMSECV with 20 Components | 1.05 | 0.53 |
| Pyruvate | Number of components for max. $R^2$ Value | 29 | 25 |
| | Number of components for min. RMSECV | >30 | 26 |
| | RMSECV with 20 Components | 1.095 | 0.601 |

### 8.5.3 Comparison of Statistical Models: Conclusions

This section describes a comparison of the performances of PCR and PLSR statistical models when applied to the same set of ATR-FTIR spectra. PLSR was the best-performing of the two models, when applied to both ATR-FTIR ratio spectra and ATR-FTIR single-beam spectra, with respect to the modelling of data and predictive accuracy. These results may be explained by the differing mechanisms by which the two models operate: PCR is an unsupervised technique that does not consider the dependent variable when constructing principal components to explain the variation in the data whilst PLSR, as a supervised technique, does consider the dependent variable.

These results suggested that predictive statistical modelling could successfully be used to analyse the spectra generated by an ATR-FTIR spectroscopy-based sensor for glucose, lactate and pyruvate. The results presented in this section led to the selection of the PLSR model for further refinement and testing.

## 8.6 ATR-FTIR: Effect of Spectral Range

Having chosen to analyse the acquired ATR-FTIR spectra using a predictive PLSR model, attempts were made to optimise its performance. The intention behind the use of the model was to predict the concentrations of glucose, lactate and pyruvate directly from the ATR-FTIR spectra of solutions containing one, two or three of those compounds. As a result, it was concluded that the most important parameter of the PLSR model was the degree of error in its prediction of glucose, lactate and pyruvate concentrations. This section describes the work undertaken to minimise that error.

One factor that was assumed to have a significant impact on the error in prediction of the model was the spectral range over which the model was applied. A systematic study was therefore carried out to determine which spectral interval yielded the lowest RMSECV. This parameter was again selected over the RMSEP in order to retain the size of the training dataset. Minimisation of the RMSECV was achieved by assessing two spectral parameters: the size of the interval and the region of the spectrum in which the interval was located. The assessed interval sizes were: 100, 200, 300, 400, 500, 600, 700, 800, 900 and 1000 $cm^{-1}$. The region of the spectrum over which the interval was located was defined by the 'interval start point', which marked the lowest end of the interval range (in $cm^{-1}$). Interval start points occurred every 100 $cm^{-1}$.

Intervals of all selected sizes were assessed at each interval start point. For example, for an interval start point of 1000 $cm^{-1}$, the following intervals were assessed:

- 1000 - 1100 $cm^{-1}$ (Interval size = 100 $cm^{-1}$)
- 1000 - 1200 $cm^{-1}$ (Interval size = 200 $cm^{-1}$)

- 1000 - 1300 $cm^{-1}$ (Interval size = 300 $cm^{-1}$)
- 1000 - 1400 $cm^{-1}$ (Interval size = 400 $cm^{-1}$)
- 1000 - 1500 $cm^{-1}$ (Interval size = 500 $cm^{-1}$)
- 1000 - 1600 $cm^{-1}$ (Interval size = 600 $cm^{-1}$)
- 1000 - 1700 $cm^{-1}$ (Interval size = 700 $cm^{-1}$)
- 1000 - 1800 $cm^{-1}$ (Interval size = 800 $cm^{-1}$)
- 1000 - 1900 $cm^{-1}$ (Interval size = 900 $cm^{-1}$)
- 1000 - 2000 $cm^{-1}$ (Interval size = 1000 $cm^{-1}$)

A PLSR model was applied to every selected spectral interval and was calibrated using the leave-one-out method of cross-validation. At each interval, the model was iterated multiple times using a different number of components, up to a maximum of 20 components, until the overall RMSECV for all three compounds was minimised. The minimised RMSECV, and the number of components needed to achieve it, were recorded for each interval. This procedure was carried out separately on the datasets of ratio ATR-FTIR spectra and single-beam ATR-FTIR spectra and was applied to the spectral range 4000 - 650 $cm^{-1}$.

### 8.6.1 Effect of Spectral Range: ATR-FTIR Ratio Spectra

The results of the interval study carried out on ATR-FTIR ratio spectra are summarised in Figure 8.8. The centre of each coloured rectangle in the figure can be mapped to an interval start point ($x$-axis) and an interval size ($y$-axis), whilst the colour of the rectangle reflects the lowest-achievable RMSECV of the model when it is applied to the specified spectral interval using a maximum of 20 components. It can be seen that the overall RMSECV for all compounds was lowest for intervals with a starting point between 700 – 1400 $cm^{-1}$. This could be predicted from the work described in Chapter 6, in which the majority of absorbance peaks in the ATR-FTIR spectra of glucose, lactate and pyruvate were located in the fingerprint region of the spectrum.

The interval yielding the lowest overall RMSECV had a size of 600 $cm^{-1}$ and was located at the 900 – 1500 $cm^{-1}$ region of the spectrum. The overall RMSECV of this interval was 0.226 mM, whilst the RMSECV for the prediction of the concentrations, in mM, of each individual compound over this interval were:

- **Glucose:** 0.20
- **Lactate:** 0.08

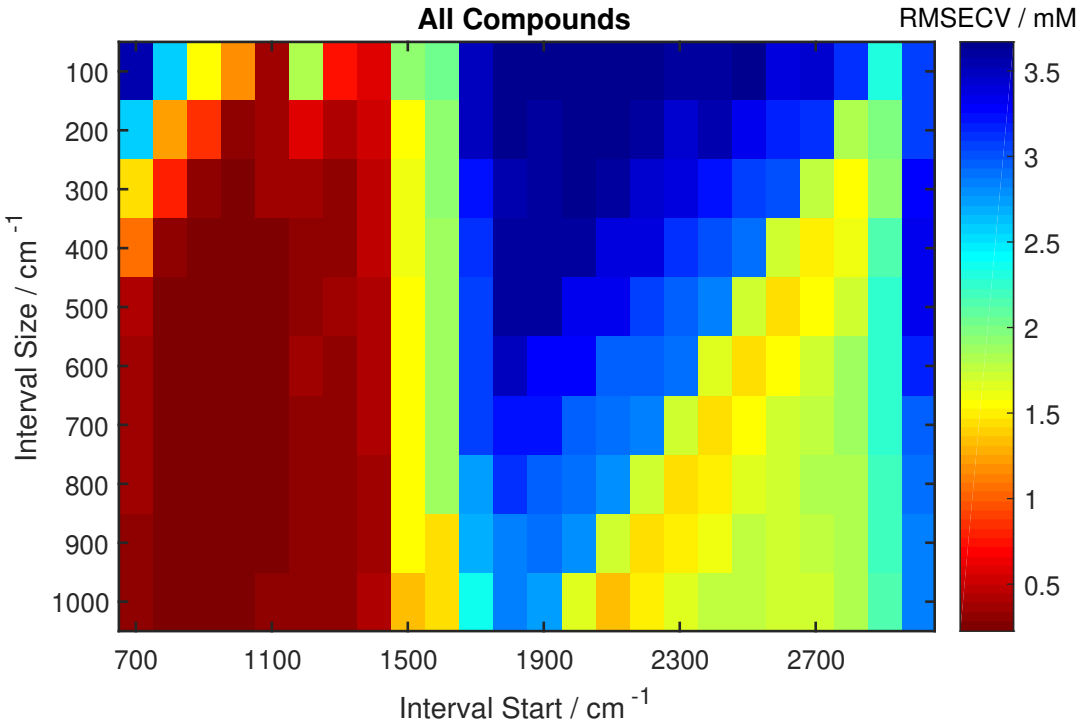


***Figure 8.8:*** *A colourmap showing the effect of spectral interval location and size on the RMSECV of a PLSR model applied to ATR-FTIR ratio spectra.*

- **Pyruvate:** 0.068

A 20-component model was required in order to achieve these RMSECV values. These errors were lower than those achieved by applying the PLSR model over the whole spectrum, as seen in Section 8.5.1, and therefore this study was successful in improving the predictive performance of PLSR when applied to ATR-FTIR ratio spectra.

### 8.6.2 Effect of Spectral Range: ATR-FTIR Single-Beam Spectra

The results of the interval study carried out on ATR-FTIR single-beam spectra are summarised in Figure 8.9.

These results show a general increase in the overall RMSECV across all intervals when compared with the analysis of ATR-FTIR ratio spectra. This trend is in agreement with the observation in Section 8.5.2 that statistical modelling of single-beam ATR-FTIR spectra is more complex than that of ATR-FTIR ratio spectra. It can be seen from the figure that the intervals yielding the lowest overall RMSECV are those between 200 – 400 $^{-1}$ in length which begin at 900 cm$^{-1}$ or 1000 cm$^{-1}$.

The interval which produced the lowest overall RMSECV had a size of 400 cm$^{-1}$ and was located at the 900 – 1300 cm$^{-1}$ region of the spectrum. A 20-component

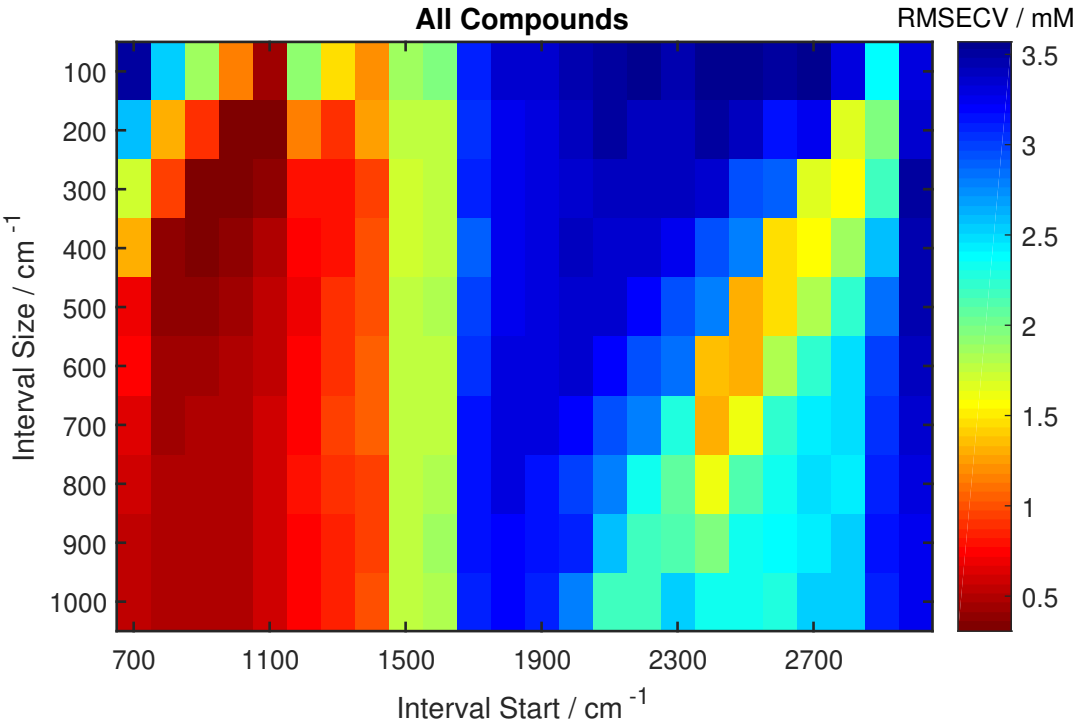


***Figure 8.9:*** *A colourmap showing the effect of spectral interval location and size on the RMSECV of a PLSR model applied to ATR-FTIR single-beam spectra.*

model was required in order to achieve an overall RMSECV for this interval of 0.306 mM. The RMSECV for the prediction of the concentrations, in mM, of each individual compound over this interval were:

- **Glucose:** 0.26
- **Lactate:** 0.12
- **Pyruvate:** 0.112

Once again, the RMSECV for the prediction of the concentration of each individual compound was lower than that achieved when PLSR was applied over the whole spectral range, as seen in Section 8.5.2, meaning that this study was successful in improving the predictive performance of the model when applied to ATR-FTIR single-beam spectra.

### 8.6.3 Effect of Spectral Range: Conclusions

This section has described the work undertaken to lower the RMSECV of a PLSR model, applied to the prediction of glucose, lactate and pyruvate concentrations from ATR-FTIR spectra, by identifying an optimum spectral range over which to apply

the model. The values of the RMSECV generated for both ratio and single-beam ATR-FTIR spectra were successfully lowered from those obtained by applying the same model over the whole spectrum. The model achieved a lower overall RMSECV value, as well as lower RMSECV values for the prediction of all three compounds, when applied to ratio spectra than when applied to single-beam spectra.

## 8.7 ATR-FTIR: Prediction of LPR

The LPR is an important indicator of patient outcome following TBI, as discussed in Section 2.4.3, with a value of 25 considered to be the pathological threshold.[7] Accurate calculation of the LPR would therefore be an important indicator of the performance of an ATR-FTIR-based sensor for metabolic profiling of TBI patients.

The ability of the optimised PLSR models to accurately detect the LPR from ATR-FTIR spectral data was analysed by randomly dividing the spectra into 'training' and 'test' datasets. A test dataset size of 64 spectra, corresponding to approximately 10% of the dataset, was chosen in order to maximise the size of the training set. PLSR was carried out on the training dataset, over the spectral region identified in Section 8.6 as yielding the lowest overall RMSECV, and calibrated using leave-one-out cross-validation. The calibrated model was then applied to the test dataset for the prediction of glucose, lactate and pyruvate concentrations and the predicted LPR was determined by dividing the predicted concentration of lactate by the predicted concentration of pyruvate for each sample. The actual LPR was calculated by dividing the observed concentrations of lactate and pyruvate for each sample in the dataset. This process was used to predict the LPR from both ratio and single-beam spectra.

### 8.7.1 ATR-FTIR: Prediction of LPR from Ratio Spectra

The PLSR model used to predict the LPR from the dataset of ATR-FTIR ratio spectra was applied over the spectral range 1500 - 900 $cm^{-1}$ and used 20 components, the combination identified in Section 8.6 as yielding the lowest overall RMSECV. A comparison of the observed and predicted values of the LPR can be seen in Figure 8.10(a).

It is clear from the figure that there was a significant error in the prediction of LPR values. Most notably, a number of the predicted values are negative, which indicates that the PLSR model had predicted negative concentration values for either lactate or pyruvate. The $R^2$ value for a linear relationship between the observed and predicted values of the LPR was 0.10, which confirms a significant lack of agreement between the two sets of values and hence a large error in the prediction of the LPR. The magnitude of the error in LPR prediction is explained by the fact that the individual errors in the prediction of lactate and pyruvate were compounded by the division of

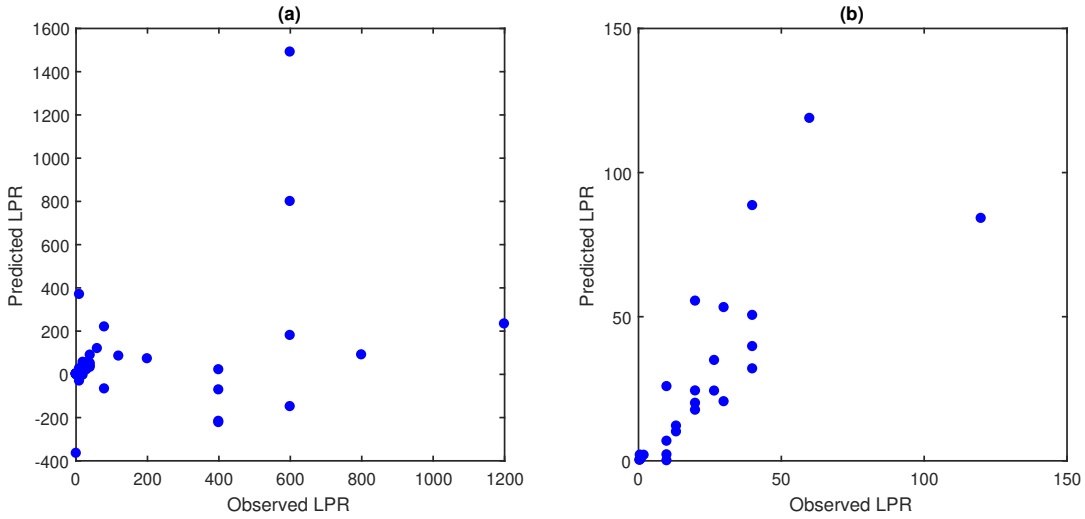


***Figure 8.10:*** *Scatter plots showing the observed vs. predicted LPR. Predicted values of the LPR were derived from the concentrations of lactate and pyruvate predicted from ATR-FTIR ratio spectra using a PLSR model. Plot (a) shows all results, whilst (b) shows only the region containing the most data points.*

the two values to generate the predicted LPR.

However, it was noted that when the scale of Figure 8.10(a) was adjusted to show only the region of the plot in which the majority of the data points were located, the relationship between the observed and predicted LPR appeared did appear to be qualitatively more linear (Figure 8.10(b)).

### 8.7.2 ATR-FTIR: Prediction of LPR from Single-Beam Spectra

A 20-component PLSR model was used to predict the LPR from ATR-FTIR single-beam spectra and was applied over the spectral range identified in Section 8.6 as yielding the lowest overall RMSECV (1300 - 900 $cm^{-1}$). A comparison of the observed and predicted values of the LPR is shown in Figure 8.11. Once again, there was a significant error in the prediction of the LPR, as confirmed by an $R^2$ value for a linear relationship of the data of 0.04. In addition, several of the predicted LPR values were negative, indicating that the PLSR model had again generated negative values of the concentrations of lactate or pyruvate.

The prediction of the LPR from ATR-FTIR ratio spectra was more accurate than that obtained using ATR-FTIR single-beam spectra. This was expected due to the higher RMSECV exhibited by a PLSR model when applied to single-beam spectra.

### 8.7.3 Prediction of LPR: Conclusions

This section describes an attempt to predict the LPR from ATR-FTIR spectra via a straightforward division of the concentrations of lactate and pyruvate predicted using

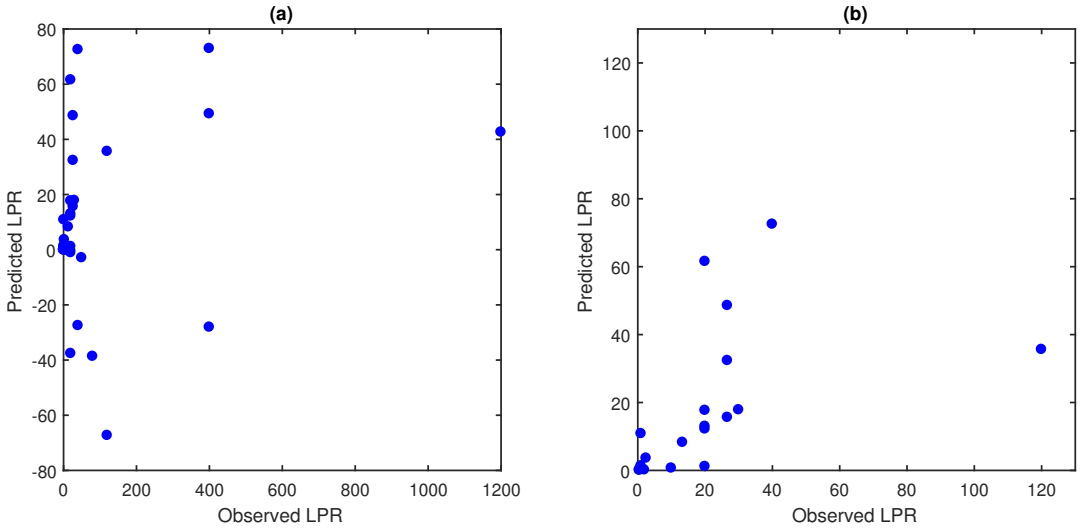


***Figure 8.11:*** *Scatter plots showing the observed vs. predicted LPR. Predicted values of the LPR were derived from the concentrations of lactate and pyruvate predicted from ATR-FTIR single-beam spectra using a PLSR model. Plot (a) shows all results, whilst (b) shows only the region containing the most data points.*

a PLSR model. It has been shown that the RMSEP currently achieved by the model, particularly with respect to the prediction of pyruvate concentrations, was too high to allow accurate prediction of the LPR using this method. Of particular concern was the prediction of negative LPR values, for both ratio and single-beam spectra, which indicate that the PLSR models had calculated negative values for the concentration of either lactate or pyruvate. This generation of invalid predictions shows that, in their current form, the models are not suitable for use in the clinic. However, it is noted that the RMSEP may have been affected by the reduction in the size of the training datasets of ratio and single-beam spectra, which was caused by the separation of the datasets into 'training' and 'test' datasets.

## 8.8 Conclusions

This chapter has described a systematic study of the potential of ATR-FTIR to be used as the basis of a sensor for the analysis of glucose, lactate and pyruvate concentrations present in microdialysate from TBI patients. A range of synthetic solutions of glucose, lactate and pyruvate, contaning one, two or three compounds, was rationally selected using patient data and reported literature values. Prepared samples were analysed via ATR-FTIR spectroscopy, using a seven-reflection ZnSe crystal, to yield two large datasets of 643 ratio spectra and 643 single-beam spectra.

Two statistical models were applied to each dataset: PCR and PLSR. It was found that PLSR performed better at both the modelling and prediction of data and

therefore this model was selected for optimisation. A systematic study identified an optimum spectral range over which the model should be applied, which minimised the overall RMSECV, of 1500 – 900 $cm^{-1}$ for ATR-FTIR ratio spectra and 1300 – 900 $cm^{-1}$ for single-beam spectra. In both cases, 20 components were required to achieve the minimum RMSECV.

The application of the optimised PLSR model to ATR-FTIR ratio spectra was found to yield a lower RMSECV, both overall and for each compound studied, than that obtained when the model was applied to single-beam spectra. This was explained by the additional information contained within single-beam spectra, which are affected by instrument optics and the sample environment, which is not present in ratio spectra due to the way in which it is derived.

The viability of using ATR-FTIR spectroscopy, in combination with the optimised PLSR model, for metabolic profiling of TBI patients can be assessed by comparing the RMSECV of the optimised PLSR model with the value of the lowest concentration of each compound that a developed sensor would be required to detect. This is due to the fact that, in order to accurately quantify a given concentration, the error in measurement must be lower than that concentration. It can therefore be assumed that the RMSECV for the prediction of each compound must be lower than the minimum possible clinical concentration of that compound in order for a developed sensor to perform accurately over the whole clinical range. A comparison of these values for the optimised PLSR model applied to ATR-FTIR ratio spectra is shown in Table 8.7.

***Table 8.7:*** *A comparison of the RMSECV of the optimised PLSR model, as applied to the detection of glucose, lactate and pyruvate from ATR-FTIR ratio spectra, with the lowest concentration of each compound that a developed sensor would be required to detect.*

| Compound | RMSECV / mM | Minimum Concentration / mM |
|---|---|---|
| Glucose | 0.2 | 0.1 |
| Lactate | 0.08 | 0.1 |
| Pyruvate | 0.068 | 0.01 |

It is shown in Table 8.7 that the RMSECV for the prediction of lactate concentrations was below the lowest limit that a developed ATR-FTIR sensor woud be required to detect. This error was therefore assumed to be acceptable. The RMSECV for the prediction of glucose concentrations is double the lowest concentration that a developed sensor would be required to detect. This is considered a promising result which may be improved upon with further model refinement, such as that achieved with a larger dataset. However, the RMSECV in the prediction of pyruvate concentrations is six times higher than the required limit of detection, which is an unacceptable level of accuracy. It is not clear whether model optimisation alone would be sufficient to improve this value or whether changes to the experimental setup would be necessary.

This is discussed further in Chapter 10.

# Chapter 9

# Analysis of Glucose, Lactate and Pyruvate Mixtures via Transmission-FTIR Spectroscopy

This chapter describes the selection and optimisation of a statistical model for the prediction of glucose, lactate and pyruvate concentrations from transmission-FTIR spectra of solutions containing one, two or all three compounds. This study was designed to be compared directly with the corresponding study of ATR-FTIR spectra described in Chapter 8. The aims of this study were thus two-fold: one aim was to determine the accuracy with which clinically-relevant concentrations of glucose, lactate and pyruvate could be predicted from transmission-FTIR spectra, in order to assess the feasibility of using transmission-FTIR spectroscopy for on-line metabolic profiling of TBI patients. The second aim of this study was to compare its results with those generated by the ATR-FTIR spectroscopy study to allow a comparison of the two techniques and determine which one holds the most promise for development into an on-line sensor.

As discussed in Chapter 8, clinical microdialysate samples were not used for the identification or optimisation of the statistical model used in this work. Instead, identical synthetic samples to those used in the ATR-FTIR spectroscopy study were freshly prepared and analysed via transmission-FTIR spectroscopy using a 50 $\mu$m path length. Subsequent analysis of the acquired spectra followed the same methods as those described in Chapter 8. The performances of two linear regression models (PCR and PLSR) were compared and PLSR was found to generate the most promising results. This model was subsequently optimised and used to estimate the LPR of the spectral data. Finally, the optimised PLSR model was applied predictively to the transmission-FTIR spectra of six clinical samples. This latter experimental step was performed only during this transmission-FTIR study, and not during the ATR-FTIR

study, due to the fact that the volumes of clinical samples were significantly lower than the sample volumes required for the acquisition of ATR-FTIR spectra.

## 9.1 Mixture Selection

The two- and three component mixtures selected in Chapter 8 were freshly prepared again for use in this study. The pure solutions prepared specifically for use in the ATR-FTIR study were also freshly prepared and used in this work. However, the total number of single-component spectra analysed in this study was slightly different to the number analysed in Chapter 8, as a result of the later addition to the ATR-FTIR study of data acquired during the ATR-FTIR crystal study. The equivalent transmission-FTIR accessory work was conducted to identify the most suitable path length for use in this transmission-FTIR study, as described in Section 6.4.2. It was carried out only on solutions of glucose, and used fewer concentrations than the ATR-FTIR crystal study, meaning that the addition of the data to that acquired in this study did not increase the size of the dataset to the same degree. The single-component solutions analysed in this study, including those analysed as part of the path length study, are therefore summarised in Table 9.1.

***Table 9.1:*** *Concentrations of glucose, lactate and pyruvate studied as pure solutions via transmission-FTIR spectroscopy, including those from the transmission-FTIR path length study.*

| Glucose / mM | Lactate / mM | Pyruvate / mM |
|---|---|---|
| 0.05 | 0.05 | 0.005 |
| 0.10 | 0.10 | 0.01 |
| 0.20 | 0.20 | 0.02 |
| 0.40 | 0.50 | 0.05 |
| 0.70 | 2.00 | 0.10 |
| 1.00 | 4.00 | 0.15 |
| 1.50 | 6.00 | 0.20 |
| 3.00 | 10.00 | 1.00 |
| 5.00 | | |
| 6.00 | | |
| 10.0 | | |
| 24.0 | | |

## 9.2 Data Acquisition

Data acquisition followed a very similar protocol to that used for the ATR-FTIR mixture study. The main difference between the two protocols was the fact that spectra acquired for this study were obtained using the Specac Pearl Liquid Transmission Accessory for the Perkin Elmer Spectrum 100 FTIR Spectrometer, coupled with an

Oyster cell of 50 $\mu$m path length. The 50 $\mu$m path length had previously been identified, from a selection of path lengths, as exhibiting the best performance in the detection of pure solutions of glucose, lactate and pyruvate (Section 6.4.2).

Three aliquots of each solution were analysed and two transmission-FTIR spectra were acquired of each aliquot: one ratio spectrum, in which perfusion fluid was used as the background, and one single-beam spectrum. Spectra of perfusion fluid only, in which the concentrations of glucose, lactate and pyruvate were zero, were also acquired. A total of 8 aliquots of perfusion fluid were analysed and two spectra were acquired of each aliquot: one ratio spectrum, in which perfusion fluid was also used as the background, and one single-beam spectrum.

This process was used to acquire two large datasets of 575 spectra: one containing transmission-FTIR ratio spectra and one containing transmission-FTIR single-beam spectra. As with the ATR-FTIR study, each dataset was used in its entirety for the analysis described in this chapter, without differentiating between the spectra of one-, two- and three-component solutions.

A sample of the spectra from each dataset can be seen in Figures 9.1 and 9.2. The spectra plotted in this figure were selected by choosing every 35th spectrum from a list of all spectra ordered by increasing glucose concentration.

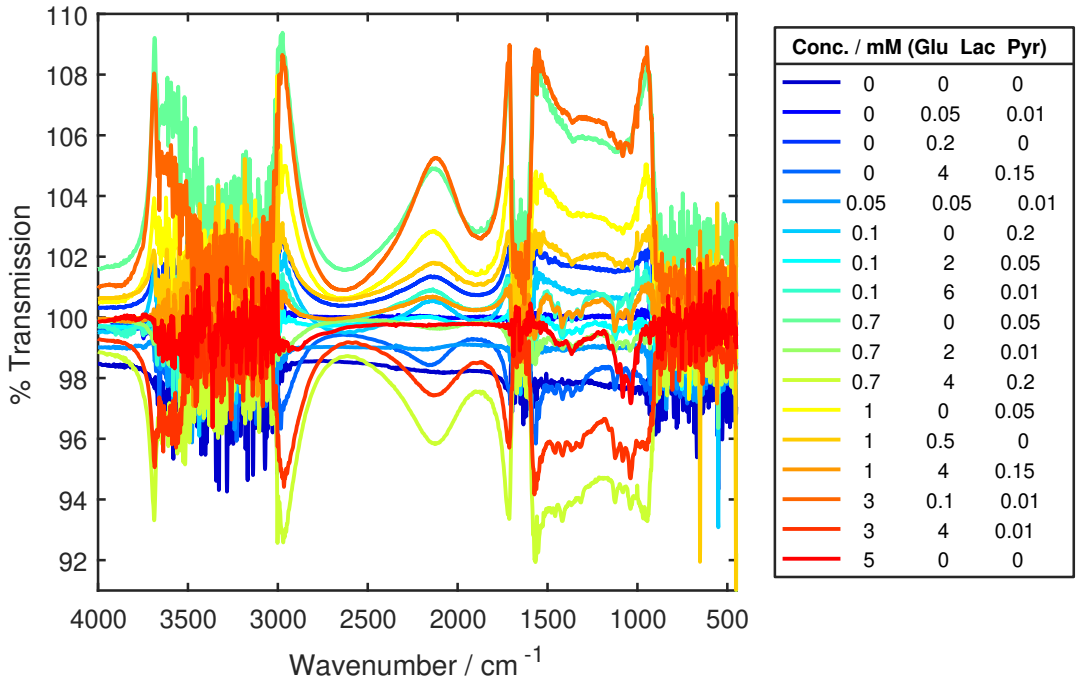


***Figure 9.1:*** *A randomly-selected sample of the transmission-FTIR ratio spectra acquired for the transmission-FTIR mixture study. Concentrations are listed in the horizontal order: glucose - lactate - pyruvate.*

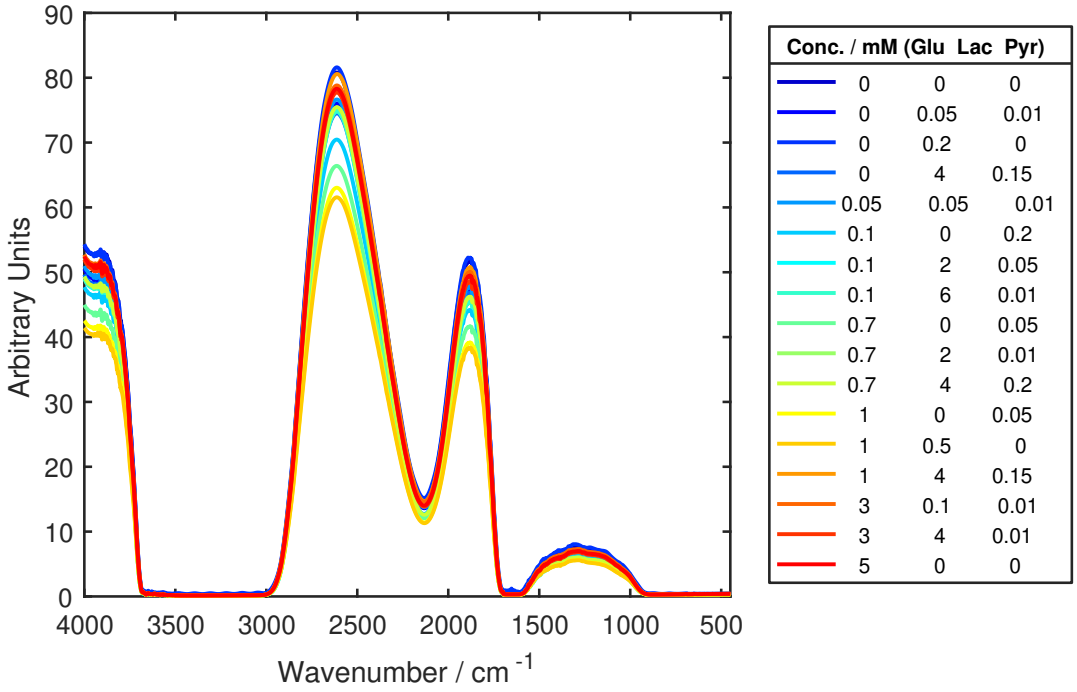


***Figure 9.2:*** *A randomly-selected sample of the transmission-FTIR single-beam spectra acquired for the transmission-FTIR mixture study. Concentrations are listed in the horizontal order: glucose - lactate - pyruvate.*

### 9.2.1 Data Acquisition: Conclusions

This section has described the process used to generate two large datasets of transmission-FTIR spectra, one containing ratio spectra and one containing single-beam spectra, both of which were acquired using the same set of samples.

## 9.3 Transmission-FTIR: Comparison of Statistical Models

The transmission-FTIR spectral datasets were initially analysed using the two linear regression models employed during the first stage of the ATR-FTIR study: PCR and PLSR. As with the ATR-FTIR study, it was considered logical to apply the model to the maximum possible spectral range, whilst avoiding regions of significant spectral noise. Transmission-FTIR spectra of aqueous solutions contain higher levels of noise than ATR-FTIR spectra, as discussed in Chapter 6, due to the strong absorption of IR radiation by water molecules. It can be seen in Figure 9.1 that the largest regions of noise in transmission-FTIR spectra lie between 3700 – 3000 $cm^{-1}$ and 800 – 450 $cm^{-1}$. The models were therefore applied to the spectral range 3000 – 800 $cm^{-1}$ thoughout this work, in order to avoid these regions.

Both models were applied in turn to each of the datasets and a maximum limit

of 30 components was imposed. The performance of the models was compared using the same criteria as those used in Chapter 8: the number of components needed to achieve the maximum $R^2$ value, the number of components required to minimise the RMSECV, and the RMSECV in prediction of glucose, lactate and pyruvate concentrations achieved when a PLSR model of 20 components was used.

### 9.3.1 PCR *vs.* PLSR: Ratio Transmission-FTIR Spectra

A summary of the performance of a PCR model applied to the transmission-FTIR ratio spectra dataset is shown in Figure 9.3.

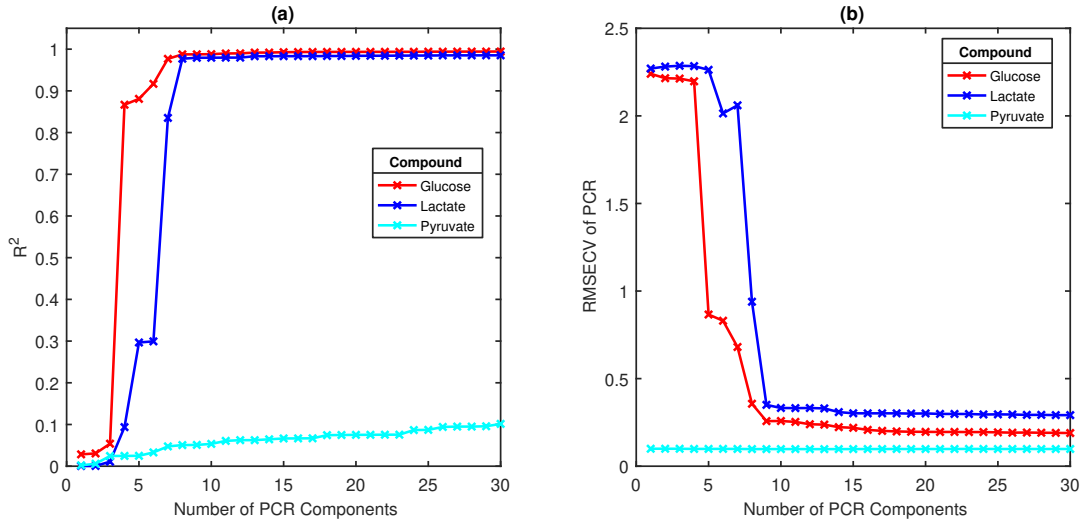


***Figure 9.3:*** *A summary of the performance of a PCR model applied to transmission-FTIR ratio spectra of glucose, lactate and pyruvate. The change in $R^2$ with an increasing number of model components (a) and the change in the RMSECV in predicted concentrations with an increasing number of model components (b), calculated using leave-one-out cross-validation, are shown for each compound.*

It can be seen in Figure 9.3 that, using PCR, both glucose and lactate were accurately modelled with fewer than ten components. The RMSECV of glucose and lactate were also minimised using a model of fewer than ten components. However, the most striking feature of the data was the extremely poor performance of PCR with respect to the modelling and prediction of pyruvate concentrations. The $R^2$ value of the PCR model of pyruvate was close to zero, even when a 30-component model was used, and the RMSECV in prediction of pyruvate concentrations appears to have been unaffected by the number of PCR components used. It was initially thought that these effects may be due to an error in the data, but no such error could be found. Finally, it was concluded that the noise in the spectral region over which the model was applied, particularly at 1600 $cm^{-1}$ where multiple pyruvate peaks are based, was sufficient to mask the contribution of pyruvate to the overall spectrum.

A summary of the performance of a PLSR model applied to the dataset of transmission-FTIR ratio spectra is shown in Figure 9.4

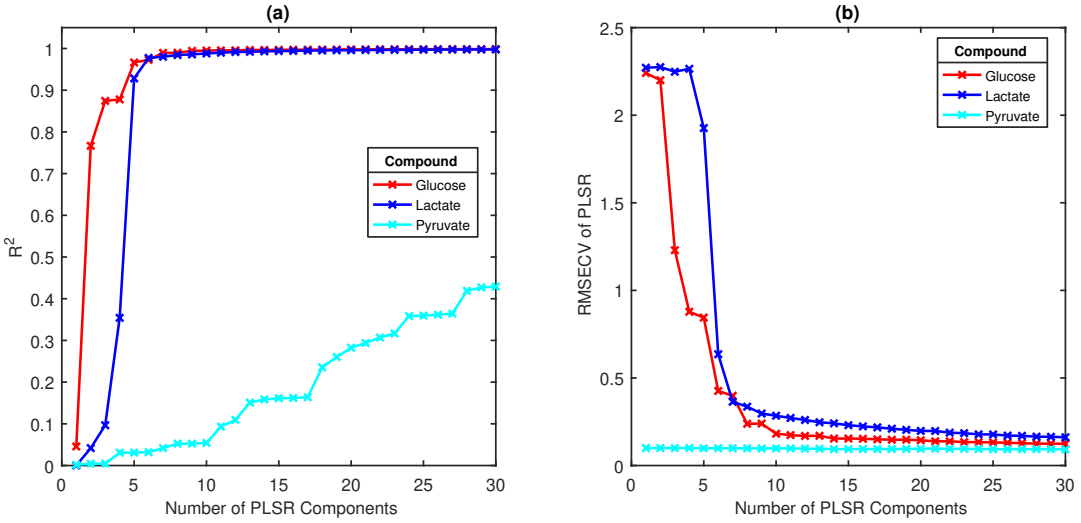


***Figure 9.4:*** *A summary of the performance of a PLSR model applied to transmission-FTIR ratio spectra of glucose, lactate and pyruvate. The change in $R^2$ with an increasing number of model components (a) and the change in the RMSECV in predicted concentrations with an increasing number of model components (b), calculated using leave-one-out cross-validation, are shown for each compound.*

Once again, the poor performance of the model when applied to the modelling and prediction of pyruvate concentrations was the most striking feature of Figure 9.4. The trends exhibited by the PLSR model for each compound were broadly similar to those observed for the PCR model, athough the PLSR model generated better results according to the predefined criteria for model comparison. A quantitative comparison of the PCR and PLSR models, when applied to transmission-FTIR ratio spectra, is provided in Table 9.2.

***Table 9.2:*** *A summary of the performance of PCR and PLSR statistical models when applied to transmission-FTIR ratio spectra.*

| Compound | Parameter | PCR | PLSR |
|---|---|---|---|
| Glucose | Number of components for max. $R^2$ Value | 8 | 7 |
| | Number of components for min. RMSECV | 17 | 14 |
| | RMSECV with 20 components | 0.20 | 0.14 |
| Lactate | Number of components for max. $R^2$ Value | 8 | 6 |
| | Number of components for min. RMSECV | 14 | 14 |
| | RMSECV with 20 components | 0.30 | 0.20 |
| Pyruvate | Number of components for max. $R^2$ Value | >30 | >30 |
| | Number of components for min. RMSECV | 1 | 1 |
| | RMSECV with 20 Components | 0.098 | 0.096 |

The data presented in Table 9.2 confirmed the general trends observed from the

graphical data. PLSR was the better performing model for glucose and lactate by all measured criteria. Interestingly, there was very little difference in the performance of the two models when applied to pyruvate, suggesting again that the contribution of pyruvate to the spectral dataset was minimal.

### 9.3.2 PCR *vs.* PLSR: Single-Beam Transmission-FTIR Spectra

A summary of the performances of the PCR and PLSR models applied to the dataset of transmission-FTIR single-beam spectra are shown in Figures 9.5 and 9.6, respectively. Once again, the most noticeable feature of the data was the equally poor performance of both models when applied to pyruvate.

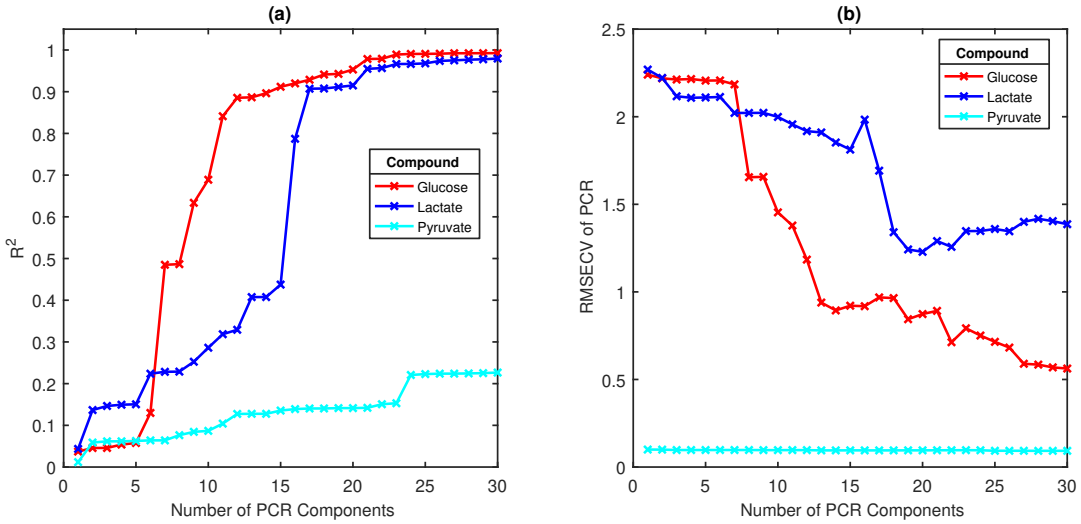


***Figure 9.5:*** *A summary of the performance of a PCR model applied to transmission-FTIR single-beam spectra of glucose, lactate and pyruvate. The change in $R^2$ with an increasing number of model components (a) and the change in the RMSECV in predicted concentrations with an increasing number of model components (b), calculated using leave-one-out cross-validation, are shown for each compound.*

The PLSR model was able to accurately model the glucose and lactate data with fewer components than the number required by the PCR model. The difference between the predictive performance of the two models when applied to glucose and lactate was less stark, but PLSR was again the better-performing model by the criteria considered. One interesting feature of the PCR model was that the relationship between the number of PCR components and the RMSECV in glucose and lactate concentrations appeared to show less correlation than had previously been observed. In the data gathered thus far, an increase in the number of PCR components would lead to a decrease in the RMSECV of the model until the predictive limit of the model was reached. However, in Figure 9.5 it can be seen that, although the general trend was in agreement with that usually observed, there were instances where an increase

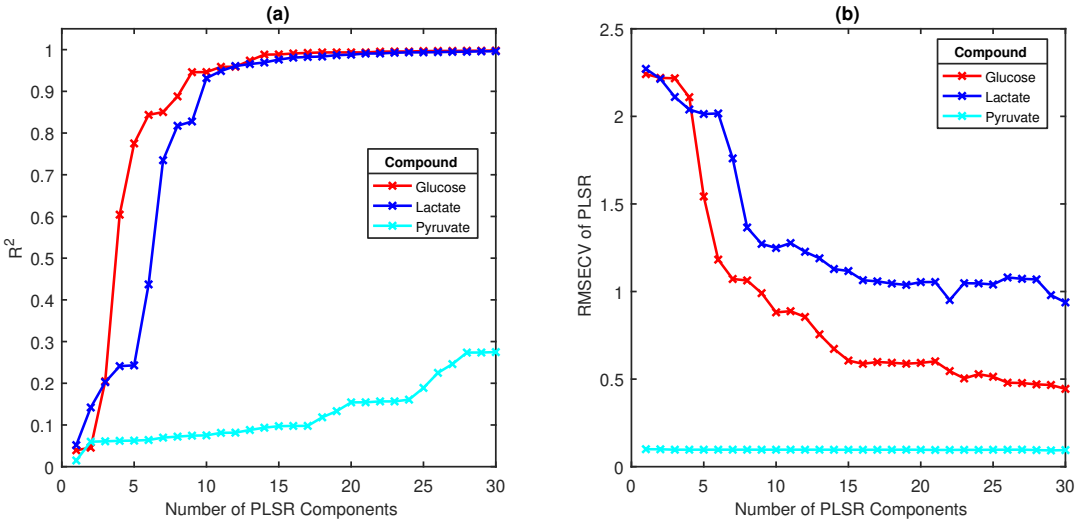


***Figure 9.6:*** *A summary of the performance of a PLSR model applied to transmission-FTIR single-beam spectra of glucose, lactate and pyruvate. The change in $R^2$ with an increasing number of model components (a) and the change in the RMSECV in predicted concentrations with an increasing number of model components (b), calculated using leave-one-out cross-validation, are shown for each compound.*

in the number of model components lead to an increase in the RMSECV, most notably in the transition from 15 to 16 components in the prediction of lactate concentrations.

The performances of PCR and PLSR when applied to transmission-FTIR single-beam spectra are summarised in Table 9.3. In general, the PLSR model was confirmed to produce the better results. One notable exception is in the number of components needed to minimise the RMSECV in the prediction of lactate, which was lower for the PCR model than the PLSR model due to the aforementioned variation in the relationship between the RMSECV and the number of model components.

***Table 9.3:*** *A summary of the performance of PCR and PLSR statistical models when applied to transmission-FTIR single-beam spectra.*

| Compound | Parameter | PCR | PLSR |
|---|---|---|---|
| Glucose | Number of components for max. $R^2$ Value | 23 | 14 |
| | Number of components for min. RMSECV | 29 | 26 |
| | RMSECV with 20 Components | 0.87 | 0.59 |
| Lactate | Number of components for max. $R^2$ Value | 23 | 21 |
| | Number of components for min. RMSECV | 20 | 30 |
| | RMSECV with 20 Components | 1.23 | 1.05 |
| Pyruvate | Number of components for max. $R^2$ Value | >30 | >30 |
| | Number of components for min. RMSECV | 1 | 1 |
| | RMSECV with 20 Components | 0.095 | 0.097 |

### 9.3.3 Comparison of Statistical Models: Conclusions

This section describes a comparison of the performances of PCR and PLSR statistical models when applied to the same sets of transmission-FTIR ratio and single-beam spectra. The PLSR model generally produced better results then the PCR model for both the modelling and prediction of glucose and lactate concentrations, for both datasets, as observed in the equivalent study of ATR-FTIR spectral data. However, in contrast to the study of ATR-FTIR spectra, both models performed extremely poorly when applied to the modelling and prediction of pyruvate concentrations. The reason for this was unknown, but it was hypothesised that the increased spectral noise in transmission-FTIR spectra of aqueous solutions, when compared with the spectral noise seen in equivalent ATR-FTIR spectra, may have masked the contribution of pyruvate to the spectra.

Both models perfomed less well at both the modelling and prediction of glucose and lactate concentrations when applied to the single-beam dataset than when applied to the ratio dataset. The performances of the two models when applied to pyruvate were similar for both the single-beam and ratio datasets.

These results suggested that predictive statistical modelling could successfully be used to analyse transmission-FTIR spectra of glucose and lactate. Based on the results presented in this section, the PLSR model was selected for further refinement to improve the predictive accuracy of the model when applied to glucose and lactate and to determine whether its performance with respect to pyruvate could be improved.

## 9.4 Transmission-FTIR: Effect of Spectral Range

An interval analysis, identical to that carried out during the study of ATR-FTIR spectra, was performed on both transmission-FTIR datasets to determine the region of the spectrum to which the PLSR model should be applied in order to minimise the RMSECV in the prediction of glucose, lactate and pyruvate concentrations. The analysis was carried out as described in Section 8.6 and was applied to the spectral range 3000 - 800 $cm^{-1}$.

### 9.4.1 Spectral Range: Transmission-FTIR Ratio Spectra

The results of the interval study carried out on transmission-FTIR ratio spectra are summarised in Figure 9.7.

It is clear from the figure that interval start points between 900 – 1100 $cm^{-1}$ yielded the lowest overall RMSECV in the prediction of the concentrations of all compounds. The lowest RMSECV of 0.202 mM was achieved using an interval range of 1000 – 1500 $cm^{-1}$ and a 15-component model. Using these parameters, the achievable RMSECV, in mM, for each individual compound were:

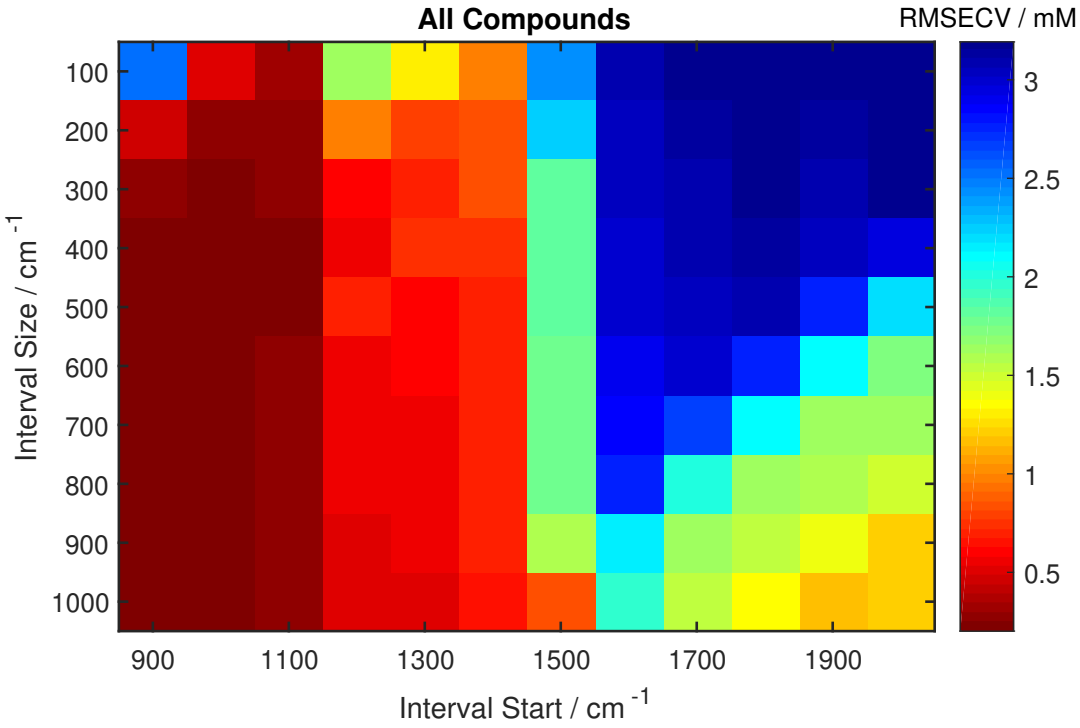


***Figure 9.7:*** *A colourmap showing the effect of spectral interval location and size on the overall RMSECV of a PLSR model applied to transmission-FTIR ratio spectra.*

- **Glucose:** 0.12
- **Lactate:** 0.15
- **Pyruvate:** 0.070

These values of the RMSECV achieved for each compound were lower than those achieved in the previous section when a 20-component model was applied across the whole spectral range, indicating that the model had been improved. Notably, the RMSECV in the prediction of pyruvate concentrations, which was found in the previous section to be very poor, had reduced by approximately 30%.

### 9.4.2 Spectral Range: Transmission-FTIR Single-Beam Spectra

The results of the interval study carried out on transmission-FTIR single-beam spectra are summarised in Figure 9.8. The data indicated that the lowest values of the RMSECV were achieved using intervals of 300 –500 $cm^{-1}$ in size, with a start point between 900 – 1100 $cm^{-1}$.

The interval which produced the lowest overall RMSECV had a size of 400 $cm^{-1}$ and was located at the 1000 – 1400 $cm^{-1}$ region of the spectrum. A 19-component model was required in order to achieve an overall RMSECV for this interval of 0.224.

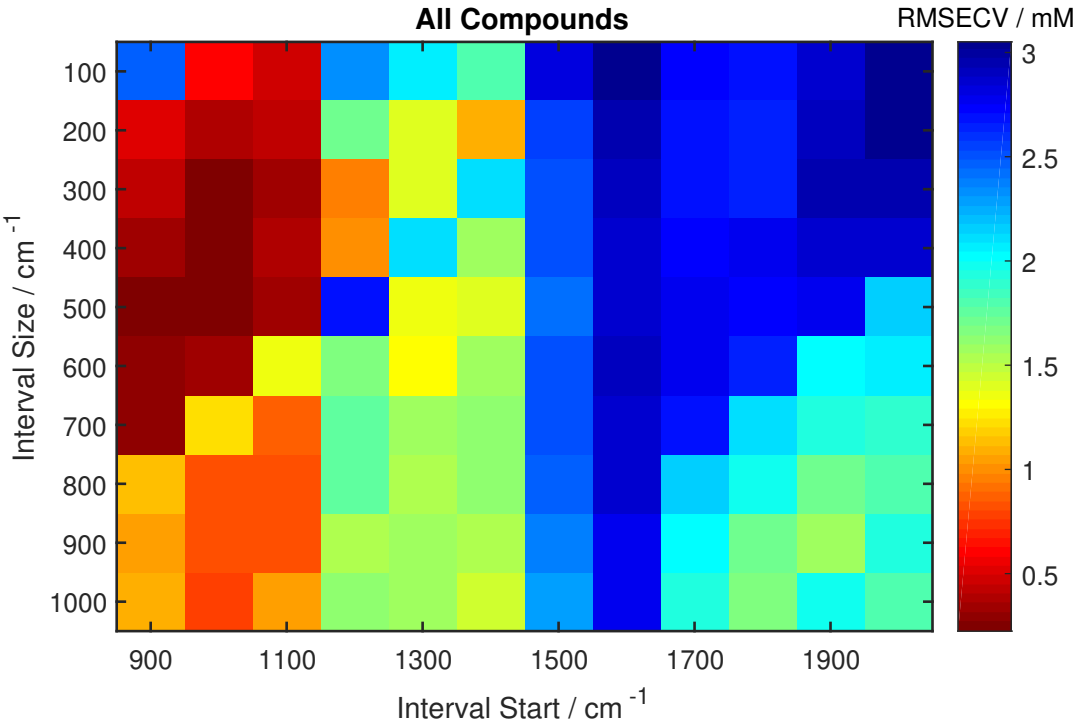


***Figure 9.8:*** *A colourmap showing the effect of spectral interval location and size on the overall RMSECV of a PLSR model applied to transmission-FTIR single-beam spectra.*

The RMSECV in the prediction of the concentrations, in mM, of each individual compound over this interval were:

- **Glucose:** 0.12
- **Lactate:** 0.17
- **Pyruvate:** 0.071

Once again, the RMSECV in the prediction of pyruvate concentrations was reduced by approximately 30% compared to the value generated when a 20-component PLSR model was applied across the whole spectral range. The RMSECV for glucose and lactate was also reduced, indicating that the model had successfully been optimised.

### 9.4.3 Effect of Spectral Range: Conclusions

This section describes the work undertaken to optimise the predictive performance of PLSR, as measured by the RMSECV, when applied to both ratio and single-beam transmission-FTIR spectra. The RMSECV was reduced for the prediction of the concentrations of all compounds of interest, compared with the respective values achieved

by a PLSR model applied over the whole spectral range, indicating that this aim had been achieved. Significantly, the RMSECV for pyruvate was reduced by approximately 30% for both ratio and single-beam spectra.

The application of the PLSR model to transmission-FTIR ratio spectra was found to yield slightly lower RMSECV values for lactate and pyruvate than when the model was applied to transmission-FTIR single-beam spectra. The achieved RMSECV in the prediction of glucose concentrations was the same for both datasets. This was a contrast to the results generated by the interval study carried out on ATR-FTIR spectra, in which the application of PLSR to ATR-FTIR ratio spectra generated significantly lower values of the RMSECV, for all compounds, than when the model was applied to ATR-FTIR single-beam spectra.

## 9.5 Transmission-FTIR: Prediction of LPR

An attempt was made to predict the LPR from both transmission-FTIR datasets, using the same method as that applied in the equivalent ATR-FTIR study. A test dataset of 57 spectra, corresponding to approximately 10% of the total dataset, was chosen in order to maximise the size of the training set. PLSR was applied to the training dataset, over the spectral region identified by the interval studies as yielding the lowest overall RMSECV, and calibrated using leave-one-out cross-validation. The calibrated model was then applied to the spectra in the test dataset to generate predictions of glucose, lactate and pyruvate concentrations. The predicted LPR was determined by dividing the predicted lactate concentration by that of pyruvate for each sample. The actual LPR was calculated by dividing the observed concentrations of lactate and pyruvate for each sample in the dataset.

### 9.5.1 Prediction of LPR from Ratio Spectra

Predictions of the LPR from transmission-FTIR ratio spectra were generated by applying a 15-component PLSR model to the 1500 – 1000 $cm^{-1}$ region of the datset. A comparison of the observed and predicted values of the LPR is shown in Figure 9.9.

As seen in Figure 9.9(a), there was very little correlation between the observed and predicted values of the LPR, as confirmed by a calculated $R^2$ value of 0.00. However, when the plot shown in Figure 9.9(a) was scaled to show only the region where the majority of the datapoints were located (Figure 9.9(b)) there did appear to be a linear relationship in the data, suggesting that the overall $R^2$ value was affected by outlying data points with very large errors. In addition, one value of the LPR was predicted to be negative, indicating that the PLSR model had calculated a negative value for the concentration of either lactate or pyruvate. The magnitude of the error in LPR prediction is explained by the fact that the individual errors in the prediction

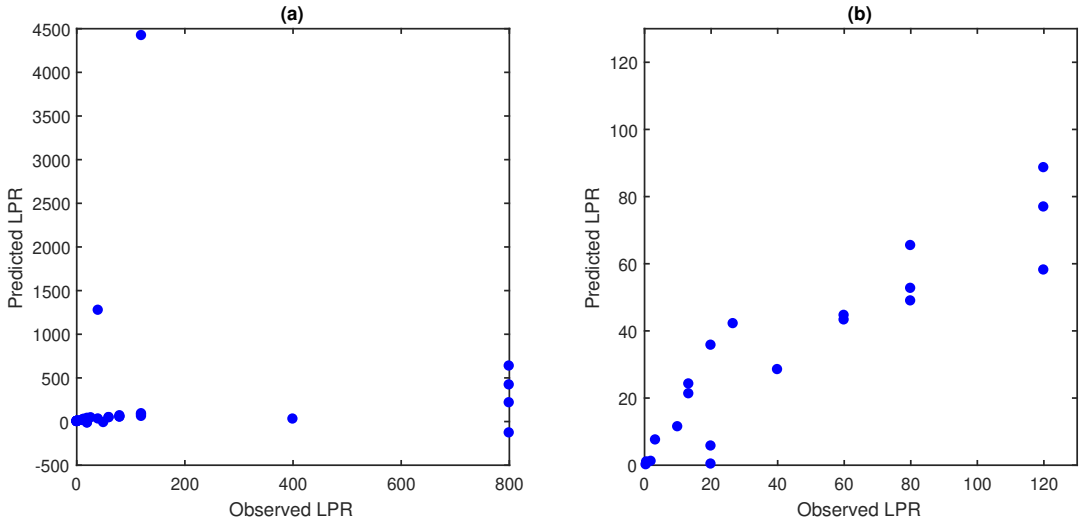


***Figure 9.9:*** *Scatter plots showing the observed vs. predicted LPR. Predicted values of the LPR were derived from the division of the concentrations of lactate and pyruvate predicted from transmission-FTIR ratio spectra using a PLSR model. Plot (a) shows all results, whilst (b) shows only the region containing the most data points.*

of lactate and pyruvate were compounded by the division of the two values to generate the predicted LPR.

### 9.5.2 Prediction of LPR from Single-Beam Spectra

The PLSR model used to predict the LPR from transmission-FTIR single-beam spectra used 19 components and was applied over the spectral range identified as yielding the lowest overall RMSECV (1400 - 1000 $cm^{-1}$). A comparison of the observed and predicted values of the LPR is shown in Figure 9.10(a). Once again, there was a significant error in the prediction of the LPR, as confirmed by an $R^2$ value for a linear relationship of the data of 0.01, but a more qualitatively linear relationship was observed when the plot was scaled to show only the region where the majority of the datapoints were located (Figure 9.10(b)). A small number of predicted LPR values were negative and therefore it was concluded that the PLSR model had, once again, predicted negative concentrations of either lactate or pyruvate.

### 9.5.3 Prediction of LPR: Conclusions

This section describes an attempt to predict the LPR from both ratio and single-beam transmission-FTIR spectra, via a straightforward division of the concentrations of lactate and pyruvate predicted using a PLSR model. It has been shown that the RMSEP of the model, particularly with respect to the prediction of pyruvate concentrations, was too high to allow accurate prediction of the LPR using this method. A particular

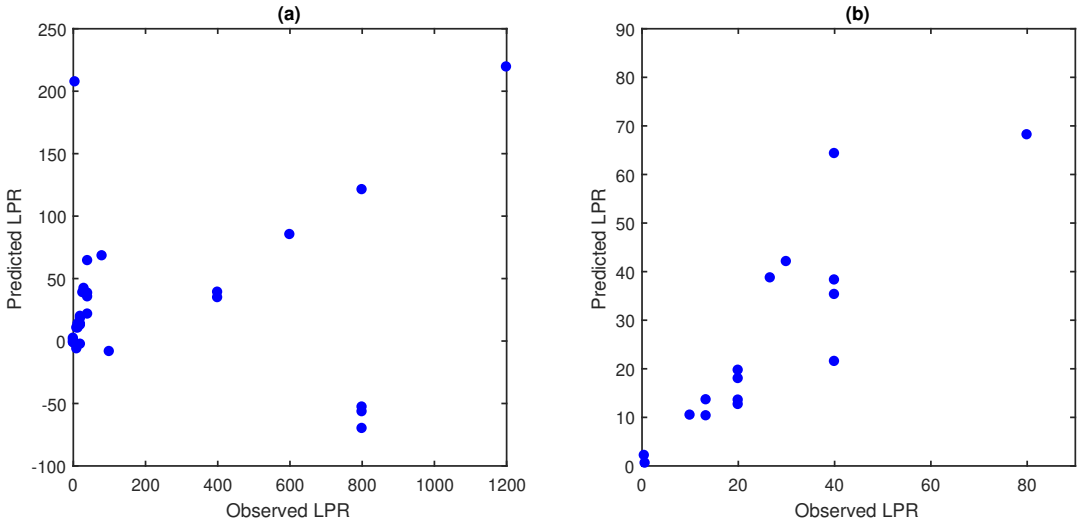


***Figure 9.10:*** *Scatter plots showing the observed vs. predicted LPR. Predicted values of the LPR were derived from the division of the concentrations of lactate and pyruvate predicted from transmission-FTIR single-beam spectra using a PLSR model. Plot (a) shows all results, whilst (b) shows only the region containing the most data points.*

concern was the prediction of invalid negative values of the concentrations of lactate and pyruvate. These results correlate with those obtained during the equivalent ATR-FTIR study, although it was noted that fewer negative concentration values of lactate and pyruvate were predicted during this transmission-FTIR study.

## 9.6 Transmission-FTIR: Analysis of Clinical Samples

The optimised PLSR model was predictively applied to the transmission-FTIR spectra of the six clinical microdialysate samples analysed in Section 6.3, in order to gain an insight into how applicable the results generated in this chapter might be to clinical samples. As explained in Section 6.3, this study could not be performed with ATR-FTIR spectroscopy due to the small volumes of the clinical samples.

Both ratio and single-beam transmission-FTIR spectra of the microdialysate samples were acquired and used as two separate test datasets. For each type of spectrum, the equivalent transmission-FTIR dataset of 575 spectra generated using synthetic samples was used as a training dataset. The training dataset was converted to absorbance data and mean-centred before being used to train a PLSR model using leave-one-out cross-validation. The test datasets were also converted to absorbance values and mean-centred before the model was applied.

Initially, a 20-component PLSR model was trained and applied to the test dataset over the full spectral range of 3000 – 800 $cm^{-1}$. The model was then trained and applied a second time, using the spectral interval and number of components identi-

fied in Section 9.4 as yielding the lowest overall RMSECV. This process provided an insight into whether the model optimisation achieved in this study would be directly applicable to clinical samples.

### 9.6.1 Analysis of Clinical Samples: Ratio Spectra

This section describes the prediction of glucose, lactate and pyruvate concentrations from transmission-FTIR ratio spectra of clinical samples.

The predictions generated by a 20-component PLSR model, applied over the full spectral range (3000 – 800 $cm^{-1}$), are compared with the observed values of the analyte concentrations in Figure 9.11.

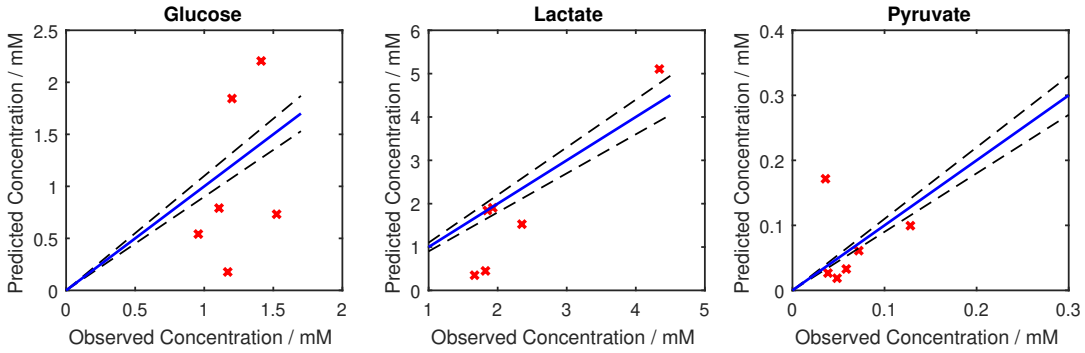


***Figure 9.11:*** *A comparison of the concentrations of glucose, lactate and pyruvate predicted from transmission-FTIR ratio spectra of clinical samples, calculated using a 20-component PLSR model applied over the spectral range 3000 – 800 $cm^{-1}$, with the observed concentrations measured using the ISCUS Flex Microdialysis Analyser. The solid blue line represents a perfect correlation of the observed and predicted concentrations, whilst the dashed black lines indicate 10% error intervals.*

The results in Figure 9.11 show that the predicted glucose concentrations did not fall within 10% of the observed concentration for any sample. This was also the case for the prediction of pyruvate concentrations. The concentration of lactate was predicted to within 10% of the observed concentration for two samples, yet the prediction of lactate concentrations within the remaining samples was significantly outside the 10% boundary.

Application of a 15-component PLSR model over the spectral range 1500 - 1000 $cm^{-1}$ was found, during the interval study described in Section 9.4, to produce the lowest RSMECV of the large transmission-FTIR ratio spectra dataset. This model was therefore applied to the transmission-FTIR ratio spectra of the clinical microdialysate samples to determine whether it would improve the predictive accuracy. The concentrations of glucose, lactate and pyruvate predicted by this model, and their comparison with the observed concentrations, are shown in Figure 9.12.

The data shown in Figure 9.12 indicated that the accuracy in prediction of glu-

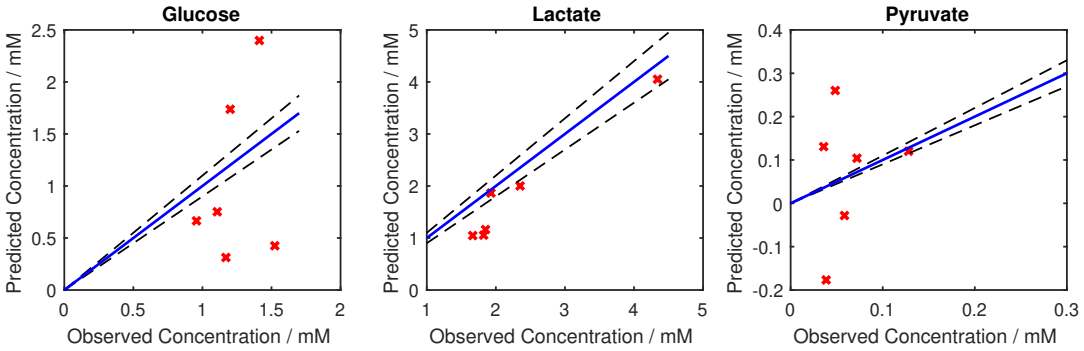


***Figure 9.12:*** *A comparison of the concentrations of glucose, lactate and pyruvate predicted from transmission-FTIR ratio spectra of clinical samples, calculated using a 15-component PLSR model applied over the spectral range 1500 – 1000 cm$^{-1}$, with the observed concentrations measured using the ISCUS Flex Microdialysis Analyser. The solid blue line represents an exact fit of the observed and predicted concentrations, whilst the dashed black lines indicate 10% error intervals.*

cose concentrations changed very little with the optimised model, as indicated by a qualitative examination of the correlation between observed and predicted values. The accuracy in prediction of lactate concentrations appeared to have improved, whilst the prediction of pyruvate concentrations appeared to have become less accurate. These results contradicted the findings of the interval study and suggested that a developed sensor would need to carry out a similar study to find the optimum range over which to apply a PLSR model to minimise the overall error in prediction of clinical samples.

### 9.6.2 Analysis of Clinical Samples: Single-Beam Spectra

This section describes the prediction of glucose, lactate and pyruvate concentrations from transmission-FTIR single-beam spectra of clinical samples.

The predictions generated by a 20-component PLSR model applied over the full spectral range (3000 – 800 cm$^{-1}$) are shown in Figure 9.13. It is immediately clear from this figure that the prediction of glucose, lactate and pyruvate concentrations from transmission-FTIR single-beam spectra was less accurate than a prediction from transmission-FTIR ratio spectra. This conclusion was in agreement with the results generated using synthetic samples.

The interval study described in Chapter 9.4 found that the overall RMSECV in the prediction of glucose, lactate and pyruvate concentrations from transmission-FTIR single-beam spectra was minimised using a 19-component PLSR model over the spectral range 1400 – 1000 cm$^{-1}$. This model was predictively applied to the transmission-FTIR single-beam spectra of the clinical samples, to determine whether it would improve the accuracy in prediction of glucose, lactate and pyruvate concentrations. The results of this study, shown in Figure 9.14, indicated that the accuracy

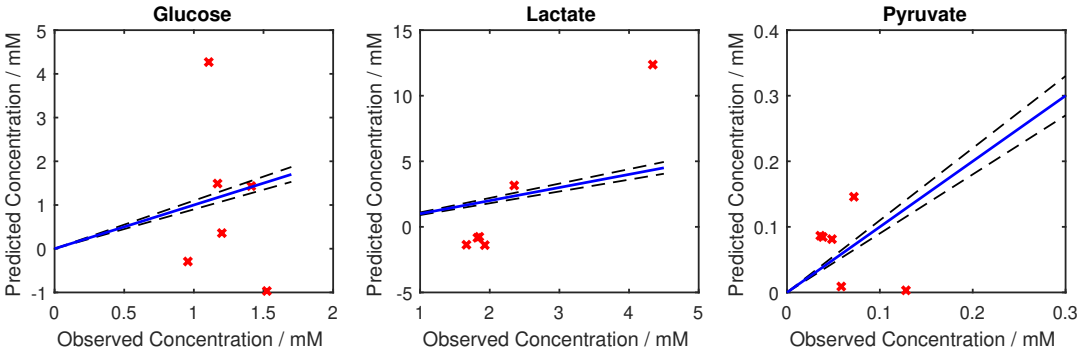


***Figure 9.13:*** *A comparison of the concentrations of glucose, lactate and pyruvate predicted from transmission-FTIR single-beam spectra of clinical samples, calculated using a 20-component PLSR model applied over the spectral range 3000 – 800 $cm^{-1}$, with the observed concentrations measured using the ISCUS Flex Microdialysis Analyser. The solid blue line represents an exact fit of the observed and predicted concentrations, whilst the dashed black lines indicate 10% error intervals.*

in prediction of glucose and lactate concentrations had increased from that of the PLSR model applied over the full spectral range, whilst the accuracy in prediction of pyruvate concentrations had decreased.

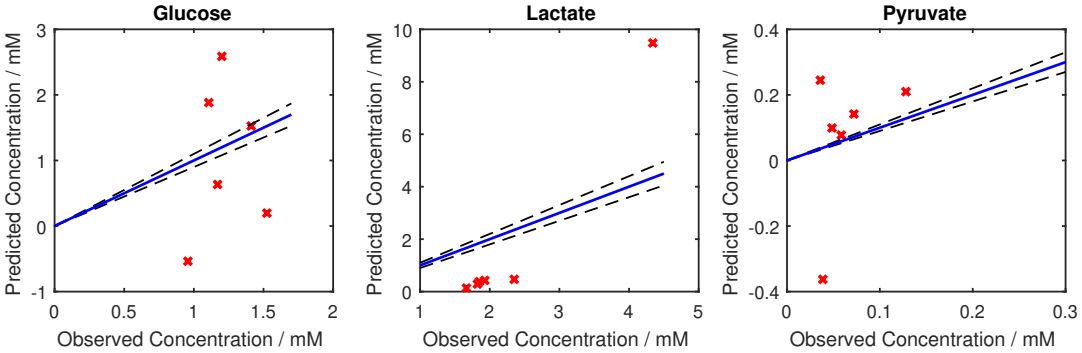


***Figure 9.14:*** *A comparison of the concentrations of glucose, lactate and pyruvate predicted from transmission-FTIR single-beam spectra of clinical samples, calculated using a 19-component PLSR model applied over the spectral range 1400 – 1000 $cm^{-1}$, with the observed concentrations measured using the ISCUS Flex Microdialysis Analyser. The solid blue line represents an exact fit of the observed and predicted concentrations, whilst the dashed black lines indicate 10% error intervals.*

### 9.6.3 Analysis of Clinical Samples: Conclusions

This section has described the application of a PLSR model, trained on a large dataset of transmission-FTIR spectra of synthetic solutions of glucose, lactate and pyruvate, to the prediction of glucose, lactate and pyruvate concentrations in clinical microdialysate samples. The errors in prediction for each spectrum type and model used

are summarised in Table 9.4.

***Table 9.4:*** *A summary of the performance of PLSR models when predictively applied to both ratio and single-beam transmission-FTIR spectra of clinical microdialysate samples.*

| Spectrum Type | Model Range | No. of Components | Compound RMSEP / mM | | |
|---|---|---|---|---|---|
| | | | Glucose | Lactate | Pyruvate |
| Ratio | 3000 – 800 | 20 | 0.40 | 0.52 | 0.034 |
| | 1500 - 1000 | 15 | 0.44 | 0.30 | 0.078 |
| Single-Beam | 3000 – 800 | 20 | 1.02 | 2.35 | 0.04 |
| | 1400 – 1000 | 19 | 0.62 | 1.47 | 0.11 |

The errors in prediction, for all compounds and both types of spectrum, are larger than would be acceptable for a developed sensor. This may be due to overfitting of the model to the training data, as all tested models used a relatively high number of components. Alternatively, the errors in prediction may be due to the fact that the model used to predict the glucose, lactate and pyruvate concentrations had been calibrated using spectra of synthetic solutions. The clinical solutions were likely to have contained a number of molecules in addition to glucose, lactate and pyruvate, as discussed in Section 6.2, and these were not reflected in the training data. It is likely that both of these factors contributed to the generation of predictive errors.

The trend observed in the analysis of synthetic samples, in which a predictive PLSR model generally performed better in the analysis of ratio spectra than single-beam spectra, was also found to be the case in this study. However, the models that had been optimised for use with synthetic samples, through the identification of the spectral range and number of model components that yielded the lowest overall RMSECV, did not always improve the predictive performance of the model when applied to clinical samples. It can be seen from Table 9.4 that the prediction of glucose and pyruvate concentrations from transmission-FTIR ratio spectra became less accurate when the optimised model was applied.

Overall, these results suggest that transmission-FTIR spectroscopy could be combined with a predictive PLSR model to analyse clinical microdialysis samples, although it is apparent that the model would need to be optimised using data from clinical samples.

## 9.7 Conclusions

This chapter has described a systematic study of the potential of transmission-FTIR to be used as the basis of a sensor for the analysis of glucose, lactate and pyruvate concentrations. The experiments carried out during this study were the same as those carried out for the systematic ATR-FTIR study described in Chapter 8, in order to allow a comparison of the generated data.

Many of the general trends observed in the ATR-FTIR study were also seen in the results generated by this study. PLSR generally perfomed better than PCR in the modelling and prediction of both ratio and single-beam spectra. Further studies carried out using PLSR showed that the prediction of glucose, lactate and pyruvate concentrations from ratio spectra was generally more accurate than prediction from single-beam transmission-FTIR spectra.

The RMSECV for the prediction of glucose, lactate and pyruvate concentrations from transmission-FTIR ratio spectra, acquired following a systematic study to identify the spectral range and number of model components that minimised the RMSECV, are summarised in Table 9.5. The table compares these errors with the minimum concentration of each compound that a developed sensor for the metabolic profiliing of TBI patients would be required to detect.

***Table 9.5:*** *A comparison of the RMSECV of the optimised PLSR model, as applied to the detection of glucose, lactate and pyruvate from transmission-FTIR ratio spectra, with the lowest concentration of each compound that a developed sensor would be required to detect.*

| Compound | RMSECV / mM | Minimum Concentration / mM |
|---|---|---|
| Glucose | 0.12 | 0.1 |
| Lactate | 0.15 | 0.1 |
| Pyruvate | 0.07 | 0.01 |

The data in Table 9.5 indicated that the RMSECV for all compounds would need to be lowered further before the model could successfully be used to detect clinically-relevant concentrations of glucose, lactate and pyruvate with the desired accuracy. The RMSECV for pyruvate requires the most significant improvement, as was found in the ATR-FTIR study. In order to allow a direct comparison of both studies, the table summarising the ATR-FTIR results is reproduced in Table 9.6.

***Table 9.6:*** *A comparison of the RMSECV of the optimised PLSR model, as applied to the detection of glucose, lactate and pyruvate from ATR-FTIR ratio spectra, with the lowest concentration of each compound that a developed sensor would be required to detect.*

| Compound | RMSECV / mM | Minimum Concentration / mM |
|---|---|---|
| Glucose | 0.2 | 0.1 |
| Lactate | 0.08 | 0.1 |
| Pyruvate | 0.068 | 0.01 |

A comparison of the data in Tables 9.5 and 9.6 shows that there is not a clear distinction in the predictive performance of PLSR applied to ATR-FTIR and transmission-FTIR ratio spectra. The optimised prediction of glucose concentrations yielded an RMSECV that was approximately 50% lower for transmission-FTIR spectra than for ATR-FTIR spectra. Conversely, the optimised prediction of lactate concentrations

yielded an RMSECV that was approximately 50% lower for ATR-FTIR spectra than for transmission-FTIR spectra. The error in pyruvate prediction was similar for both ATR-FTIR and transmission-FTIR spectra. The optimised spectral intervals over which the PLSR models were applied in order to achieve these RMSECV values were similar for the transmission-FTIR and ATR-FTIR ratio spectra (1000 – 1500 $cm^{-1}$ and 900 – 1500 $cm^{-1}$, respectively). However, the number of model components required was lower for transmission-FTIR spectra than for ATR-FTIR spectra (15 components *vs.* 20 components, respectively), indicating that the model of the transmission-FTIR spectral data was less complex.

Prediction of the LPR via a straightforward division of the lactate and pyruvate concentrations predicted from transmission-FTIR spectra, using the optimised PLSR models, generated very large errors for both ratio and single-beam spectra. Some negative LPR values were predicted, for both ratio and single-beam spectra, showing that the PLSR models had calculated invalid negative values of the lactate and pyruvate concentrations. This was also the case when applying the same method to ATR-FTIR spectra.

Finally, two PLSR models, trained on the transmission-FTIR ratio and single-beam spectra of synthetic solutions generated during this study, were predictively applied to the transmission-FTIR ratio and single-beam spectra of six clinical microdialysate samples. Once again, the predictive performance of the model applied to ratio spectra was more accurate than the performance of that applied to single-beam spectra. The modelling of both spectrum types produced a RMSEP for each compound that was higher than those achieved for the prediction of concentrations from synthetic samples. This was thought to be due to a combination of two factors: the fact that the model was trained on spectra of synthetic solutions, whilst clinical solutions contain a number of competing molecules that were not present in the synthetic samples, and overfitting of the model to the training data. However, the results are encouraging and suggest that, with further work, it may be possible to reach the required RMSEP for each compound in clinical microdialysate samples. This is discussed further in Chaper 10.

# Chapter 10

# Discussion and Future Outlook

This Chapter provides a brief overview of the results presented in this thesis. The conclusions arising from this work, with respect to the stated aim of this thesis, are subsequently discussed and suggestions for further work are made.

## 10.1 Summary of Work

The stated aim of the thesis was to determine whether vibrational spectroscopy could be used as the basis of an on-line sensor for metabolic profiling of TBI patients. This aim was first addressed by comparing the ability of two forms of vibrational spectroscopy, FTIR spectroscopy and Raman spectroscopy, to detect glucose, lactate and pyruvate in solution. All results were assessed against the specifications required of the developed on-line sensor, as listed in Section 2.6.

The initial investigation into the ability of FTIR spectroscopy to detect glucose, lactate and pyruvate in solution was carried out using two techniques: ATR-FTIR spectroscopy and transmission-FTIR spectroscopy. ATR-FTIR spectroscopy was chosen due to its relative insensitivity to water, which was expected to be a significant advantage of the technique, given the highly dilute nature of clinical microdialysis samples. Transmission-FTIR, on the other hand, is highly sensitive to water but was selected for investigation because it is arguably the most simple of the available FTIR spectroscopic techniques and was thus expected to be the most amenable to miniaturisation into a bedside device.

ATR-FTIR spectroscopy and transmission-FTIR spectroscopy were used to analyse solutions of glucose, lactate and pyruvate in perfusion fluid. The compounds were analysed both as pure solutions and as a three-component mixture and peaks unique to each compound were successfully identified. Consideration was given to the nature and likely concentration of other compounds which may be present in microdialysate samples from TBI patients. Two of these compounds, glycerol and glutamate, were studied via ATR-FTIR and transmission-FTIR spectroscopy both as single-component

solutions and as five-component solutions of glucose, lactate, pyruvate, glycerol and glutamate. This study indicated that peaks unique to the three analytes of interest would still be visible against a background of glycerol and glutamate when all compounds were present at clinically-relevant concentrations. Finally, transmission-FTIR spectroscopy was used to acquire FTIR spectra of six clinical microdialysate samples. Characterisation of these spectra revealed that peaks unique to glucose and lactate could be identified but the intensity of pyruvate absorption peaks was too low to allow their identification.

Following these studies, FTIR spectroscopy was considered a promising technique for inclusion in an on-line sensor for metabolic profiling of TBI patients. It was concluded that in-depth studies should be carried out into the ability to accurately identify glucose, lactate and pyruvate concentrations from both ATR-FTIR and transmission-FTIR spectra. Systematic studies were therefore carried out to determine which ATR-FTIR crystal and transmission-FTIR path length should be used for these in-depth investigations.

Raman spectroscopy was investigated as a possible technique upon which to base an on-line sensor for metabolic profiling of TBI patients due to its insensitivity to water, potential for miniaturisation into a bedside device and previous reported use in medical applications. It was quickly established that Raman spectroscopy of glucose, lactate and pyruvate was too insensitive to enable the detection of these compounds at clinically-relevant concentrations. A SERS-based sensor using silver colloids suspended in solution was proposed as an alternative and its feasibility was assessed using cysteine as a model analyte. However, an assessment of the difficulties involved in implementing this device, combined with the promising results generated by the initial FTIR spectroscopy study, led to the decision not to proceed further with SERS.

The in-depth investigations of ATR-FTIR and transmission-FTIR spectroscopy were based on the analysis of synthetic solutions containing glucose, lactate and pyruvate at clinically-relevant concentrations. Both investigations followed the same workflow in order to allow the results obtained using each technique to be compared.

The first stage in each investigation was to compare the relative performances of PCR and PLSR in the modelling and prediction of glucose, lactate and pyruvate concentrations from both ratio and single-beam spectra. PLSR was the best-performing model for all types of spectra and was selected for further optimisation. The model was optimised to determine the spectral interval and number of components which yielded the lowest overall RMSECV. These model parameters were used to generate a prediction of the LPR via a division of the predicted concentrations of lactate and pyruvate.

Finally, two PLSR models trained on transmission-FTIR ratio and single-beam spectra were used to predict the concentrations of glucose, lactate and pyruvate from

the transmission-FTIR ratio and single-beam spectra of clinical samples. The errors in prediction were higher than those obtained for models applied to the spectra of synthetic samples, but were considered promising.

## 10.2 Conclusions

Following the work described in this thesis, it is recommended that an on-line sensor for continuous metabolic profiling of TBI patients is not based on Raman spectroscopy due to its inherent insensitivity, particularly with respect to the detection of molecules, such as glucose, lactate and pyruvate, which exhibit a low Raman scattering intensity. The use of SERS in such a sensor is also not recommended due to inherent characteristics of the SERS technique which would complicate the operation of the device and affect its reliability.

The results generated in this work suggest that it may be feasible to produce a sensor for on-line metabolic profiling of TBI patients that is based upon a combination of FTIR spectroscopy and statistical modelling, although further reduction of the RMSECV would be required. These results strongly suggest that PLSR would be a more appropriate statistical model than PCR for the analysis of spectra. In addition, the results indicate that a sensor based on predictive PLSR modelling of FTIR spectra should be used to analyse ratio spectra, rather than single-beam spectra, in order to minimise the error in prediction.

Based upon the results generated in this work, it is concluded that there is little overall difference in the predictive accuracy of a PLSR model applied to ratio spectra acquired using ATR-FTIR or transmission-FTIR. It is therefore concluded that the differences between ATR-FTIR and transmission-FTIR spectra, as observed in Section 6.1, do not appear to have had an impact on the predictive accuracy of PLSR. This is thought to be due to the fact that the spectral intervals identified as yielding the lowest RMSECV, for both ATR-FTIR and transmission-FTIR spectra, did not incorporate regions in which the spectra were significantly different. Regions of significant water-induced noise ($3700 - 3000\ cm^{-1}$, $1700 - 1600\ cm^{-1}$ and $900 - 450\ cm^{-1}$) were excluded from the optimised intervals, as was the region in which peaks are absent from the ATR-FTIR spectra of lactate and pyruvate due to orientation effects ($1500 - 1600\ cm^{-1}$). A final decision regarding which form of FTIR spectroscopy would be most suitable for integration into an on-line sensor for metabolic profiling of TBI patients could therefore be based on practical aspects of device design, such as which would be easier to miniaturise. In this instance, it is likely that transmission-FTIR would be the recommended technique as the miniaturisaton of the crystals used in ATR-FTIR would be difficult.

The prediction of the LPR via a division of the predicted concentrations of lactate and pyruvate was determined not to be feasible with the current error in prediction

of the two compounds. An alternative method may be to generate a statistical model for the prediction of the LPR directly from FTIR spectra; however, this would be extremely complex. It is therefore recommended that attempts are made to reduce the error in prediction of the two compounds, and the resulting improvement in the LPR assessed, before the construction of such a model is attempted.

It should be noted that the FTIR spectra acquired, and subsequently analysed, in this work required approximately 2.5 minutes to generate. This length of time is compatible with the temporal resolution required of a sensor for on-line metabolic profiling of TBI patients, which necessitates the taking of a measurement at least once every five minutes.

## 10.3 Considerations for Future Device Development

An on-line sensor for metabolic profiling of TBI patients that is based upon a combination of FTIR spectroscopy and statistical modelling would require a higher predictive accuracy than has been achieved in this work, particularly with respect to pyruvate. The ideal way to improve the accuracy in prediction would be to improve the signal-to-noise ratio of the spectral data acquired. An obvious way in which this could be achieved would be to improve the instrumental setup used to acquire the data. A developed sensor would not be based on a commercially-available spectrometer, such as that used in this work, but would comprise a bespoke combination of commercially-available components. As a result, there would be numerous opportunities to improve the hardware of the instrument compared with the hardware of the spectrometer used in this work. For example, the use of QCLs in FTIR spectroscopy is reported to produce spectra with a higher signal-to-noise ratio than that achieved with SiC globar light sources, such as that used in this work. The integration of a QCL into the final device would impose a limit on the region of the spectrum to be analysed, as an individual QCL will emit only a narrow range of wavelengths of electromagnetic radiation. However, the interval data presented in Chapters 8 and 9 suggest that the use of small spectral intervals can improve the error in prediction. One obvious disadvantage of the use of a QCL would be a significant increase in the cost of the device.

It may also be possible to improve the signal-to-noise ratio of spectra using a technique known as surface-enhanced infrared absorption spectroscopy, which is based upon the same principles as SERS. However, this is not recommended as it would introduce the same complications that were encountered using SERS.

If the quality of spectral data could not be improved sufficiently to achieve the desired accuracy in the prediction of glucose, lactate and pyruvate concentrations, further development of the statistical model used to analyse the data would be necessary. It is possible that, at very low concentrations, the data are not linear. If this is

the case, it may be necessary to apply a non-linear statistical model to the data, such as nonlinear regression.

The analysis of clinical samples via a PLSR model trained on the transmission-FTIR spectra of the synthetic solutions generated in this work has highlighted the importance of training a final model on spectra of clinical samples. However, it is recommended that this work is carried out using the hardware and sensing chip applied to the final device, in order to ensure that the effects of these components can be accounted for by the model.

Consideration would also need to be given to the calibration of the device to ensure that the measured concentrations of glucose, lactate and pyruvate remain accurate. The frequency with which this would need to be carried out would depend upon the stability of the device. For example, the enzyme-based rsMD device described in Chapter 4 is reportedly re-calibrated every three hours.[112]

A final consideration for the development of a sensor relates to the generation of background spectra. It has been shown in this work that the application of both PLSR and PCR to FTIR ratio spectra yields a lower RMSECV than that achieved when the models are applied to FTIR single-beam spectra. The generation of FTIR ratio spectra requires the acquisition of background spectra, which would need to be generated on a regular basis in order to ensure the background continued to reflect the environment of the sensor. This would require a sensing chip with an additional channel for the introduction of a suitable reference sample and may require an automated process to ensure that device operation is not labour-intensive.

## 10.4 Concluding Remarks

The work presented in this thesis has shown that it may be possible to improve upon the current method for metabolic profiling of TBI patients, using a sensor based upon FTIR spectroscopy. It is hoped that the results presented here, and the conclusions drawn from them, will be useful in guiding the next phase of sensor development.

# Appendices

# Appendix A

# Combinations of Glucose, Lactate and Pyruvate Analysed in Mixture Studies

## A.1 Three-Component Mixtures

The concentrations of glucose, lactate and pyruvate in each of the three-component mixtures studied via ATR-FTIR spectroscopy and transmission-FTIR spectroscopy in their respective mixture studies are shown in Table A.1.

***Table A.1:*** *The concentrations of glucose, lactate and pyruvate in the three-component mixture analysed as part of the ATR-FTIR spectroscopy and transmission-FTIR spectroscopy mixture studies.*

| Glucose / mM | Lactate / mM | Pyruvate / mM |
|---|---|---|
| 0.05 | 0.05 | 0.005 |
| 0.05 | 2.00 | 0.005 |
| 0.10 | 0.10 | 0.005 |
| 0.10 | 0.10 | 0.010 |
| 0.10 | 0.10 | 0.050 |
| 0.10 | 0.10 | 0.100 |
| 0.10 | 0.10 | 0.150 |
| 0.10 | 0.10 | 0.200 |
| 0.10 | 2.00 | 0.005 |
| 0.10 | 2.00 | 0.010 |
| 0.10 | 2.00 | 0.050 |
| 0.10 | 2.00 | 0.100 |

*Continued on next page*

Table A.1 – *Continued from previous page*

| **Glucose / mM** | **Lactate/ mM** | **Pyruvate / mM** |
|---|---|---|
| 0.10 | 2.00 | 0.150 |
| 0.10 | 2.00 | 0.200 |
| 0.10 | 4.00 | 0.005 |
| 0.10 | 4.00 | 0.010 |
| 0.10 | 4.00 | 0.050 |
| 0.10 | 4.00 | 0.100 |
| 0.10 | 4.00 | 0.150 |
| 0.10 | 4.00 | 0.200 |
| 0.10 | 6.00 | 0.005 |
| 0.10 | 6.00 | 0.010 |
| 0.10 | 6.00 | 0.050 |
| 0.10 | 6.00 | 0.100 |
| 0.10 | 6.00 | 0.150 |
| 0.10 | 6.00 | 0.200 |
| 0.70 | 0.10 | 0.005 |
| 0.70 | 0.10 | 0.010 |
| 0.70 | 0.10 | 0.050 |
| 0.70 | 0.10 | 0.100 |
| 0.70 | 0.10 | 0.150 |
| 0.70 | 0.10 | 0.200 |
| 0.70 | 2.00 | 0.005 |
| 0.70 | 2.00 | 0.010 |
| 0.70 | 2.00 | 0.050 |
| 0.70 | 2.00 | 0.100 |
| 0.70 | 2.00 | 0.150 |
| 0.70 | 2.00 | 0.200 |
| 0.70 | 4.00 | 0.005 |
| 0.70 | 4.00 | 0.010 |
| 0.70 | 4.00 | 0.050 |
| 0.70 | 4.00 | 0.100 |
| 0.70 | 4.00 | 0.150 |
| 0.70 | 4.00 | 0.200 |
| 0.70 | 6.00 | 0.005 |
| 0.70 | 6.00 | 0.010 |
| 0.70 | 6.00 | 0.050 |
| 0.70 | 6.00 | 0.100 |
| 0.70 | 6.00 | 0.150 |

*Continued on next page*

Table A.1 – *Continued from previous page*

| **Glucose / mM** | **Lactate/ mM** | **Pyruvate / mM** |
|---|---|---|
| 0.70 | 6.00 | 0.200 |
| 1.00 | 0.05 | 0.005 |
| 1.00 | 0.10 | 0.005 |
| 1.00 | 0.10 | 0.010 |
| 1.00 | 0.10 | 0.050 |
| 1.00 | 0.10 | 0.100 |
| 1.00 | 0.10 | 0.150 |
| 1.00 | 0.10 | 0.200 |
| 1.00 | 2.00 | 0.005 |
| 1.00 | 2.00 | 0.010 |
| 1.00 | 2.00 | 0.050 |
| 1.00 | 2.00 | 0.100 |
| 1.00 | 2.00 | 0.150 |
| 1.00 | 2.00 | 0.200 |
| 1.00 | 4.00 | 0.005 |
| 1.00 | 4.00 | 0.010 |
| 1.00 | 4.00 | 0.050 |
| 1.00 | 4.00 | 0.100 |
| 1.00 | 4.00 | 0.150 |
| 1.00 | 4.00 | 0.200 |
| 1.00 | 6.00 | 0.005 |
| 1.00 | 6.00 | 0.010 |
| 1.00 | 6.00 | 0.050 |
| 1.00 | 6.00 | 0.100 |
| 1.00 | 6.00 | 0.150 |
| 1.00 | 6.00 | 0.200 |
| 3.00 | 0.10 | 0.005 |
| 3.00 | 0.10 | 0.010 |
| 3.00 | 0.10 | 0.050 |
| 3.00 | 0.10 | 0.100 |
| 3.00 | 0.10 | 0.150 |
| 3.00 | 0.10 | 0.200 |
| 3.00 | 2.00 | 0.005 |
| 3.00 | 2.00 | 0.010 |
| 3.00 | 2.00 | 0.050 |
| 3.00 | 2.00 | 0.100 |
| 3.00 | 2.00 | 0.150 |

*Continued on next page*

Table A.1 – *Continued from previous page*

| Glucose / mM | Lactate/ mM | Pyruvate / mM |
|---|---|---|
| 3.00 | 2.00 | 0.200 |
| 3.00 | 4.00 | 0.005 |
| 3.00 | 4.00 | 0.010 |
| 3.00 | 4.00 | 0.050 |
| 3.00 | 4.00 | 0.100 |
| 3.00 | 4.00 | 0.150 |
| 3.00 | 4.00 | 0.200 |
| 3.00 | 6.00 | 0.005 |
| 3.00 | 6.00 | 0.010 |
| 3.00 | 6.00 | 0.050 |
| 3.00 | 6.00 | 0.100 |
| 3.00 | 6.00 | 0.150 |
| 3.00 | 6.00 | 0.200 |

## A.2 Two-Component Mixtures

The concentrations of glucose, lactate and pyruvate in each of the two-component mixtures studied via ATR-FTIR spectroscopy and transmission-FTIR spectroscopy in their respective mixture studies are shown in Table A.2.

***Table A.2:*** *The concentrations of glucose, lactate and pyruvate in the two-component mixtures analysed as part of the ATR-FTIR spectroscopy and transmission-FTIR spectroscopy mixture studies.*

| Glucose / mM | Lactate / mM | Pyruvate / mM |
|---|---|---|
| 0.00 | 0.05 | 0.005 |
| 0.00 | 0.05 | 0.010 |
| 0.00 | 0.05 | 0.050 |
| 0.00 | 0.05 | 0.150 |
| 0.00 | 0.05 | 0.200 |
| 0.00 | 0.10 | 0.005 |
| 0.00 | 0.10 | 0.010 |
| 0.00 | 0.10 | 0.050 |
| 0.00 | 0.10 | 0.150 |
| 0.00 | 0.10 | 0.200 |

*Continued on next page*

Table A.2 – *Continued from previous page*

| **Glucose / mM** | **Lactate/ mM** | **Pyruvate / mM** |
|---|---|---|
| 0.00 | 0.50 | 0.005 |
| 0.00 | 0.50 | 0.010 |
| 0.00 | 0.50 | 0.050 |
| 0.00 | 0.50 | 0.150 |
| 0.00 | 0.50 | 0.200 |
| 0.00 | 4.00 | 0.005 |
| 0.00 | 4.00 | 0.010 |
| 0.00 | 4.00 | 0.050 |
| 0.00 | 4.00 | 0.150 |
| 0.00 | 4.00 | 0.200 |
| 0.05 | 0.00 | 0.005 |
| 0.05 | 0.00 | 0.010 |
| 0.05 | 0.00 | 0.050 |
| 0.05 | 0.00 | 0.150 |
| 0.05 | 0.00 | 0.200 |
| 0.05 | 0.05 | 0.000 |
| 0.05 | 0.10 | 0.000 |
| 0.05 | 0.50 | 0.000 |
| 0.05 | 4.00 | 0.000 |
| 0.10 | 0.00 | 0.005 |
| 0.10 | 0.00 | 0.010 |
| 0.10 | 0.00 | 0.050 |
| 0.10 | 0.00 | 0.150 |
| 0.10 | 0.00 | 0.200 |
| 0.10 | 0.05 | 0.000 |
| 0.10 | 0.10 | 0.000 |
| 0.10 | 0.50 | 0.000 |
| 0.10 | 4.00 | 0.000 |
| 0.70 | 0.00 | 0.005 |
| 0.70 | 0.00 | 0.010 |
| 0.70 | 0.00 | 0.050 |
| 0.70 | 0.00 | 0.150 |
| 0.70 | 0.00 | 0.200 |
| 0.70 | 0.05 | 0.000 |
| 0.70 | 0.10 | 0.000 |
| 0.70 | 0.50 | 0.000 |
| 0.70 | 4.00 | 0.000 |

*Continued on next page*

Table A.2 – *Continued from previous page*

| **Glucose / mM** | **Lactate/ mM** | **Pyruvate / mM** |
|---|---|---|
| 1.00 | 0.00 | 0.005 |
| 1.00 | 0.00 | 0.010 |
| 1.00 | 0.00 | 0.050 |
| 1.00 | 0.00 | 0.150 |
| 1.00 | 0.00 | 0.200 |
| 1.00 | 0.05 | 0.000 |
| 1.00 | 0.10 | 0.000 |
| 1.00 | 0.50 | 0.000 |
| 1.00 | 4.00 | 0.000 |

# Bibliography


[1] A. I. R. Maas, N. Stocchetti and R. Bullock, *Lancet Neurol.*, 2008, **7**, 728–741.

[2] B. Roozenbeek, A. I. Maas and D. K. Menon, *Nat. Rev. Neurol.*, 2013, **9**, 231–236.

[3] *Head Injury: Triage, Assessment, Investigation and Early Management of Head Injury in Children, Young People and Adults*, National Institute for Health and Care Excellence Costing Report, 2014.

[4] K. E. Saatman, A. C. Duhaime, R. Bullock, A. I. R. Maas, A. Valadka and G. T. Manley, *J. Neurotrauma*, 2008, **25**, 719–738.

[5] J. Ghajar, *The Lancet*, 2000, **356**, 923–929.

[6] I. Jalloh, K. L. H. Carpenter, A. Helmy, T. A. Carpenter, D. K. Menon and P. J. Hutchinson, *Metab. Brain Dis.*, 2015, **30**, 615–632.

[7] P. J. Hutchinson, I. Jalloh, A.Helmy, K. L. H. Carpenter, E. Rostami, B. M. Bellander, M. G. Boutelle, J. W. Chen, J. Claassen, C. Dahyot-Fizelier, P. Enblad, C. N. Gallagher, R. Helbok, L. Hillered, P. D. L. Roux, S. Magnoni, a. D. K. M. H. S. Mangat, C. H. Nordström, K. H. O'Phelan, M. Oddo, J. P. Barcena, C. Robertson, E. Ronne-Engström, J. Sahuquillo, M. Smith, N. Stocchetti, A. Belli, A. T. Carpenter, J. P. Coles, M. Czosnyka, N. Dizdar, J. C. Goodman, A. K. Gupta, T. H. Nielsen, N. Marklund, A. Montcriol, M. T. O'Connell, M. A. Poca, A. Sarrafzadeh, R. J. Shannon, J. Skjøth-Rasmussen, P. Smielewski, J. F. Stover, I. Timofeev, P. Vespa, E. Zavala and U. Ungerstedt, *Intensive Care Med.*, 2015, **41**, 1517–1528.

[8] A. Helmy, K. L. H. Carpenter, D. K. Menon, J. D. Pickard and P. J. A. Hutchinson, *J. Cereb. Blood Flow Metab.*, 2011, **31**, 658–670.

[9] K. L. H. Carpenter, I. Timofeev, P. G. Al-Rawi, D. K. Menon, J. D. Pickard and P. J. Hutchinson, *Acta Neurochir. Suppl.*, 2008, **102**, 207–213.

[10] CMA/Microdialysis, *ISCUS Flex Microdialysis Analyser Technical Manual*, 2008.

[11] Y. Tholance, G. Barcelos, I. Quadrio, B. Renaud, F. Dailler and A. Perret-Liaudet, *Clin. Chim. Acta*, 2011, **412**, 647–654.

[12] P. Mergenthaler, U. Lindauer, G. A. Dienel and A. Meisel, *Trends Neurosci.*, 2013, **36**, 587–597.

[13] P. Reinstrup, N. Ståhl, P. Mellergård, T. Uski, U. Ungerstedt and C. H. Nordström, *Neurosurgery*, 2000, **47**, 701–710.

[14] S. Sahu, D. S. Nag, A. Swain and D. P. Samaddar, *World J. Biol. Chem.*, 2017, **8**, 21–31.

[15] I. Jalloh, K. L. H. Carpenter, P. Grice, D. J. Howe, A. Mason, C. N. Gallagher, A. Helmy, M. P. Murphy, D. K. Menon, T. A. Carpenter, J. D. Pickard and P. J. Hutchinson, *J. Cereb. Blood Flow Metab.*, 2015, **35**, 111–120.

[16] I. Timofeev, K. L. H. Carpenter, J. Nortjie, P. G. Al-Rawi, M. T. O'Connell, M. Czosnyka, P. Smielewski, J. D. Pickard, D. K. Menon, P. J. Kirkpatrick, A. K. Gupta and P. J. Hutchinson, *Brain*, 2011, **134**, 484–494.

[17] A. Helmy, K. L. H. Carpenter and P. J. Hutchinson, *Curr. Med. Chem.*, 2007, **14**, 1525–1537.

[18] T. Paraforou, K. Paterakis, K. Fountas, G. Paraforos, A. Chovas, A. Tasiou, M. Mpakopoulou, D. Papadopoulos, A. Karavellis and A. Komnos, *BMC Res. Notes*, 2011, **4**, 1–6.

[19] C. N. Gallagher, K. L. H. Carpenter, P. Grice, D. J. Howe, A. Mason, I. Timofeev, D. K. Menon, P. J. Kirkpatrick, J. D. Pickard, G. R. Sutherland and P. J. Hutchinson, *Brain*, 2009, **132**, 2839–2849.

[20] K. L. H. Carpenter, I. Jalloh, C. N. Gallagher, P. Grice, D. J. Howe, A. Mason, I. Timofeev, A. Helmy, M. P. Murphy, D. K. Menon, P. J. Kirkpatrick, T. A. Carpenter, G. R. Sutherland, J. D. Pickard and P. J. Hutchinson, *Eur. J. Pharm. Sci.*, 2014, **57**, 87–97.

[21] H. J. Butler, L. Ashton, B. Bird, G. Cinque, K. Curtis, J. Dorney, K. Esmond-White, N. Fullwood, B. Gardner, P. L. Martin-Hirsch, M. J. Walsh, M. R. McAinsh, N. Stone and F. L. Martin, *Nat. Protoc.*, 2016, **11**, 664–687.

[22] C. L. Haynes, A. D. McFarland and R. P. V. Duyne, *Anal. Chem.*, 2005, **77**, 338A–346A.

[23] M. L. Juan, M. Righini and R. Quidant, *Nat. Photonics*, 2011, **5**, 349–356.

[24] A. P. F. Turner, *Chem. Soc. Rev.*, 2013, **42**, 3184–3196.

[25] H. Yao, A. J. Shum, M. Cowan, I. Lähdesmäki and B. A. Parviz, *Biosens. Bioelectron.*, 2011, **26**, 3290–3296.

[26] H. Lee, T. K. Choi, Y. B. Lee, H. R. Cho, R. Ghaffari, L. Wang, H. J. Choi, T. D. Chung, N. Lu, T. Hyeon, S. H. Choi and D. H. Kim, *Nat. Nanotechnol.*, 2016, **11**, 566–572.

[27] J. R. Anusha, C. J. Raj, B. B. Cho, A. T. Fleming, K. H. Yu and B. C. Kim, *Sens. Actuators, B*, 2015, **215**, 536–543.

[28] S. K. Krishnan, E. Prokhorov, D. Bahena, R. Esparza and M. Meyyappan, *ACS Omega*, 2017, **2**, 1896–1904.

[29] M. Mazaheri, H. Aashuri and A. Simchi, *Sens. Actuators, B*, 2017, **251**, 462–471.

[30] Y. Tang, Q. Liu, Z. Jiang, X. Yang, M. Wei and M. Zhang, *Sens. Actuators, B*, 2017, **251**, 1096–1103.

[31] M. Jarosz, R. P. Socha, P. Jóźwik and G. D. Sulka, *Appl. Surf. Sci.*, 2017, **408**, 96–102.

[32] J. Zhang, C. Xu, R. Zhang, X. Guo, J. Wang, X. Zhang, D. Zhang and B. Yuan, *Mater. Lett.*, 2018, **210**, 291–294.

[33] S. J. Cho, H. B. Noh, M. S. Won, C. H. Cho, K. B. Kim and Y. B. Shim, *Biosens. Bioelectron.*, 2018, **99**, 471–478.

[34] S. Soylemez, B. Yoon, L. Toppare and T. M. Swager, *ACS Sens.*, 2017, **2**, 1123–1127.

[35] C. Jiang, J. Zhu, Z. Li, J. Luo, J. Wang and Y. Sun, *RSC Adv.*, 2017, **7**, 44463–44469.

[36] Y. M. Wang, J. W. Liu, J. H. Jiang and W. Zhong, *Anal. Bioanal. Chem.*, 2017, **409**, 4225–4232.

[37] W. Dong, L. Yang and Y. Huang, *Talanta*, 2017, **167**, 359–366.

[38] L. Jin, Z. Meng, Y. Zhang, S. Cai, Z. Zhang, C. Li, L. Shang and Y. Shen, *ACS Appl. Mater. Interfaces*, 2017, **9**, 10027–10033.

[39] Q. Li, G. Tang, X. Xiong, Y. Cao, L. Chen, F. Xu and H. Tan, *Sens. Actuators, B*, 2015, **215**, 86–92.

[40] Z. Huang, J. Yang, L. Zhang, X. Geng, J. Ge, Y. Hu and Z. Li, *Anal. Methods*, 2017, **9**, 4275–4281.

[41] L. Wang, X. Kang and D. Pan, *Inorg. Chem.*, 2017, **56**, 6122–6130.

[42] L. Chen, L. Chen, M. Dotzert, C. W. J. Melling and J. Zhang, *J. Nanobiotechnol.*, 2017, **15**, 1–9.

[43] S. O. Alijanpour, R. Akhoondi and M. J. Chaichi, *J. Anal. Chem.*, 2017, **72**, 120–127.

[44] J. Ghosh, R. Ghosh and P. K. Giri, *Sens. Actuators, B*, 2018, **254**, 681–689.

[45] C. Wang, Y. Li and Y. Wei, *Sens. Actuators, B*, 2017, **247**, 595–601.

[46] H. Li, L. Zhu, X. Zhu and H. Zhang, *Sens. Actuators, B*, 2017, **246**, 819–825.

[47] M. Liang, Y. Ren, H. Zhang, Y. Ma, X. Niu and X. Chen, *Luminescence*, 2017, **32**, 1031–1038.

[48] F. Molaabasi, S. Hosseinkhani, A. A. Moosavi-Movahedi and M. Shamsipur, *RSC Adv.*, 2015, **5**, 33123–33135.

[49] C. Li, X. Chen, F. Zhang, X. He, G. Fang, J. Liu and S. Wang, *Anal. Chem.*, 2017, **89**, 10431–10438.

[50] C. Liu, Y. Sheng, Y. Sun, J. Feng, S. Wang, J. Zhang, J. Xu and D. Jiang, *Biosens. Bioelectron.*, 2015, **70**, 455–461.

[51] J. S. Hansen, T. Hoeg-Jensen and J. B. Christensen, *Tetrahedron*, 2017, **73**, 3010–3013.

[52] Z. Zhang, R. T. K. Kwok, Y. Yu, B. Z. Tang and K. M. Ng, *ACS Appl. Mater. Interfaces*, 2017, **9**, 38153–38158.

[53] A. L. Hu, Y. H. Liu, H. H. Deng, G. L. Hong, A. L. Liu, X. H. Lin, X. H. Xia and W. Chen, *Biosens. Bioelectron.*, 2014, **61**, 374–378.

[54] D. Calabria, C. Caliceti, M. Zangheri, M. Mirasoli, P. Simoni and A. Roda, *Biosens. Bioelectron.*, 2017, **94**, 124–130.

[55] Q. Chen, T. Sun, X. Song, Q. Ran, C. Yu, J. Yang, H. Feng, L. Yu and D. Wei, *Nanotechnology*, 2017, **28**, 315501–1–315501–9.

[56] S. RoyChoudhury, P. Manickam, Y. Umasankar and S. Bhansali, *ECS Trans.*, 2015, **69**, 7–15.

[57] J. Kim, G. Valdés-Ramírez, A. J. Bandodkar, W. Jia, A. G. Martinez, J. Ramírez, P. Mercier and J. Wang, *Analyst*, 2014, **139**, 1632–1636.

[58] W. Jia, A. J. Bandodkar, G. Valdés-Ramírez, J. R. Windmiller, Z. Yang, J. Ramírez, G. Chan and J. Wang, *Anal. Chem.*, 2013, **85**, 6553–6560.

[59] N. V. Zaryanov, V. N. Nikitina, E. V. Karpova, E. E. Karyakina and A. A. Karyakin, *Anal. Chem.*, 2017, **89**, 11198–11202.

[60] A. S. Martín, S. Ceballo, F. Baeza-Lehnert, R. Lerchundi, R. Valdebenito, Y. Contreras-Baeza, K. Alegría and L. F. Barros, *PLoS One*, 2014, **9**, 1–9.

[61] N. Gajovic, G. Binyamin, A. Warsinke, F. W. Scheller and A. Heller, *Anal. Chem.*, 2000, **72**, 2963–2968.

[62] M. Azhar, J. Mandon, A. H. Neerincx, Z. Liu, J. Mink, P. J. F. M. Merkus, S. M. Cristescu and F. J. M. Harren, *Appl. Phys. B*, 2017, **123**, 268–1–7.

[63] V. Lirtsman, M. Golosovsky and D. Davidov, *Rev. Sci. Instrum.*, 2017, **88**, 103105–1–7.

[64] K. Ataka, S. T. Stripp and J. Heberle, *Biochim. Biophys. Acta*, 2013, **1828**, 2283–2293.

[65] R. Ebrahimifard, S. van den Driesche, H. Breiteneder, C. Hafner and M. J. Vellekoop, *Sens. Actuators, B*, 2017, **247**, 981–991.

[66] R. Ríos-Reina, R. M. Callejón, C. Oliver-Pozo, J. M. Amigo and D. L. García-González, *Food Control*, 2017, **78**, 230–237.

[67] J. Zhang, P. Huang, Z. Wang and H. Dong, *Biosci. Rep.*, 2017, **37**, 1–10.

[68] O. J. Old, L. M. Fullwood, R. Scott, G. R. Lloyd, L. M. Almond, N. A. Shepherd, N. Stone, H. Barr and C. Kendall, *Anal. Methods*, 2014, **6**, 3901–3917.

[69] J. Nallala, G. R. Lloyd, N. Shepherd and N. Stone, *Analyst*, 2016, **141**, 630–639.

[70] J. Nallala, G. R. Lloyd, M. Hermes, N. Shepherd and N. Stone, *Vib. Spectrosc.*, 2017, **91**, 83–91.

[71] F. Palombo, M. Madami, D. Fioretto, J. Nallala, H. Barr, A. David and N. Stone, *J. Biophotonics*, 2016, **9**, 694–700.

[72] O. J. Old, G. R. Lloyd, J. Nallala, M. Isabelle, L. M. Almond, N. A. Shepherd, C. A. Kendall, A. C. Shore, H. Barr and N. Stone, *Analyst*, 2017, **142**, 1227–1234.

[73] C. Petibois, A. M. Melin, A. Perromat, G. Cazorla and G. Déléris, *J. Lab. Clin. Med.*, 2000, **135**, 210–215.

[74] D. Lafrance, L. C. Lands and D. H. Burns, *Talanta*, 2003, **60**, 635–641.

[75] M. Meinke, H. Albrecht, C. Antoniou and H. Richter, *J. Biomed. Opt.*, 2008, **13**, 014021–1–6.

[76] S. Liakat, K. A. Bors, L. Xu, C. M. Woods, J. Doyle and C. F. Gmachi, *Biomed. Opt. Express*, 2014, **5**, 2397–2404.

[77] S. Liakat, K. A. Bors, T. Y. Huang, A. P. M. Michel, E. Zanghi and C. F. Gmachl, *Biomed. Opt. Express*, 2013, **4**, 1083–1090.

[78] J. Kuligowski, G. Quintás, M. de la Guardia and B. Lendl, *Anal. Chim. Acta*, 2010, **679**, 31–42.

[79] A. V. Ewing, G. S. Clarke and S. G. Kazarian, *Biomicrofluidics*, 2016, **10**, 024125–1–13.

[80] G. R. Lloyd, J. Wood, C. Kendall, T. Cook, N. Shepherd and N. Stone, *Vib. Spectrosc.*, 2012, **60**, 43–49.

[81] P. Crow, B. Barrass, C. Kendall, M. Hart-Prieto, M. Wright, R. Persad and N. Stone, *Br. J. Cancer*, 2005, **92**, 2166–2170.

[82] Y. Yue, J. J. Wang, P. A. M. Basheer, J. J. Boland and Y. Bai, *Constr. Build. Mater.*, 2017, **135**, 369–376.

[83] M. Jermyn, K. Mok, J. Mercier, J. Desroches, J. Pichette, K. Saint-Arnaud, L. Bernstein, M. C. Guiot, K. Petrecca and F. Leblond, *Sci. Transl. Med.*, 2015, **7**, 1–11.

[84] I. E. I. Petterson, J. C. C. Day, L. M. Fullwood, B. Gardner and N. Stone, *Anal. Bioanal. Chem.*, 2015, **407**, 8311–8320.

[85] G. R. Lloyd, L. E. Orr, J. Christie-Brown, K. McCarthy, S. Rose, M. Thomas and N. Stone, *Analyst*, 2013, **138**, 3900–3908.

[86] A. Rajput, S. Kumar and J. P. Singh, *Analyst*, 2017, **142**, 3959–3966.

[87] G. Barbillon, V. E. Sandana, C. Humbert, B. Bélier, D. J. Rogers, F. H. Teherani, P. Bove, R. McClintock and M. Razeghi, *J. Mater. Chem.*, 2017, **5**, 3528–3535.

[88] F. Xu, S. Xie, H. Xu, X. Chen, H. Yu and L. Wang, *Appl. Surf. Sci.*, 2017, **410**, 566–573.

[89] C. Y. Zhang, R. Hao, B. Zhao, Y. Z. Fu, Y. W. Hao and Y. Q. Liu, *J. Mater. Sci.*, 2017, **52**, 11391–11401.

[90] J. Li, W. Zhang, H. Lei and B. Li, *Nano Res.*, 2017, 1–9.

[91] Y. Liu, C. Xu, Z. Zhu, Q. Zhu, A. G. Manohari and Z. Shi, *Appl. Surf. Sci.*, 2018, **427**, 830–836.

[92] Y. Zhao, X. Li, Y. Liu, L. Zhang, F. Wang and Y. Lu, *Sens. Actuators, B*, 2017, **247**, 850–857.

[93] S. Yuan, F. Ge, M. Zhou, Z. Cai and S. Guang, *Nanoscale Res. Lett.*, 2017, **12**, 1–5.

[94] Y. Kang, L. Zhang, H. Zhang, T. Wu and Y. Du, *J. Appl. Spectrosc.*, 2017, **84**, 225–230.

[95] X. Yang, Y. He, X. Wang and R. Yuan, *Appl. Surf. Sci.*, 2017, **416**, 581–586.

[96] Y. Wu, T. Jiang, Z. Wu and R. Yu, *Biosens. Bioelectron.*, 2018, **99**, 646–652.

[97] Y. Zhang, P. Yang, M. Abubaker, H. Muhammed, S. K. Alsaiari, B. Moosa, A. Almalik, A. Kumar, E. Ringe and N. M. Khashab, *ACS Appl. Mater. Interfaces*, 2017, **9**, 37597–37605.

[98] H. Shi, N. Chen, Y. Su, H. Wang and Y. He, *Anal. Chem.*, 2017, **89**, 10279–10285.

[99] W. Zhou, Y. F. Tian, B. C. Yin and B. C. Ye, *Anal. Chem.*, 2017, **89**, 6120–6128.

[100] A. Zengin, U. Tamer and T. Caykara, *J. Raman Spectrosc.*, 2017, **48**, 668–672.

[101] K. E. Shafer-Peltier, C. L. Haynes, M. R. Glucksberg and R. P. V. Duyne, *J. Am. Chem. Soc.*, 2003, **125**, 588–593.

[102] N. C. Shah, O. Lyandres, J. T. W. Jr., M. R. Glucksberg and R. P. V. Duyne, *Anal. Chem.*, 2007, **79**, 6927–6932.

[103] K. Ma, J. M. Yuen, N. C. Shah, J. T. Walsh, M. R. Glucksberg and R. P. V. Duyne, *Anal. Chem.*, 2011, **83**, 9146–9152.

[104] B. Sharma, P. Bugga, L. R. Madison, A. I. Henry, M. G. Blaber, N. G. Greeneltch, N. Chiang, M. Mrksich, G. C. Schatz and R. P. V. Duyne, *J. Am. Chem. Soc.*, 2016, **138**, 13952–13959.

[105] A. M. K. Enejder, T. G. Scecina, J. Oh, M. Hunter, W. C. Shih, S. Sasic, G. L. Horowitz and M. S. Feld, *J. Biomed. Opt.*, 2005, **10**, 031114–1–9.

[106] A. Tycova, J. Prikryl and F. Foret, *Electrophoresis*, 2017, **38**, 1977–1987.

[107] O. M. Buja, O. D. Gordan, N. Leopold, A. Morschhauser, J. Nestler and D. R. T. Zahn, *Beilstein J. Nanotechnol.*, 2017, **8**, 237–243.

[108] D. A. Jones, M. C. Parkin, H. Langemann, H. Landolt, S. E. Hopwood, A. J. Strong and M. G. Boutelle, *J. Electroanal. Chem.*, 2002, **538–539**, 243–252.

[109] M. C. Parkin, S. E. Hopwood, A. J. Strong and M. G. Boutelle, *Trends Anal. Chem.*, 2003, **22**, 487–497.

[110] D. Feuerstein, A. Manning, P. Hashemi, R. Bhatia, M. Fabricius, C. Tolias, C. Pahl, M. Ervine, A. J. Strong and M. G. Boutelle, *J. Cereb. Blood Flow Metab.*, 2010, **30**, 1343–1355.

[111] M. L. Rogers, P. A. Brennan, C. L. Leong, S. A. N. Gowers, T. Aldridge, T. K. Mellor and M. G. Boutelle, *Anal. Bioanal. Chem.*, 2013, **405**, 3881–3888.

[112] M. L. Rogers, D. Feuerstein, C. L. Leong, M. Takagaki, X. Niu, R. Graf and M. G. Boutelle, *ACS Chem. Neurosci.*, 2013, **4**, 799–807.

[113] M. L. Rogers, C. L. Leong, S. A. N. Gowers, I. C. Samper, S. J. Jewell, A. Khan, L. McCarthy, C. Pahl, C. M. Tolias, D. C. Walsh, A. J. Strong and M. G. Boutelle, *J. Cereb. Blood Flow Metab.*, 2017, **37**, 1883–1895.

[114] R. Kurita, K. Hayashi, X. Fan, K. Yamamoto, T. Kato and O. Niwa, *Sens. Actuators, B*, 2002, **87**, 296–303.

[115] C. K. Su, S. C. Yen, T. W. Li and Y. C. Sun, *Anal. Chem.*, 2016, **88**, 6265–6273.

[116] J. Zhao, Unpublished.

[117] G. Socrates, *Infrared Characteristic Group Frequencies*, Wiley & Sons Ltd, 2nd edn., 1994.

[118] *Contact and Orientation Effects in FT-IR ATR Spectra*, 2011.

[119] *Orientation Effects in ATR Spectra*, Perkin Elmer technical report, 2012.

[120] T. Clausen, O. L. Alves, M. Reinert, E. Doppenberg, A. Zauner and R. Bullock, *J. Neurosurg.*, 2005, **103**, 233–238.

[121] D. W. Nelson, B. Thornquist, R. M. MacCallum, H. Nyström, A. Holst, A. Rudehill, M. Wanecek, B. M. Bellander and E. Weitzberg, *BMC Med.*, 2011, **9**, 1–17.

[122] *ATR Accessories: An Overview*, Perkin Elmer technical report, 2004.

[123] *How to Select an Infrared Transmission Window*, Pike Technologies Application Note 0602.

[124] J. Shao, M. Lin, Y. Li, X. Li, J. Liu, J. Liang and H. Yao, *PLoS One*, 2012, **7**, e48127–1–e48127–6.

[125] C. H. Munro, W. E. Smith, M. Garner, J. Clarkson and P. C. White, *Langmuir*, 1995, **11**, 3712–3720.

[126] S. Nie and S. R. Emory, *Science*, 1997, **275**, 1102–1106.

[127] K. S. Lee and M. A. El-Sayed, *J. Phys. Chem. B*, 2006, **110**, 19220–19225.

[128] S. Kruszewski and M. Cyrankiewicz, *Acta Phys. Pol., A*, 2012, **121**, A68–A74.

[129] J. T. Edsall, J. W. Otvos and A. Rich, *J. Am. Chem. Soc.*, 1950, **72**, 474–477.

[130] G. D. Fleming, J. J. Finnerty, M. Campos-Vallette, F. Célis, A. E. Aliaga, C. Fredes and R. Koch, *J. Raman Spectrosc.*, 2009, **40**, 632–638.

[131] S. F. Parker, *Chem. Phys.*, 2013, **424**, 75–79.

[132] M. Kaminski, A. Kudelski and M. Pecul, *Journal of Physical Chemistry B*, 2012, **116**, 4976–4990.

[133] C. Jing and Y. Fang, *Chem. Phys.*, 2007, **332**, 27–32.

[134] *Raman Data and Analysis*, HORIBA Jobin Yvon application note.